QUANTUM CONTROL OF MOLECULAR FRAGMENTATION IN STRONG LASER FIELDS

by

MOHAMMAD ZOHRABI

B.S., University of Tehran, IRAN, 2003
M.S., Institute for Advanced Studies in Basic Sciences, IRAN, 2006

AN ABSTRACT OF A DISSERTATION

submitted in partial fulfillment of the
requirements for the degree

DOCTOR OF PHILOSOPHY

Department of Physics
College of Arts and Sciences

KANSAS STATE UNIVERSITY
Manhattan, Kansas
2014

Abstract

Present advances in laser technology allow the production of ultrashort ($\lesssim$5 fs, approaching single cycle at 800 nm), intense tabletop laser pulses. At these high intensities laser-matter interactions cannot be described with perturbation theory since multiphoton processes are involved. This is in contrast to photodissociation by the absorption of a single photon, which is well described by perturbation theory. For example, at high intensities ($\gtrsim 5 \times 10^{13}$ W/cm^2) the fragmentation of molecular hydrogen ions has been observed via the absorption of three or more photons. In another example, an intriguing dissociation mechanism has been observed where molecular hydrogen ions seem to fragment by apparently absorbing no photons. This is actually a two photon process, photoabsorption followed by stimulated emission, resulting in low energy fragments. We are interested in exploring these kinds of multiphoton processes.

Our research group has studied the dynamics and control of fragmentation induced by strong laser fields in a variety of molecular targets. The main goal is to provide a basic understanding of fragmentation mechanisms and possible control schemes of benchmark systems such as H_2^+. This knowledge is further extended to more complex systems like the benchmark H_3^+ polyatomic and other molecules. In this dissertation, we report research based on two types of experiments. In the first part, we describe laser-induced fragmentation of molecular ion-beam targets. In the latter part, we discuss the formation of highly-excited neutral fragments from hydrogen molecules using ultrashort laser pulses. In carrying out these experiments, we have also extended experimental techniques beyond their previous capabilities.

We have performed a few experiments to advance our understanding of laser-induced fragmentation of molecular-ion beams. For instance, we explored vibrationally resolved spectra of O_2^+ dissociation using various wavelengths. We observed a vibrational suppression effect in the dissociation spectra due to the small magnitude of the dipole transition moment, which depends

on the photon energy — a phenomenon known as Cooper minima. By changing the laser wavelength, the Cooper minima shift, a fact that was used to identify the dissociation pathways. In another project, we studied the carrier-envelope phase (CEP) dependences of highly-excited fragments from hydrogen molecules. General CEP theory predicts a CEP dependence in the total dissociation yield due to the interference of dissociation pathways differing by an even net number of photons, and our measurements are consistent with this prediction. Moreover, we were able to extract the difference in the net number of photons involved in the interfering pathways by using a Fourier analysis. In terms of our experimental method, we have implemented a pump-probe style technique on a thin molecular ion-beam target and explored the feasibility of such experiments. The results presented in this work should lead to a better understanding of the dynamics and control in molecular fragmentation induced by intense laser fields.

QUANTUM CONTROL OF MOLECULAR FRAGMENTATION IN STRONG LASER FIELDS

by

MOHAMMAD ZOHRABI

B.S., University of Tehran, IRAN, 2003
M.S., Institute for Advanced Studies in Basic Sciences, IRAN, 2006

A DISSERTATION

submitted in partial fulfillment of the
requirements for the degree

DOCTOR OF PHILOSOPHY

Department of Physics
College of Arts and Sciences

KANSAS STATE UNIVERSITY
Manhattan, Kansas
2014

Approved by:

Major Professor
Itzik Ben-Itzhak

Copyright

Abstract

Present advances in laser technology allow the production of ultrashort ($\lesssim$5 fs, approaching single cycle at 800 nm), intense tabletop laser pulses. At these high intensities laser-matter interactions cannot be described with perturbation theory since multiphoton processes are involved. This is in contrast to photodissociation by the absorption of a single photon, which is well described by perturbation theory. For example, at high intensities ($\gtrsim 5 \times 10^{13}$ W/cm^2) the fragmentation of molecular hydrogen ions has been observed via the absorption of three or more photons. In another example, an intriguing dissociation mechanism has been observed where molecular hydrogen ions seem to fragment by apparently absorbing no photons. This is actually a two photon process, photoabsorption followed by stimulated emission, resulting in low energy fragments. We are interested in exploring these kinds of multiphoton processes.

Our research group has studied the dynamics and control of fragmentation induced by strong laser fields in a variety of molecular targets. The main goal is to provide a basic understanding of fragmentation mechanisms and possible control schemes of benchmark systems such as H_2^+. This knowledge is further extended to more complex systems like the benchmark H_3^+ polyatomic and other molecules. In this dissertation, we report research based on two types of experiments. In the first part, we describe laser-induced fragmentation of molecular ion-beam targets. In the latter part, we discuss the formation of highly-excited neutral fragments from hydrogen molecules using ultrashort laser pulses. In carrying out these experiments, we have also extended experimental techniques beyond their previous capabilities.

We have performed a few experiments to advance our understanding of laser-induced fragmentation of molecular-ion beams. For instance, we explored vibrationally resolved spectra of O_2^+ dissociation using various wavelengths. We observed a vibrational suppression effect in the dissociation spectra due to the small magnitude of the dipole transition moment, which depends

on the photon energy — a phenomenon known as Cooper minima. By changing the laser wavelength, the Cooper minima shift, a fact that was used to identify the dissociation pathways. In another project, we studied the carrier-envelope phase (CEP) dependences of highly-excited fragments from hydrogen molecules. General CEP theory predicts a CEP dependence in the total dissociation yield due to the interference of dissociation pathways differing by an even net number of photons, and our measurements are consistent with this prediction. Moreover, we were able to extract the difference in the net number of photons involved in the interfering pathways by using a Fourier analysis. In terms of our experimental method, we have implemented a pump-probe style technique on a thin molecular ion-beam target and explored the feasibility of such experiments. The results presented in this work should lead to a better understanding of the dynamics and control in molecular fragmentation induced by intense laser fields.

Table of Contents

List of Figures

List of Tables

Acknowledgments

I am indebted to many people for helping me to reach this stage. It has not been easy at times, but always a pleasure, and in many ways enjoyable. I owe a number of people a personal thanks. I would like to express my deepest thanks to my advisor, Professor Itzik Ben-Itzhak. Working with him and his group was a truly enjoyable and rewarding experience. His patience, encouragement, and immense knowledge combined with his perpetual enthusiasm were key motivations throughout my Ph.D. He imbued me with his infectious optimism and taught me to be meticulous during my research. I would like to thank Dr. Kevin Carnes for his endless support and curiosity during our discussions as well as patiently educating us on how to code in SpecTcl. Kevin, thank you for proofreading this dissertation and teaching me how to write in lucid and mellifluous English. I would like to acknowledge Professor Brett Esry for his critical views on scientific works. He taught me how to be a better physicist by questioning basic physics knowledge, and I greatly enjoyed learning AMO physics from the courses he taught. His support and helpful discussions were crucial for finalizing many of my projects. I would like to express my sincere thanks to Professor Brett Esry, Professor Ryszard Jankowiak, Dr. Carlos Trallero, Dr. Kevin Carnes, and Dr. Hayder Rasheed for kindly agreeing to be on my thesis committee. Moreover, I am grateful that Dr. Charles Fehrenbach was kind enough to serve as a proxy for Dr. Kevin Carnes at my defense.

I am very grateful for having the opportunity of being part of the outstanding research at the J. R. Macdonald Laboratory. The lab has provided the best infrastructure and equipment as well as an excellent working atmosphere with great researchers that like to help one another. Working with Itzik's creative group was gratifying. It is no overstatement to say that without the consistent guidance, tutelage, and encouragement of our previous post-doc, Jarlath McKenna, and senior group members such as A. Max Sayler, Bishwanath Gaire, and Nora G. Kling, this thesis

would never have existed. Jarlath, we spent endless hours in the lab together, and your passion for scientific research inspired me. You taught me how to sort and analyze the data, and I greatly appreciate all of your help. Max, I learned a lot about our electronics, detectors, and how our data acquisition really works from you. Bishwanath, before you graduated, you and I were the only members of our group. I enjoyed our time in the lab, and your Ph.D. research on improving our apparatus so that we could measure breakup with nearly zero kinetic energy release has benefited my work immensely. I should also thank all of our current group members, Utuq Ablikim, Ben Berry, Bethany Jochim and Travis Severt. Utuq and Bishwanath, we shared long hours in the lab trying to run experiments, and it was all enjoyable. Ben, you helped in the analysis of the excited fragments. Bethany and Travis, you were both our summer REU students, and I am glad that you are part of our group and wish you all the best for your ongoing research. I also wish to acknowledge an excellent collaboration with Dr. Eric Wells and his group, which has resulted in many interesting coherent control experiments. I learned a lot from these exciting research opportunities. I was fortunate to be involved in multiple collaborative experiments carried out at the J. R. Macdonald Laboratory with Dr. Oded Heber, Dr. Uri Lev and Dr. Leigh Graham. I wish to thank Dr. Thorsten Weber, Dr. Allen Landers, my advisor Itzik, and Professor Lew Cocke for giving me the opportunity to be engaged in exciting experiments at the Advanced Light Source at Berkeley National Laboratory.

To my colleagues at Kansas State University, a major thank you. Varun "Mac" Makhija, we had a great time together, and I always find your passion inspiring. Thank you for all the fruitful discussions. I met many wonderful new friends during my Ph.D., and I would like to name a few: Dr. Sean McBride, Dr. Varun "Mac" Makhija, Dr. Bachana Lomsadze, Dr. Jackie Chini, Dr. Michael Chini, Wes Erbsen, Dr. Leigh Graham, Dustin Ursrey, Brandon Rigsbee, Dr. Yujun Wang, Neda Dadashzadeh, Dr. Nora Kling, Bethany Jochim, Utuq Ablikim, Travis Severt, Ben Berry, Dr. Sankar De, Dr. Matthias Kling, Dr. Irina Bocharova, Dr. Christian Madsen, Dr. Maia Magrakvelidze, Sachiko Toda, Dr. Chris Nakamura, Dr. Jesus Hernández, Dr. Fatima Anis, Dr. Siddique Khan, Dr. Fran Mateycik, Dr. Zhenhua Wang, Dr. Matthias Kübel, Jianjun Hua,

Dr. Kelsie Betsch, Aram Vajdi, Adam Summers, and soon to be Dr. Shuo Zeng. Sean, Mac, Bachana, Shuo, and Wes, we had great time together, and I enjoyed every moments of my time, so thank you. You guys made my Ph.D. study more pleasant. Leigh, I enjoyed our collaboration and your visit to Kansas State University. You have a great personality, and I wish you luck in your future career. Many thanks must also go to Professor Brett Esry's group members for invaluable theoretical contributions to this work. Neda, thank you for all the positive energy and cooking delicious food, specifically tasty fesenjoon.

I wish to thank Professor Zenghu Chang's group (especially Dr. Hiroki Mashiko, Dr. Steve Gilbertson, Dr. Kun "Harry" Zhao, Dr. Michael Chini, and Dr. Baozhen Zhao) for helping and educating me about the KLS laser system in the early stages of my research career. I would like to thank Dr. Vinod's Kumarapan's group (Dr. Ren Xiaoming and Dr. Varum Makhija) for contributing to the laser-matter experiments with the KLS laser system. Thank you, Dr. Charles Fehrenbach, for your unlimited support with the ECR ion source and PULSAR laser system. I am also thankful for the technical support provided by many excellent staff members at the J. R. Macdonald Laboratory. Mike Wells and Al Rankin have always been helpful with vacuum systems and have guided us in designing a great number of components used in the experiments presented in this dissertation. Scott Chainey has been a great help in all matters related to our electronics. I wish to thank Vince Needham for his endless assistance in resolving our computer issues and LabVIEW bugs. Lastly, I was fortunate to be a part of Physics department at Kansas State University. A warm thanks goes to all the nice people in the Physics department.

Finally, I would like to thank my family for their support over all these years. Mom, Dad, and Dina, you were always encouraging. A special thanks to my aunt and uncle, Leah and Reza, for your ceaseless love and care during my research. I am deeply indebted to both of you, and I will never forget all the assistance you provided when I came to the United States. I am very happy to have found many new friends here in Kansas, especially the most wonderful person in my life, my lovely wife, Amy. A special thanks to you for your everlasting love, patience, encouragement, and support at every turn. You are amazing, and I look forward to our future together.

Financial support from the Chemical Sciences, Geosciences, and Biosciences Division, Office of Basic Energy Sciences, Office of Science, U.S. Department of Energy is fully acknowledged.

Dedication

Dedicated to my parents, my sister, my friends, and my lovely wife, Amy

تقدیم به پدر، مادر، خواهر و ایمی عزیزم

List of abbreviations

AMO atomic, molecular, and optical physics
ASE amplified spontaneous emission
ATD above-threshold dissociation
ATI above-threshold ionization
BO Born-Oppenheimer
BR branching ratios
BS bond softening
BBO Beta-barium borate
CI configuration interaction
CM center-of-mass
CEP carrier-envelope phase
CFD constant-fraction discriminator
CPA chirped-pulse amplification
DFG difference-frequency generation
ECR electron cyclotron resonance
EIT electromagnetically induced transparency
FC Faraday cup
FEL free electron laser
FTL Fourier-transform limited
FTI frustrated tunneling ionization
FROG frequency resolved optical gating
FTSI Fourier transform spectral interferometry
FWHM full-width at half-maximum
GSD ground state dissociation
GVD group-velocity dispersion
HHG high-harmonic generation
HCF hollow-core fiber
IS imaging spectrometer
KDP potassium dihydrogen phosphate
KER kinetic energy release
KLS Kansas light source
LFI longitudinal field imaging
LIMDI laser-induced molecular dissociation imaging
LATFI longitudinal and transverse field imaging
MCP microchannel plate
NAC non-adiabatic coupling

OPG optical parametric generation
OPA optical parametric amplification
PG polarization gating
PAP parametric asymmetry plot
PEC potential energy curve
SD self diffraction
SH second harmonic
SHG second-harmonic generation
SFG sum-frequency generation
SPM self-phase modulation
TDC time-to-digital converter
THG third-harmonic generation
TOF time-of-flight
TISE time-independent Schrödinger equation
TDSE time-dependent Schrödinger equation
VMI velocity map imaging
ZPD zero-photon dissociation

Chapter 1

Introduction

Contents

1.1 Overview

Understanding molecular structure and dynamics is an essential part of molecular science studies. More than a century ago, early experiments led by von Laue, the Braggs (father and son), Pauling, and others explored the nature of chemical bonds by X-ray crystallography [1–7], which resulted in the 1914 Nobel Prize [8]. Advances in X-ray crystallography contributed significantly to the understanding of the molecular structure of DNA and its replication mechanism [9, 10]. Chemical reactions are dynamical processes in which the structure of a system changes on a fast time scale. In 1940s and 1950s, chemical reactions were studied on the milli- to micro-second time scales [11–15]. In the late sixties and seventies, chemical reactions in solutions were studied with picosecond resolution [16–21]. In the 1960s, chemical reaction studies using molecular beams were developed, which later earned the 1986 Nobel Prize for Herschbach, Lee and Polanyi [22].

In the past 30 years, the advent of ultrafast pulses of light has allowed scientists to study chemical reactions on the femtosecond (fs) and attosecond[1] (as) time scales. Pioneering experiments by Zewail *et al.* [23, 24] used the pump-probe experimental technique, in which a pump pulse initiates

[1] A femtosecond and an attosecond are 10^{-15} and 10^{-18} seconds, respectively.

a dynamical process and a second pulse (probe) is used to examine the evolution of the process. This area of science in which the molecular reaction dynamics are studied on extremely short time scales (fs) is referred to as *femtochemistry* and was awarded the 1999 Nobel Prize in chemistry [25].

Nowadays, ultrashort laser pulses are so intense that perturbation theory approaches describing the laser-matter interaction break down, leading to nonlinear phenomena, namely multiphoton processes. The simplest diatomic molecule consist of two protons bound by an electron, namely hydrogen molecular ion. Most of the experiments have used H_2 and its isotopic D_2 molecules as a target in a laser field. In particular, the hydrogen molecular ion is produced by ionizing the neutral H_2 molecules. In most of the experiments, the same laser pulses are used to study laser interaction, in which the interpretation of results from first step ionization followed by dissociation or ionization can be difficult. In the early 90s, Bucksbaum *et al.* [26] reported molecular bond softening (BS) in H_2^+ from H_2 target due to interaction with strong laser fields, resulting in dissociation to H^++H. Photodissociation of H_2^+ following the absorption of a single photon is well studied [27–29]. 800 nm laser pulses can photodissociate H_2^+ from high vibrational levels but not from the lower vibrational levels. Therefore, a molecule with lower vibrational states dissociates via absorption and stimulated emission of several photons. Finally, in the case of H_2^+, the bond is softened and the molecule is fragmented by absorption of net one photon [26]. Bucksbaum *et al.* [30] also demonstrated that molecules can absorb a net number of photons larger than the minimum necessary to dissociate. This phenomenon is referred to as above-threshold dissociation (ATD) and is well studied [26, 31–37].

The development of ultrashort tabletop laser systems has enabled researchers to explore and control molecular dynamics induced by the laser field [38–48]. Recently, control of molecular dynamics by using excited vibrational or rotational nuclear wavepackets has been realized [49–51]. The control aspect of molecular reactions has drawn great attention within the atomic, molecular, and optical physics (AMO) community. Several control schemes have been introduced in the weak- and strong-field regimes [38, 40, 42–44, 52–59] and two examples are given below.

Tannor, Rice, and Koslof [42–44] suggested a "pump-dump" process, in which a first laser

pulse is used to excite a ground electronic state to a higher electronic state (pump). A second laser pulse stimulates emission back to a lower electronic state (dump). Careful control of the timing between the two pulses can be used to enhance the production of specific final products. In addition to the timing between the laser pulses, optimizing the shape of the laser pulses is used to achieve optimal control. For more on optimal control theory see Refs. [52, 60–69], and references therein. In a different approach, Shapiro and Brumer [38, 52–54] proposed a control scheme through interference between different pathways leading to a specific final state. By tailoring the spectral phase of the laser pulse, i.e. pulse shaping, one can enhance or suppress the final product. Nowadays, tailoring the amplitude and phase of ultrashort laser pulses is accomplished by various pulse shaping methods [70].

In both of the control schemes described above, one can identify the control parameters for a given system and implement them to achieve control over the process of interest. However, in a different approach, one can search through parameter space and use the outcome of the process as feedback to optimize the results. In this approach, a genetic or self-learning algorithm can be beneficial. For instance, pulse-shaping techniques become a practical tool when self-learning feedback loop algorithms are employed and is referred to as adaptive femtosecond control [40, 55–59]. In short, the experimental outcome is utilized as a feedback for the learning algorithm, in which the amplitudes and/or phases of the laser pulses are adjusted. Thus, the final objective is achieved in an iterative way. For example, this method was successfully applied to control photodissociation in the gas and liquid phases [40, 57]. Recently, this method was extended to strong-field control of the isomerization dynamics in acetylene molecules [71]. The drawback of this method is that extracting the physics involved in the process leading to control remains challenging. Therefore, studying systems that are better understood can be a good way to pursue control experiments. A few examples of these studies are reviewed below.

Control employing simple shaped laser pulses, for example chirped pulses, is used in several experiments. For instance, experiments using a shaped femtosecond laser pulse show a strong chirp dependence in the ionization yield of sodium dimers [72]. Prabhudesai *et al.* [73] explored

H_2^+ dissociation and observed an up and down shift in the kinetic energy release kinetic energy release (KER) of specific vibrational levels that corresponds to different chirp signs. The follow-up study of Natan *et al.* [74] reported an enhancement in the strong-field dissociation yield of low-lying vibrational levels ($v \leq 6$) of H_2^+ by varying the magnitude and sign of the chirp.

Another class of studies uses the relative phase between two-color laser fields or the carrier-envelope phase (CEP) as a control parameter. Control of molecular reactions using these parameters has been predicted [75–78] and observed [48, 79–90]. In the case of a two-color field, control is achieved by varying the relative phase between the two frequencies [48, 75–90]. Sheehy *et al.* [48] observed spatial asymmetry in the emission direction of ionic fragments of HD as a function of this relative phase following the dissociation of HD^+. Another type of control is known as channel asymmetry and relates to control of the dissociation products, or branching ratios, which are distinguishable in a heteronuclear molecule. For instance, HD^+ may preferentially dissociate to either $H^+ + D(1s)$ or $H(1s) + D^+$ [75, 76]. This channel asymmetry, to our knowledge, has never been observed in CEP or two-color control experiments. In fact, Sheehy *et al.* [48] specifically report no channel asymmetry in a two-color experiment on HD (532 nm and 1064 nm) which is in agreement with theory [75]. Control of spatial asymmetry in various molecular targets has been observed by other groups using two-color laser fields [48, 79, 81, 85, 87, 88] or CEP [80, 82–84, 89, 90].

Finally, it is essential to note that this introduction is general, while more specific background relevant to each project is given at the beginning of each section due to the wide range of work covered.

1.2 Our Focus

At J.R. Macdonald Laboratory, our group focuses mainly on investigating the interaction between ultrashort laser pulses and molecular ion-beam targets. For this purpose, we have studied benchmark diatomic systems, such as H_2^+, for which the theoretical treatment is nearly exact [36, 89, 91–96]. This research has been extended to the fragmentation of benchmark polyatomic targets such as H_3^+, D_3^+,and D_2H^+ [97–101]. We have also explored the laser-induced fragmentation of more

complex molecular ion-beam targets such as, O_2^+, N_2^+, CO^+, NO^+, CO^{2+}, NO^{2+}, N_2O^+, CO_2^+ etc. [37, 102–105]. The overall goal of these studies is to understand the mechanism underlying the laser-induced molecular fragmentation of benchmark systems and utilizing this knowledge to explore more complex system.

Our group's research has not been limited to molecular ion-beam targets. For instance, in a collaborative work led by Eric Wells from Augustana College, we have implemented a closed-loop feedback method in which the pulse shape was adjusted using a genetic algorithm supplied with experimental feedback from a velocity map imaging (VMI) apparatus [71, 106–109]. In another study, our group has explored the production mechanism of highly excited D^* fragments from D_2 molecules employing a time-of-flight (TOF) method [98]. In these measurements, we examined the frustrated tunneling ionization (FTI) mechanism introduced by Manschwetus *et al.* [110] as well as other production mechanisms such as electron recollision. Our measurements of D^* formation include a study of dependence on pulse duration, intensity and ellipticity as well as the angular distribution dependence of D^* formation.

In particular, my research has been focused on a variety of projects that have the common theme of controlling molecular processes. I was involved in two families of experiments as described in this dissertation. In the early part of my research, I was focused on understanding and controlling laser-induced fragmentation in molecular ion-beam targets. For instance, in the experiment carried out on dissociation of an O_2^+ target, we implemented the knowledge gained from our previous study [102] to explore the Cooper minima in the vibrationally resolved dissociation spectra of O_2^+ using various wavelengths (784 nm, 392 nm, and 261 nm). In another study, we investigated the chirp dependence in the dissociation of HD^+ which leads to two distinguishable final products, namely H^++D($1s$) and H($1s$)+D^+. In the second phase of my research, I studied a neutral hydrogen molecule target for which the CEP dependence of the formation of highly excited fragments was explored. One of our goals was to examine theoretical predictions of CEP dependeces by Esry and coworkers [76, 111, 112] for a complex system such as a D_2 Rydberg series. In addition, I used Fourier analysis to extract information about the difference in the net number of

photons involved in the interfering pathways. In parallel to my research, I attempted to advance our experimental capabilities by improving the flux of second-harmonics as well as generating third harmonics via difference-frequency generation. Lastly, I implemented the pump-probe technique to study laser-induced fragmentation on molecular ion-beam targets.

1.3 Document Structure

Our goal was to gain an understanding of nuclear dynamics induced by ultrashort laser pulses. For this purpose various laser parameters were varied. One of our tasks is to identify the proper control parameters. A few of these parameters are bandwidth, wavelength, chirp, relative phase between multi-color, time delay of pump-probe pulses, pulse shaping by changing the spectral phase and/or amplitude, and carrier-envelope phase (CEP). The basic concepts of the laser systems and various pulse characterization methods used in this work are described in Chapter 2. This dissertation is comprised of two main research efforts associated with the two families of experiments conducted. Chapter 3 covers the experimental results from laser-induced dissociation of molecular ion-beam targets. In Chapter 4, control via the CEP has been observed experimentally in the fragmentation of D_2 molecules into Rydberg deuterium fragments.

More specifically, Chapter 3 focuses on laser-induced molecular dissociation. The chapter starts by describing the imaging method used for these studies followed by the experimental results using different laser parameters and targets. The experimental results within this chapter are composed of:

Section 3.3 – Vibrationally-resolved structure in O_2^+ dissociation using a few wavelengths

Section 3.4 – Rudimentary coherent control

- Effective bandwidth narrowing – linear chirp effect in dissociation of H_2^+
- Chirp effect in zero photon dissociation of HD^+

Section 3.5 – Branching ratios in the dissociation of HD^+ using a "single-color" laser field

Section 3.6 – Control over dissociation of a molecular-ion beam by a two-color laser field

Section 3.7 – Developing pump-probe studies of molecular ion-beam fragmentation

Each section includes a brief introduction followed by a short section describing the relevant experimental details. Then we discuss the results of each study with a brief summary.

Chapter 4 presents the results of control via the carrier-envelope phase of D^* formation in D_2 fragmentation. In the beginning we present the method used for measuring these highly excited fragments. A general theory of CEP [111] dependences attributes the oscillations of these observables to interference between dissociation pathways involving a different net number of photons. Finally, in Chapter 5, the conclusion and perspectives for future work are given.

Chapter 2

Intense Ultrashort Laser Pulses

Contents

Synopsis. Experimental studies of molecular fragmentation in a strong field have been improved greatly by the advancement of laser systems in the past decades. One of the prime instruments used for these studies is the amplified Ti:Sapphire laser source. This light source is commercially available with pulse durations of 20–100 fs and pulse energies of a few mJ to a few hundred mJ [113–119]. Nowadays, the central wavelength and spectral bandwidth of a laser pulse can be modified by a number of nonlinear techniques. Generating ultrashort laser pulses of about 5 fs is accomplished through a nonlinear process called self-phase modulation (SPM) [120, 121]. The experiments in this work have been carried out using femtosecond laser pulses at a few wavelengths and various pulse durations. In this chapter, the general principle of a femtosecond kHz

Ti:Sapphire laser system is briefly described. In addition, the nonlinear process leading to the generation of the second and third harmonics of the fundamental frequency of the laser pulse is explained. The technique used for generating ultrashort laser pulses from a Ti:Sapphire laser is presented. Multiple pulse characterization methods, which are used in this work to characterize different laser pulses, are summarized. Lastly, the characterization of carrier-envelope phase (CEP) of ultrashort laser pulses using the stereo above-threshold ionization (ATI) spectrometer is discussed [122, 123].

2.1 Introduction

All the experiments presented in this work use femtosecond laser systems located at the JRM laboratory. The electric field of the laser pulses can be written in both the time and frequency domains. For convenience, the electric field is represented by a complex quantity, however the measured electric fields are real [120]. The electric field can be written as

$$\begin{aligned} \tilde{E}(\omega) &= \int_{-\infty}^{\infty} E(t) e^{-i\omega t}\, dt = \left|\tilde{E}(\omega)\right| e^{i\Phi(\omega)} \\ E(t) &= \frac{1}{2\pi} \int_{\infty}^{-\infty} \tilde{E}(\omega) e^{i\omega t}\, d\omega, \end{aligned} \tag{2.1}$$

where $\left|\tilde{E}(\omega)\right|$ represent the spectral amplitude, and $\Phi(\omega)$ and is the spectral phases. The complex field in the frequency domain is the Fourier transform of the temporal field. Because $E(t)$ is a real function and $\tilde{E}(\omega) = \tilde{E}^*(\omega)$. For a Gaussian laser pulse, the relation between the frequency bandwidth measured at full-width at half-maximum (FWHM), $\Delta\omega$, and pulse duration (FWHM), $\Delta\tau$, is given by a time-bandwidth product [124], $\Delta\omega\,\Delta\tau \geq \frac{0.441}{2\pi}$ or $\frac{c\,\Delta\lambda\Delta\tau}{\lambda^2} \geq 0.441$, where c is the speed of light, λ is the central wavelength and $\Delta\lambda$ is the spectral bandwidth in nm. The constant, 0.441, depends on the pulse shape (see Ref. [124]).

For a given spectral bandwidth, the shortest laser pulse duration, the so-called Fourier-transform limited (FTL) pulse duration, is calculated by the time-bandwidth product. For a FTL laser pulse, all the frequency components have zero phase difference with respect to the central frequency.

2.2 Femtosecond kHz Laser Systems

Two laser systems were used for the work presented in this dissertation. Both lasers systems, located in the James R. Macdonald Laboratory, are based on a Ti:Sapphire oscillator and a Ti:Sapphire multipass amplifier. The first is a homemade laser system named the Kansas light source (KLS). This system generates linearly s-polarized[1] laser pulses, duration of 25–30 fs FWHM in intensity, with 2 mJ energy at a repetition rate of 2 kHz and a central wavelength of ∼790 nm. The second laser system, which we call PULSAR, produces linearly p-polarized ultrashort laser pulses, 21 fs FWHM in intensity, with 2 mJ energy at a repetition rate of 10 kHz and a central wavelength around 800 nm. The schematic layout of our optics table is described in Appendix A.

The operating principles of Ti:Sapphire oscillators and amplifiers for these two systems are briefly described in the following section. Following that, a concise description of how to generate, compress and characterize few-cycle laser pulses is given.

2.2.1 Oscillator

The femtosecond laser pulses are generated by pumping a Ti:Sapphire crystal with a continuous 532 nm laser beam. The laser pulses are generated through a mechanism called Kerr-lens mode-locking [125, 126], in which the nonlinear medium behaves as a lens for a laser beam with a Gaussian intensity profile. In other words, the refractive index of the medium, n, depends on the intensity of the laser field, $n(I) = n_0 + In_2$ [120]. Here, n_0 is the low-field value of the refractive index at some center frequency, ω_0, n_2 is the nonlinear refractive index, which is material dependent, and I is the laser pulse intensity. In most laser materials $n_2 > 0$, and hence the laser pulse increases the refractive index.

The laser pulses, in both of our systems, are generated in a Kerr-lens mode-locked Ti:Sapphire oscillator with a repetition rate of ∼80 MHz and output power of a few hundred mW (see Table 2.1 for more specific details). The group-velocity dispersion (GVD) is compensated by a pair of prisms in the PULSAR oscillator and a pair of chirped mirrors in the KLS oscillator. The oscillator output

[1] s- and p-polarized light are linearly polarized, with electric fields perpendicular and parallel to the optics table, respectively.

	KLS	PULSAR
Repetition rate (MHz)	78	75.2
Average power (mW)	350	>300
Bandwidth (nm)	90	80
Pulse energy (nJ)	4.5	4
Pulse duration (fs)	12	14
Central wavelength (nm)	790	780

Table 2.1: Typical operation parameters for the KLS and PULSAR oscillators.

is split into two pulse trains. Half of the beam is used to seed the amplifier and the other half is sent toward a f-2f interferometer used for CEP stabilization [127–132]. A typical spectrum of the PULSAR oscillator during mode-locked operation is shown in Fig. 2.1(a).

2.2.2 Multipass Amplifier and Compressor

The laser pulses generated by the oscillator are too weak (few nJ) to use for the strong-field experiments presented in this dissertation. These pulses need to be amplified while maintaining the spectral bandwidth of the oscillator pulses. The amplification is based on the concept introduced by Strickland and Mourou [133], which is called chirped-pulse amplification (CPA). The amplifier can be divided into a few main components: a stretcher, a multipass amplifier, and a compressor. A detailed description of a CPA femtosecond laser system can be found in Ref. [124]. A schematic view of a laser system using the CPA concept is shown in Fig. 2.2. In such a system, the laser pulses provided by the oscillator are stretched in time to avoid damage to the amplifier gain medium. A grating-based stretcher is used in both of our systems, to stretch the pulses to tens of ps.

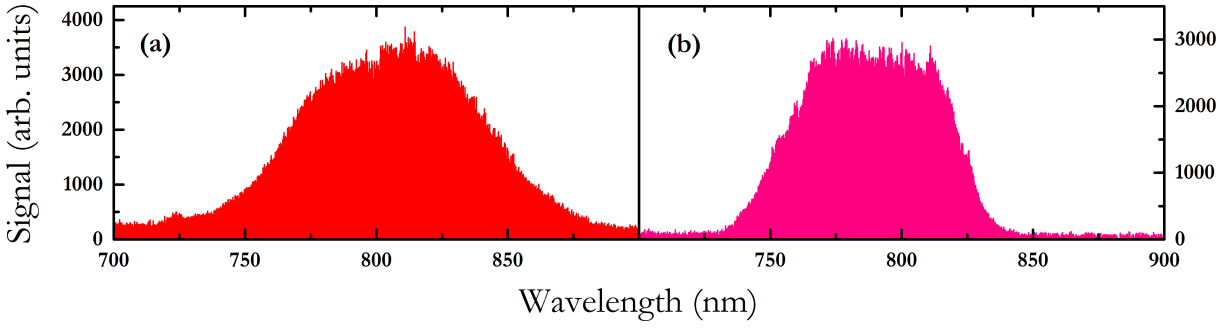

Figure 2.1: Typical PULSAR spectra measured after the (a) oscillator and (b) amplifier.

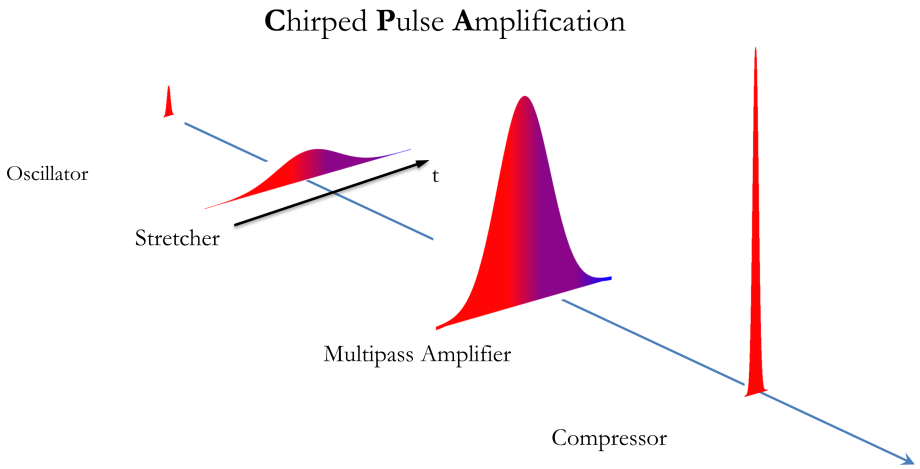

Figure 2.2: A schematic view of the evolution of pulse duration and amplitude during chirped-pulse amplification (CPA).

After the stretcher, a single pulse is selected out of many by a Pockels cell [134] to reduced the repetition rate. For instance, in the case of the KLS, 2 pulses are amplified out of 78000 pulses from the oscillator, resulting in a repetition rate of 2 kHz. These "lucky" pulses are further amplified through the multipass amplifier. In both of our systems, the amplifier gain medium consists of a Ti:Sapphire crystal, which is pumped by a Nd:YAG laser. In the KLS, the amplification occurs by passing the stretched pulses fourteen times through the gain medium. After the first seven passes, a second Pockels cell is introduced to block the amplified spontaneous emission (ASE). For more details on the KLS system and its application see Refs. [115, 135–139].

In the PULSAR system, the amplification takes place in two stages [113]. In the first stage, the seed beam is stretched and selected though a Pockels cell to maintain a 10 kHz repetition rate. The beam is then amplified in a fourteen pass amplifier with a Ti:Sapphire gain medium. The pulse energy is 1 mJ after this stage. A second Pockels cell is introduced to reduce the ASE. The beam is further amplified through a second Ti:Sapphire crystal in a bowtie-shaped amplifier with 5 passes to acquire 2 mJ of pulse energy. In the KLS, the Ti:Sapphire crystal is cooled down by a liquid nitrogen reservoir. This reservoir needs to be refilled every 8–10 hours. However, the PULSAR crystals are cooled down using a closed-loop, liquid helium cryogenic cooler. This allows for continuous operation of PULSAR under stable conditions.

The chirped output pulses are sent to a grating-based compressor to reduce the pulse duration to approximately the Fourier-transform limit (FTL). In principle, a pair of gratings will add enough negative GVD to compensate for the chirp introduced by the stretcher and propagation through the whole system.

2.2.3 Spectral Broadening

An intense ultrashort laser pulse can cause self phase modulation (SPM) by traveling through a medium, which is a nonlinear effect due to the variation of the index of refraction with the intensity of the laser pulse [120]. In other words, the index of refraction depends on the temporal intensity profile of the laser pulse, $n(\omega, I) = n_0(\omega) + n_2 I(t)$ (see Section 2.2.1). The intensity dependence of the refractive index leads to a nonlinear phase shift, given by $\phi(t) = \omega_0 t - kz = \omega_0 t - (2\pi/\lambda_0)n(I)z$, where ω_0 and λ_0 are the carrier frequency and wavelength. SPM induces a frequency chirp in the temporal profile of the laser pulse resulting in spectral broadening. The chirp after laser propagation of distance L can be written as,

$$\omega(t) = \frac{\partial \phi(t)}{\partial t} = \omega_0 - \frac{2\pi n_2 L}{\lambda} \frac{\partial}{\partial t} I(t). \tag{2.2}$$

The concept of spectral broadening through SPM in a hollow-core fiber (HCF) filled with gas was first introduced by Nisoli *et al.* [121]. This method is widely used for the generation of ultrashort high energy laser pulses [140–144]. In an optical fiber, the index of refraction of the core is higher than the index of refraction in the cladding, resulting in total internal reflection [145]. This is one of the main reasons for using these fibers for communication purposes. The light can travel a long distance with no losses even if the fiber is bent. In contrast, in a HCF the index of refraction is higher in the cladding, the light is guided through the fiber by grazing incidence reflection from the walls [146, 147]. The light can then escape through the walls of the fiber, causing such a fiber to be lossy. Therefore, the HCF must be kept straight so that the fundamental mode can propagate in the fiber with minimum losses.

Marcatili and Schmeltzer [148] calculated the modes for a hollow-core fiber with a radius a in cylindrical coordinates, with the assumption of $a \gg \lambda$. The EH_{11} mode has the lowest loss, and

the intensity profile of this mode can be written as,

$$I_{EH_{11}}(r) = I_0 J_0^2(\frac{2.405r}{a}),\ r < a, \tag{2.3}$$

where J_0 is the zeroth-order Bessel function, and I_0 is the peak intensity [148]. A Gaussian beam intensity profile is usually defined as $I_{Gaussian}(r) = I_0 \exp(-\frac{2r^2}{r_0^2})$, where I_0 is the peak intensity and r_0 is the radius of the Gaussian beam at the focus. To achieve the maximum transmission (coupling) through the fiber, Abrams [149] calculated the optimum focus size for a Gaussian beam coupling. The optimal focus size for the most efficient coupling was found to be $r_0 = 0.64a$ [149–151].

In our setup, the laser is focused by a spherical lens at the entrance of a meter long single mode HCF filled with a noble gas. The schematic of our HCF setup used with the PULSAR laser is shown in Fig. 2.3(a). For a Gaussian beam, the spot size at the focus is related to the beam radius as $r_0 = \lambda f/\pi d$, where d is the beam radius before the focusing lens and f is the focal length of the lens [152]. We can easily calculate the focusing distance needed to obtain maximum efficiency,

$$f = \frac{0.64\pi da}{\lambda}. \tag{2.4}$$

We used a HCF with a core diameter of 250 μm and a focal length of 1.5 m to achieve maximum coupling efficiency. Air fluctuation and temperature gradients cause laser beam pointing instability. To improve the pointing stability at the entrance of the HCF, the laser beam is split after the focusing lens with a beamsplitter. The reflected beam is sent through a beam-pointing stabilization unit from TEM Messtechnik [153] for the PULSAR laser. (The KLS uses a homemade stabilization unit called ALPS, which was developed by Prof. DePaola's group [154]). In the stabilization unit, a small portion of the beam reaches two detectors, which form a straight line. The position of the beam on each detector is calibrated. Each detector acts as an iris and the feedback from each detector controls the mirror before and after the focusing lens (M_1 and M_2 in Fig. 2.3(c)). The mirrors are equipped with stepper motors and piezo-based actuators for slow and fast adjustment, respectively.

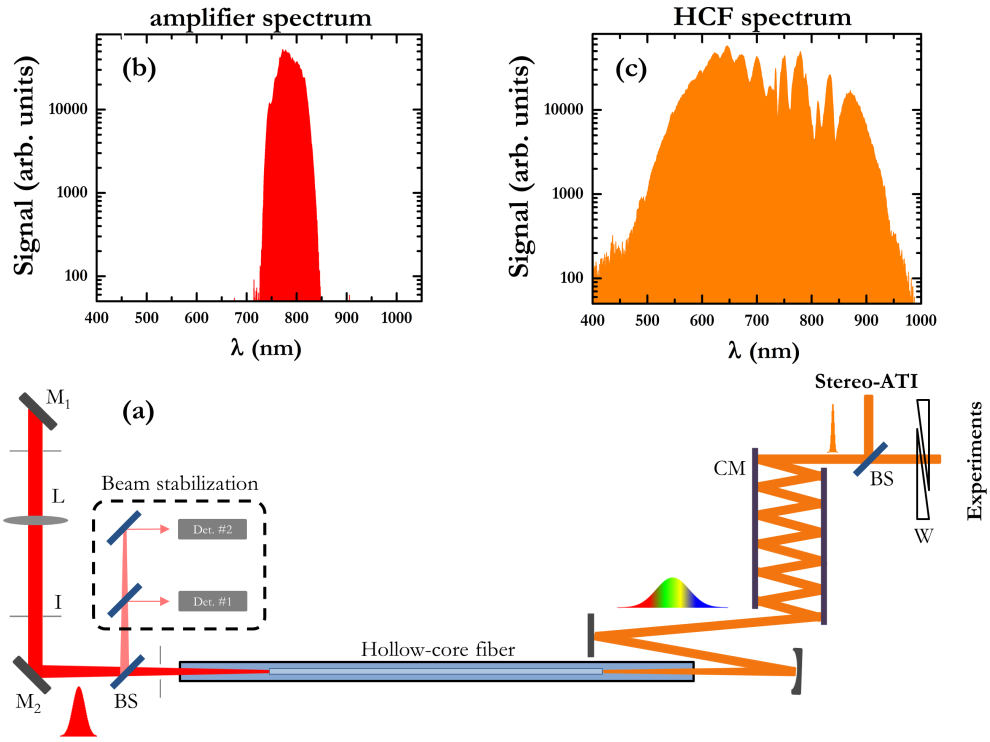

Figure 2.3: (a) Simplified schematic of spectral broadening through HCF and chirped mirror compressor at PULSAR. M: mirror; L:lens; I:iris; CM:chirped mirrors; BS:beamsplitter; W:glass wedge. (b) The amplifier spectrum. (c) The HCF spectrum after the chirped mirrors.

The main spectral broadening in the HCF occurs due to SPM. In addition, traveling a long distance in the nonlinear medium of the fiber will cause positive dispersion. A set of chirped mirrors (7 pairs) is used to introduce negative dispersion to compensate for the positive dispersion caused by the fiber, as shown schematically in Fig. 2.3(a). Typically, the laser pulses are negatively chirped after all the chirped mirrors to allow fine tuning "on target". The amount of negative dispersion can be calculated for the optical elements used in the path to the experimental apparatus (thickness of glass, length of propagation in the air, etc.). However, the dispersion can be optimized in the main experimental chamber by introducing a pair of movable wedges. By using this fine tuning approach, several experimental setups at different distances from the short-pulse source can use the beam simultaneously.

Argon and neon are used in the HCF setup to spectrally broaden the amplified laser pulses. To avoid ionization, the input laser peak intensity should be smaller than the ionization threshold of

the gas used in the the HCF. Neon has a higher ionization potential than argon and can be used to broaden laser pulses with higher input pulse energy. An input pulse energy of 0.9 mJ is used with the neon-filled HCF at a pressure of 2 bar to generate a broad spectrum with pulse energy of 0.4 mJ. A typical spectrum from the neon-filled HCF is shown in Fig. 2.3(c). The original spectrum of the amplifier is plotted in Fig. 2.3(b) with a bandwidth of 60 nm FWHM. This pulse is spectrally broadened to FWHM >200 nm as shown in Fig. 2.3(c). Different tools can be used to characterize the pulse duration as explained in section 2.5.

2.3 Frequency Doubling and Tripling Using Intense Femtosecond Laser Pulses

2.3.1 Nonlinear Optics

This section provides a brief introduction to nonlinear optics, specifically nonlinear frequency conversion. Ultrashort laser pulses can have a high intensity inside a medium. At low intensity, the polarization, $\boldsymbol{P}$, depends linearly on the electric field, $\boldsymbol{E}$, as $\boldsymbol{P} = \chi \boldsymbol{E}$, where χ is the electric susceptibility. At high intensity, this linear relationship breaks down. One can expand the polarization into higher orders of electric field [120, 152],

$$P(E) = \chi^{(1)}E + \chi^{(2)}E^2 + \chi^{(3)}E^3 + ..., \tag{2.5}$$

For simplicity, both E and P are written as scalar quantities. The second and third terms are the nonlinear part of the polarization. The coefficients $\chi^{(n)}$ are high-order nonlinear optical susceptibilities. The nonlinear polarization is the source term in the nonlinear wave equation [120]. As a result, new frequencies can be generated through the dependence on the higher orders of the electric field. The simplest nonlinear process can be generated through the second-order susceptibility, $\chi^{(2)}$. By assuming an electric field $E = E_0 e^{-i\omega t}$, the second-order polarization, $P^{(2)}(E) = \chi^{(2)}E_0^2 e^{-i(2\omega)t}$, acquires a contribution at twice the fundamental frequency ω. This process is called second-harmonic generation (SHG) [155].

Nonlinear Processes	$\chi^{(n)}$	Phase Matching Condition	Descriptions
sum-frequency generation (SFG)	$\chi^{(2)}$	$\omega_s = \omega_1 + \omega_2$	Two frequencies ω_1 and ω_2 are added to yield the signal at ω_s
difference-frequency generation (DFG)	$\chi^{(2)}$	$\omega_s = \omega_1 - \omega_2$	Two frequencies ω_1 and ω_2 are subtracted to yield the signal at ω_s
second-harmonic generation (SHG)	$\chi^{(2)}$	$\omega_s = 2\omega_1$	Frequency doubling of ω_1
third-harmonic generation (THG)	$\chi^{(3)}$	$\omega_s = 3\omega_1$	Frequency tripling of ω_1
third-harmonic generation through SHG + SFG	$\chi^{(2)}$	$\omega_s = 2\omega_1 + \omega_1$	Frequency tripling of ω_1 by SHG plus SFG with ω_1
optical parametric generation/amplification (OPG/OPA)	$\chi^{(2)}$	$\omega_s = \omega_p - \omega_i$	The signal is the difference between the pump and idler

Table 2.2: List of few well-known nonlinear processes.

2.3.2 Second Harmonic Generation

By employing the proper nonlinear medium, intense laser pulses can be frequency-doubled. The second harmonic (SH) yield depends quadratically on the intensity of the original beam. The choice of $\chi^{(2)}$ will affect the SH yield. For instance, the second-order susceptibility $\chi^{(2)}$ vanishes for crystals with an inversion symmetry. Some of the most common materials with second-order susceptibility include Beta-barium borate (BBO), potassium dihydrogen phosphate (KDP), lithium niobate ($LiNbO_3$), quartz, barium titanate ($BaTiO_3$) and lithium triborate (LBO) [156]. There are several nonlinear processes which lead to a conversion of light frequencies as listed in Table 2.2.

In the work presented in this dissertation, we used the sum-frequency generation (SFG) process to generate second-harmonics and we used SFG to generate third-harmonics. The second-harmonic is generated through a phase matching process. For a SFG process, the phase matching condition is simply written as, $k_3 = k_1 + k_2$, or $n_3\omega_3 = n_1\omega_1 + n_2\omega_2$. For the SHG process ($\omega_3 = 2\omega_1$), the phase matching condition reduces to $n(\omega_3) = n(\omega_1)$. To fulfill this equation, we use birefringent crystals.

The description of a birefringent crystal can be found in Ref. [120]. The simplest birefringent crystal is a uniaxial crystal consisting of an ordinary and extraordinary axis. The uniaxial bire-

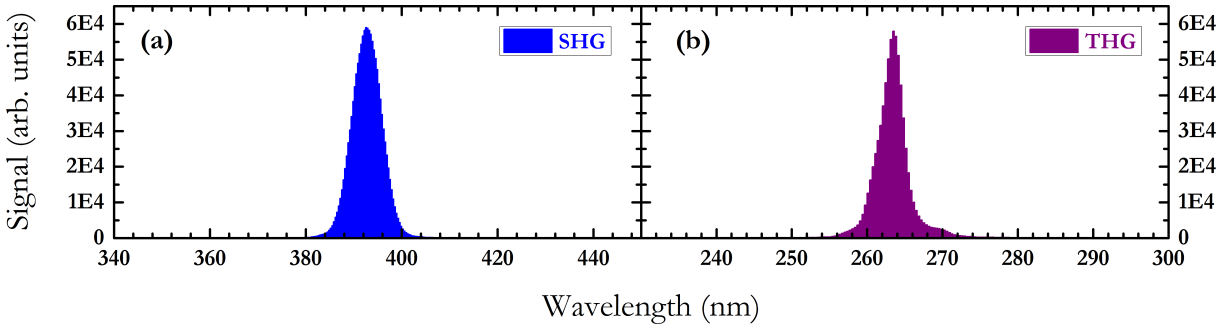

Figure 2.4: The typical measured (a) SHG and (b) THG spectra.

fringent crystals have refractive indices that depend on the polarization of the incident light. The refractive index in a polarization direction perpendicular to the optical axis of the crystal is n_o, which is not angle dependent. The beam that propagates on this axis is called the ordinary beam (o-beam), whereas the polarization of an extraordinary beam (e-beam) lies in the principal plane. The refractive index depends on the angle the crystal was cut, and it can be determined by the index ellipsoid [120, 157].

The phase matching condition can be satisfied through several approaches [120, 158]. In one approach, known as angle tuning, the axis of the crystal is rotated to match the laser beam polarization direction. In a different approach, phase matching is fulfilled by adjusting the wavelengths of the laser beams (wavelength tuning), or by temperature tuning of the birefringence of the crystal. For the SHG process, we used the angle tuning approach for a negative uniaxial BBO crystal. In this case, the ω_3 can be an extraordinary wave and ω_1 is an ordinary wave resulting in the phase matching condition of $n_e(2\omega, \theta) = n_o(\omega)$. A type-I BBO crystal with a cut angle of 29.2° and a thickness of 250 μm is used to generate second-harmonic laser pulses. As discussed earlier, the polarization direction of the fundamental wave and the second harmonic signal are perpendicular to each other for this crystal as they propagate on different optical axes. We use a polarization-sensitive harmonic separator (sometimes called a dichroic beamsplitter) to further separate the fundamental frequency pulses from the second-harmonic laser pulses. The incident beam is collimated to half of its original size to enhance the second-harmonic generation. We were able to achieve 30–40% conversion efficiency. Figure 2.4(a) shows the spectrum of the second harmonic

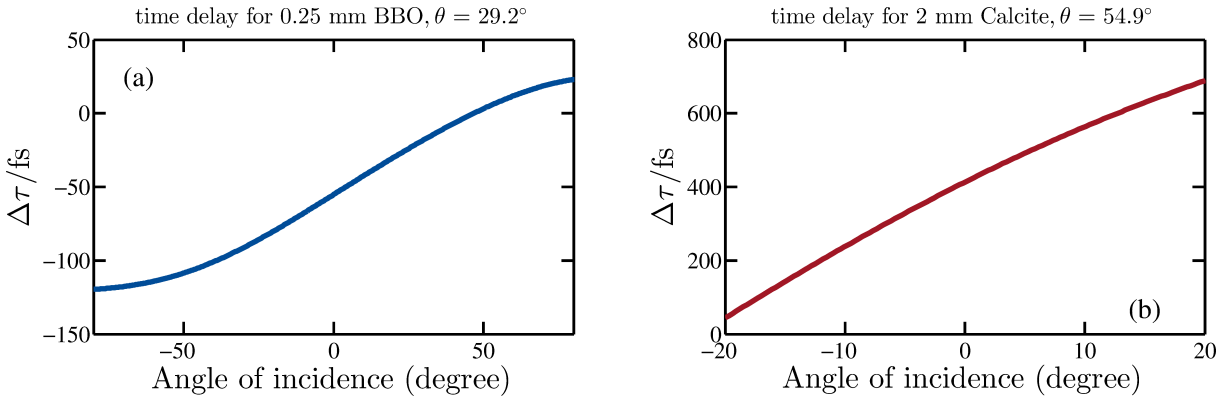

Figure 2.5: Time delay between the fundamental and second-harmonic for (a) a BBO crystal with 250 μm thickness and 29.2° cut angle and (b) a calcite crystal with 2 mm thickness and 152° cut angle.

pulses measured with a fiber optic spectrometer from CVI Melles Griot [159]. The second-harmonic laser pulses are sent toward a portable SD-FROG for pulse characterization, which is discussed in detail in section 2.5.2.1.

For a type-I BBO crystal with normal incidence, the time delay between the fundamental wavelength and second-harmonic pulses is calculated to be 194 fs/mm [156, 160]. The time delay between the fundamental and second harmonic for a given BBO crystal cut angle and thickness can be calculated as a function of incident angle. We follow the derivation in Ref. [157] and have written a short code that calculates this time delay. Figure 2.5(a) shows the relative time delay between the fundamental and second-harmonic pulses as a function of incidence angle for a BBO crystal with 250 μm thickness and 29.2° cut angle. It's clear that normal incidence results in a -55 fs time delay. The negative sign means that the second-harmonic pulse lags behind the fundamental pulse. The importance of this time delay becomes more clear as both of the laser pulses (fundamental and second-harmonic) are needed to perform an experiment. For instance, third-harmonic generation requires both the fundamental and second-harmonic laser pulses, as is discussed in detail in the next section. Another example is the generation of a collinear two-color beam for molecular fragmentation studies, which is described in section 2.4. For two-color experiments, a proper adjustment of the time delay between the fundamental and second-harmonic frequencies is essential.

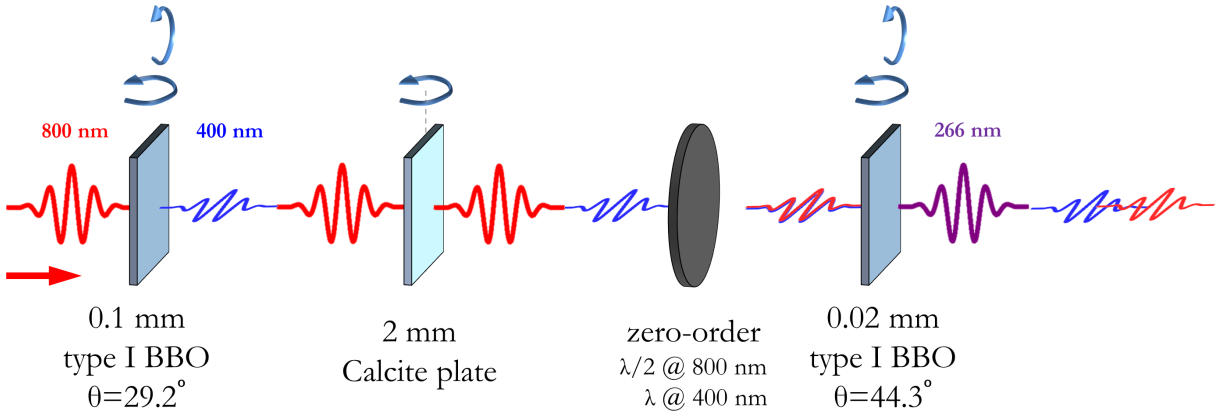

Figure 2.6: The schematic setup for third harmonic generation from the fundamental laser wavelength. The laser propagates from left to right, as shown by an arrow (see text for more details).

2.3.3 Third Harmonic Generation

To generate ultrashort laser pulses with a central wavelength at 266 nm, a combination of SHG and SFG processes is used. A schematic of a collinear setup for third-harmonic generation (THG) is shown in Fig. 2.6. The first step is the generation of the second-harmonic as described above. In the second step, a calcite plate is used to adjust the time delay between the fundamental and the second-harmonic pulse. For this purpose, the calcite is tilted by a few degrees, as shown schematically by an arrow in Fig. 2.6. After the calcite the second-harmonic pulses are ahead of the fundamental laser pulses in time. A zero-order half waveplate is used to rotate the fundamental polarization by 90° from *s*- to *p*-polarized light. The passage through the waveplate causes the two pulses to nearly overlap in time. The calcite plate is used for fine tuning of the time delay between the fundamental and second-harmonic pulses. Figure 2.5(b) shows the relative time delay between the fundamental and second harmonic as a function of incident angle for a calcite plate with the same properties as the one used in the experiment.

To generate the THG efficiently, the polarization of the fundamental and second-harmonic have to be horizontal and the time delay between the two pulse has to be minimized. The two pulses are overlapped temporally and spatially in a type-I BBO crystal with a thickness of 20 μm and cut angle of 44.3° to generate THG through the SFG process. The THG pulse is then separated from the fundamental and second harmonic by using 4 reflective dichroic beamsplitters. The conversion

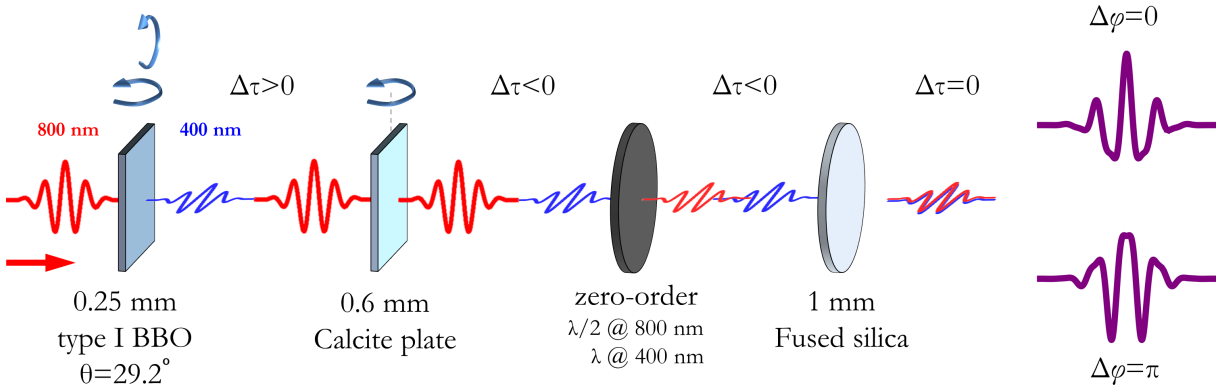

Figure 2.7: The schematic two-color setup; the laser propagates from left to right (see text for more details).

efficiency of the THG process is only a few percent. For instance, a 1.3 mJ laser pulse at 800 nm is used to generate THG pulses with 15 μJ pulse energy (conversion efficiency of 1.1%). The typical spectrum of the THG laser pulses measured with a fiber optic spectrometer from CVI Melles Griot [159] is shown in Fig. 2.4(b) with a central wavelength at 263 nm. The THG laser pulses generated in this section are used to study the dissociation of an O_2^+ molecular-ion beam as discussed in section 3.3.4. The detail alignment procedure for third-harmonic production is described in Appendix B.

2.4 Generation of Two-Color Laser Pulses

The schematic setup to generate a two-color laser field in a collinear geometry is depicted in Fig. 2.7. The setup consists of a BBO crystal for SHG, a calcite plate to adjust the delay between the fundamental and the second-harmonic light and a zero-order $\lambda/2$ waveplate at 800 nm in order to rotate the polarization of the fundamental by 90° and the second-harmonic pulse by 180°. The two laser pulses are temporally overlapped after propagation through 1 mm fused silica (entrance window). By tilting the calcite plate, the relative phase between the fundamental and second-harmonic field is controlled from 0 to π. As a result, the maximum of the two-color electric field can point in the positive or negative direction. Examples of such fields are shown in Fig. 2.7 for relative phases of 0 and π.

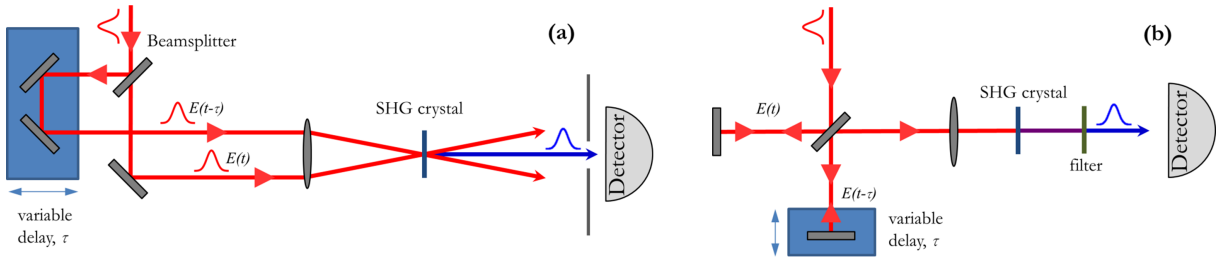

Figure 2.8: Autocorrelator schematics (a) intensity autocorrelator and (b) interferometric autocorrelator.

2.5 Pulse Characterizations

During the past decades, several methods have been employed to characterize ultrashort laser pulses. In all of these methods, the goal is to reconstruct the electric field of the laser through different algorithms. The basic principles of the methods that we have used in the lab are introduced in this section. In the first and second subsections, I will focus on the autocorrelation and frequency resolved optical gating (FROG) techniques, respectively.

2.5.1 Autocorrelation

In the autocorrelation technique, the pulse duration of laser pulses can be characterized by overlapping two replicas of the pulse in a nonlinear medium, as a function of the delay, τ, between them. Several autocorrelation methods exist, such as the intensity and interferometric autocorrelators, shown schematically in Fig. 2.8(a) and (b), respectively. In an intensity autocorrelator the two laser pulses are crossed at an angle in a nonlinear medium such as a BBO crystal, while in an interferometric autocorrelator the two replicas are overlapped in a nonlinear medium in a collinear geometry (see Fig. 2.8(a) and (b)). The second-harmonic yield is then measured as a function of delay between the two pulses. For the experiments described in this dissertation, the interferometric autocorrelation was used to characterize the pulse duration.

The laser pulse electric field can be generally written as $\mathbf{E}(t) = E(t)e^{i[\omega t+\varphi(t)]}$, where $E(t)$ is the pulse envelope, ω is the carrier frequency and $\varphi(t)$ is the phase of the pulse. The interferometric autocorrelation signal $I(\tau)$ for an electric field $\mathbf{E}(t)$ can be written as [161]:

$$I(\tau) = \int_{-\infty}^{\infty} \left| [\mathbf{E}(t) + \mathbf{E}(t-\tau)]^2 \right|^2 \mathrm{d}t. \tag{2.6}$$

Using the electric field defined earlier the signal can be expanded to:

$$\begin{aligned} I(\tau) \;=\; \int_{-\infty}^{\infty} \Big| & 2E^4(t) + 4E^2(t)E^2(t-\tau) \\ & + 4E(t)E(t-\tau)[E^2(t) + E^2(t-\tau)]\cos[\omega\tau + \varphi(t) - \varphi(t-\tau)] \\ & + 2E^2(t)E^2(t-\tau)\cos[2(\omega\tau + \varphi(t) - \varphi(t-\tau))] \Big| \mathrm{d}t. \end{aligned} \tag{2.7}$$

For zero delay the signal reduces to,

$$I(\tau = 0) \;=\; 16 \int_{-\infty}^{\infty} E^4(t)\mathrm{d}t, \tag{2.8}$$

and for delays far from overlap, the signal can be written as,

$$I(\tau \to \infty) \;=\; 2 \int_{-\infty}^{\infty} E^4(t)\mathrm{d}t. \tag{2.9}$$

From the ratio of Eq. 2.8 and Eq. 2.9, we can see that the contrast for the autocorrelation signal is 8:1. For a chirped Gaussian laser pulse, the electric field can be written as $E(t) = e^{[-2ln2(1+ib)(\frac{t}{T})^2]-i\omega t}$, where b is the chirp parameter and T is defined as the FWHM of the envelope. For a Gaussian pulse the autocorrelation signal is expressed as,

$$\begin{aligned} I(\tau) \;=& 1 + 2\, e^{[-2ln2(\frac{\tau}{T})^2]} \\ & + 4\, e^{[-2ln2\frac{b^2+3}{4}(\frac{\tau}{T})^2]} \cos[-2ln2\frac{b}{2}(\frac{\tau}{T})]\cos[\omega\tau] \\ & + \; e^{[-2ln2(b^2+1)(\frac{\tau}{T})^2]} \cos[2\omega\tau]. \end{aligned} \tag{2.10}$$

For FTL Gaussian laser pulses(no chirp, b=0), the autocorrelation signal is reduced to,

$$\begin{aligned} I(\tau) \;=& 1 + 2\, e^{[-2ln2(\frac{\tau}{T})^2]} \\ & + 4\, e^{[-\frac{3}{2}ln2(\frac{\tau}{T})^2]} \cos[\omega\tau] \\ & + \; e^{[-2ln2(\frac{\tau}{T})^2]} \cos[2\omega\tau]. \end{aligned} \tag{2.11}$$

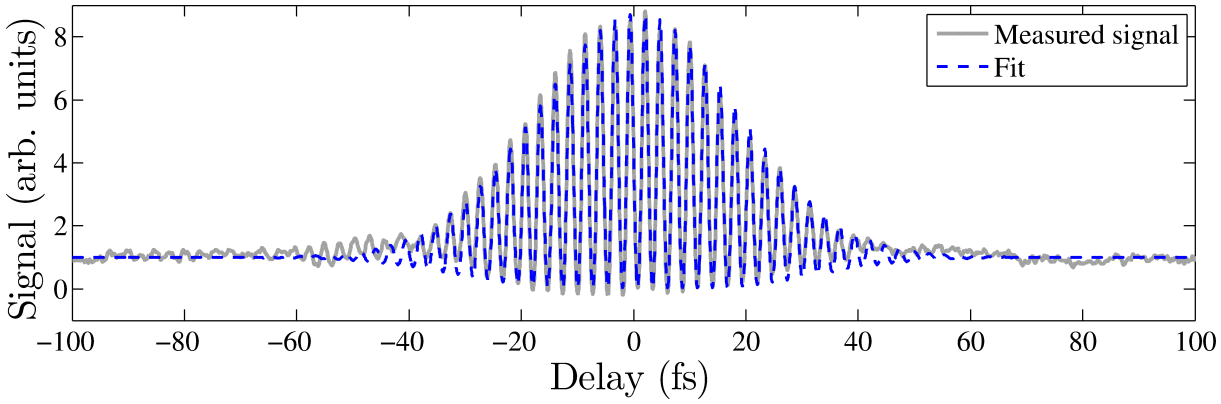

Figure 2.9: Second order interferometric autocorrelation trace. A measured autocorrelation trace for FTL laser pulses is plotted as the grey curve. The corresponding calculated autocorrelation trace is plotted (dashed line – blue curve) by assuming a flat phase across the spectrum (Eq. 2.11). The result of the fit is 27 fs FWHM for a Gaussian pulse with central wavelength of 800 nm.

This equation consists of three terms, a DC term (1^{st}), which does not oscillate, an oscillatory term (2^{nd}) with carrier frequency of ω, and an oscillatory term (3^{rd}) with carrier frequency of 2ω. The last two terms result in constructive and destructive interference leading to the autocorrelation trace. The interferometric autocorrelation trace measured for FTL laser pulses is shown in Fig. 2.9. The autocorrelation trace is obtained using an autocorrelator from Femtolasers [162]. The ratio of the peak to background is 8:1 as expected from our earlier discussion. The measured trace shows a clear oscillation as a result of the interference between the 2^{nd} and 3^{rd} terms in Eq. 2.11. To estimate the FWHM of pulses used in the experiment, we can use the analytical expression given by Eq. 2.11 with the assumption that the spectral phase is constant across the laser pulse. Based on Eq. 2.11, we can generate an autocorrelation trace to fit the experimental trace with the FWHM as a fit parameter. Figure 2.9 shows the fit as a dashed line (blue). We find that the FWHM of the intensity is 27 fs with central frequency of 800 nm. Figure 2.10 presents an autocorrelation trace for a short pulse generated through spectral broadening in HCF using the PULSAR laser as described earlier. The fit shows an autocorrelation trace for 6 fs FWHM of intensity with central frequency of 740 nm. The interferometric autocorrelation include some practical limitations. For instance, Yamane *et al.* [163] pointed out the bandwidth limitation of the SHG for pulses shorter than 5 fs. The autocorrelation methods are not very sensitive to laser pulse shapes. Ambiguity of

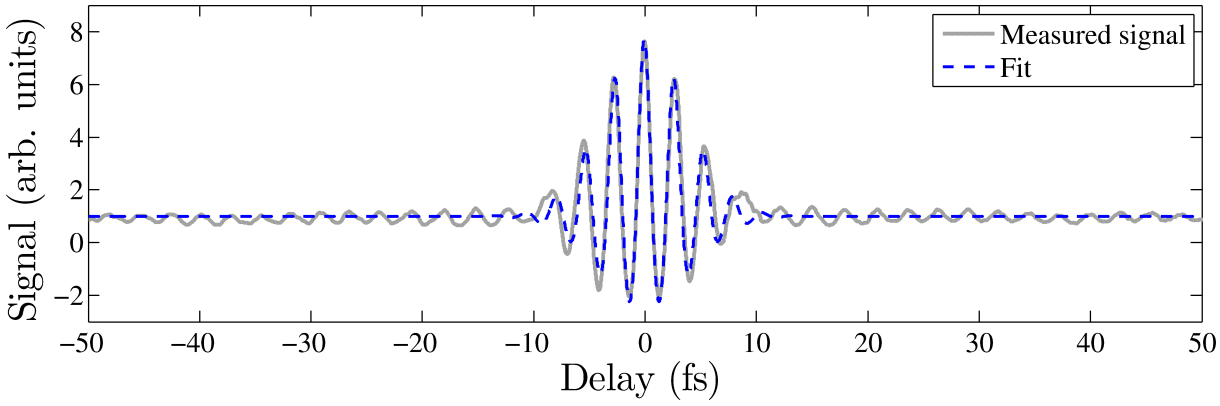

Figure 2.10: Second order interferometric autocorrelation trace. A measured autocorrelation trace for FTL laser pulses is plotted as the grey curve. The corresponding calculated autocorrelation trace is plotted (dashed line – blue curve) by assuming a flat phase across the spectrum (Eq. 2.11). The result of the fit is 6 fs FWHM for a Gaussian pulse with central wavelength of 740 nm.

ultrashort pulse shapes retrieved from the autocorrelation was studied by Chung and Weiner [164].

To sum up, we can use the interferometric autocorrelator to characterize pulse duration and chirp of the ultrashort laser pulses. The analytical expression (Eq. 2.10) is used to estimate the pulse duration and the amount of chirp in the measured spectrum. Similar information can be obtained by means of another technique called Frequency Resolved Optical Gating (FROG), which is described below.

2.5.2 FROG

More information about the laser pulse can be obtained by measuring the spectrally resolved autocorrelation signal. For instance, instead of measuring the yield of the SHG signal as a function of delay for the intensity autocorrelator measurements described earlier, one can measure the spectrum of the SHG signal as a function of delay between two pulses [165]. This technique is called frequency resolved optical gating (FROG) and can be used to fully characterize ultrafast laser pulses [165–168]. There are various different schemes of FROG which are widely used [169]. These self-referencing techniques use the original pulse $E(t)$ to gate itself by separating it into two identical replicas and crossing them within a nonlinear medium as described earlier. The measured signal is spectrally resolved as a function of the relative delay τ between the two replicas. The

final FROG trace (i.e., spectrogram) is a 2D map of pulse intensity as a function of delay time and frequency (or wavelength). Some of the well-known FROG methods are SHG-FROG, PG-FROG and SD-FROG. The SHG-FROG has a temporal ambiguity, in which one can not distinguish between negatively and positively chirped laser pulses. In the experiments performed in this work, we used the SHG-FROG and SD-FROG methods described below to characterize our laser pulses.

2.5.2.1 SHG-FROG

The schematic of a SHG-FROG is similar to the schematic of the autocorrelator as shown in Fig. 2.8(a), in which the detector used for autocorrelator measurements has been replaced by a spectrometer. In a SHG-FROG configuration, we measure the spectrum of the second harmonic signal as a function of delay. This is called the spectrogram of the autocorrelation between two pulses. The mathematical expression for a SHG-FROG signal is written as,

$$I_{FROG}^{SHG}(\omega,\tau) = \left| \int_{-\infty}^{\infty} E(t)E(t-\tau)e^{-i\omega t}\mathrm{d}t \right|^2 , \tag{2.12}$$

where $E(t)$ is the pulse electric field. An iterative deconvolution algorithm is used to reconstruct the electric field, magnitude and phase of the laser pulse [170, 171]. However, some ambiguities exist in this process. The iterative process does't always result in a unique solution, and the SHG-FROG is insensitive to time inversion. There are many different variants of SHG-FROG available with different properties, such as a scanning SHG-FROG, single-shot SHG-FROG and an interferometric version [172–174]. We used a scanning SHG-FROG as well as a single-shot SHG-FROG for the work presented in this dissertation [172].

Figure 2.11(a) shows a measured FROG trace for FTL laser pulses with central frequency of 790 nm acquired by using a single-shot SHG-FROG. Figure 2.11(b) is the corresponding reconstructed temporal intensity profile (normalized to 1) and phase obtained by using the iterative algorithm. The result is a pulse duration of 25 fs FWHM in intensity.

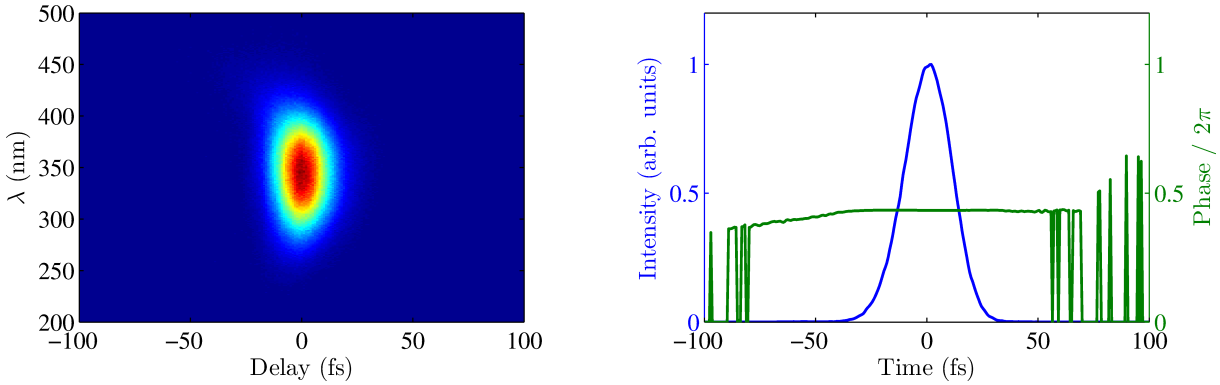

Figure 2.11: (a) Measured FROG trace for FTL laser pulses using a single-shot SHG-FROG. (b) The corresponding reconstructed temporal intensity profile (normalized to 1) and phase as a function of time with FWHM of 25 fs.

2.5.2.2 SD-FROG

To characterize the second harmonic pulses from the SFG process described in Section 2.3.1, we employed a SD-FROG setup [167, 175]. The SD stands for self-diffraction and uses a third-order nonlinear process. The SD-FROG we used has a similar configuration as the intensity autocorrelator discussed earlier, where the nonlinear medium is a thin piece of quartz (or other third-order nonlinear medium such as fused silica). The two laser beams are focused in this nonlinear medium and overlapped temporally and spatially. Due to the nonlinear Kerr effect, the index of refraction changes as a function of intensity, $n = n_0 + n_2 I$ (see Section 2.2.1). The interference between the two pulses induces a sinusoidal intensity pattern, often called a transient refractive index grating [169]. Each beam is then diffracted from this grating within the medium. The spectrometer is used to measure the spectrum of one of the diffracted signals as a function of delay between the two incident pulses. The result is a FROG trace, which is shown in Fig. 2.12.

SD-FROG requires a relatively high pulse energy and can be applied in various spectral regions. The SD-FROG has been used to characterize short laser pulses in the deep UV region [175]. Since the self diffraction is not a phase-match process [176], the angle between the beams must be kept small ($\lesssim 2^\circ$) and the nonlinear medium has to be thin ($\lesssim 100$ μm) [168, 177]. Figure 2.12(a) shows a typical SD-FROG trace for SHG laser pulses with central wavelength of 395 nm. The SHG signal is produced by propagation through a 250 μm BBO type I crystal. The SHG signal is

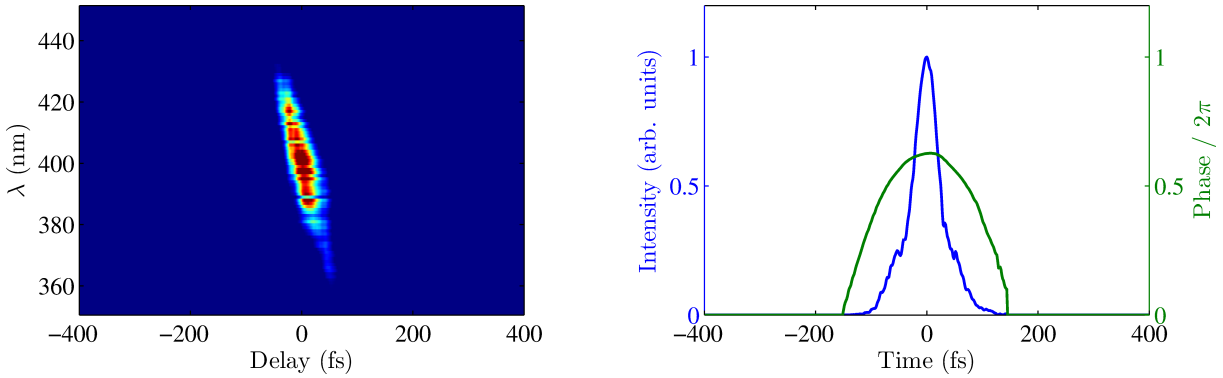

Figure 2.12: (a) Measured SD-FROG trace for the SHG signal. (b) The corresponding retrieved temporal intensity profile (normalized to 1) and phase as a function of time with FWHM of 53 fs.

separated from the fundamental beam by using a polarization-sensitive harmonic separator 1 mm thick. The beam propagates through a few meters of air and 1 mm of fused silica to interact with an ion beam target. A small portion of this beam is sent toward our portable SD-FROG setup for characterization.

The measured trace is positively chirped as the "red" spectral components precede the "blue" components for the measured UV laser pulses. This is due to the travel through several optical elements and air. This extra chirp can be compensated by using a proper set of chirped mirrors. A commercial FROG3 program, based on an iterative FROG algorithm, is used to reconstruct the electric field amplitude and phase in the time and frequency domain. Figure 2.12(b) shows the retrieved temporal intensity amplitude and phase in the time domain. The parabolic shape of the phase indicates a positive chirp. The reconstructed intensity profile results in a pulse duration of ∼53 fs FWHM, which is longer than the predicted FTL laser pulse due to the positive chirp described earlier.

2.6 Carrier Envelope Phase Tagging

2.6.1 Definition of the Carrier-Envelope Phase

The electric field of an ultrashort laser pulse can be described mathematically as

$$E(t) = E_0(t)\cos(\omega\, t + \varphi), \tag{2.13}$$

where $E_0(t)$ represents the envelope of the pulse and is normally written as a Gaussian function, $e^{-\frac{t^2}{\tau^2}}$. The carrier-envelope phase (CEP), φ, corresponds to the offset phase between the maximum of the intensity envelope and the maximum of the electric field. Figure 2.13 shows the schematic of an ultrashort laser pulse for two different CEP values. There are several methods to measure the CEP of laser pulses. The two best-known methods for characterizing the CEP of ultrashort laser pulses are f-2f interferometry and stereo-ATI electron detection. In the measurement presented in this work, we used a stereo-ATI technique implemented by our previous group member Nora G. Kling [123, 178].

2.6.1.1 The f-2f Interferometer

The optical method called f-2f interferometry relies on the spectral interference of a low (frequency doubled) and a high frequency component of the laser-pulse spectrum. By overlapping these frequency components spectrally, an interference pattern emerges, which contains information about the CEP. There are several variants of f-2f available to measure the CEP of an oscillator beam or an amplified beam (before and after HCF). The CEP information can be retrieved by employing Fourier transform spectral interferometry Fourier transform spectral interferometry (FTSI) [179]. More details can be found in Refs. [180, 181].

The first measurement of the CEP of a many-cycle femtosecond laser pulse was introduced by Jones and coworkers [129], followed by several other experiments [131, 142, 182, 183]. Nowadays, this method is widely used for few- and chirped many-cycle laser pulses. Recently, the CEP characterization was carried out for optical parametric amplifier (OPA) laser pulses at 1.8 μm wavelength [184, 185]. As mentioned earlier, we use a stereo-ATI spectrometer method described

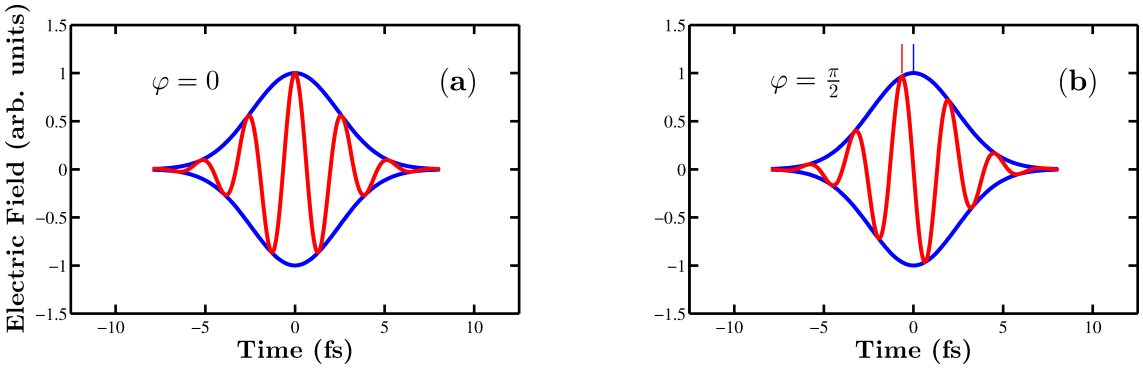

Figure 2.13: Schematic of an ultrashort laser pulse electric field (red) and envelope (blue) for two different CEPs (a) φ=0 and (b) $\varphi = \frac{\pi}{2}$.

briefly below to characterize CEP in this work.

2.6.1.2 Stereo-ATI Spectrometer

A stereo-ATI spectrometer is a setup used to determine the CEP of ultrashort laser pulses through measuring the recollision electron in the ionization of a noble gas. The recollision process can be illustrated by a three-step model[2] [186–188], corresponding to a high-order above threshold ionization (ATI) peak in the photoelectron spectrum [189–191].

In the three-step model, the returning electron is scattered from the parent ion and gains kinetic energy up to $10U_p$, where $U_p = \frac{I}{4\omega^2}$ is the pondermotive energy, I is the laser intensity and ω is the laser central frequency. These electrons are highly sensitive to the shape of the electric field and thus the CEP. The instrument consists of two microchannel plate (MCP) detectors assembled back-to-back. The left and right photoelectron distributions are measured for each laser shot along the polarization axis. Figure 2.14(a) shows the schematic of the setup.

The asymmetry parameter is defined as $\mathcal{A} = \frac{N_L - N_R}{N_L + N_R} \cong \sin(\varphi + \varphi_0)$. Herein, N_L and N_R are the integrated electron yields on the left and right detector, respectively. Furthermore, the ATI spectrum appears to be sinusoidal with respect to the phase and the phase is energy dependent [122,

[2] In the first step, the electron tunnels through the potential barrier. In the 2nd step, the electron accelerates in the laser field and then gets rescattered from the parent ion.

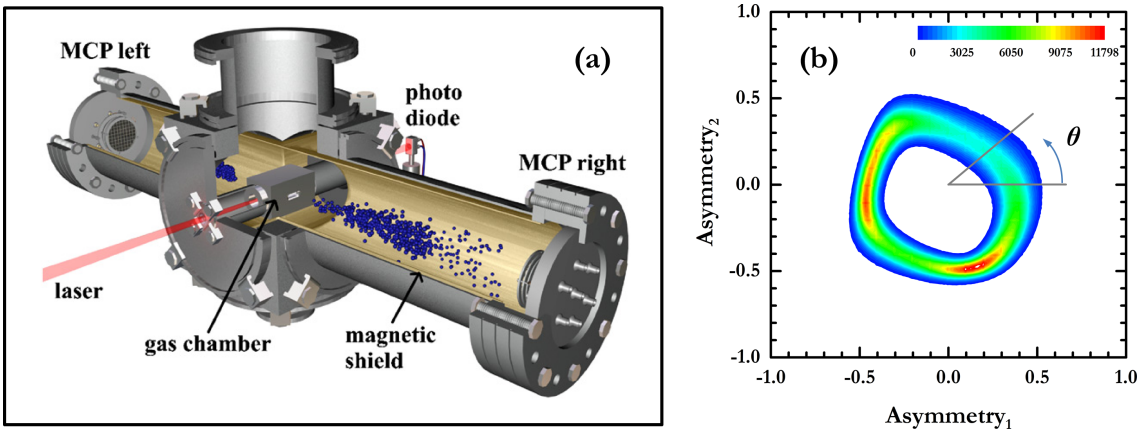

Figure 2.14: (a) Schematic of CEP phasemeter used in this dissertation (adapted from Ref. [123]). (b) The asymmetry parameters for two different energy ranges are plotted versus each other. Each point corresponds to a certain CEP value.

123, 192–194]. The CEP can be retrieved as,

$$\varphi \cong arcsin(\alpha \frac{N_L - N_R}{N_L + N_R}) - \varphi_0, \tag{2.14}$$

where α is a scaling factor to ensure the argument in the *arcsin* ranges from -1 to 1. However, the CEP determined this way has an ambiguity of π. To determine the CEP without ambiguity, the asymmetry for two energy regions can be compared [192]. For this purpose, the asymmetry for one energy region is plotted versus the other as shown in Fig. 2.14(b) [122, 123, 192, 193]. Each point on this plot represent a certain CEP value. The method to extract the CEP from the angle θ in Fig. 2.14(b) is described in Refs. [178, 195, 196]. For the experimental results presented in Chapter 4, the stereo-ATI was used to trace the CEP of every laser shot.

Chapter 3

Molecular Ion Beam Studies

Contents

3.1 Introduction

In this chapter, we will present our results using various molecular ion-beam targets with different laser parameters. The experimental results are composed of:

- Vibrationally-Resolved Structure in O_2^+ Dissociation Using a Few Wavelengths
- Rudimentary Coherent Control
  - Effective Bandwidth Narrowing — Linear Chirp Effect in Dissociation of H_2^+
  - Chirp Effect in Zero Photon Dissociation of HD^+
- Branching Ratios in the Dissociation of HD^+ Using an Intense Ultrafast "Single-Color" Laser Field
- Control over Dissociation of a Molecular Ion Beam by Two-Color Laser Field — ω–2ω
- Pump-probe Studies of Molecular Ion-beam Fragmentation

3.2 Experimental Method

The experimental results presented in this chapter are based upon the laser-induced molecular dissociation imaging (LIMDI) technique developed by Ben-Itzhak's group [91, 92, 197, 198]. In this method, coincidence 3D momentum imaging is implemented to study fragmentation of a molecular-ion beam induced by intense ultrashort laser pulses. Using a molecular ion-beam target has a few advantages and disadvantages, which will be discussed briefly. The molecular-ion beam can be used to study benchmark molecules, such as one-electron diatomic molecules, H_2^+, and the simplest polyatomic molecule, H_3^+, as well as their isotopologues. For the benchmark H_2^+ molecules, accurate theoretical treatment of the interaction with a strong laser field is feasible [199–202]. Moreover, fragmentation of H_3^+ in an intense laser field has been studied [97–101, 203–207]. The neutral H_3 is unstable in its ground state; therefore exploring H_3^+ as an ion-beam target in the laboratory is essential.

Typically, H_2^+ is generated in strong-field studies by ionizing H_2 during the laser pulse (See, for example, previous experimental and theoretical studies of H_2^+ [26, 199, 200, 208–210]). In this case, the H_2^+ initial vibrational states are populated coherently. Starting with an H_2^+ ion-beam target results in a well-defined Franck-Condon distribution of initial vibrational levels [28, 211]. These states are populated incoherently.

The target molecular ions have a few keV of kinetic energy, and as a result the neutral fragments can be detected. In other words, dissociation processes can be studied in a kinematically complete manner. One of the main disadvantages of using ion-beam targets is their low target density in comparison with neutral targets. For instance, in a typical ion-beam experiment the target density is about $\sim 10^5$ molecules/cm^3, while the density of a neutral target is estimated to be around $\sim 10^{12}$ molecules/cm^3. Therefore, time dependent studies that require high statistics data could be challenging when using ion-beam targets. We will discuss two examples of such measurements performed on ion-beam targets later in this chapter.

The main components needed to perform this kind of experiment are (i) an intense ultrafast laser system, (ii) an ion source to generate the molecular ion-beam target and the related ion optics, (iii) a method for crossing the laser with the molecular-ion beam, (iv) a momentum imaging apparatus to measure the breakup fragments, and lastly (v) a procedure to convert the measured signals to the 3D initial momentum of each breakup channels. The characteristics of the laser system used in our measurements were described in the previous chapter. The schematic diagram of our experimental apparatus is shown in Fig. 3.1(a) and (b), and the various elements are described in the following section.

3.2.1 Ion Source

The molecular ions are generated via fast electron impact ionization in an electron cyclotron resonance (ECR) ion source [212–214]. It is worth mentioning that the electron impact ionization mechanism produces ions through vertical transitions, in which the vibrational population approximately follows the Franck-Condon factors [28, 211]. To extract the molecular ions, the ion source is held on a positive acceleration voltage in the range of 5–28 kV. A constant flow of gas is leaked

into the source through a dosing valve[1] to maintain the constant ion current. The beam current is monitored with a movable Faraday cup (FC) along the beam line. The first Faraday cup (labeled as FC1 in Fig. 3.1) measures the total current produced by the ion source. The ion source produces a variety of ion species and the total current at the output of the source is between 20 and 200 μA, which depends on conditions of the source such as the target gas, the pressure in the source and the electron impact energy.

The desired beam of ions is momentum-selected by a magnetic field (labeled as M1 in Fig. 3.1). By adjusting the magnetic field, the molecular ions of momentum p and charge q are deflected to pass through a four-jaw slit and collected in a Faraday cup (FC2). We record the beam current at various places along the beam line as a function of the magnetic field strength (monitored with a Hall probe).

3.2.2 Ion Optics

We use two quadrupole lenses to focus the beam at the interaction region. A quadruple lens consists of four hyperbolic electrodes placed symmetrically around the beam axis [215]. These lenses are typically assembled as doublets or triplets to focus the beam in both transverse directions [216]. In the schematic drawings in Fig. 3.1(a) and (b), the quadrupole lenses are labeled as Q_1 and Q_2. The first quadrupole lens is mounted close to the source while the 2$^{\text{nd}}$ quadrupole lens is after the second magnet, M2. The quadrupole lenses are implemented to produce a collimated beam with a cross section of about 0.8×0.8 mm^2 in the last Faraday cup (FC4). This FC4 is mounted on an XY-manipulator stage, which can be adjusted to collect the ion beam. In addition to the quadrupole lenses, we use a series of electrostatic deflectors (consisting of parallel plates and labeled DP in Fig. 3.1(a) and (b)) to steer the ion beam in the horizontal and vertical directions. The ion-beam current is measured during the tuning process with different Faraday cups along the beam path. For instance, a current of ∼2 nA is measured on the Faraday cup FC4 for a 10 keV H_2^+ ion beam.

To reduced the rate of scattered particles on the detector, the ion beam is chopped in syn-

[1] Pfeiffer, UDV 046

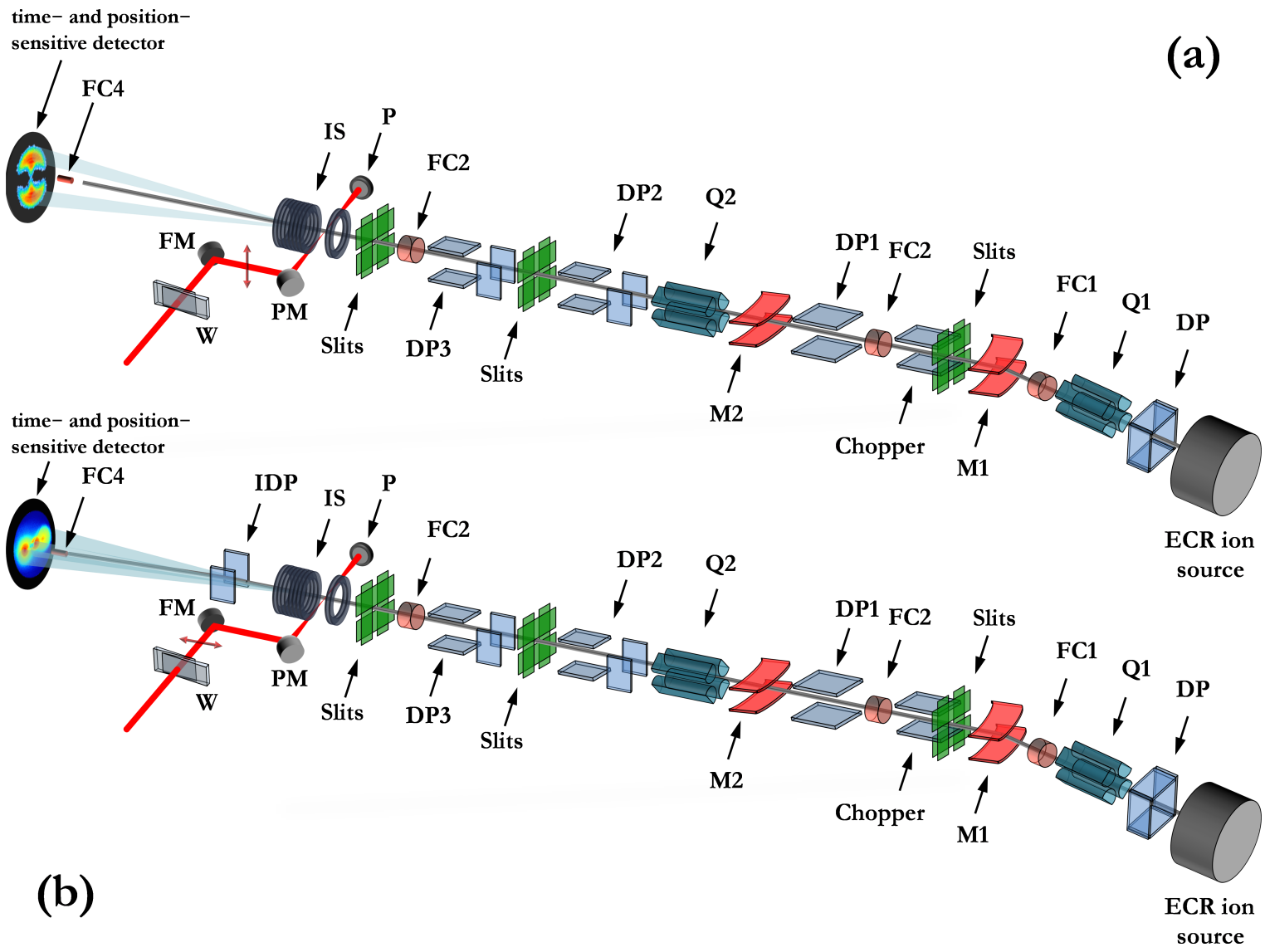

Figure 3.1: Side-view schematic of the ECR beam line used for the (a) LFI and (b) LATFI methods (see text for more details). (Acronym key: ECR – Electron Cyclotron Resonance; DP – Deflector plate; Q – Quadrupole lens; FC – Faraday cup; M – Magnet; P – Power meter; IS – Imaging spectrometer; IDP – Imaging deflection plate; PM – parabolic mirror; FM – Flat mirror; W – wedges).

chronization with the laser pulses. This chopper, shown in Fig. 3.1, is comprised of parallel plates mounted on four-jaw slits to produce a movable deflector. This configuration allows the chopper to be close to the ion beam. By applying a weak voltage to the plates, the ions are deflected away from the defined path. When the voltages are switched off, the ion beam returns to the path that was being tuned previously. In our experiment, the ion beam is present a few μs before the laser pulses arrive at the interaction region and stays on for a few μs after the laser pulse.

3.2.3 Imaging Set-up

Following acceleration and momentum-selection of the molecular ions, the ion beam is transported to the laser interaction region, where it is crossed orthogonally by the focused laser beam, with the laser polarization oriented perpendicular to both beam directions. The choice of ion beam energy is a compromise, low enough to improve the KER resolution but high enough to assure an acceptable detection efficiency, especially for the neutral fragments.

A static electric field is applied in the interaction region using a longitudinal spectrometer (marked as imaging spectrometer (IS) in Fig. 3.1(a) and (b)), in order to accelerate the charged molecular fragments toward a time- and position-sensitive detector [217] such that all fragments, neutral and ion, are separated by time-of-flight (TOF) and measured in coincidence. The schematic of the setup is shown in Fig. 3.1(a). This method is called longitudinal field imaging (LFI) [197, 198]. The measurement relies on the fragments having sufficient dissociation energy transverse to the ion-beam direction to separate them from the Faraday cup (FC4) — with the drawback that those with insufficient energy (KER $\lesssim 0.1$ eV) are blocked.

We further improved this imaging method by adding a transverse static electric field (provided by an imaging deflector, in Fig. 3.1(b)) after the imaging spectrometer to deflect the charged fragments in position. This allows the measurement of low KER down to near 0 eV (limited by the energy resolution). This method is called longitudinal and transverse field imaging (LATFI) [198], and is depicted in Fig. 3.1(b). The primary molecular-ion beam is deflected and collected in FC4.

The dissociation fragments are measured in coincidence in both methods, thus enabling the unambiguous identification of different fragmentation channels, such as $H^+ + H$ dissociation or

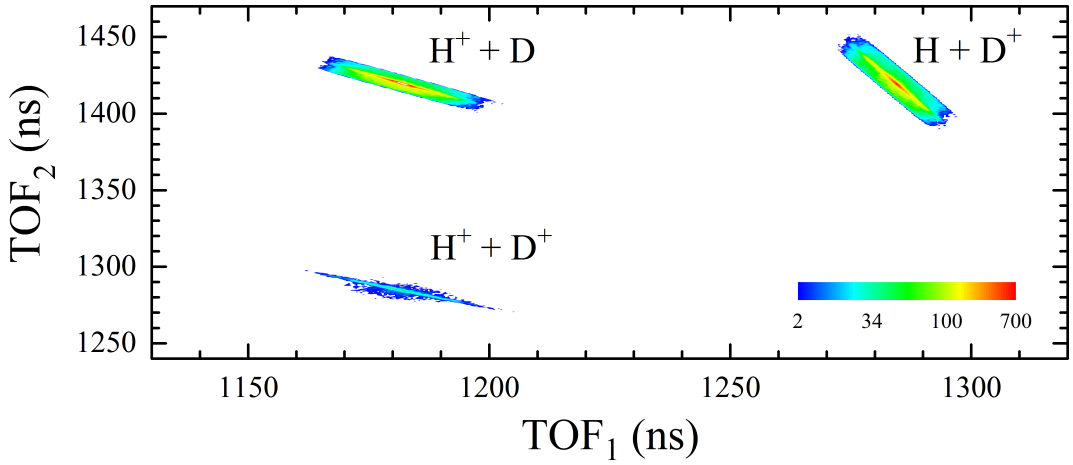

Figure 3.2: Density plot of coincidence TOF gated using momentum conservation for HD^+ fragmentation induced by 33 fs FTL linearly polarized (s-polarized) laser pulses with 4×10^{15} W/cm^2 peak intensity.

$H^+ + H^+$ ionization [91, 92]. A typical coincidence TOF spectrum of HD^+ fragmentation by ultrashort laser pulses is shown in Fig. 3.2. The horizontal axis is the TOF of the first hit and the vertical axis represents the TOF of the second hit. True coincidence events lie along diagonals, which are labeled accordingly. The figure clearly demonstrates the separation of dissociation and ionization channels.

Figure 3.3(a) and (c) show typical TOF spectra using the LFI and LATFI methods, respectively, while Fig. 3.3(b) and (d) present the position spectra for each of these methods. The polarization is parallel to the detector in the LFI method, while the polarization is along the beam axis in the LATFI method. The TOF for each fragmentation channel, in Fig. 3.3(c), consists of two peaks, a forward (toward) and a backward (away) peak with respect to the detector, as expected. In addition, the fragments are separated in position as shown and labeled in Fig. 3.3(d).

3.2.4 Coincidence 3D Momentum Imaging

Our coincidence 3D momentum imaging technique allows us to cleanly separate the dissociation channel of interest from other dissociative ionization channels. For this channel, we evaluate the momenta of both dissociating fragments from the TOF and position information, recorded event-by-event, therefore retrieving the complete kinematic information about the process under study.

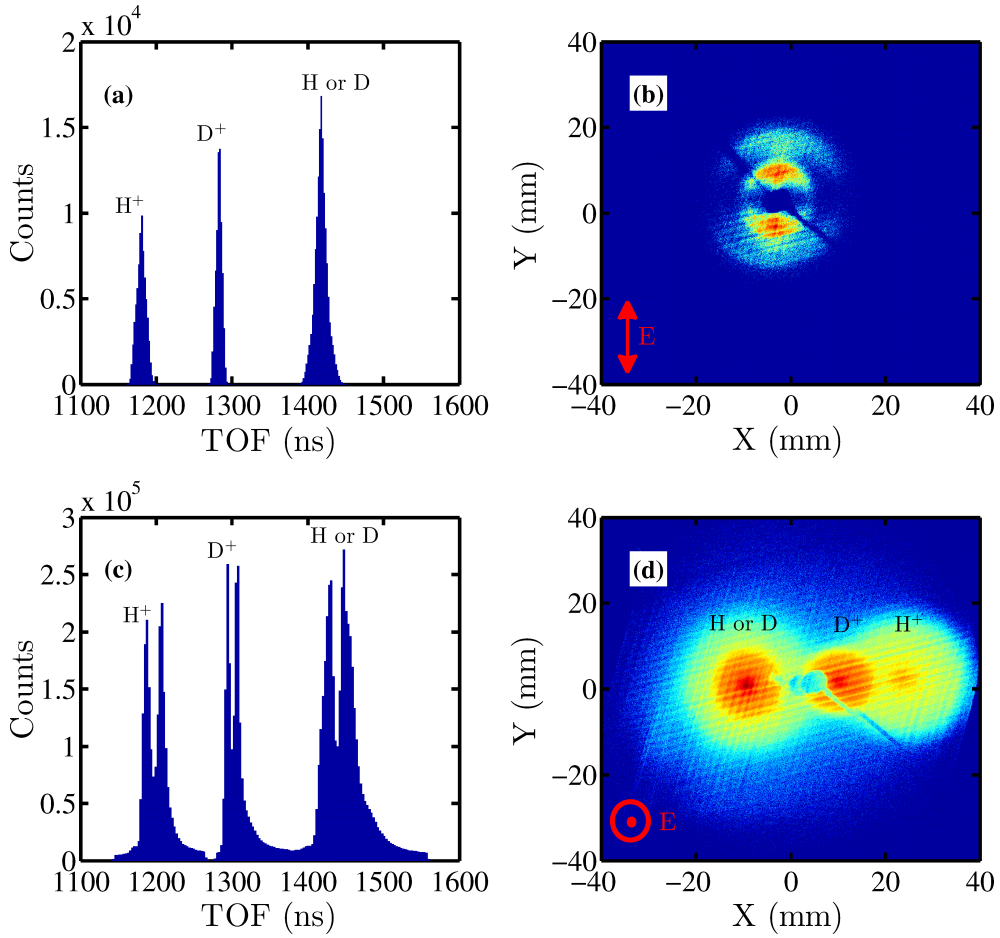

Figure 3.3: (a) TOF and (b) position spectra for a HD^+ molecular ion-beam target fragmented by a strong-field linearly polarized laser using the LFI method (see text). (c) TOF and (d) position spectra for a HD^+ molecular ion-beam target fragmented by a strong-field linearly polarized laser using the LATFI method (see text). The polarization direction is parallel (perpendicular) to the detector plane in the LFI (LATFI) method as marked on (b) and (d).

From these momenta the KER and direction of the dissociating fragments (θ, ϕ) relative to the laser polarization are determined (see further details in our previous publications [91, 92, 102, 197, 218]).

All of the time signals generated from the detector (TOF from the MCP and position signals from the delay-line anode) are measured with respect to the signal generated from a photodiode that is triggered by the laser pulses. The true time of each hit can be written as $t_j = TOF_j - t_d$, where t_d is the time difference between the time the laser pulse intersects the ion beam and the photodiode signal (including the associated time difference due to electronics) [197]. Therefore, the true TOF for each hit is measured from the interaction to the detector with an accuracy of

about 200 ps. The position of a hit, (x_j, y_j), is reconstructed from the time delay between signals arriving at the two ends of each wire, $x_j = (t_L - t_R)C_x$ and $y_j = (t_U - t_D)C_y$, where t_L, t_R, t_U, and t_D are the timing signals from the ends of the x and y wires. $C_{x,y}$ are proportional to the signal propagation speeds (scaling factors) determined by using a well-known pattern (mask) in front of the detector; for more details see Ref. [197].

The basic idea of 3D momentum imaging can be comprehended by applying no voltages to the imaging spectrometer and the imaging deflector. This method, sometimes referred to as "field-free imaging" or "fast-ion-beam photofragment spectroscopy", is discussed in previous studies [96, 219–224]. We briefly describe this method for two-body fragmentation in this section. Moreover, this method can easily be extended to three or more fragments .

The interaction point, where the laser crosses the ion beam, is defined as the z-axis origin. The measured (x,y) origin is set to be the center of the beam spot on the imaging detector. The (x,y) for the first and second hit on the detector can be evaluated from the TOF and position information. The equations for the x and y coordinates are the same; for simplicity, we only write the x-equations of the two fragments hitting the detector,

$$x_1 - x_{0_i} = (v_{0x_i} + v'_{1x})t_1 \tag{3.1a}$$

$$x_2 - x_{0_i} = (v_{0x_i} + v'_{2x})t_2, \tag{3.1b}$$

where t_1, x_1 and t_2, x_2 are the measured time and position of each hit, respectively, and x_{0_i} and v_{0x_i} are the position and center-of-mass (CM) velocity (x-components) of a specific molecular ion at the dissociation point. Lastly, v'_{1x} and v'_{2x} are the dissociation velocities along the x direction for each fragment in the CM system. The two dissociation velocities are related by momentum conservation in the CM system,

$$m_1 v'_{1x} + m_2 v'_{2x} = 0, \tag{3.2}$$

where m_1 and m_2 are the masses of the first and second fragment. There are four unknowns, v'_{1x}, v'_{2x}, v_{0x_i} and x_{0_i}, in these three equations (3.1a, 3.1b and 3.2). To solve these equations, we need to eliminate one variable. As the interaction volume defined by the tightly focused laser beam and

sub-1 mm ion beam is small, we can approximate the fragmentation position for each molecule with its average value, $\overline{x_{0_i}}$. Substituting $v'_{2x} = -\frac{m_1}{m_2}v'_{1x}$ (from momentum conservation Eq. 3.2) into Eq. 3.1b and subtracting from Eq. 3.1a yields,

$$v'_{1x} = \frac{x_1 - x_2}{t_1 + \beta t_2} + \frac{v_{0x_i}(t_2 - t_1)}{t_1 + \beta t_2}, \tag{3.3}$$

where $\beta \equiv \frac{m_1}{m_2}$ is the mass ratio of the fragments. The solution for v_{0x_i} can be evaluated as,

$$v_{0x_i} = \frac{1}{1+\beta}[\frac{x_2}{t_2} + \beta\frac{x_1}{t_1}]. \tag{3.4}$$

The y-velocity components, v_{0y_i} and v'_{1y}, can be evaluated in a similar manner. The z-component of the velocity can be evaluated from the measured TOF,

$$t_1 = \frac{d - z_i}{v_{0z_i} + v'_{1z}} \tag{3.5a}$$

$$t_2 = \frac{d - z_i}{v_{0z_i} + v'_{2z}}, \tag{3.5b}$$

which are the first and second hit on the detector, respectively. Here d is the distance from the interaction region to the detector, z_i is the location of the dissociation of a specific molecule within the interaction volume, and v_{0z_i} is the beam velocity of each molecule. The z-momentum conservation in CM is given by,

$$m_1 v'_{1z} + m_2 v'_{2z} = 0. \tag{3.6}$$

The dissociation velocities along z are linked as $v'_{2z} = -\frac{m_1}{m_2}v'_{1z}$. Again we have four unknowns, hence to solve these equations we replace z_i with its average value $\overline{z_i}$. The solutions for velocities along the z direction are given by,

$$v'_{1z} = \frac{1}{1+\beta}(\frac{d - \overline{z_i}}{t_1} - \frac{d - \overline{z_i}}{t_2}), \tag{3.7}$$

and

$$v_{0zi} = \frac{1}{1+\beta}(\frac{\beta(d - \overline{z_i})}{t_1} - \frac{d - \overline{z_i}}{t_2}). \tag{3.8}$$

We impose a reflection symmetry on the measured v'_{1z} distribution in order to specify the value of $\overline{z_i}$. After finding all the velocity components for a specific molecule, we can compute the momenta

of its fragments given by $p_{1j} = m_1 v'_{1j}$, where $j = x$, y, or z. From the momenta of both fragments, we evaluate the kinetic energy release (KER) and the direction of the dissociating fragments (θ, ϕ) relative to the laser polarization.

It is important to note that the different reaction channels cannot be distinguished by using the "field-free imaging" described above. For instance, the dissociation channel is not differentiated from the ionization channel. To overcome this difficulty, we introduce a weak longitudinal electric field around the interaction region to accelerate the ionic fragments relative to their charge-to-energy ratio. The electric field is provided by a spectrometer, which is schematically shown in Fig. 3.1 and labeled as an imaging spectrometer (IS). This static electric field modifies and separates the different fragmentation channels by their TOF as shown in Fig. 3.2.

The longitudinal electric field does not affect the (x,y) velocity components, expect for a minor correction which is discussed in detail in Refs. [197, 198]. In contrast, the z-velocity component is substantially affected by the longitudinal electric field due to the modification of the TOF formula. The TOF in the presence of an electric field can be modeled as:

$$t_1 = \frac{2d_1}{v_{0z_i}} \frac{1}{\eta_1} [\sqrt{(1+u_{1z})^2 + \eta_1(1-z'_i)} - (1+u_{1z})] + \frac{d_2}{v_{0zi}} \frac{1}{\sqrt{(1+u_{1z})^2 + \eta_1(1-z'_i)}}, \tag{3.9}$$

where d_1 and d_2 are the lengths of the electric field region and field-free region, respectively $(d = d_1 + d_2)$. $z'_i \equiv z_i/d_1$ is the scaled location of the fragmentation point, and $u_{1z} \equiv v'_{1z}/v_{0z_i}$ is the scaled dissociation velocity of the first fragment in the CM frame. Lastly, the ratio of potential and kinetic energy is defined as, $\eta_1 \equiv 0.8qV_s/\frac{1}{2}m_1 v^2_{0z_i}$, where V_s is the spectrometer voltage and q is the charge of the ion. We use SIMION [225] simulations to reproduce the measured TOF accurately and compare it with the model formula. The model formula given above reproduces the TOF to better than the accuracy of our experimental apparatus (∼100 ps). We can evaluate the v'_{1z} and v_{0z_i} velocities by using the same approximation as before, namely replacing z_i by its average value, $\overline{z_i}$. The z-direction equations are more complex, so we solve them numerically.

To summarize this section, the ion-atom break-up involves Eqs. 3.9, 3.5b and 3.6, while the ion-ion break-up channel includes Eq. 3.9 twice (for both first and second hits) and Eq. 3.6. These

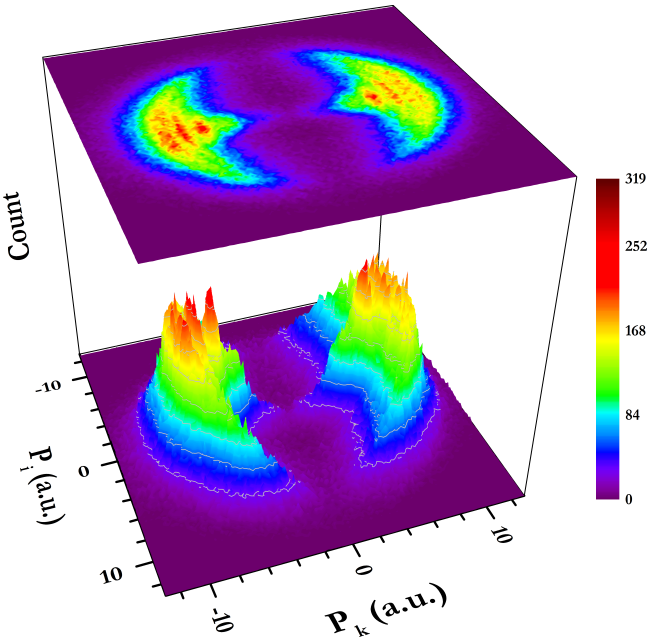

Figure 3.4: Measured 3D momentum distribution of H^+ fragments of HD^+ dissociation into H^++D. Laser polarization is along $\hat{k}$, the peak intensity $\sim 2 \times 10^{14}$ W/cm^2, the pulse duration 65 fs (positively chirped from a 23 fs FTL pulse), with a central wavelength of 790 nm. Note that the structures match the vibrational states of the HD^+ molecule, adapted from Ref [104].

equations are solved numerically to find the velocity of each fragment in the molecular frame. As an example, the reconstructed 3D momentum of H^+ from HD^+ dissociation into H^++D is shown in Fig. 3.4, where the linearly polarized laser field is along $\hat{k}$. The laser and ion beams propagate along $\hat{j}$ and $\hat{i}$, respectively, and the detector is in the $\hat{j}$-$\hat{k}$ plane. The structures along $\hat{k}$ in the momentum distribution are the products of different vibrational levels of the parent molecular ion.

3.3 Vibrationally-Resolved Structure in O_2^+ Dissociation Using a Few Wavelengths

Synopsis. Part of this section is based on Ref. [104], in which laser-induced dissociation of O_2^+ is studied in the strong-field limit using LFI method (see Section 3.2.3). In this study, linearly polarized laser pulses are used with central wavelengths of 784, 392 and 260 nm, pulse durations of 40–130 fs, and a peak intensity range of $\sim 10^{13}$–10^{15} W/cm^2. The measured kinetic energy release spectra from dissociation of O_2^+ reveal vibrational structure in strong field dissociation of multielectron molecules, which persists over a wide range of laser intensities. By evaluation of the potential energy curve (PEC), we assign the spectral energy peaks to dissociation of the ν=10–15 vibrational states of the metastable $a\,^4\Pi_u$ state via the dissociation pathway $|a\,^4\Pi_u\rangle \rightarrow |f\,^4\Pi_g - 1\omega\rangle$ — a mechanism equivalent to bond softening (BS) in H_2^+. Careful inspection unveils an apparent suppression in the dissociation of particular vibrational peaks, which is a manifestation of the well-known Cooper minima effect [95, 104].

3.3.1 Introduction

Intense ultrashort laser pulses have many applications in the physical, chemical and biological sciences as they provide an opportunity to manipulate reaction dynamics. In particular they have proven invaluable for imaging and controlling molecular dynamics through their nonlinear interaction with molecules (e.g., [80, 87]). Typically, however, molecular imaging in strong laser fields has been limited to electronic states (e.g., [81, 95, 226–229]), as high-resolution studies of individual vibrational (ν) states in strong fields are challenging and thus rare. The ability to perform ν-state specific studies opens the door to better control of molecular reactions as each ν-state can react in a different way to the strong laser field [230]. With advances in time- and position-sensitive imaging detectors, and better imaging techniques such as reaction microscopes [231, 232] and velocity map imaging (VMI) [233, 234], experimentalists are in a better position to target ν-state selective studies at low laser intensities.

One place to look for vibrational structure, which survives the strong-field interaction with

a molecule, is in the dissociative ionization of H_2. This process involves dissociation dynamics of the intermediate one-electron H_2^+ molecule. Generally, only two electronic states are involved in H_2^+ dissociation dynamics, the $1s\sigma_g$ ground state and the $2p\sigma_u$ first excited state. Higher lying electronic states can be neglected in most cases, though they do occasionally play a role (see, e.g., [36, 98, 235, 236]). In spite of the simplicity of, and the multitude of studies on, H_2 [91, 199, 200], observations of vibrational structure in its dissociative ionization, such as that by Zariyev *et al.* [237], are extremely rare. Indeed, that study was carried out using relatively long laser pulses (160 fs) that have a narrow bandwidth, which is good for spectral resolution but not amenable to time-resolved imaging experiments.

In contrast, vibrational resolution studies of H_2^+ ion beam targets are considerably more common [73, 92, 94, 95, 238–241] than other multielectron molecular-ion beam. Typically, the high ν states of H_2^+ dissociate by one-photon excitation to the repulsive $2p\sigma_u$ state on the low-intensity leading edge of the laser pulse, a fact that helps preserve the vibrational energy structure upon dissociation. It is less intuitive that vibrationally-resolved structure will appear in dissociation of more complex diatomic molecules driven by strong fields. This is in contrast to the abundance of vibrationally resolved spectra in beam fragment photodissociation studies (see, for example, Refs. [219, 242, 243]). However, the nature of dissociation under the influence of a weak or strong field is different, the first being a single photon process while the latter is strongly affected by multi-photon phenomena [199, 200]. It worth mentioning that the vibrational structure studies in strong laser field is originated from absorption and stimulated emission of many photons resulting in dissociation with net one photon.

Normally the multitude of potential energy curves and possible dissociation pathways, even in relatively simple systems like N_2^+ or O_2^+, can lead to overlap in KER peaks, that simply inhibit the observation of vibrational structure. Arguably this is the main reason for the absence of vibrationally-resolved spectra in such molecules to date.

In light of these issues, it is perhaps surprising that we do observe vibrational structure in strong-field dissociation of a multielectron molecular ion, O_2^+ — as we present here. Using intense

784 nm, 392 nm and 260 nm laser pulses we demonstrate clearly the presence of structure in the KER spectrum, following dissociation of an O_2^+ ion beam target, that can be assigned to specific ν states.

Our choice of O_2^+ to look for vibrational structure is triggered by the fact that we have explored this system previously with an intense laser, particularly its dissociation as an ion beam [102, 197]. From this earlier work we believe that we can identify a large number of its dissociation pathways. Unfortunately, at that time our imaging resolution for the ion beam fragments was insufficient to discern vibrational peaks in KER had they been present. After significant development of our crossed-beam coincidence 3D momentum imaging setup we can measure vibrationally-resolved KER spectra using shorter laser pulses in H_2^+ [95] and also in low energy dissociation of O_2^+, presented in this work.

3.3.2 Experimental Method

The laser used for these studies is KLS system (see Section 2.2) operating at 1.5 kHz repetition rate, with an output central wavelength of 784 nm, a Fourier-transform-limited pulse duration of 40 fs (FWHM in intensity), and a pulse energy of up to 1 mJ. The pulses can be converted in wavelength to 395 and 266 nm using a second and third harmonic generation β-barium borate crystal (see Section 2.3.1). The linearly polarized pulses are focused onto the O_2^+ ion beam target using an $f = 203$ mm off-axis parabolic mirror, generating intensities up to 4×10^{15} W/cm^2.

Figure 3.5(a) and (b) show the complex electronic structure of O_2^+. The PECs are adapted from Ref. [244]. For our O_2^+ ion beam measurements, oxygen gas was ionized by electron impact in an electron cyclotron resonance (ECR) ion source. This produced O_2^+ ions with about a third of the molecules in the metastable lowest quartet state, $a\,^4\Pi_u$, with a lifetime longer than a millisecond [245] and the remaining two-thirds in the doublet ground state, $X\,^2\Pi_g$ (see, for example, [246, 247]). The electron impact ionization mechanism produces ions through vertical transitions, in which the vibrational population approximately follows the Franck-Condon factors [28, 211]. The approximately Franck-Condon vibrational populations of these two electronic states are evaluated by the Franck-Condon overlap integral [248, 249] as shown in Figs. 3.6(a) and

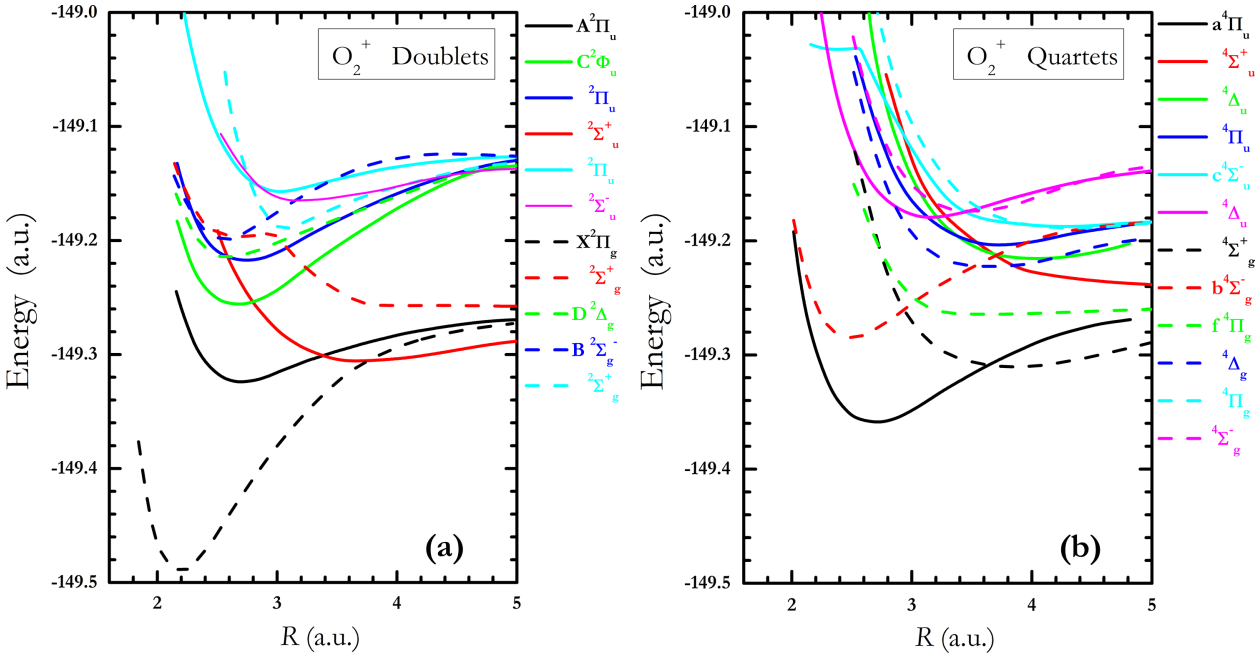

Figure 3.5: O_2^+ Born-Oppenheimer potential energy curves adapted from Ref. [244]. The (a) doublet and (b) quartet states are separated for visualization.

(b). As will be shown later, the main channel of interest in this study involves the dissociation of the $a\,^4\Pi_u$ state.

3.3.3 Results and Discussion

Typical dissociation spectra for O_2^+ are shown in Fig. 3.7. The angle θ is between the molecular dissociation axis and the laser polarization. This spectrum is rich in structure and many of the dissociation pathways responsible for the features have been identified in our earlier work [102], as well as by others (e.g., Ref. [251]). Specifically, the peak labeled β at about 1.5 eV can be assigned to the more complex dissociation pathway $|a\,^4\Pi_u\rangle \rightarrow |f\,^4\Pi_g - 1\omega\rangle \rightarrow |^4\Sigma_u^+ - 2\omega\rangle$.

The peak labeled α at about 2.3 eV reported earlier [102] is due to three-photon absorption via the pathway $|a\,^4\Pi_u\rangle \rightarrow |f\,^4\Pi_g - 3\omega\rangle$ [102]. This peak is not clearly seen in this work. Additionally, the peak labeled γ at about 0.7 eV is associated with dissociation of the O_2^+ $a\,^4\Pi_u$ state to the $^4\Sigma_u^+$ state dressed by three photons, although the exact pathway connecting these states requires further work. A few dissociation pathways that are consistent with the KER peak labeled γ in

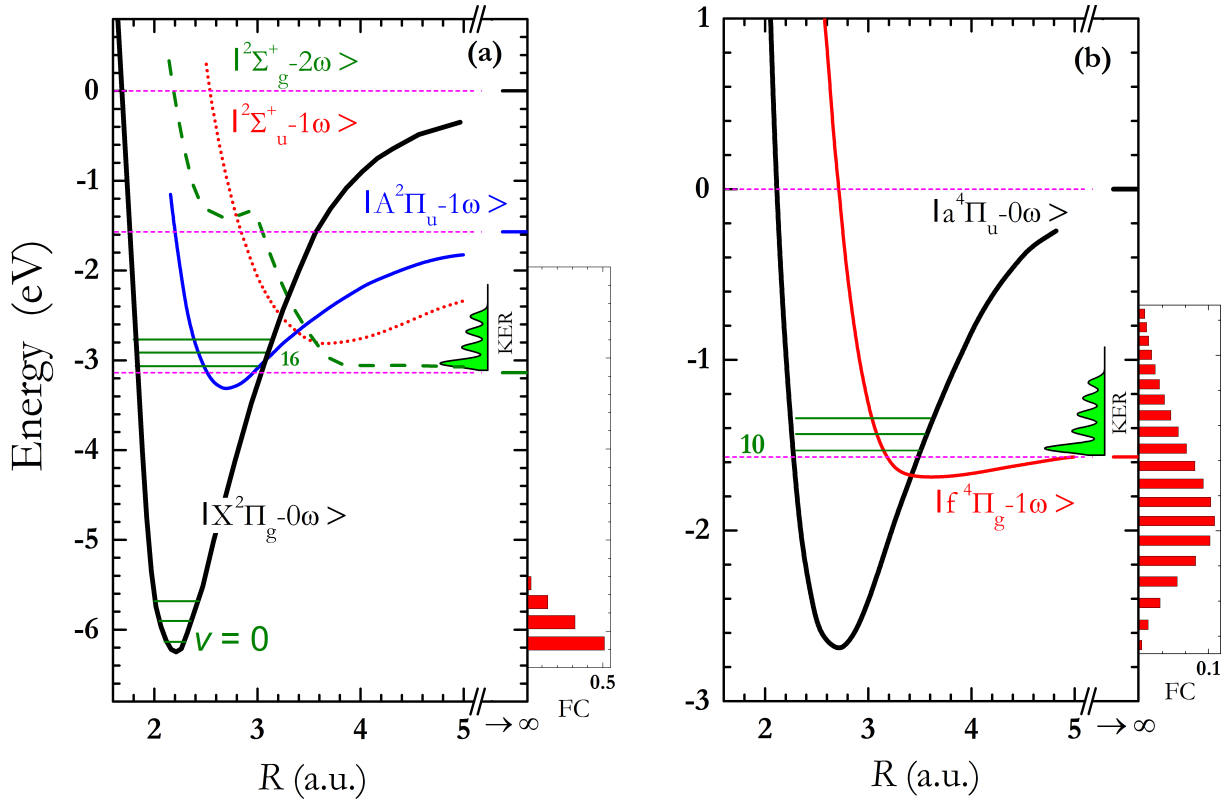

Figure 3.6: Diabatic dressed potential energy curve (PEC) diagrams of O_2^+ depicting the main dissociation pathways (see text) of the (a) $X\,^2\Pi_g$ doublet ground state and (b) $a\,^4\Pi_u$ lowest quartet state, yielding low KER. The PECs were taken from Ref. [244]. The vibrational populations, shown in the insets, are the Franck-Condon factors for vertical electron-impact ionization in the ion source. We used the phase-amplitude method [250] to evaluate the vibrational wave functions needed for the overlap integrals. A schematic vibrationally-resolved low KER spectrum is also shown in each panel.

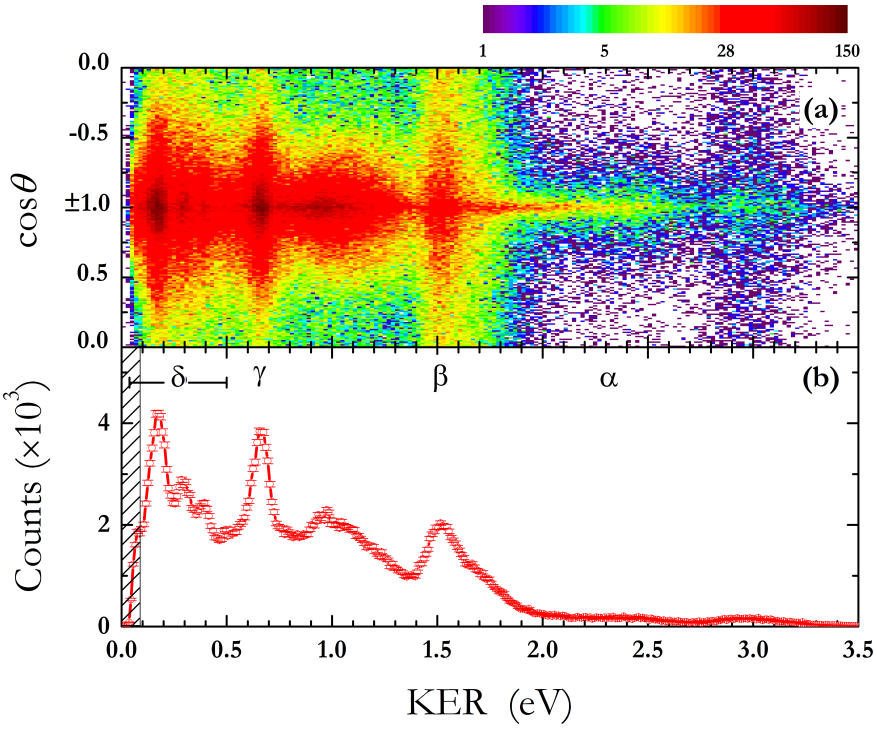

Figure 3.7: (a) KER-cosθ density plot of O_2^+ dissociation in a 784 nm, 40 fs, 4×10^{15} W/cm^2 laser pulse. (b) the KER spectrum evaluated by integrating over all angles in panel (a). The labeled KER peaks are associated with the following dissociation pathways (see text and Refs. [102, 104]): (α) $|a\,^4\Pi_u\rangle \rightarrow |f\,^4\Pi_g - 3\omega\rangle$, ($\beta$) $|a\,^4\Pi_u\rangle \rightarrow |f\,^4\Pi_g - 1\omega\rangle \rightarrow |^4\Sigma_u^+ - 2\omega\rangle$, ($\gamma$) see text, and the feature of main interest here (δ) $|a\,^4\Pi_u\rangle \rightarrow |f\,^4\Pi_g - 1\omega\rangle$ for $\nu = 10$–15 — depicted in Fig. 3.6(b). Adapted from Ref. [104]

Figs. 3.7 and 3.8 have been proposed in Ref. [251], namely:

(i) $|a\,^4\Pi_u\rangle \rightarrow |2\,^4\Pi_g^+ - 3\omega\rangle$,

(ii) $|a\,^4\Pi_u\rangle \rightarrow |f\,^4\Pi_g^+ - 1\omega\rangle \rightarrow |2\,^4\Pi_g^+ - 3\omega\rangle$,

(iii) $|a\,^4\Pi_u\rangle \rightarrow |f\,^4\Pi_g^+ - 1\omega\rangle \rightarrow |2\,^4\Pi_u^+ - 2\omega\rangle \rightarrow |2\,^4\Pi_g^+ - 3\omega\rangle$.

While these features are interesting in their own right, the focus of the present work is on the series of closely spaced, narrow, low-KER peaks labeled δ that have been reported earlier by our group [104]. For visualization, we zoom in on the KER spectrum below 0.8 eV as shown in Fig. 3.8(a). Based on their energy we suggest that all the KER peaks labeled δ are due to dissociation of the $\nu = 11$–15 states bound in the $a\,^4\Pi_u$ potential, along the pathway $|a\,^4\Pi_u\rangle \rightarrow |f\,^4\Pi_g - 1\omega\rangle$ [see Fig. 3.6(b)]. This is a net one-photon bond softening process similar to the one commonly observed in H_2^+ [26, 237]. Specifically, the peaks are centered about the energies

one would expect for dissociation by absorption of a 784 nm photon, marked by vertical ticks on Fig. 3.8(a).

The data in Fig. 3.8 is in good agreement with a fit function consisting of the sum of Gaussian peaks centered at the expected positions for $a\,^4\Pi_u(v)$ ($\nu = 11$-15) to $f\,^4\Pi_g$ transitions, and a couple of additional peaks at higher KER (specifically the γ peak and one additional Gaussian to represent the tail extending to lower KER from the peak(s) centered around 1.0 eV in Fig. 3.7(a). A common width was used for the first 5 δ peaks as expected for similar transitions [226], while the width of the remaining 2 peaks were free parameters. Note that the lowest expected KER peak ($\nu = 10$) cannot be measured in our spectrometer apparatus due to losses of very low KER fragments in the Faraday cup, and for the same reason the centroid of the $\nu = 11$ peak is slightly shifted to a higher energy (the magnitude of this shift is consistent with the one expected when convoluting the response function due to Faraday cup losses with the $\nu = 11$ Gaussian). We overcome this issue by repeating our measurement with our LATFI imaging setup [198]. Additionally, the dissociation of the ν=12 state appears to be suppressed relative to the other states (see discussion below).

To verify the pathway assigned above we present in Fig. 3.8(b) the angular distribution associated with events within the δ peaks. The measured angular distribution (open circles) conforms well to a $\cos^2\theta$ distribution as expected for a net one-photon $\Pi \rightarrow \Pi$ ($\Delta\Lambda = 0$) transition (see [102, 251]). Moreover, all the peaks in the low-KER feature δ have approximately the same intensity dependence and angular distribution as would be expected for net one-photon transitions between the same electronic states.

While so far we have discussed only dissociation pathways involving the metastable $a\,^4\Pi_u$ state of O_2^+, we can exclude the $X\,^2\Pi_g$ ground state from being responsible for the structure δ for several reasons. Firstly, we identify the most probable dissociation pathways originating from the $X\,^2\Pi_g$ state, shown in Fig. 3.6(a), as

(i) $|X\,^2\Pi_g\rangle \rightarrow |A\,^2\Pi_u - 1\omega\rangle \rightarrow |^2\Sigma_g^+ - 2\omega\rangle$, and (ii) $|X\,^2\Pi_g\rangle \rightarrow |\,^2\Sigma_u^+ - 1\omega\rangle \rightarrow |^2\Sigma_g^+ - 2\omega\rangle$,

following the procedures described in Ref. [102].

Both these pathways involve consecutive one-photon transitions and would yield the same KER

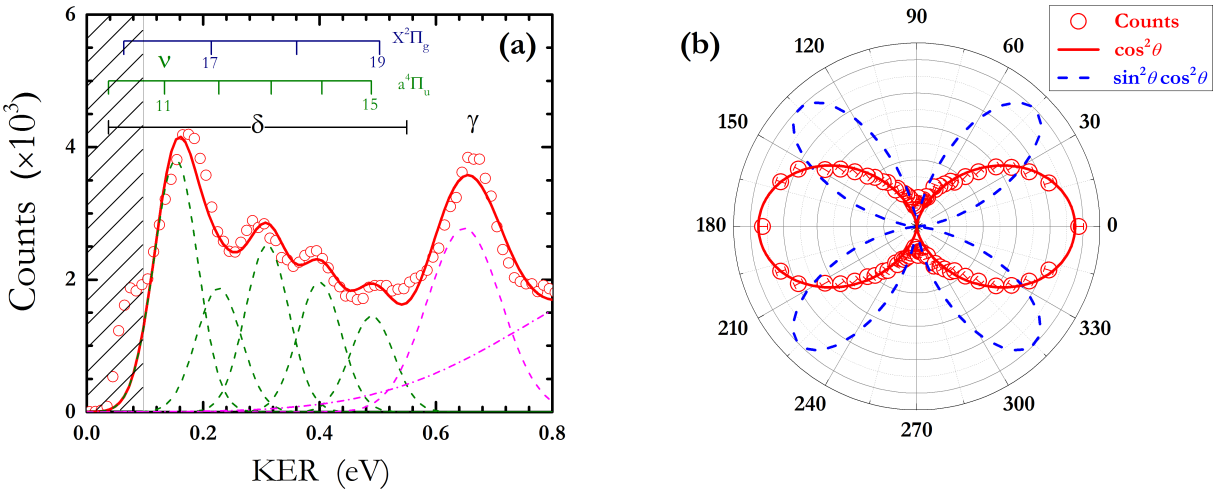

Figure 3.8: (a) The low KER spectrum of O_2^+ dissociating into O^++O in a 784 nm, 40 fs, 4×10^{15} W/cm^2 laser pulse. The fit function (thick red line), consisting of the γ (dashed magenta line) and δ (dashed green line) contributions (see text), is in good agreement with the data (open red circle). A tail of the peak centered around 1 eV [see, Fig. 3.7] is also visible at high KER (dash-dot magenta line). Note that the $\nu = 12$ is suppressed relative to the other states (see text). The blue vertical ticks at the top mark the expected positions for dissociation of the $X\,^2\Pi_g$ state, following the pathways shown in Fig. 3.6(a) (see text) — note that these KER values do not match the data as well as those associated with the $a\,^4\Pi_u$ state. (b) A polar plot of the O^++O dissociation direction relative to the laser polarization (the distribution was reflected about the polarization axis to generate the bottom part of the polar plot). Error bars are smaller than the symbols. The solid red line is a $\cos^2\theta$ distribution that fits the data well, while the dashed blue line indicates a $\sin^2\theta\cos^2\theta$ distribution which does not match the data (see text).

since they connect the same initial and final states. In principle, the resulting KER distribution would exhibit vibrational structure over a similar energy range to the δ peaks. However, as can be seen from Fig. 3.8(a), the predicted peak positions for the dissociation of the $a\,^4\Pi_u$ state match the data considerably better than those of the $X\,^2\Pi_g$ state. Furthermore, as evident in Fig. 3.6(a) the Franck-Condon population of the $X\,^2\Pi_g$ ν states involved (ν=16–19) is negligible as the population is strongly peaked near the bottom of the well [see Fig. 3.6(a)]. Secondly, the suggested dissociation pathways of the $X\,^2\Pi_g$ state should have a $\sin^2\theta\cos^2\theta$ angular distribution, as they involve one parallel ($\Delta\Lambda = 0$) and one perpendicular ($\Delta\Lambda = 1$) transition [102], but such a distribution is inconsistent with the measured data, shown in Fig. 3.8(b). Finally, the fact that the measured low-KER feature δ change slowly with laser intensities (we observe it down to 4×10^{13} W/cm^2, the lowest we have measured) also supports its assignment as a one-photon

transition, unlike the net two-photon transition involving the $X\,^2\Pi_g$ state, which we would expect to drop faster with intensity [102].

With this insight at 784 nm, we are able to predict the outcome of dissociation driven by intense 395 nm laser pulses. At 395 nm one expects that all the bound low ν states of $a\,^4\Pi_u$ should decay by $|a\,^4\Pi_u\rangle \rightarrow |f\,^4\Pi_g - 1\omega\rangle$ as the crossing between $a\,^4\Pi_u$ and the dressed $|f\,^4\Pi_g - 1\omega\rangle$ state is near the minimum of the $a\,^4\Pi_u$ potential, as shown in Fig. 3.9(a). The predicted positions of the KER peaks are indicated by the vertical ticks in Fig. 3.9(c). Indeed, they show good agreement with the measured KER spectrum in Figs. 3.9(b) and 3.9(c). This is further illustrated by the nice fit of the sum of Gaussian peaks with a common width centered at the expected positions or, as shown in Fig. 3.9(c), allowing only for a small (11 meV) common shift to compensate mainly for experimental uncertainties. The fit function also includes a couple of Gaussian peaks (due to other dissociation pathways) on either side of the δ feature as their tails overlap somewhat with this feature. Additionally, the angular distributions are similar to those for 784 nm confirming the proposed net one-photon dissociation pathway.

Careful inspection of Fig. 3.9(c) reveals an apparent suppression in the dissociation of particular ν states, namely $\nu = 3$ and 5, relative to their neighbors, given that the initial vibrational population in the $a\,^4\Pi_u$ state is smooth as seen in Fig. 3.6(b). We believe that the $|a\,^4\Pi_u(v_i)\rangle \rightarrow |f\,^4\Pi_g - 1\omega\rangle$ transitions for $\nu = 3$ and 5 are suppressed due to the small magnitude of the dipole transition moments coupling these states at this photon energy (Cooper minima) — a phenomenon we have observed in H_2^+ dissociation [95]. The same holds for the suppressed dissociation of $\nu = 12$ at 784 nm shown in Fig. 3.8(a). In the upcoming section, we discuss our ongoing investigation of this vibrational suppression phenomenon in more detail by using laser pulses with different wavelengths.

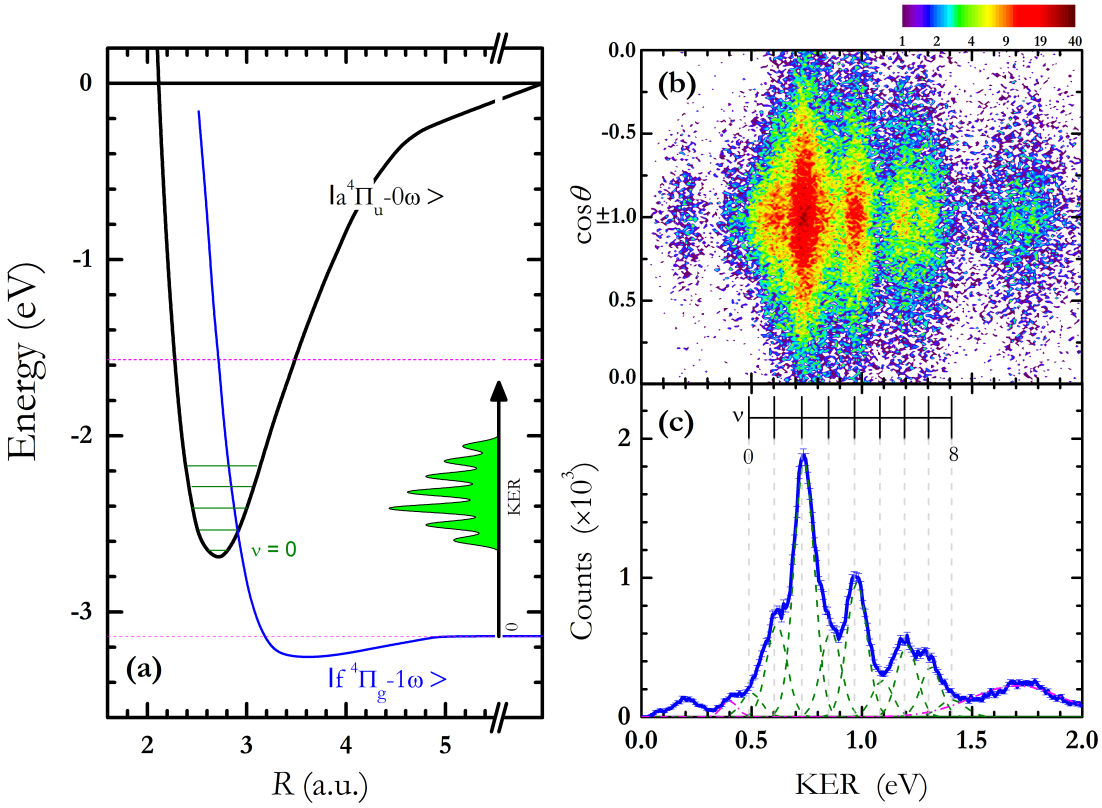

Figure 3.9: (a) Diabatic dressed potential energy curve diagram of O_2^+ depicting the $|a\,^4\Pi_u\rangle \rightarrow |f\,^4\Pi_g - 1\omega\rangle$ dissociation pathway in a 395 nm laser field. A schematic vibrationally-resolved KER spectrum is also shown in the panel. (b) Measured KER-cosθ density plot of O_2^+ dissociation in a 395 nm, 40 fs, 1×10^{14} W/cm^2 laser pulse. (c) the KER spectrum evaluated by integrating over all angles in panel (b). The measured peaks are in agreement with the position expected for $|a\,^4\Pi_u\rangle \rightarrow |f\,^4\Pi_g - 1\omega\rangle$ transitions from $\nu = 0-8$ — marked by the vertical ticks. The nice fit to the data (thick blue line) consists of Gaussian peaks representing the above transitions (dashed green lines) and a couple of free Gaussian peaks on either side of the δ feature (dot-dashed red line, see text). Note that a couple of peaks ($\nu = 3$ and 5) are suppressed in the spectrum (see Section 3.3.4).

3.3.4 Investigating Cooper Minima in Dissociation of O_2^+ in Strong-Field

Several years ago, we reported an observation of suppressed dissociation of specific H_2^+ vibrational states in intense laser pulses [95]. A calculation of H_2^+ including nuclear rotation [252, 253] reveals a suppression at ν=12 and 13 in agreement with our findings [95]. The suppression is caused by the small dipole coupling matrix element between the relevant states. This phenomenon is a manifestation of the well-known Cooper minima effect, which has been studied in photoionization processes [254]. The dynamics of H_2^+ in a strong laser field have been also interpreted by first-order perturbation theory [95]. We implement a similar approach to O_2^+ dissociation via the net one photon dissociation pathway, $|a\,^4\Pi_u\rangle \rightarrow |f\,^4\Pi_g - 1\omega\rangle$, which exhibits vibrational structure in the KER spectrum.

In our treatment, first-order time-dependent perturbation theory is used to compute transition probabilities for molecules excited from a bound electronic state to a dissociative state, for example $|a\,^4\Pi_u\rangle \rightarrow |f\,^4\Pi_g - 1\omega\rangle$ in our O_2^+ case. This is computed by

$$\frac{dP_\nu}{dE} = \pi \frac{2\ln 2}{(\Delta\omega)^2} I \left|D_\nu(E)\right|^2 \exp\left[-\left(\frac{2\sqrt{\ln 2}(\omega - \omega_{fi})}{\Delta\omega}\right)^2\right], \tag{3.10}$$

where $|D_\nu(E)|^2$ is the square of the dipole-matrix element, I is the laser peak intensity, $\Delta\omega$ is the laser bandwidth for a Gaussian laser pulse and $\omega_{fi} = E - E_\nu$. The dipole-matrix elements can be written as $D_\nu(E) = \langle \psi_{fE}(R) \left|D(R)\right| \psi_{av}(R)\rangle$, where $\psi_{fE}(R)$ is the nuclear continuum wave function of the final state and $\psi_{av}(R)$ is the vibrational wave function of the initial state. The dipole coupling between the $|a\,^4\Pi_u\rangle$ and $|f\,^4\Pi_g\rangle$ electronic states, $D(R) = \langle \Phi_{f^4\Pi_g}(\mathrm{R};\mathrm{r})|z|\Phi_{a^4\Pi_u}(\mathrm{R};\mathrm{r})\rangle$, is taken from Ref. [244]. The phase-amplitude method [250] is used to evaluate the bound vibrational wavefunctions of the $|a\,^4\Pi_u\rangle$ state and also to calculate the continuum wavefunctions, $\psi_{fE}(R)$, at specific energies on $|f\,^4\Pi_g\rangle$.

Figure 3.10 shows $|D_\nu(E)|^2$ for each vibrational state ν as a function of KER. The dips in $|D_\nu(E)|^2$, appearing as a white honeycomb structure, are the result of poor overlap between the continuum and bound wave functions as a function of KER. The solid curves show the expected

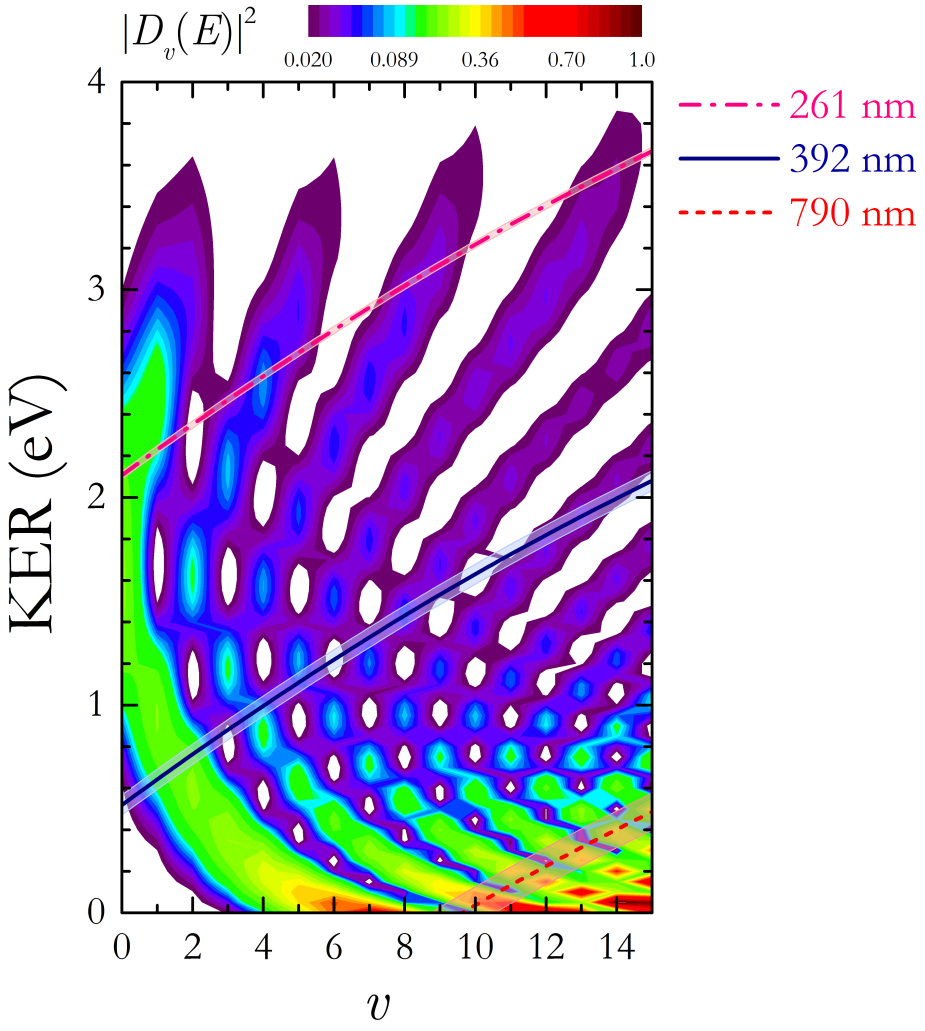

Figure 3.10: Square of the amplitude of the dipole-matrix elements ($|D_\nu(E)|^2$) for O_2^+ as a function of ν and KER. The curves show the expected KER for various wavelengths and the shaded area along these curves represent the FWHM of bandwidth estimated from the measured spectra for different wavelengths. For presentation purposes, the calculated $|D_\nu(E)|^2$ at different ν are interpolated to generate a smooth map.

KER for O_2^+ photodissociation at 784 nm, 392 nm and 260 nm. The shaded areas along these curves represent the FWHM of bandwidth estimated from the measured laser spectra. We can see that the laser bandwidth acts as a filter on the $|D_\nu(E)|^2$ map. The total dissociation probability, P_D, is then determined by $P_D = \int \frac{dP}{dE}\, dE$. The evaluated transition probabilities for different laser parameters are shown in Fig. 3.11. We repeated our measurement for three different wavelengths by using our imaging-deflector method, which enables measurement of KER down to near 0 eV [198].

Figure 3.11(a) shows the measured KER (symbol) for dissociation of O_2^+ into O^++O using 784 nm, 40 fs laser pulses with a peak intensity of $\sim 2\times10^{15}$ W/cm^2. Vertical lines (bars) in each graph represent the calculated transition probability, P_D, for different vibrational levels. The initial vibrational population in the $|a\,^4\Pi_u\rangle$ state is computed by the Franck-Condon principle, i.e. as the overlap integral of the vibrational ground state of O_2 and the vibrational states bound in the $|a\,^4\Pi_u\rangle$ potential of O_2^+. To determine the correct measured probabilities (proportional to the yield), our calculated transition probabilities are weighted by the vibrational level population of the $|a\,^4\Pi_u\rangle$ electronic state, P_ν. The darker bars in Fig. 3.11 represent the weighted probabilities for different initial vibrational levels and wavelengths. The calculated probability is scaled to the largest peak in the measured KER. The measured KER spectrum using 784 nm wavelength, shown in Fig. 3.11(a), reveals a dominant peak at 37 meV corresponding to the photodissociation of the ν=10 state. This peak was lost in our previous measurements presented earlier [see section 3.3.3 Fig. 3.8(a)], as the fragment with low KER cannot escape the Faraday cup. The KER structures measured above 0.1 eV are similar to the earlier results presented in Section 3.3.3. The calculated probabilities (vertical bars) shown in Fig. 3.11(a) match the KER spectrum "qualitatively". There is a small energy shift between the calculated results and the measured KER, which can be due to our experimental energy calibration.

It is worth noting that the experimental results are acquired at higher intensity, namely in the strong-field ($\gtrsim 10^{12}$ W/cm^2) regime, for which perturbation theory is not expected to provide quantitative results. In Ref. [95], the robustness of vibrational suppression predicted by first-order perturbation theory was examined by solving the full-dimensional time-dependent Schrödinger equation (TDSE) in the Born-Oppenheimer representation. The comparison reveals that the predictive power of perturbation theory can be used for qualitative comparison, especially when predicting the Cooper minima locations.

We conducted similar measurements employing shorter wavelengths provided by SHG and THG, following the procedure described in Section 2.3.1. Figure 3.11(b) shows the measured KER for positively chirped laser pulses of 392 nm, 52 fs pulse duration and a peak intensity of about

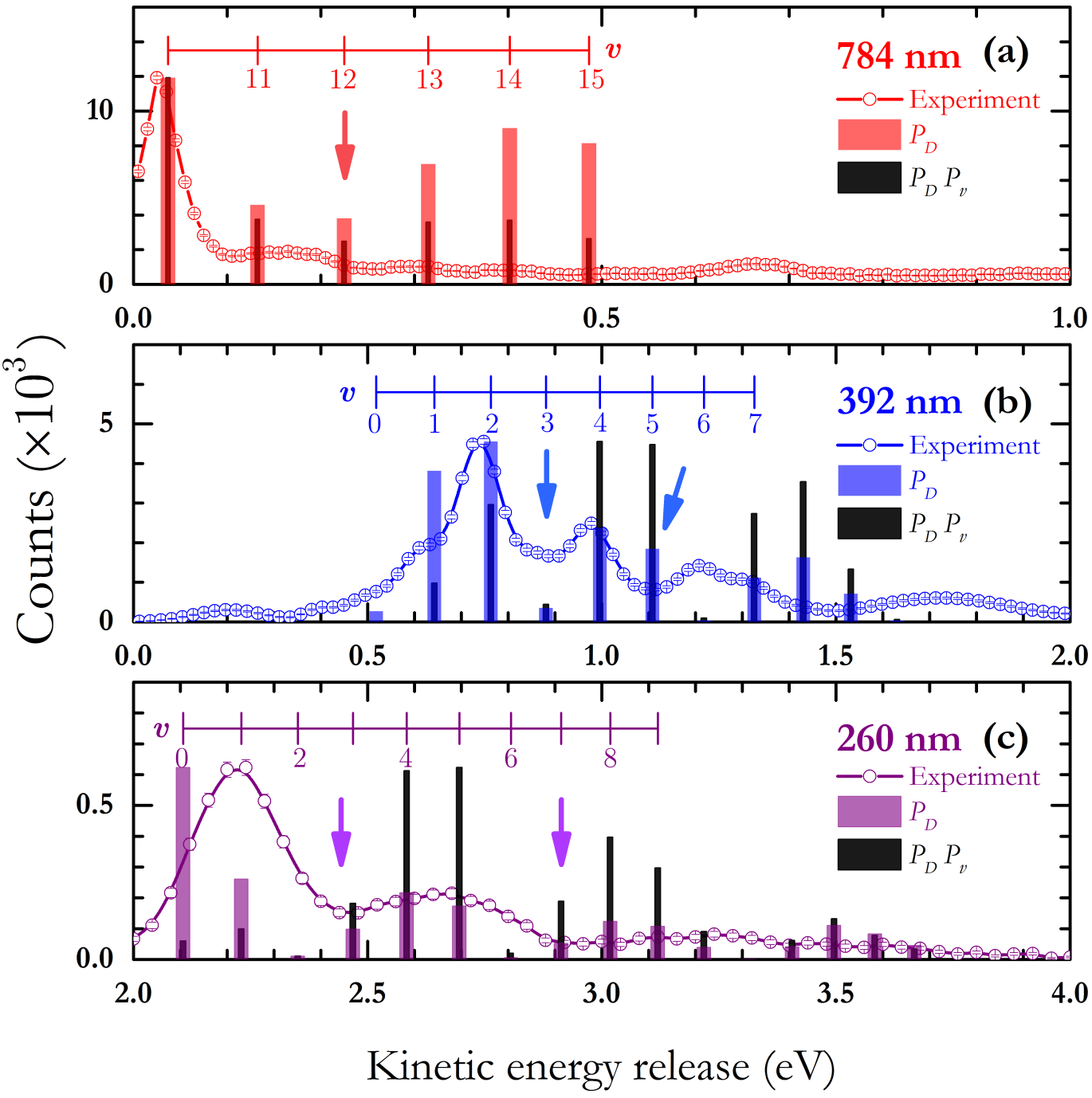

Figure 3.11: Experimental KER distributions of O_2^+ dissociation for laser pulses at (a) 784 nm, $I_0 \sim 2\times10^{15}$ W/cm^2, (b) 392 nm, $I_0 \sim 2\times10^{14}$ W/cm^2, and (c) 260 nm, $I_0 \sim 3(\pm1)\times10^{12}$ W/cm^2. (a)–(c) Dissociation probabilities are calculated by using first-order perturbation theory for the relevant central wavelength, as shown by vertical lines. The dissociation probabilities weighted by Franck-Condon factors are shown in darker color and narrower bars. The width of these bars has no physical meaning. Arrows indicate the suppression positions in the experimental results.

2×10^{14} W/cm^2. The dissociation probabilities are calculated for a one-photon transition between $|a\,^4\Pi_u\rangle$ and $|f\,^4\Pi_g\rangle$ states with a photon energy of 3.16 eV (392 nm). The dissociation probabilities, plotted as vertical bars in Fig. 3.11(b), are in reasonable agreement with the measured KER — indicating vibrational suppression at ν=3. However, the experimental results show a minimum at $\sim$ 1.1 eV, where the calculated dissociation probability is not negligible. In addition, the Franck-Condon dissociation probability does not match the experimental results, suggesting that the Franck-Condon initial population on $|a\,^4\Pi_u\rangle$ state breaks down. In modeling the Frank-Condon population, we disregard the possibility of populating $|a\,^4\Pi_u\rangle$ state through radiative decay from higher quartet states.

Finally, by employing THG, we measured the KER distribution, as shown in Fig. 3.11(c), with a central wavelength of 260 nm ($\sim$4.76 eV), a pulse duration of about 130 fs positively chirped, and a peak intensity of $\sim(3\pm1)\times10^{12}$ W/cm^2. The KER is shifted by an IR photon energy compared to SHG results as expected. A few minima are predicted by the perturbation theory around ν=2, 6 and 11. In this case too, the computed dissociation probability resembles the experimental results.

It is worth mentioning that Prabhudesai *et al.* [73] measured the kinetic energy release from H_2^+ using positively and negatively chirped laser pulses. They found that the KER of these vibrational peaks are shifted up or down depending on the sign of the chirp. Repeating our measurements with FTL laser pulses can shed light on the shift in KER due to the chirped laser pulses, resulting in a better agreement between the calculated probabilities and our measurements.

3.3.5 Summary and Outlook

In summary, vibrationally resolved KER dissociation spectra of a multielectron molecule, O_2^+, by intense ultrashort laser pulses have been measured. The vibrational structure observed persists over a wide range of laser intensities. We have identified the structure as arising from the dissociation of a subset of vibrational states (ν=10–15) of the metastable $a\,^4\Pi_u$ state via the dissociation pathway $|a\,^4\Pi_u\rangle \rightarrow |f\,^4\Pi_g - 1\omega\rangle$ for 784 nm photons. In effect this structure is equivalent to that observed previously for bond softening dissociation of H_2^+, although it can be considered as somewhat of a surprise that it survives for a multielectron system considering the complexity of the potential

energy curves of O_2^+ (see, e.g., [102, 104]).

In addition, we studied vibrationally resolved spectra of O_2^+ dissociation using shorter wavelengths of 261 and 392 nm. We observed the vibrational suppression effect in the dissociation spectra due to the small magnitude of the dipole transition moment, which depends on the photon energy — a well-studied phenomenon known as Cooper minima. We employed first-order perturbation theory to qualitatively understand the vibrational suppression in O_2^+.

With the ability to perform vibrationally resolved studies, one is in a better position to carry out strong-field control experiments targeting specific vibrational states and ultimately leading to a higher level of control. For example, one can envision a pump-probe study of the dissociative ionization of O_2. Since dissociation of individual ν states of this molecule can be imaged [104], the effects of the pump pulse on vibrational population [223] or imaging the beat vibrational period from the superposition of neighboring ν states [255, 256] can be studied in detail.

3.4 Rudimentary Coherent Control: Bandwidth Effect in Dissociation of H_2^+ and HD^+

Synopsis. A coincidence 3D momentum imaging method is employed to study the fragmentation of H_2^+ and HD^+ following interaction with an intense IR 7–25 fs FTL laser pulse. The broad bandwidth of the FTL pulse prevents observation of the vibrational peaks that one would expect to measure using longer FTL laser pulses ∼100 fs. However, by chirping the pulse either positively or negatively, while maintaining a fixed bandwidth, the measured vibrational structure is clearly resolved. The kinetic energy release of these vibrational peaks are shifted up or down depending on the sign of the chirp [73, 74, 257]. We will address the question of why the vibrational structure is observed in spite of the broad bandwidth of the chirped laser pulses. In addition, very slow fragmentation of HD^+, produced by a two-photon process called zero-photon dissociation (ZPD), is studied. The sign of the chirped laser pulses is used to control the ZPD process in dissociation into either H^++D or H+D^+.

3.4.1 Introduction

Manipulating molecular dynamics and the outcome of chemical reactions, *i.e.* coherent control, are important objectives of laser-matter interaction studies [23, 38, 53, 200, 258]. In a nutshell, controlling molecular fragmentation can be accomplished by tailoring the electric field of the laser pulse. In the last decade, rapid advancement in laser technology has made it possible to partially achieve this control goal. To name a few examples of such work, Assion *et al.* used a pulse shaper to optimize the branching ratios of different photodissociation reaction channels in organometallic chemistry [40]. Prokhorenko *et al.* studied isomerization of retinal molecules by modulating the phases and amplitudes of spectral components in the photoexcitation pulse [259]. More recently, De *et al.* used a two-color electric field to demonstrate the alignment and orientation of CO molecules [260]. Numerous other coherent control schemes have been developed, e.g. [52, 61, 261–263].

Our strategy to achieve and understand coherent control of molecular processes relies on the

use of the benchmark molecule H_2^+, for which accurate theoretical treatment of the interaction with a strong laser field is feasible. Typically, H_2^+ is generated in strong-field studies by ionizing H_2 during the laser pulse. (See, for example previous experimental and theoretical studies of H_2^+ [26, 199, 200, 208–210]). In contrast, we start with an H_2^+ ion-beam target prepared with a Franck-Condon distribution of vibrational levels [211]. The other key component of this study is the use of simply shaped pulses [73, 264], for which the laser field variation with time is well known, to conclusively elucidate the molecular response to different electric fields.

In the previous studies [73, 74, 257], pulses shaped through the application of a quadratic phase function exemplify how the effective frequency sweep (also known as chirp) can be used to manipulate the dissociation dynamics of H_2^+. Prabhudesai *et al.* [73] observed a shift in the kinetic energy release (KER) of specific vibrational levels that corresponds to the chirp sign — these findings are supported by theory [73, 265]. Later, Natan *et al.* [74] reported that the magnitude and sign of the chirp can be used as a tool to enhance the strong-field dissociation yield from the low lying vibrational levels ($\nu \leq 6$) of H_2^+. The mechanism they proposed manifests itself in the ability to dynamically control the induced avoided crossing using the instantaneous frequency.

In this work, two complementary experiments are presented. The first extends our understanding of molecular dynamics driven by chirped pulses, focusing on how such pulses can be used to reduce the width of the peaks in the measured KER spectra, therefore improving one's ability to resolve vibrational structure. Explicitly, the vibrational structure lost in interactions with broad bandwidth Fourier transform limited (FTL) pulses can be retrieved through chirping the pulse, despite maintaining the same spectral components.

The second experiment focuses on controlling a stimulated Raman process known as zero photon dissociation (ZPD) [208, 266–268]. In this process, the molecule falls apart by absorbing a zero net number of photons. Recently, the ZPD process seen in the benchmark molecules such as H_2^+ and H_3^+ has been studied in extensive detail [99, 198]. We discuss how chirp can be used as a tool to manipulate the dissociation dynamics of HD^+ with low KER. The combination of both sets of results provides a more comprehensive qualitative insight into the molecular response in an

intense laser field.

3.4.2 Experimental Method

The H_2^+ and HD^+ molecular ions are generated via electron impact ionization, then accelerated (∼7 and 10 keV, respectively), mass selected, and electrostatically focused and steered to form a well-collimated beam. The FTL laser pulses with central wavelength near 800 nm, and temporal duration of 25 fs (at 10 kHz from PULSAR) and 7 fs (at 2 kHz from KLS), are focused perpendicularly onto the target using a 250 mm spherical mirror and a 200 mm off-axis parabolic mirror, respectively. The dissociation fragments are measured in coincidence. The positions of the fragment impacts on the detector and their time of flight (TOF) are used to evaluate the full three-dimensional (3D) momentum of each fragment as discussed earlier.

3.4.3 Effective Bandwidth Narrowing — Linear Chirp Effect in Dissociation of H_2^+

Below, we discuss how a linear chirp effect in bond softening of H_2^+ can affect the vibrational structure observed in the KER spectrum compared to that obtained for a FTL pulse with similar frequency components. Later, we discuss how the laser pulse chirp controls the ZPD process in fragmentation of HD^+.

The energy resolution of the momentum imaging technique employed in this work is sufficient to clearly observe the vibrational structure in the KER spectrum for H_2^+ dissociation, as demonstrated in previous work [92, 94, 95]. It is evident from those experiments, and also from the work of others [238, 239], that the bandwidth of the laser pulse, relative to the vibrational spacing of the molecule, plays a critical role in the attainable resolution. Typically, the ∼50 fs FTL pulses used have a spectral bandwidth of about $\Delta\lambda_{\mathrm{FWHM}}$ ∼18 nm (or $\Delta E_\lambda \sim 36$ meV). This leads to an overall energy resolution of $\Delta E = \sqrt{(\Delta E_\lambda)^2 + (\Delta E_{\mathrm{KER}})^2}$, when convolved with the instrumental energy resolution, ΔE_{KER}, by assuming a one photon process in the perturbation regime. If ΔE is sufficiently smaller than the vibrational energy spacing, the individual ν-levels can be resolved.

Since pulse properties are interdependent, reducing the temporal duration of the pulse requires

a larger bandwidth. This subsequently increases ΔE_λ and broadens the KER peaks, eventually washing out any vibrational structure. Averaging over the laser intensity within the interaction region has a similar effect on the vibrational structure in the KER spectrum due to shifting of the KER peaks to lower energy with increasing intensity [92, 238]. This KER shift coupled with the broader range of intensities averaged over as the intensity increases leads to reduced energy resolution. It is therefore expected that vibrational structure would vanish with increasing bandwidth (shorter pulses) and increasing laser intensity (i.e., field strength).

The experimental results for dissociation of H_2^+, in 25 fs (FWHM of intensity) FTL laser pulses with a bandwidth of $\Delta\lambda_{FWHM} = 38$ nm ($\Delta E_\lambda \sim 73$ meV), are shown in Fig. 3.12. The top panels show the yield as a function of KER and $\cos\theta$, where θ is the angle between the measured momentum of the proton and the laser polarization. The lower panels show the KER spectrum integrated along the laser polarization in a cone with an angle of 32° ($|\cos\theta| > 0.85$).

Although the spectral bandwidth of 73 meV is still below the vibrational energy spacing, it acts to obscure vibrational resolution and effectively washes out any vibrational structure. This is especially evident below 0.8 eV ($\nu \leq 8$) where multiphoton effects play an important role in driving dissociation. Also, the vibrational structures in the KER are limited by detector resolution. For the current experimental conditions, the instrumental error in the KER is estimated to be $\Delta \mathrm{E_{KER}(eV)} \simeq 0.06\sqrt{\mathrm{KER(eV)}}$, which is about 60 meV at a KER of 1 eV (see details in Ref. [92]). Remarkably, the vibrational structure in the low-KER range ($\leq$0.8 eV) reappears for a pulse chirped positively to about 60 fs, as shown in Fig. 3.12 (c) and (d). Although not shown here, this phenomenon occurs irrespective of chirp sign. Given that this pulse, stretched to about 60 fs, has the same frequency components as the FTL pulse, it seems puzzling that the vibrational structure can be observed. This seems to suggest that the bandwidth driving dissociation is effectively narrower for the chirped pulses. The question is, *what is the mechanism responsible for this KER peak narrowing*? The answer turns out to be, heuristically speaking, a combination of the early dissociation of H_2^+ in the laser pulse and the narrower range of frequencies within that time range.

The spectral phase $\phi(\omega)$ can be used to define the group delay, which describes the relative

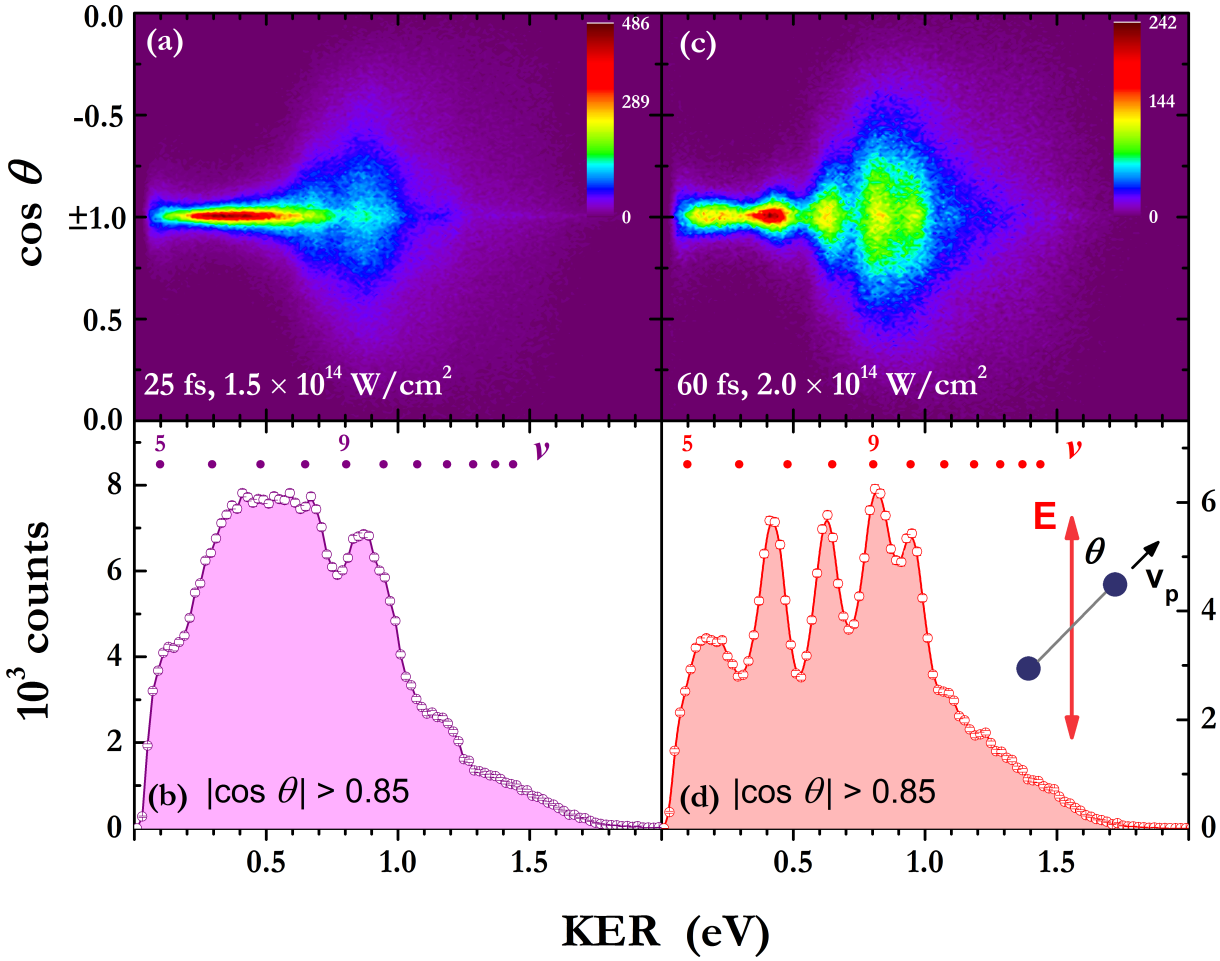

Figure 3.12: (a) and (c) KER-cos θ density plot of H_2^+ dissociation in a 790 nm, (a) 25 fs FTL and (c) positively chirped 60 fs laser pulse. (b) and (d) the KER spectra evaluated, from (a) and (c) respectively, by integrating θ over a cone with an angle of 32° along the laser polarization. The error bars are smaller than the symbols. The intensities are depicted in the figure.

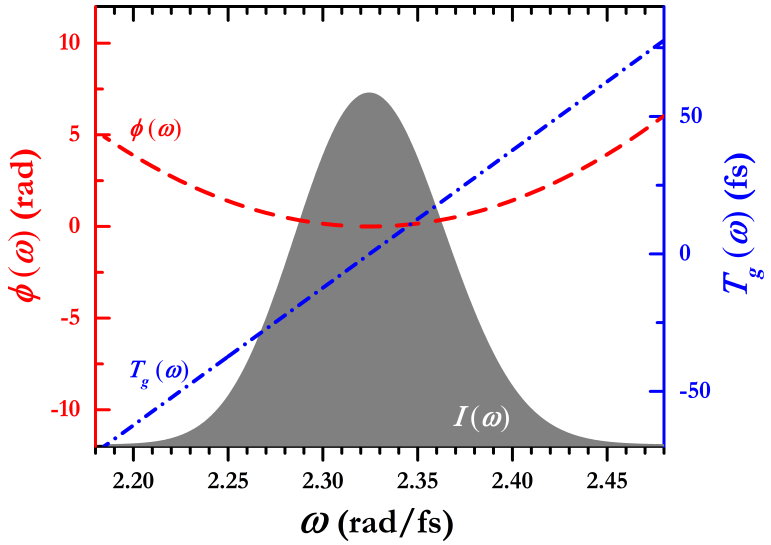

Figure 3.13: Schematic diagram illustrating (i) a Gaussian fit to the measured power spectrum $I(\omega)$, which is normalized to 1, (ii) the applied quadratic phase function $\phi(\omega)$ with $\phi'' = 500$ fs^2 (red dashed), and (iii) the resulting linear group delay $T_g(\omega)$ (blue dot-dashed), which subsequently leads to a "frequency sweep" within the pulse (see text).

temporal delay of each spectral component, as $T_g(\omega) = \frac{\delta\phi}{\delta\omega}$ [269]. For the shortest pulses, i.e. FTL pulses, the spectral phase $\phi(\omega)$ is constant and each frequency has an equal probability during the pulse duration. If an additional quadratic phase function $\frac{1}{2}\phi''(\omega-\omega_0)^2$ is added, the corresponding $T_g(\omega)$ is linear, leading to a linear increase in frequencies with time (frequency sweep), known as chirp [120]. This concept is shown schematically in Fig. 3.13 for the experimental pulse parameters. Figure 3.13 presents a Gaussian fit to the measured power spectrum $I(\omega)$ for 800 nm, 25 fs laser pulses (color-shaded peak). The spectral pulse intensity has been normalized to 1. A quadratic phase function, $\phi''(\omega-\omega_0)^2$, is applied in the spectral domain, where ϕ'' is chosen to be 500 fs^2 (red dashed) resulting in a positively chirped laser pulse duration of 60 fs.

We return to the temporal behavior of H_2^+ dissociation — a key ingredient of our explanation. Based on our previous theoretical studies, it is known that an H_2^+ target dissociates early in a sufficiently intense laser pulse, that is, well before the pulse reaches its peak intensity [73]. The time-dependent dissociation probabilities of H_2^+ in a 120 fs (FWHM) FTL pulse with 2×10^{13} W/cm^2 were calculated by numerically solving the time-dependent Schrödinger equation (TDSE) [92] (see ν=7–9 in Fig. 3.14). One should note that these calculations do not include rotation, and as a

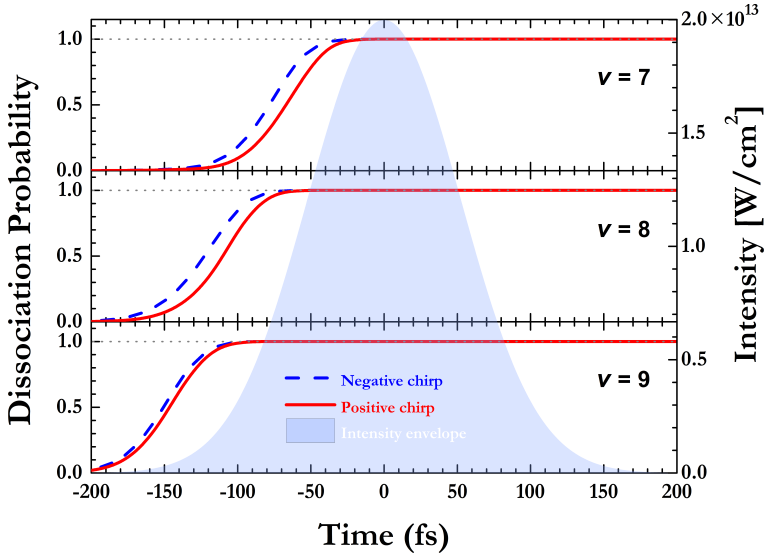

Figure 3.14: Calculated time-dependent dissociation probability for a few vibrational levels of H_2^+, using a 30 fs FTL laser pulse positively and negatively chirped to 120 fs . Negative (dashed-blue) and positive (solid-red) chirps are plotted for the peak intensity $\sim 2\times10^{13}$ W/cm^2 with the intensity envelope depicted by the blue-shaded peak.

result the dissociation probability saturates at lower intensities than would be the case if rotation were included. Therefore, our calculations were conducted at a lower intensity than the one used in the experiment. This also compensates partly for the intensity variation over the interaction volume. These relatively simple calculations demonstrate that the ν=7–9 states are depleted before the peak of the pulse [see Fig. 3.14] — an important point in the interpretation of our observation.

Specifically, the early dissociation saturation of the ν=7–9 states implies that a limited range of frequencies, situated on the leading edge of the linearly chirped pulse, are responsible for dissociation, while the contribution of frequencies at the pulse trailing edge is suppressed. This combination of temporal redistribution of frequencies in a chirped pulse and early dissociation in the pulse lead to the peak narrowing observed in the KER spectrum, shown in Fig. 3.12(d). Furthermore, this simplistic model conforms to the observation reported by Prabhudesai *et al.* [73], which demonstrates a shift in the KER spectra in the direction of the chirp due to the frequency sweep in the pulse. A quantitative comparison of the exact time range and the corresponding frequencies involved in the process depends on the parameters of the specific laser pulse and requires an increasingly sophisticated calculation, which includes intensity averaging and is beyond the scope of

this work. However, it is important to note that the exact time window where saturation occurs is not critical for our qualitative model explaining the "effective bandwidth narrowing" caused by the H_2^+ dissociation early in a chirped pulse.

The foundation of our empirical model, describing how vibrational structure ordinarily obscured for an FTL pulse can be retrieved by introducing a frequency sweep, comes from first-order perturbation theory. This is the case for the interpretation of many other phenomena controlled by chirped pulses [95, 270, 271], which have been effectively used as a tool to control numerous processes, including selective population transfer in two-level and three-level atomic systems as well as tracking the evolution of vibrational wavepackets [264, 272–275].

To summarize this section, the combination of the early dissociation of H_2^+ in the intense laser pulse and the reduced frequency range within the leading edge of a chirped pulse results in the narrowing of the measured KER peaks, giving the appearance of improved energy resolution. In the following section, we extend the notion that the interplay between the molecular response to the field and the frequency distribution in the pulse can be used to manipulate the KER spectra by providing an example of control in the low-KER dissociation of HD^+.

3.4.4 Chirp Effect in Zero Photon Dissociation of HD^+

The H_2^+ molecular ion, due to its simplicity, has been a benchmark system for developing our understanding of the interaction of strong laser fields with molecules [199, 200, 209, 267]. In spite of this intensive research effort surprising phenomena still emerge even for this simplest molecule, in big part due to the rapid advances in laser technology providing shorter, more intense and better controlled laser pulses.

One such intriguing phenomenon, the dissociation of H_2^+ by a strong rapidly changing laser field with the net absorption of zero number of photons, was suggested a couple of decades ago by the calculations of Giusti-Suzor and Mies [266] and the experimental work of Posthumus, Frasinski and co-workers [208, 267]. However, clear experimental and theoretical evidence for this zero-photon dissociation (ZPD) process has only recently been reported [198, 276]. The mechanism responsible for ZPD, illustrated schematically in Fig. 3.15(a), involves two photons, specifically the absorption

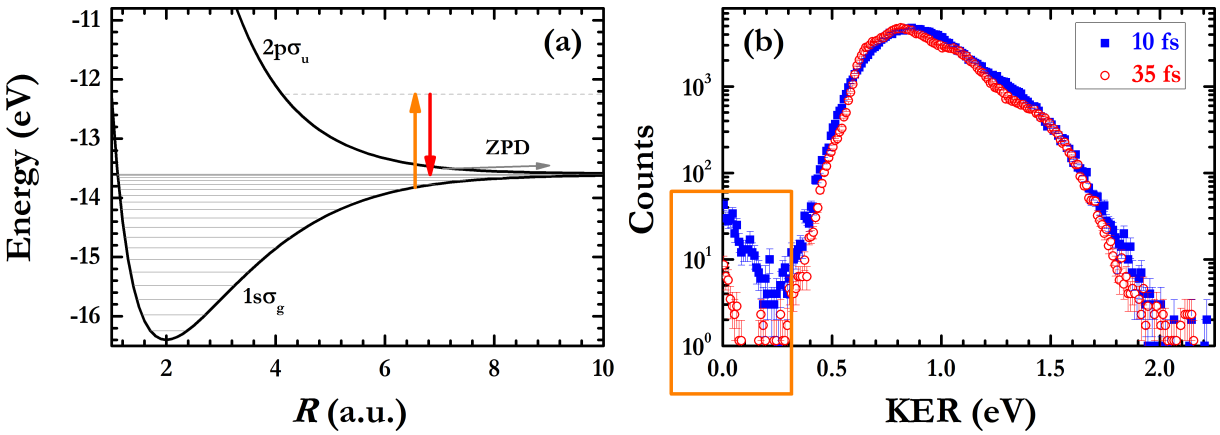

Figure 3.15: Born-Oppenheimer PECs of the H_2^+ ground and first excited electronic states illustrating the stimulated Raman scattering process responsible for ZPD. The absorption of the photon is indicated by a vertical upward arrow, while the emission of a photon is shown as a downward arrow. (b) Measured KER distribution for H_2^+ dissociating into H^++H using 10 and 35 fs laser pulses with a peak intensity of 10^{13} W/cm^2. Both sets of plots are normalized at their peak. Adapted from Gaire *et al.* [198].

of a more energetic photon followed by the stimulated emission of a less energetic photon, both within the bandwidth of the laser pulse. This is known as stimulated Raman scattering as shown in Fig. 3.15(a). The energy difference between the two photons overcomes the binding of the molecular ion and the excess energy leads to a small KER upon dissociation. This model suggests that only vibrational states bound by less than the bandwidth energy can undergo ZPD. Moreover, it leads to the expectation that a large bandwidth, presently available by pulse compression to a few femtoseconds, will enhance the ZPD yield as has been recently demonstrated [198, 276].

The calculation performed by Anis and Esry [253], using the 3D time-dependent Schrödinger equation for H_2^+ in the Born-Oppenheimer representation, shows similar results between the experiment and theory [198, 276]. For instance, these calculations confirm that the ZPD is significantly enhanced for laser pulses with larger spectral bandwidth. It is worth mentioning that the benefit of theory becomes clear in assigning the origin of different structures in the KER spectrum. The effect of the pulse duration is qualitatively explored in our measurement. Figure 3.15(b) presents our measured KER distribution for H_2^+ dissociating into H^++H using 10 and 35 fs laser pulses with a peak intensity of 10^{13} W/cm^2. The results suggest that the broad spectral bandwidth is

necessary to produce the ZPD effect.

This two-photon picture, which is supported by complete quantum mechanical calculations [253], leads to the intuitive notion that the ZPD yield could be controlled by chirping the laser pulse [198]. More precisely, a negative chirp of an ultrashort (i.e., large bandwidth) laser pulse will increase the chances for absorbing a more energetic photon first and stimulating emission of a lower energy photon second, in comparison to a transform limited pulse, therefore enhancing the ZPD probability. Likewise, a positive chirp should accomplish the opposite and, therefore, allow us to suppress ZPD.

In this section, we demonstrate exactly this kind of control over ZPD in HD^+. We have measured ZPD of an HD^+ beam target in intense laser pulses chirped from a 7 fs FTL pulse. We have also solved numerically the time-dependent Schrödinger equation for H_2^+ in the Born-Oppenheimer representation. The calculation includes nuclear rotation while excluding ionization. It turns out that ionization is negligible at the intensity used in this study [252].

Figure 3.16(a) shows the results of the theoretical calculation for H_2^+ dissociation [277]. The dissociation probability density is shown as a function of KER for various laser parameters. The solid line displays the dissociation probability density for 8 fs FTL pulses with a peak intensity of 10^{13} W/cm^2. The dashed and dash-dotted lines display the dissociation probability density for positively and negatively chirped laser pulses from the 8 fs FTL laser pulses, respectively. The inset shows the zoomed in version for the low KER region (0–0.25 eV) in order to show the difference between different pulse parameters. From Fig 3.16(a), it is clear that the ZPD contribution near 0 eV reduces for the positively chirped pulse (dashed line), while the dissociation probability for negatively chirped laser pulses (dash-dotted line) shows enhancement in comparison to the FTL (solid line) results.

The measured KER for dissociation of HD^+ using 7 fs laser pulses with the peak intensity of 2×10^{13} W/cm^2 is shown in Fig. 3.16(b). The positively chirped laser pulses are generated by adding extra glass to the optical path, while the negatively chirped laser pulses are produced by reducing the amount of glass required to generate an FTL pulse at the interaction point. The

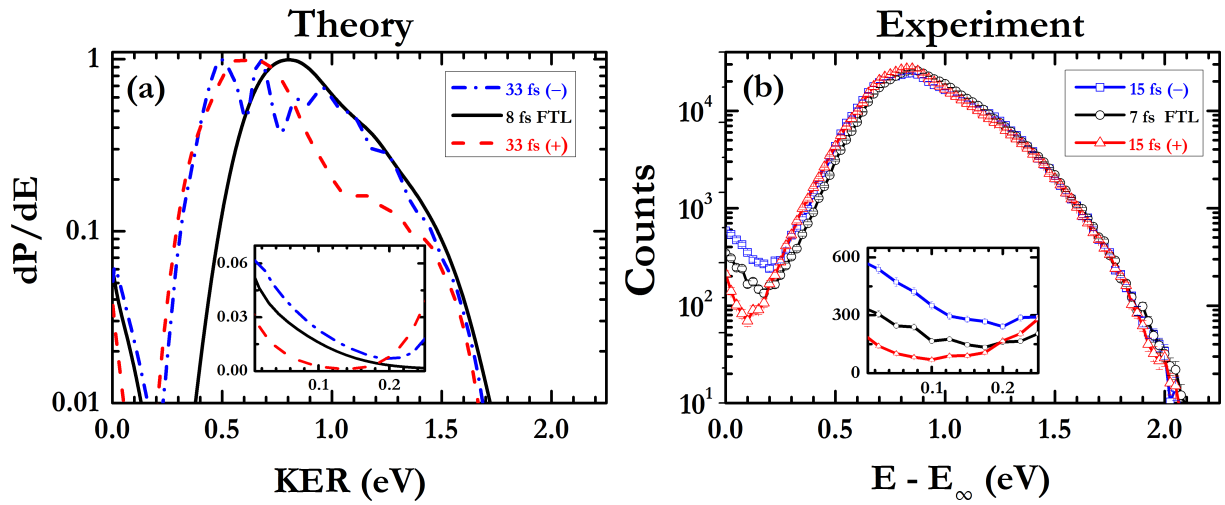

Figure 3.16: (a) Dissociation probability density of H_2^+ as a function of KER calculated for FTL 8 fs and 33 fs positively and negatively chirped from FTL 8 fs laser pulses at 10^{13} W/cm^2. (b) Measured KER distribution for HD^+ dissociating into H^++D and H+D^+ using 7 fs FTL, 15 fs positively and negatively chirped laser pulses. The FTL is at an intensity of 2×10^{13} W/cm^2 and the chirped laser pulses have a peak intensity of 1×10^{13} W/cm^2.

dissociation of HD^+ leads to two distinguishable final products, namely H^++D and H+D^+. The energy gap between these two channels at the separated atom limit is only 3.7 meV [278–280]. The dissociation yields from both channels are added together and plotted as a function of energy with respect to the lowest dissociation limit (H^++D) to mimic the expected behavior of H_2+. Results of our measurement show considerable differences between FTL and chirped laser pulses. The main peak around 0.8 eV is due to bond softening. There are some differences in this KER region which will be discussed in detail in the next section.

As shown in Fig. 3.16(b), for negatively chirped pulses the relative ZPD yield is higher than the ZPD yield for FTL and positively chirped laser pulses. Moreover, the positively chirped laser pulses show a suppression in the ZPD yield. Our findings follow the simple interpretation introduced earlier. For a negatively chirped laser pulse, the blue end of the spectrum is leading in the pulse. Following the stimulated Raman picture, we expect to absorb a higher frequency photon (more energetic) early in the pulse and emit a lower frequency photon (lower in energy) later within the negatively chirped pulse. As a result a ZPD yield would be more favorable for such a laser pulse. By reversing the order of photon energy within the pulse (going to a positively

chirped laser pulse), we would expect a suppression in the ZPD yield as shown in Fig. 3.16(b). Both experiment and theory are in good quantitative agreement, showing ZPD enhancement for negatively chirped laser pulses and suppression for positively chirped pulses.

To summarize this section, we have shown that by rearranging the frequency components within a pulse (chirp), we can control the ZPD yield. Moreover, a negatively chirped pulse is used to enhance the ZPD yield associated with the dissociation of high vibrational states ($v \geq 10$). This idea is further examined by solving the TDSE for different chirp parameters of the laser pulse.

3.5 Branching Ratios of HD^+ Dissociated by Intense Ultrafast "Single-Color" Laser Fields

Synopsis. We have studied laser-induced dissociation of molecular-ion beams using a coincidence 3D momentum imaging technique. Here, we focus mainly on the simplest heteronuclear molecule, HD^+, (using 25-65 fs laser pulses) as a model for more complex systems. We use deuterium tagging to distinguish the different final products and thus study how to control one outcome over another. The preference for HD^+ to dissociate into either H^++D or H+D^+ is a good example of this kind of control — usually referred to as controlling the branching ratios (BR). One would expect the H^++D dissociation channel, associated with the HD^+ electronic ground state, to be similar to the H+D^+ dissociation when produced by the bond-softening mechanism [94]. This is mainly due to the high kinetic energy released through bond-softening in comparison to the energy gap between the two dissociation limits [280]. Our measured branching ratio contradicts this prediction, exhibiting differences between these two channels in the KER region (0.5-1.2 eV). Furthermore, theoretical calculations show asymmetry in the branching ratio for several laser parameters in various KER regions. In addition, our measured branching ratios using broad bandwidth laser pulses show the expected dominance of dissociation into the electronic ground state, H^++D, over dissociation into H+D^+ for very slow fragmentation (0-0.2 eV), similar to what is observed in ground state dissociation (GSD) initiated by the half-cycle pulse of a swift proton (ion) [281–283].

3.5.1 Introduction

One of the goals of laser-matter studies is to coherently control molecular fragmentation [38, 53, 54]. Achieving control over chemical reactions requires a comprehensive knowledge about the system of interest. The technological achievements in the past decade allow us to study molecular fragmentation on well-defined potential-energy surfaces using ultrashort laser pulses. For instance, controlling *spatial asymmetry* is explored in dissociative ionization of neutral molecules by altering the CEP of a few cycle laser field [80, 82–84, 284–286]. In addition, the relative phase of a two-color laser field is used to control spatial asymmetry as well as molecular alignment and

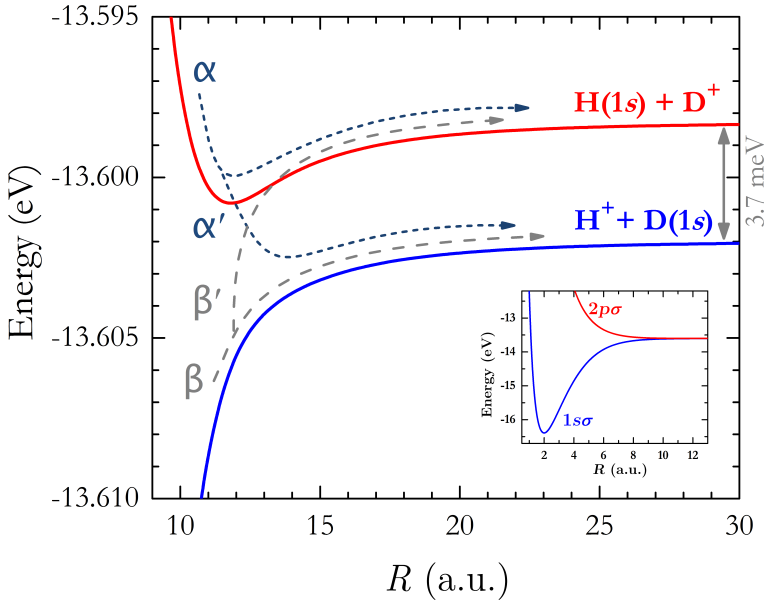

Figure 3.17: Potential energy curves of HD^+ showing the splitting of the $1s\sigma$ and $2p\sigma$ states at large internuclear distance, R. The inset shows the Born-Oppenheimer potential energy curves. For the description of the pathways α, β, α' and β', see text.

orientation [45, 48, 75, 79, 81, 88, 260, 287–291].

One of the most important aspects of control is the manipulation of the yield of the final product in a chemical reaction. This idea of controlling the *branching ratio* of the final products has been studied extensively [23, 40, 56, 292–296]. The molecular hydrogen ion isotopologue, HD^+, is the simplest heteronuclear diatomic molecule and exhibits two distinguishable dissociation limits, separated by 3.7 meV, namely H^++D(1s) and D^++H(1s) [278–281]. The two lowest adiabatic potential energy curves (PEC) of HD^+ (the $1s\sigma$ ground state and the $2p\sigma$ first-excited state) are plotted in Fig. 3.17. The mass difference between the proton and the deuteron results in an energy gap due to a so-called Born-Oppenheimer approximation breakdown.

Figure 3.17 shows the $1s\sigma$ and $2p\sigma$ PECs at large internuclear distance, while the sketched arrows indicate transitions between these states due to strong non-adiabatic coupling around 12 a.u. [280]. The non-Born-Oppenheimer, charge-exchange coupling will further mix the channels independent of the laser field via pathways α' and β' as shown in Fig. 3.17. For instance, the dissociation process originating on the $2p\sigma$ state through absorption of n photons, labeled as

pathway α, can go through a radiationless transition to the lower state, $1s\sigma$, shown schematically by pathway α', and interfere with dissociation initiated on the $1s\sigma$ state, pathway β, and vice versa. Based on the accumulated phase along the dissociation pathways, interference can be constructive or destructive. As a result by varying laser parameters, such as chirp, we can control the interference on an individual dissociative channel and therefore control the branching ratio of the final dissociation products. Normally, dissociation energies of more than ∼50 meV produce an equal mixture of the two states [282, 297] due to the small energy gap of 3.7 meV, making the asymmetry observed at such high KER even more surprising.

The behavior of the benchmark molecule, HD^+, in a strong laser field remains challenging for theorists as very few *ab initio* calculations have been performed. The full quantum-mechanical treatment involves permanent dipole coupling in conjunction with non-adiabatic coupling terms [76, 280, 281, 298–303]. In the following sections, we present experimental and theoretical evidence of such a control mechanism on the branching ratio of HD^+ dissociation by FTL and chirped laser pulses.

3.5.2 Experimental Method and Data Analysis

The longitudinal and transverse field imaging (LATFI) method is employed (see Section 3.2.3) to study dissociation of an HD^+ ion beam target experimentally using chirped laser pulses. In this method, the charged and neutral fragments are separated in time and position [see Fig. 3.3(c) and (d)]. Laser pulses of 25 fs with a 795 nm central wavelength are provided at a 2 kHz repetition rate by the KLS laser system. The laser pulses are further chirped positively or negatively by adjusting the distance between the KLS compressor gratings. The laser pulses are focused to a peak intensity of 2.5×10^{14} W/cm^2 by an off-axis parabolic mirror with a focal length of 203 mm. Recall, the dissociation and ionization channels (H^++D, H+D^+ and H^++D^+) are measured in coincidence and distinguished from each other (see Sec. 3.2.3 and Fig. 3.2).

The reconstructed 3D momenta for the dissociation channels are shown in Fig. 3.18. The top row shows the 3D momentum for dissociation of HD^+ into H^++D. The laser direction is along $\hat{k}$, which is along the ion beam direction, while $\hat{i}$ and $\hat{j}$ are in the plane of the detector. The bottom

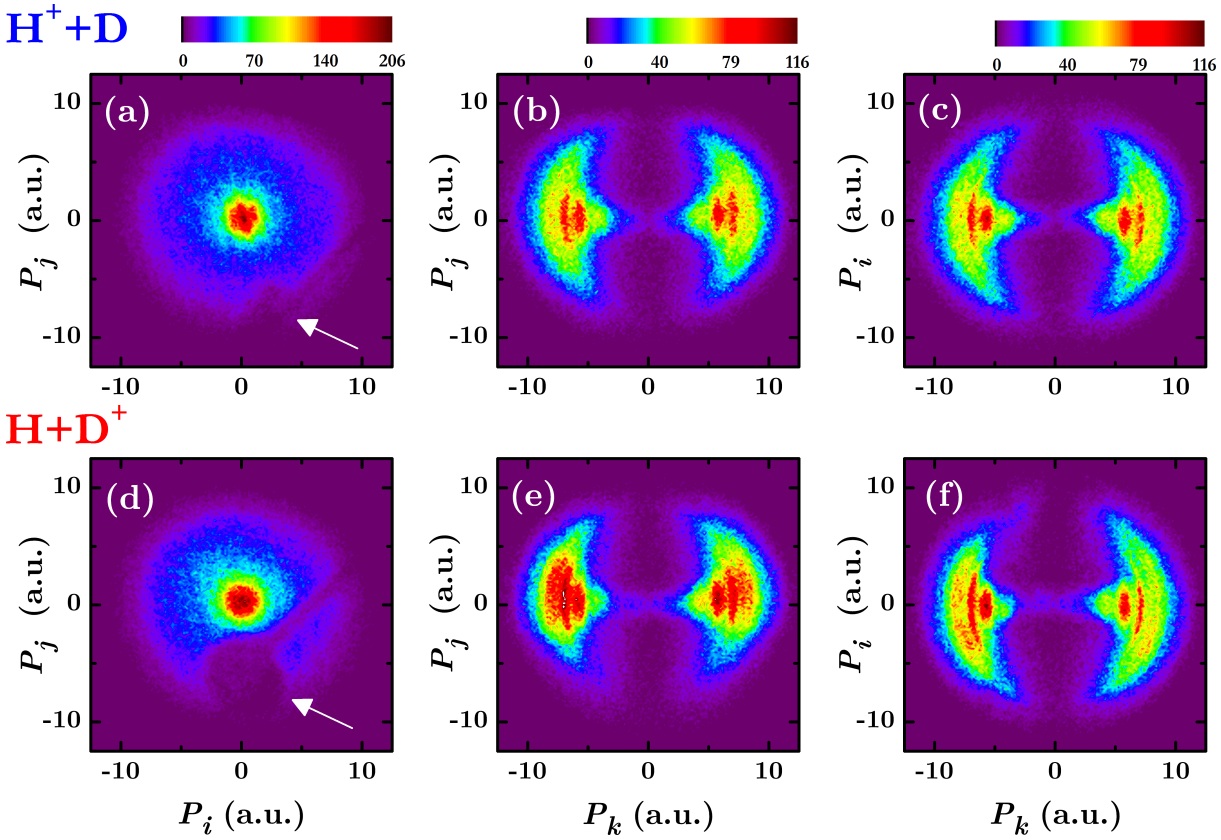

Figure 3.18: The 2D map of counts as a function of momentum components for the H^++D channel is plotted from (a) to (c) where the axes are (a) P_i and P_j, (b) P_k and P_j, and (c) P_k and P_i. The H+D^+ channel is plotted from (d) to (f) with (d) P_i and P_j, (e) P_k and P_j, and (f) P_k and P_i axes. The laser polarization is along the $\hat{k}$ direction. Arrows point to the losses in the spectra caused by the Faraday cup and the rod holding it.

row shows similar results for dissociation into H+D^+. The H^+ and D^+ fragments are deflected along the $\hat{j}$ direction by a static electric field [see Fig. 3.3(d)]. As a result, some portion of the fragments is lost, as shown by arrows in Fig. 3.18(a) and (d), due to the "shadow" that the Faraday cup casts on the position spectra.

To compare these two channels quantitatively, only events within a cone, with an angle of 18° along the polarization direction, are accepted. In this case, the momenta distributions for both channels do not suffer from any losses due to our detection method, as shown in Fig. 3.19. In addition, the theoretical calculations introduced later are performed for aligned HD^+ molecules, which makes the comparison between theory and experiment more valid.

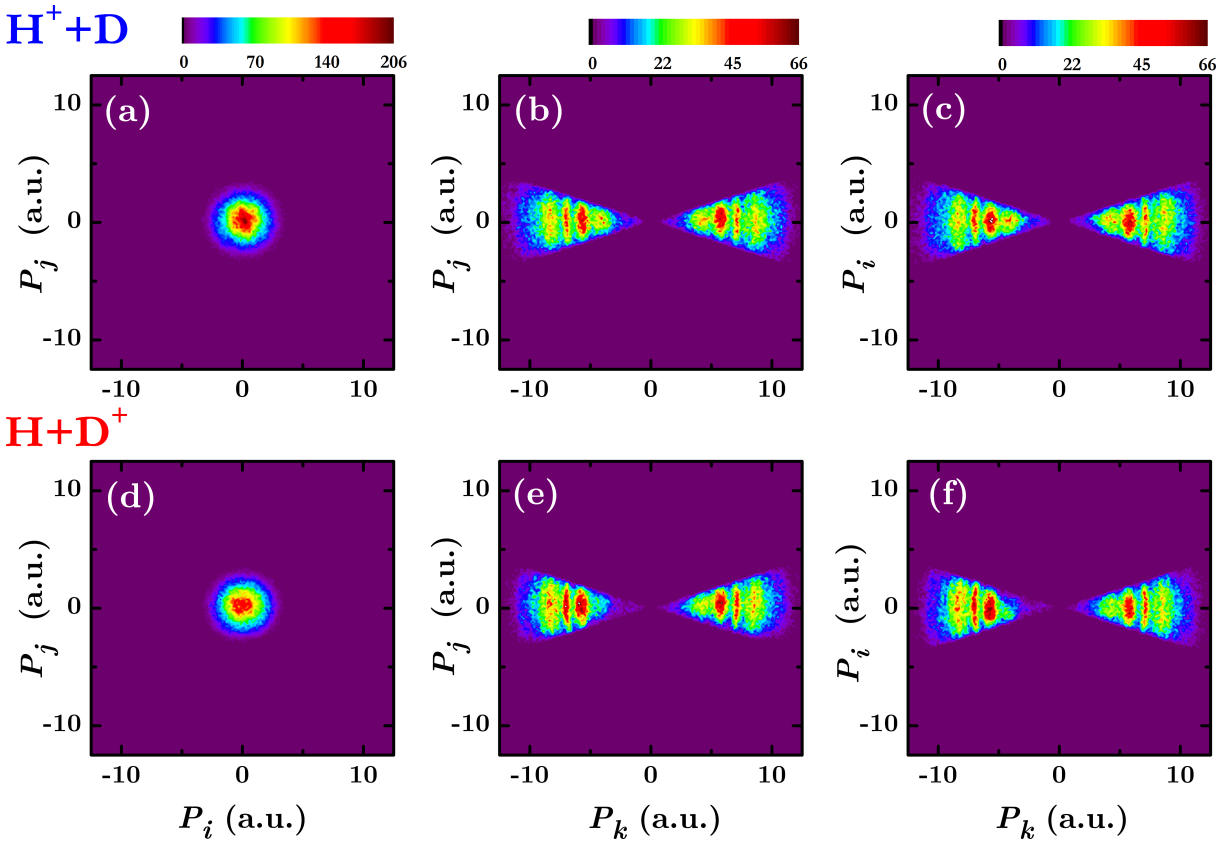

Figure 3.19: The 2D map of counts as a function of momentum components. The counts are integrated within a cone angle of 18° around the laser polarization. The H^++D channel is plotted from (a) to (c), as a function of (a) P_i and P_j, (b) P_k and P_j, and (c) P_k and P_i. The H+D^+ channel is plotted from (d) to (f), as a function of (d) P_i and P_j, (e) P_k and P_j, and (f) P_k and P_i. The laser polarization is along the $\hat{k}$ direction.

3.5.3 Results

From the measured 3D momenta, the KER are calculated for individual channels. As mentioned earlier, the energy gap between the two dissociation limits in HD^+ is only 3.7 meV [278–281].

The KER on the upper channel (H+D^+) are shifted by 3.7 meV, such that all energies are measured with respect to the lowest dissociation limit ,*i.e.* the H^++D($1s$) channel. Figure 3.20(a) shows the number of dissociation events as a function of energy for 25 fs FTL laser pulses with a peak intensity of 2.5×10^{14} W/cm^2, while Fig. 3.20(b) shows the results for laser pulses of 65 fs positively chirped from 25 fs FTL with a peak intensity of 1.0×10^{14} W/cm^2.

The measured energy spectrum for FTL laser pulses does not show any structure in this energy

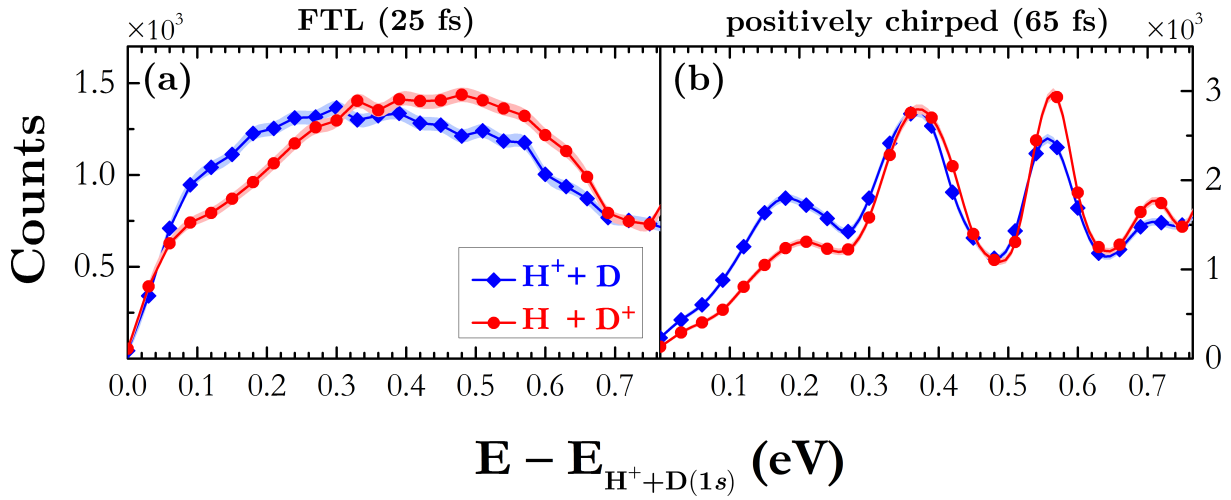

Figure 3.20: Measured number of dissociation events as a function of energy for (a) 25 fs FTL and (b) 65 fs positively chirped laser pulses with peak intensities of 2.5×10^{14} W/cm^2 and 1.0×10^{14} W/cm^2, respectively. The error bars appear as shaded areas and denote the statistical error in the data.

range. In contrast, the measured energy for 65 fs positively chirped laser pulses reveals vibrational structure similar to the H_2^+ (discussed in Section 3.4). Moreover, there are significant differences between dissociation into H^++D (blue diamonds) and H+D^+ (red circles) for both laser pulses. The differences in the dissociation probability can be associated with the permanent dipole and non-adiabatic coupling of HD^+ (see Section 3.5.4).

To quantify our results, the branching ratios defined as

$$\begin{aligned} \mathrm{BR}_{[H^+ + D]} &= \frac{N_{[H^+ + D]}}{N_{[H^+ + D]} + N_{[H + D^+]}} \\ \mathrm{BR}_{[H + D^+]} &= \frac{N_{[H + D^+]}}{N_{[H^+ + D]} + N_{[H + D^+]}}, \end{aligned} \tag{3.11}$$

are evaluated. Here, N is the number of counts within a cone angle of 18° around the laser polarization. The results for the branching ratios of the two channels are displayed in Fig. 3.21(a) and (b) for the FTL and positively chirped laser pulses, respectively. As stated earlier, one would expect the branching ratio of dissociation to either H^++D or H+D^+ to be 50% for energies significantly larger than the energy gap between the two dissociation limits ($E \gg 3.7$ meV) [278–281]. However, Figure. 3.21(a) and (b) show a significant asymmetry in the branching ratio between these two channels. Moreover, the asymmetry changes with dissociation energy. In particular, the branching

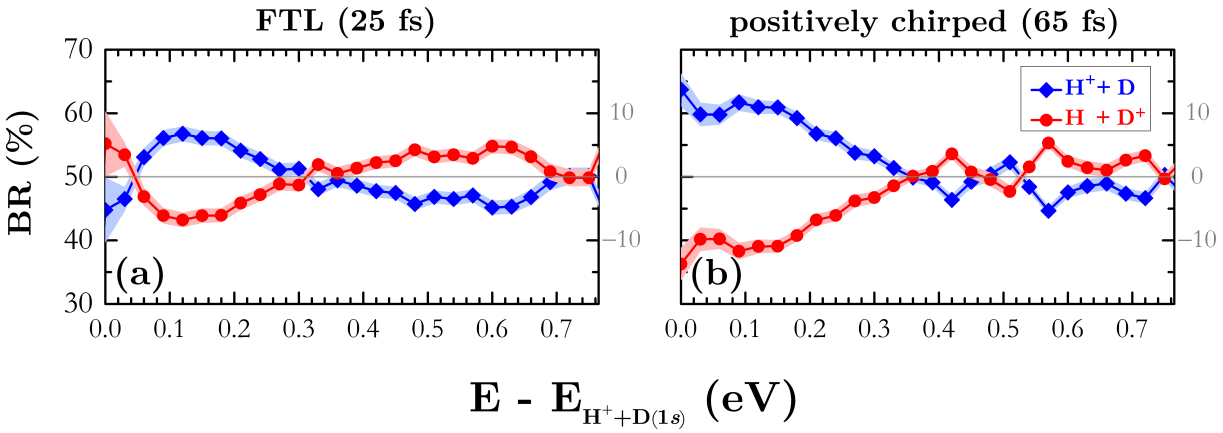

Figure 3.21: Branching ratio for dissociation of HD^+ into H^++D and H+D^+ channels for (a) 25 fs FTL and (b) 65 fs positively chirped laser pulses with peak intensities of 2.5×10^{14} W/cm^2 and 1.0×10^{14} W/cm^2, respectively. For better comparison, a 50% offset is subtracted from the branching ratios to ensure oscillation around zero as displayed by a second axis in grey. The error bars appear as shaded areas and denote the statistical error in the data.

ratio for the H^++D channel at the low energy region ($\leq$0.4e V) increases for positively chirped laser pulses in comparison to FTL pulses. For instance, at 0.1 eV the offset-subtracted branching ratio of dissociation to the H^++D increases from 6% for FTL pulses to 12% for positively chirped laser pulses, a factor of 2 enhancement. This is also evident in Fig 3.20(a) and (b), which shows the number of dissociation events in each channel as a function of energy.

Transitions between the $1s\sigma$ and $2p\sigma$ states can be categorized into radiative and nonradiative (radiationless) transitions. The transition dipole moment between the $1s\sigma$ and $2p\sigma$ increases from the equilibrium internuclear distance ($\sim$2 a.u.) and peaks around 11 a.u. [see Fig. 3.22(a)]. This radiative coupling rapidly falls to zero after passing the internuclear distance of 12 a.u. and becomes insignificant above R =15 a.u. [280]. Radiative transitions between the $1s\sigma$ and $2p\sigma$ states occur when the transition dipole moment matrix elements are significant. In comparison, the permanent dipole moments are diminished at small internuclear distance ($R \leq$8 a.u.), as shown in Fig. 3.22(a). However, the permanent dipole moments diverge above $R \sim$9.5 a.u. The permanent dipole moment becomes important at large internuclear distances resulting in radiative transitions while the transition dipole moments are insignificant at large internuclear distance.

The non-adiabatic coupling is important when the energy gap between two potential energy

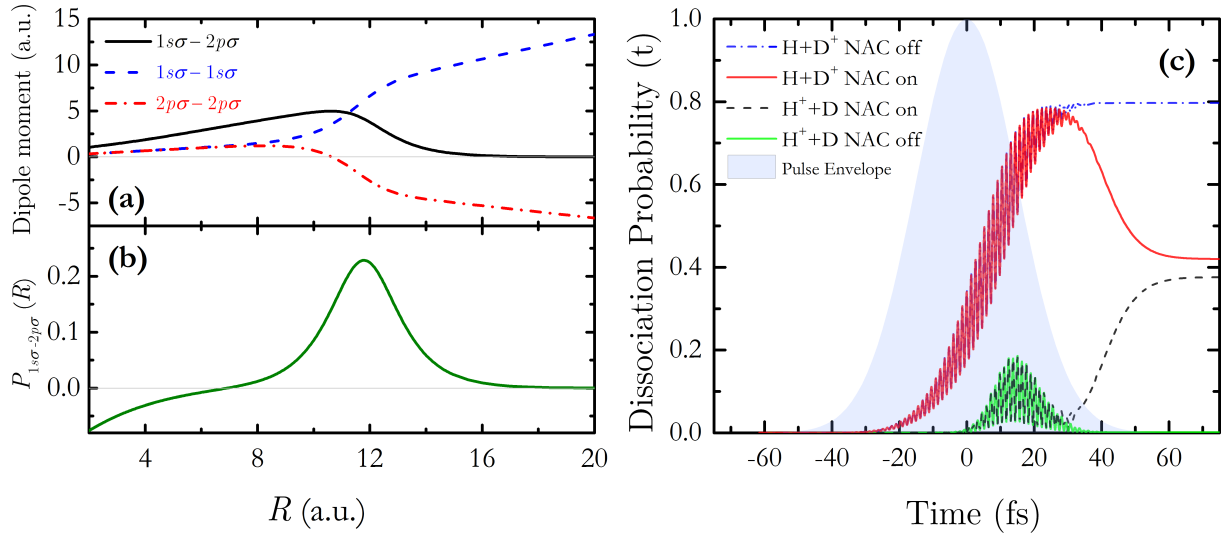

Figure 3.22: (a) Transition dipole moment ($1s\sigma$-$2p\sigma$, solid curve) and permanent dipole moment ($1s\sigma$–$1s\sigma$ dashed curve, $2p\sigma$-$2p\sigma$ dashed dotted curve) of HD^+, including the nuclear contribution, (b) the non-adiabatic coupling between $1s\sigma$ and $2p\sigma$ states, $P_{1s\sigma-2p\sigma}(R)$, calculated by Esry and Sadeghpour [280]. (c) Dissociation probability on $1s\sigma$ and $2p\sigma$ as a function of time from an initial state ν=8 is calculated by turning the non-adiabatic coupling (NAC) terms on and off. The dissociation probabilities illustrate the effect of non-adiabatic coupling terms resulting in mixing between the $1s\sigma$ and $2p\sigma$ states (see text). Adapted from [305].

curves become small. In this case, the Born-Oppenheimer approximation breaks down and the rate for non-adiabatic transitions depends on the energy gap. In the HD^+, the non-adiabatic coupling is effective in a narrow region of R($\sim$10–15 a.u.) resulting in nonradiative transitions, which cause mixing between the $1s\sigma$ and $2p\sigma$ states. The non-adiabatic coupling between the two lowest potential curves of HD^+, $1s\sigma$ and $2p\sigma$, is depicted in Fig. 3.22(b). The branching ratio observed between dissociating into either H^++D or H+D^+ originates from the contribution of various transition probabilities. The relative transition probabilities can be controlled by various laser parameters to some extent. For instance, recently branching ratios in the dissociation of HCl^+ and HD^+ were studied theoretically as a function of pulse duration, laser intensity and wavelength [303, 304]. For deeper understanding of our experimental findings, the theoretical treatment of this system was carried out by Rigsbee and Esry [305] as discussed below.

3.5.4 Theory

The calculations carried out by Rigsbee and Esry [305] are based on solutions to the time-dependent Schrödinger equation (TDSE)

$$\imath\frac{\partial}{\partial t}\vec{F}(R,t) = [\mathbf{H_0}(R) + \mathbf{V}(R,t)]\,\vec{F}(R,t), \tag{3.12}$$

where $\mathbf{H}_0(R)$ denotes the field-free Hamiltonian, $\mathbf{V}(R,t)$ describes the laser-molecule interaction, $\vec{F}(R,t)$ is the radial wavefunction, and R is the internuclear distance. The calculations of the field-free Hamiltonian and dipole matrix elements have been outlined in detail in Ref. [280]. Here, we provide a short description of the essential details that pertain to the present work. To capture more physics found in HD^+, the model extends beyond the standard Born-Oppenheimer (BO) approximation by explicitly including the symmetry breaking terms in the adiabatic Hamiltonian. The resulting mixture of *gerade* and *ungerade* symmetries gives adiabatic potentials that have the correct asymptotic thresholds and exhibit avoided crossings which give rise to non-adiabatic transitions. The field-free Hamiltonian takes the form

$$\mathbf{H_0}(R) = -\frac{1}{2\mu}\left(\mathbf{I}\frac{\partial^2}{\partial R^2} + \mathbf{2P}(R)\frac{\partial}{\partial R} + \mathbf{Q}(R)\right) + U(R), \tag{3.13}$$

where μ is the nuclear reduced mass, $\mathbf{I}$ is the unit matrix, $\mathbf{U}(R)$ are the adiabatic potential energy curves, and $\mathbf{P}(R)$ and $\mathbf{Q}(R)$ are the first- and second-order radial coupling terms. The diagonal matrix elements of $\mathbf{Q}$ give corrections to our potential that yield the upper-bound for the vibrational energies of the the lowest electronic channel. The off-diagonal elements of $\mathbf{P}$ describe the coupling between the electronic states. The adiabatic potentials are plotted in Fig. 3.17. The non-adiabatic coupling is the strongest roughly around 12 a.u. (atomic units are used throughout unless specified otherwise), as shown in Fig. 3.22(b). Here we note that these couplings are field-free and can alter the dissociation probability in a given channel significantly.

From Eq. 3.13 it is clear that nuclear rotation is neglected in the calculation. The essential physics that we explore in this section does not depend significantly on nuclear rotation. Furthermore, the laser parameters allow us to only consider the lowest two dissociation channels, $1s\sigma$ and

$2p\sigma$, and neglect ionization. The laser-molecule interaction is

$$\mathbf{V}(R,t) = \mathbf{D}(R)E(t), \tag{3.14}$$

where $\mathbf{D}(R)$ is the dipole matrix which includes both permanent and transition dipole terms, and $\mathbf{E}(t)$ is the electric field given by

$$E(t) = E_0\, e^{-\left(\frac{t^2}{\tau^2}\right)} \cos(\omega\, t). \tag{3.15}$$

Here ω is the central laser frequency and $\tau = \sqrt{2\ln 2}\,\tau_{FWHM}$, with τ_{FWHM} the FWHM pulse duration. The initial wavefunction is chosen to correspond to a single vibrational state of HD^+. This state is propagated until a time that the electric field is negligible and the probability transfer due to the coupling of the $1s\sigma$ and $2p\sigma$ states has ceased. At the end of propagation, the solution of the TDSE is projected onto energy-normalized scattering states to obtain the energy spectrum of the dissociating fragments. These states are obtained by matching numerical solutions of the time-independent Schrödinger equation (TISE) for the continuum nuclear wavefunctions to asymptotic solutions which take the form of energy-normalized plane waves outgoing on a single dissociation channel.

Figure 3.22(c) demonstrates the non-adiabatic coupling (NAC) effect for the dissociation from an initial vibrational state, ν=8, where the dissociation probability changes by roughly 50% after the electric field has become negligible. Non-adiabatic coupling causes the dissociation probability of both channels to change significantly after the laser pulse. This coupling in addition to the small asymptotic energy separation of the HD^+ potentials poses considerable challenges when one wishes to discern the pathway the molecule took to dissociate. In particular, signs indicating pathways involving permanent dipole transitions overlap with pathways involving electronic and non-adiabatic transitions.

The Franck-Condon averaged dissociation probabilities, calculated as a function of energy for FTL 25 fs and positively chirped 65 fs laser pulses, are shown in Fig. 3.23(a) and (b), respectively. There are clear differences in the energy spectrum between FTL and positively chirped pulses, as

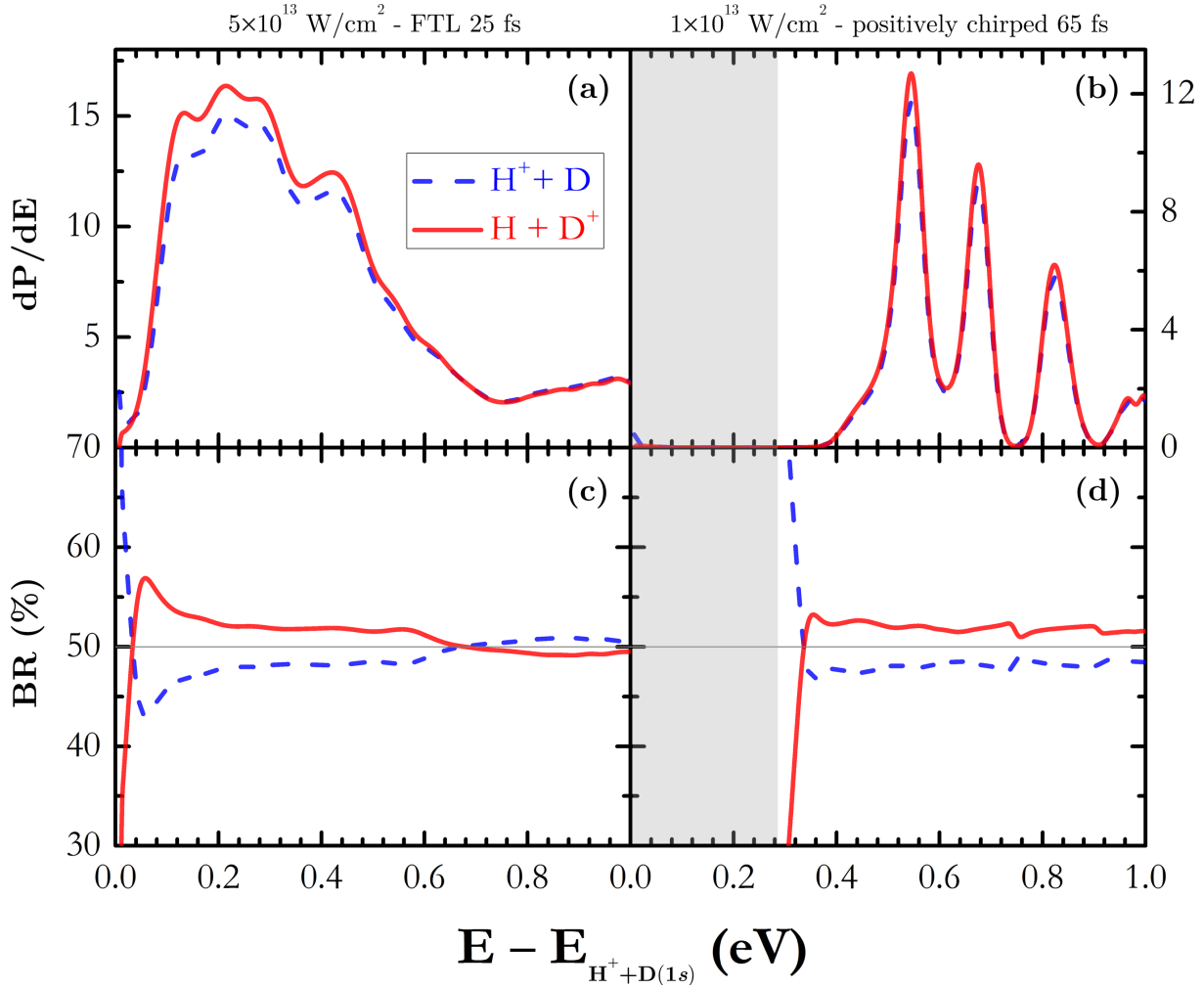

Figure 3.23: The Franck-Condon averaged dissociation probability as a function of energy is calculated for (a) a FTL 25 fs and (b) a 65 fs positively chirped pulse with a peak intensity of 5×10^{13} W/cm^2 and 1×10^{13} W/cm^2, respectively. The branching ratios of HD^+ dissociation as a function of energy are calculated for (c) a FTL 25 fs and (d) a 65 fs positively chirped pulse.

discussed in Section 3.4. Moreover, the branching ratio shows a preference to dissociate into the $H+D^+$ channel for a wide range of energies (0.1–0.65 eV for FTL and 0.35–1.0 eV for positively chirped laser pulses). The calculated branching ratio is a few percent off from 50%, and it is sensitive to the pulse duration and intensity variation of the laser pulses. One would expect that the intensity-averaging "washes out" these features due to the intensity dependence of the branching ratio. However, the experimental results reveal a prominent asymmetry in the branching ratios for various laser parameters.

The calculations are in qualitative agreement with the measured branching ratios in the sense that the theoretical calculations reveal differences in dissociation probability to either of these channels. Nevertheless, the dissociation probabilities are highly sensitive to the laser parameters. An investigation of the effect of chirp as well as the effect of longer pulses may shed more light on whether or not control over the product branching ratios is feasible with chirped pulses. It is worth mentioning that recently a few theoretical works have been reported on the branching ratios of HD^+ and HCl^+ [303, 304]. These studies suggest that the strength of different interactions (transition dipole, permanent dipole, and non-adiabatic coupling) can be responsible for control of the final product.

3.5.5 Pathways

To provide an explanation for our findings, we use the Floquet light-dressed potential curves [199, 306, 307] of HD^+ at 790 nm, as displayed in Fig. 3.24. The permanent dipole moment in HD^+ causes extra dissociation pathways. For instance, HD^+ can dissociate through the crossing marked by 2ω in Fig. 3.24. The molecule can break apart either directly along the two-photon pathway, $|1s\sigma - 0\omega\rangle \rightarrow |2p\sigma - 2\omega\rangle$, or along the adiabatic net one-photon pathway, $|1s\sigma - 0\omega\rangle \rightarrow |2p\sigma - 2\omega\rangle \rightarrow |1s\sigma - 1\omega\rangle$. The importance of the permanent dipole moment becomes clear when dissociation initiated from the permanent dipole moment (2ω crossing) can interfere with the bond-softening path from $|1s\sigma - 0\omega\rangle \rightarrow |2p\sigma - 1\omega\rangle$, through the 1ω crossing.

Dissociation through the permanent dipole pathway, $|1s\sigma - 0\omega\rangle \rightarrow |2p\sigma - 2\omega\rangle \rightarrow |1s\sigma - 1\omega\rangle$, results in a KER of ~0.2 eV. This pathway overlaps in energy with the one-photon dissociation of ν=6. Furthermore, the dissociation through $1s\sigma$ and $2p\sigma$ gets mixed due to non-adiabatic coupling around R ~12 a.u. As a result, understanding the branching ratio between these two dissociation limits can be complex due to competition between different couplings (transition dipole, permanent dipole and non-adiabatic coupling).

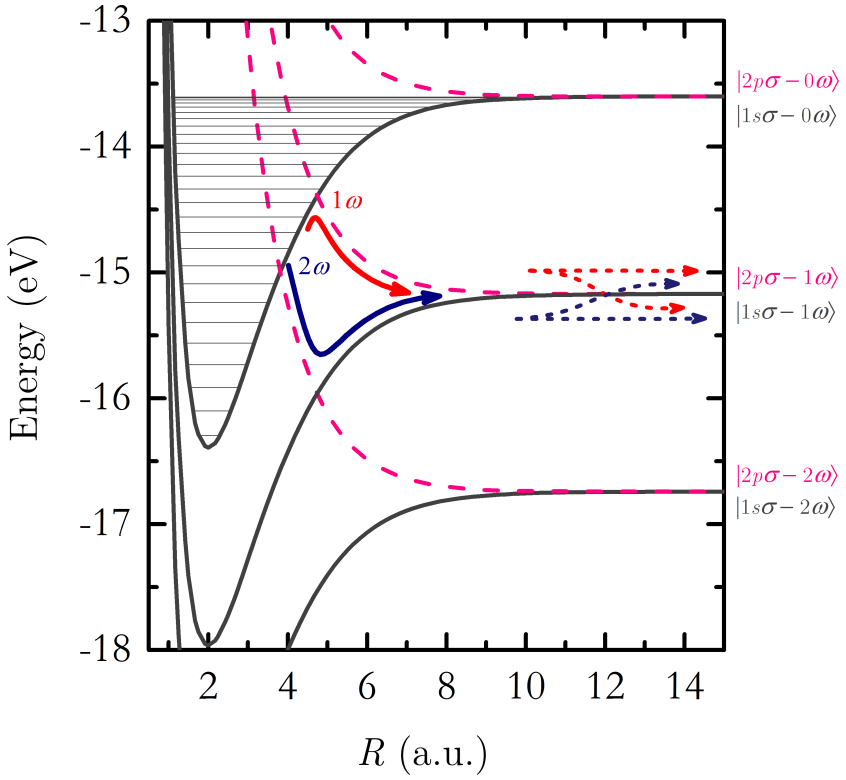

Figure 3.24: Dressed Born-Oppenheimer potential energy curves as a function of internuclear distance R for HD^+. The solid arrows show the adiabatic dissociation pathways and the labels denote the electronic states dressed by n photons. The short-dashed arrows depict transition due to non-adiabatic coupling around R ~12 a.u. The permanent dipole moment in HD^+ results in dissociation pathways such as $|1s\sigma - 0\omega\rangle \rightarrow |2p\sigma - 2\omega\rangle \rightarrow |1s\sigma - 1\omega\rangle$.

3.5.6 Channel Asymmetry in Zero Photon Dissociation of HD^+

In this section, we explore the channel asymmetry in the zero-photon dissociation (ZPD) process of HD^+ using broad spectral bandwidth 7 fs laser pulses. This stimulated Raman process leading to ZPD is observable because of the broad spectral bandwidth provided by short laser pulses, as discussed earlier in section 3.4.4. Previously, we demonstrated that the chirp laser parameter can be used to enhance or suppress the ZPD process (see Section 3.4.4). Figure 3.25 displays the measured energy distribution for HD^+ dissociation using ~16 fs pulses (a) negatively and (c) positively chirped from 7 fs FTL laser pulses with a peak intensity of 1×10^{13} W/cm^2 and (b) ~7 fs FTL with a peak intensity of 2×10^{13} W/cm^2. The branching ratios for various laser parameters are evaluated as a function of energy in Fig. 3.25(d)–(f).

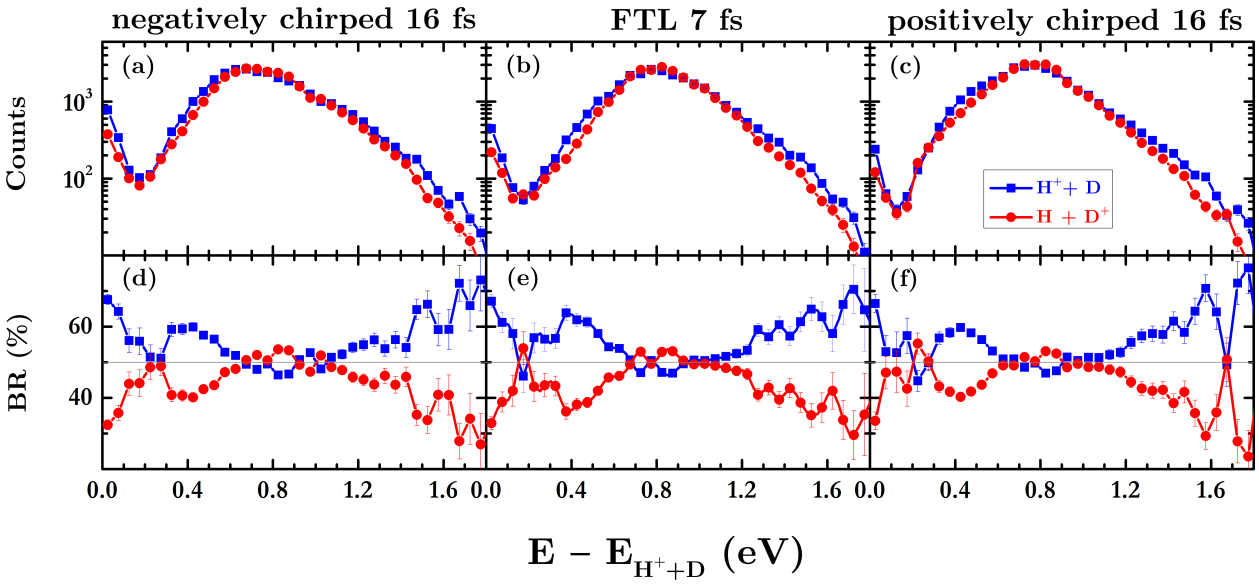

Figure 3.25: Measured energy distribution for HD^+ dissociation using (a)∼16 fs negatively chirped from 7 fs FTL pulses with a peak intensity of 1×10^{13} W/cm^2, (b) ∼7 fs FTL with a peak intensity of 2×10^{13} W/cm^2 and (c) ∼16 fs positively chirped from 7 fs FTL pulses with a peak intensity of 1×10^{13} W/cm^2. The error bars denote the statistical uncertainty in the data and are smaller than the symbols. Branching ratios are evaluated from the energy distribution for the same (d) negatively chirped, (e) FTL and (f) positively chirped laser pulses presented in panels (a)-(c).

It is clear that in the ZPD region (≤0.2 eV) the break up preferentially leads to the lowest dissociation channel, H^++D. However, the results show no significant chirp dependence. The channel asymmetry and total yield are calculated as

$$\mathcal{A}_{ch} = \frac{N_{[H^+ + D]} - N_{[H + D^+]}}{N_{[H^+ + D]} + N_{[H + D^+]}} \qquad (3.16)$$
$$\mathcal{Y} = N_{[H^+ + D]} + N_{[H + D^+]},$$

where N is the number of counts for each channel. The channel asymmetry is simply defined as the difference between the branching ratios presented in Fig 3.25(d)–(f). The measured channel asymmetries for FTL and chirped laser pulses are plotted in Fig. 3.26(a). It is obvious that channel asymmetry in HD^+ is a function of dissociation energy. However, the results show no clear chirp dependence, possibly because of the poor statistics in the ZPD region, as shown by the evaluated error bars in Fig 3.26(a).

On the other hand, the total yield shown in Fig. 3.26(b) follows the theoretical prediction dis-

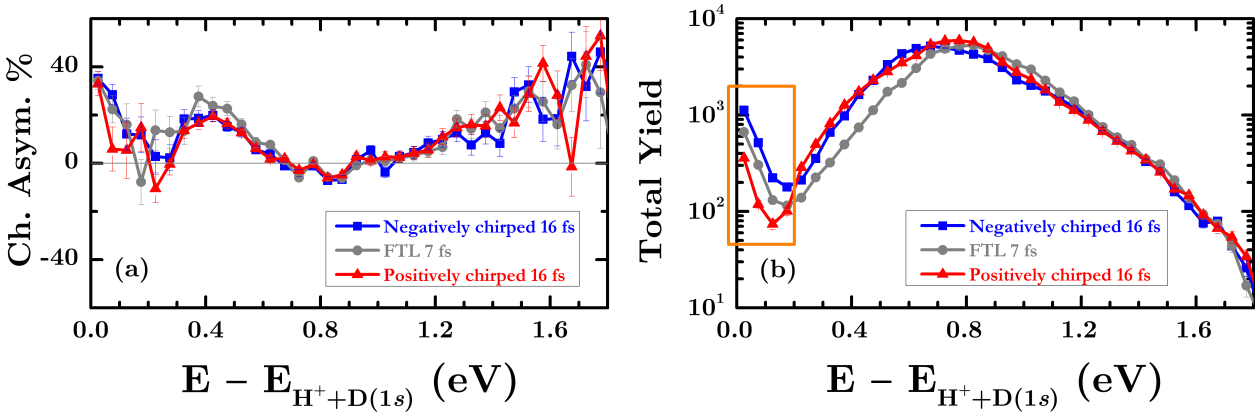

Figure 3.26: The (a) channel asymmetry and (b) total yield (sum of both channels) as a function of energy for negatively chirped, FTL and positively chirped laser pulses with the same laser parameters as in Fig. 3.25(a)-(c)

cussed in the earlier section [see Fig. 3.16(a)]. In brief, the ZPD process is enhanced for negatively chirped laser pulses in comparison to FTL laser pulses with the same bandwidth. Heuristically speaking, by using negatively chirped laser pulses, one would expect to absorb a higher energy photon early in the pulse followed by stimulated emission of lower energy photons resulting in enhancement of the ZPD process — associated with a simplistic stimulated Raman picture. This reasoning suggests that reversing the order of absorbed and emitted photons (positively chirped laser pulse) should lead to suppression of the ZPD process in agreement with the experimental results shown in Fig 3.26(b). Future experimental studies using broader bandwidth laser pulses (4–5 fs) and higher repetition rates may reveal the chirp dependence in the channel asymmetry. In addition, theoretical calculations can be used to guide our experimental work by suggesting the optimum laser parameters needed to measure such a channel asymmetry.

3.5.7 Summary and Outlook

In summary, we have taken a major stride forward by demonstrating control of the final product in the dissociation of the simplest heteronuclear molecule, HD^+, using intense single-color laser fields. Dissociation of HD^+ molecules are studied experimentally and theoretically using intense ultrashort 25 fs FTL and positively chirped 65 fs laser pulses (similar results are observed for negatively chirped pulses and are not shown for brevity). The permanent dipole moment allows

transitions within the same electronic state [see Fig. 3.22(a)], therefore opening new pathways for dissociation. Deviation from equal break up into H^++D or H+D^+ was observed both in experiment and theory. Theory and experiment suggest that control of the branching ratio is possible using various laser parameters, and more investigation is necessary to achieve better control over the final product.

We show experimentally that the H^++D channel, associated with the HD^+ electronic ground state, dominates over dissociation into H+D^+ for very slow fragmentation (low KER) of HD^+ produced by a two-photon process called (net) zero-photon dissociation (ZPD), as expected.

3.6 Control over Dissociation of a Molecular Ion Beam by Two-Color Laser Field — ω–2ω

Synopsis. In the first two-pulse, pump-probe style experiment of its kind[2], control over the dissociation of a molecular-ion beam is demonstrated by using the phase delay between the 790 and 395 nm components of an intense two-color laser field. A clear spatial asymmetry is detected in the emission direction of D_2^+ and HD^+ dissociation fragments. The results are interpreted in terms of an interference between vibrationally-resolved dissociation pathways and are qualitatively well reproduced by 3D time-dependent Schrödinger equation calculations carried out by Esry and coworkers.

3.6.1 Introduction

Strong-field laser control of molecular reactions is becoming practicable nowadays. Control has been predicted [75–78] and realized [48, 79–90] by varying the relative phase of a two-color laser field [75] or the carrier-envelope phase (CEP) of a few-cycle laser pulse [76]. So far, most of the experimental work has been carried out on gas targets of neutral molecules where relatively high target densities are possible. Pushing laser control to the domain of molecular ion-beam targets opens the door to the exploration of a whole new range of systems as exemplified by the recent strong-field experiments on H_3^+ [97, 203].

By comparison with neutral targets, however, molecular-ion beam work is still fairly new. It is less than a decade since the pioneering groups of Figger [238, 309] and Williams [310] first introduced molecular-ion beams to intense ultrafast lasers. In fact, only within the past few years have more frequent studies emerged [73, 91, 239]. In this section we take a major stride forward by demonstrating the first systematic control experiments on D_2^+ and HD^+ beams using intense two-color laser fields.

The difficulties with ion beams stem from their low densities. For example, our typical beam has $\sim 10^5$ molecules/cm^3, which is dramatically lower than a conventional neutral jet that has $>10^{11}$

[2]This section is based on a manuscript by J. McKenna *et al.* [308]

molecules/cm^3. The lower count rates that result make scanning the phase of a two-color field or CEP-stabilized pulse challenging, particularly if the fragments are to be measured in coincidence as carried out here. Despite this hurdle, there are several key advantages to ion beams (in addition to new systems to explore) that make them attractive from the perspective of strong-field control experiments (see Section 3.2).

One advantage is in identifying the origin of control. The control exercised over neutral molecules is due to the interference of channels excited by either electron recollision following ionization of the neutral (e.g. [80]) or multiphoton absorption (e.g. [83]), which are difficult to separate if their kinetic energy release (KER) is similar. With ion beams, electron recollision can be eliminated, making it easier to explore control by multiphoton processes. Additionally, ionic and neutral fragments can be measured in coincidence allowing dissociation events to be distinguished from ionization [91]. Another advantage is that vibrationally resolved dissociation spectra are quite common for ion beams (e.g. [73, 95, 238]), whereas for neutral targets they are rare [209]. Hence, one can cleanly observe which initial vibrational states ν are controlled, as will be shown here. Furthermore, without the need to ionize the neutral molecule within the same laser pulse, it is possible to explore control at lower intensities.

Two different types of control are predicted. The first affects a spatial asymmetry in the direction of ionic and neutral fragments following dissociation [75–78], and has been observed in several experiments already [48, 79–90]. The second type produces a channel asymmetry and relates to control of the dissociation products, which are clearly distinguishable in a heteronuclear molecule. For example, HD^+ may preferentially dissociate to either H^++D($1s$) or H($1s$)+D^+ [75, 76]. This channel asymmetry, to our knowledge, has never been observed in CEP or two-color control experiments. In fact, Sheehy *et al.* [48] specifically report no channel asymmetry in a two-color experiment on HD (532 nm and 1064 nm), despite seeing a spatial asymmetry—seemingly in agreement with theory [75].

3.6.2 Experimental Methods

In this section, we experimentally demonstrate spatial asymmetry types of control. By varying the relative phase between temporally-overlapped 790 nm and 395 nm pulses, we control the spatial asymmetry in the dissociation of D_2^+, measured using coincidence 3D momentum imaging (see Section 3.2) [91]. The details of the two-color configuration can be found in Section 2.4. In short, the two-color field is generated collinearly from a Ti:sapphire laser; 30 fs, 2 mJ, 790 nm pulses at 1.5 kHz [139]. The pulses are frequency-doubled to create orthogonally polarized 395 and 790 nm light. The relative phase between these 'two-color' pulses is controlled using a birefringent calcite crystal with the 395 nm polarization aligned to the extraordinary (fast) axis and the 790 nm polarization aligned to the ordinary (slow) axis. Rotation of the calcite crystal about the optical axis introduces a delay between the two pulses, i.e. a relative phase. The 790 nm polarization is subsequently rotated to the same axis as the 395 nm and focused onto the ion beam target using an $f = 203$ mm off-axis parabolic mirror. A small deviation between the polarization direction of 790 nm light and the calcite crystal axis results in unwanted polarization rotated by 90°. The outcome is an unclear momentum distribution which is identified as an artifact, as described in Appendix C.

The 7 keV D_2^+ or HD^+ beam (current 3 nA; cross-section $\sim 0.6 \times 0.6\,\text{mm}^2$) is crossed with focused laser pulses that dissociate the molecular ions. The resulting fragments, ions and neutrals, are imaged using a time- and position-sensitive detector that provides kinematically complete information on the dissociation. By varying the relative phase between 790 nm and 395 nm pulses, we control the spatial asymmetry in the dissociation of the D_2^+ molecular ion-beam target. Similar spatial asymmetry is also seen in HD^+, however no channel asymmetry between $H^+ + D(1s)$ and $H(1s) + D^+$ is observed. This is due to the different symmetries in the two dissociation products, which results in a delay independent signal and will be discussed later. Due to the clarity of the experimental data it is immediately apparent which dissociation pathways give rise to the control interference. Even so, we justify our interpretation by solving the 3D time-dependent Schrödinger equation including nuclear rotation. The theory results qualitatively agree well with experiment.

3.6.3 Results and Discussions

3.6.3.1 D_2^+

The interfering pathways can be conveniently identified in the diabatic Floquet Born-Oppenheimer potentials [200] shown in Fig. 3.27. Figure 3.27 displays the lowest Born-Oppenheimer potentials, $1s\sigma_g$ and $2p\sigma_u$, of D_2^+ in the diabatic Floquet representation (light-dressed states) for a mixed 790 nm and 395 nm field. The curve labels, $\pm n\omega$, indicate the absorption (–) and emission (+) of n photons, where ω refers to the frequency of 790 nm light. Hence, the absorption of one 395 nm photon equates to -2ω. Following dipole selection rules, however, one should associate even parity nuclear angular momentum N states (N even) with the $1s\sigma_g$ channel and odd parity (N odd) with $2p\sigma_u$, independent of n.

In the figure, three pathways are labeled. Pathway α denotes absorption of one 790 nm photon with the $v \sim 13$ states of D_2^+ dissociating by bond softening [26, 31, 200] through the $|1s\sigma_g - 0\omega\rangle \rightarrow |2p\sigma_u - 1\omega\rangle$ crossing. Intensities above roughly 10^{12} W/cm^2 can drive dissociation from states down to $v \sim 7$ along this pathway. Pathway β is the 395 nm equivalent of α: $v \sim 8$ dissociates via the $|1s\sigma_g - 0\omega\rangle \rightarrow |2p\sigma_u - 2\omega\rangle$ crossing. Pathway γ is a direct result of mixing the 790 nm and 395 nm fields and corresponds to the absorption of one 395 nm photon followed by the stimulated emission of one 790 nm photon, i.e. $|1s\sigma_g - 0\omega\rangle \rightarrow |2p\sigma_u - 2\omega\rangle \rightarrow |1s\sigma_g - 1\omega\rangle$.

The recipe for observing an asymmetry is well-documented by earlier theoretical studies of Esry and coworkers [111, 112]. To recap, for a given initial ν state there needs to be two (or more) dissociation pathways that lead to different final channels (i.e. one to $1s\sigma_g$ and the other to $2p\sigma_u$) and that contribute at the same KER. Additionally, if the amplitudes of these pathways are similar, then the asymmetry will be large. The obvious candidates for an interference from the pathways shown in Fig. 3.27 are pathways α and γ. For example, $v \sim 8$ may dissociate along α leading to $|2p\sigma_u - 1\omega\rangle$, or along γ leading to $|1s\sigma_g - 1\omega\rangle$, both overlapping with KER$\simeq$0.3 eV and having odd and even nuclear parity, respectively.

Knowing the interfering pathways allows us to predict the periodicity of any observable in $\omega\tau$ where τ is the time delay between the pulses [311]. If m 395 nm photons are absorbed along one

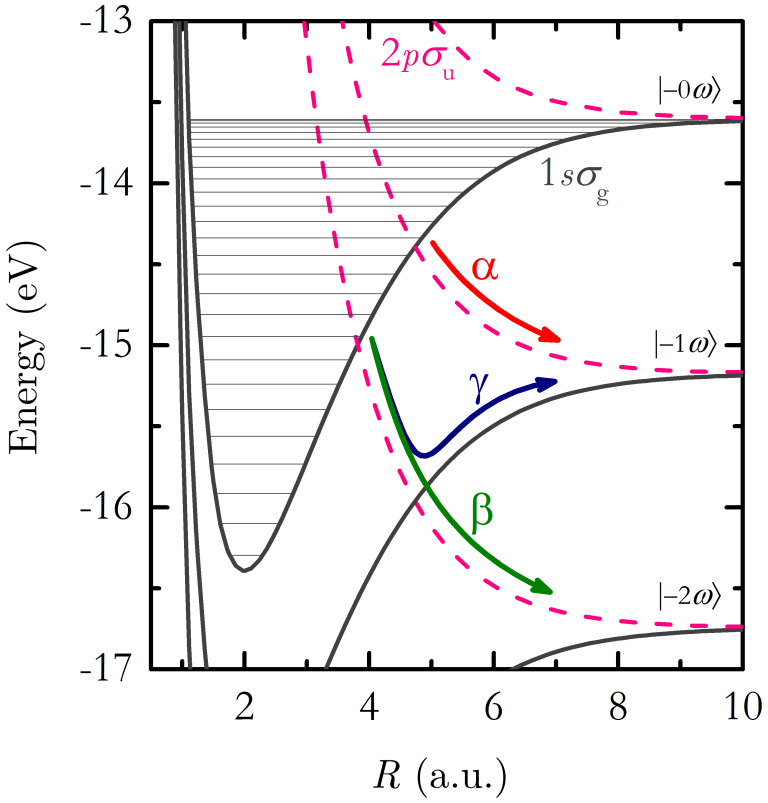

Figure 3.27: Diabatic Floquet Born-Oppenheimer potentials of D_2^+. The potential energy curves are adapted from Ref. [280]. For simplicity, nuclear rotation has not been included.

pathway and m' along the other, then their interference contributes a periodicity of $\pi/|m-m'|$ to the asymmetry. Since pathway α has net absorption of m=0 395 nm photons and pathway γ has net absorption of m'=1 395 nm photon, the asymmetry will exhibit sinusoidal behavior in $\omega\tau$ with period π. That is, if A_α and A_γ are the amplitudes for pathways α and γ at a given KER along the laser polarization, then the "up" and "down" signals we expect are, respectively,

$$|A_\alpha \pm A_\gamma|^2 = |A_\alpha|^2 + |A_\gamma|^2 \pm 2|A_\alpha||A_\gamma| \cos(\phi + 2\omega\tau), \tag{3.17}$$

where ϕ is the $\omega\tau$-independent phase difference between α and γ [311]. Interestingly, Eq. (3.17) suggests that ϕ can be directly measured at $\omega\tau$=0.

Kinetic energy release and angular distributions for D_2^+ dissociation are shown in Fig. 3.28 for (a) 790 nm (6×10^{14} W/cm^2), (b) 395 nm (4×10^{12} W/cm^2) and (c) a mixed two-color field of the 790 nm and 395 nm pulses. Figure 3.28(d) is integrated over all angles. Dissociation at 790 nm

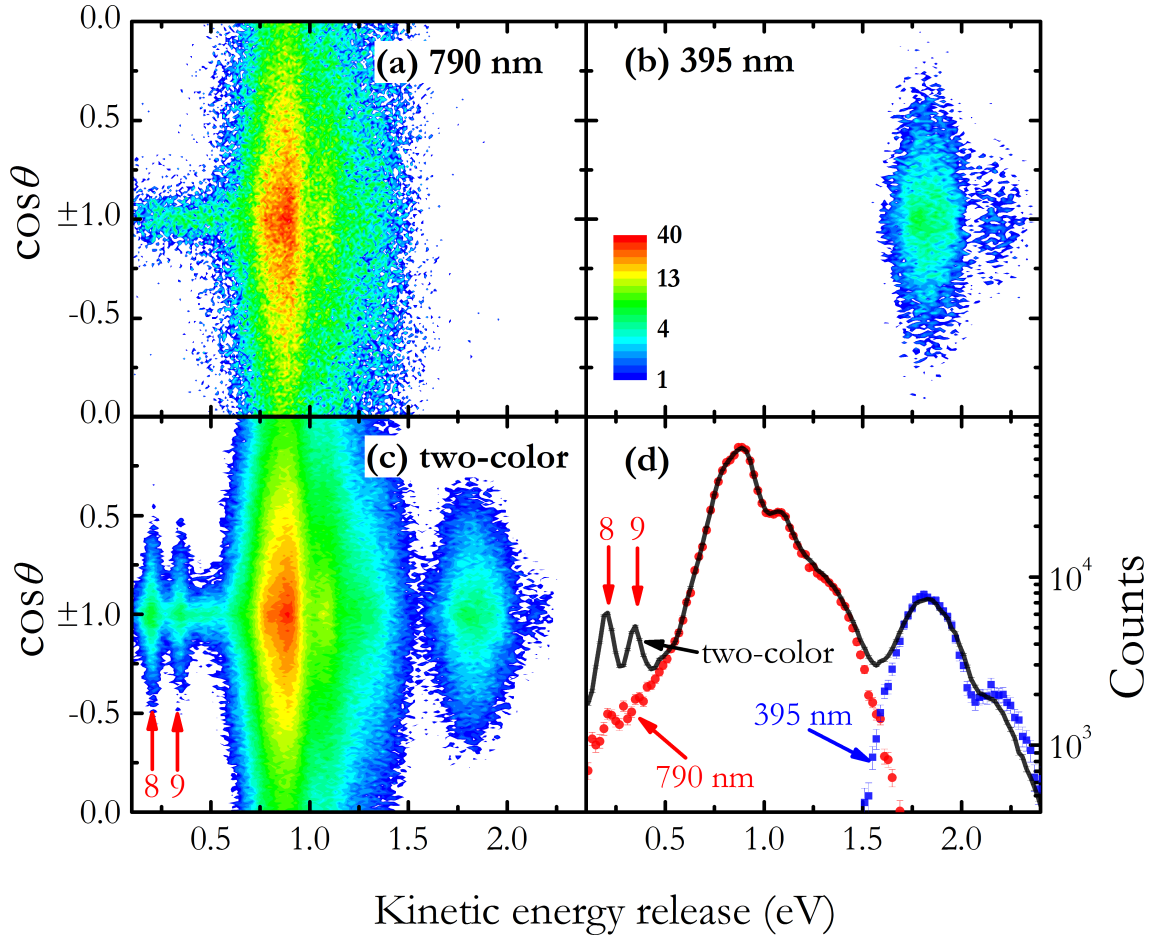

Figure 3.28: KER-cosθ (θ relative to laser polarization) plots for dissociation of D_2^+ for (a) 790 nm, 6×10^{14} W/cm^2, (c) 395 nm, 4×10^{12} W/cm^2, and (c) a mixed two-color field for the pulses used in (a) and (b). The 1D KER distributions corresponding to (a–c) are shown in (d). Error bars denote statistical uncertainty.

comes from pathway α in Fig. 3.27 while dissociation at 395 nm comes from pathway β (see discussion above). The signature of pathway γ in the mixed two-color field is the two prominent peaks marked by vertical arrows in Figs. 3.28(c) and (d). These peaks at KER=0.21 and 0.35 eV relate to dissociation of $v\sim8$ and 9, respectively, and are absent when only 790 or 395 nm pulses are used. To observe an *up-down* asymmetry it is important that $v\sim8$ and 9 can also dissociate via pathway α by bond softening. This is evidenced by the aligned feature below 0.5 eV in Fig. 3.28(a) at 790 nm.

The asymmetry presented here originates from the interference of pathways α and γ at

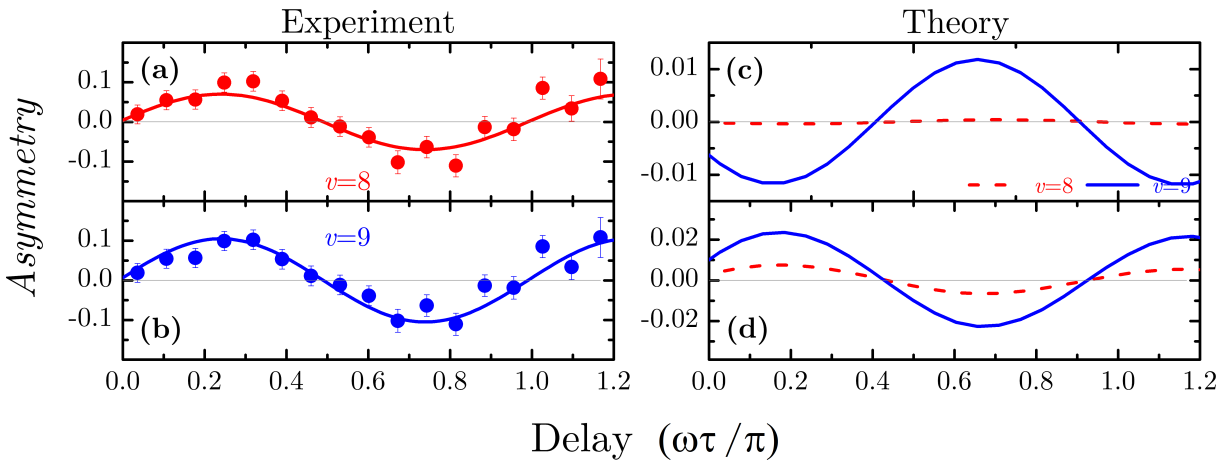

Figure 3.29: Two-color measurements using 790 nm, 6×10^{14} W/cm^2 pulses mixed with 395 nm, 4×10^{12} W/cm^2 pulses: D_2^+ asymmetry for (a) ν ~8 (0.14<KER<0.27 eV) and (b) ν ~9 (0.27<KER<0.42 eV), respectively. The curves in (a) and (b) are sinusoidal fits with π periodicity. Error bars denote statistical uncertainty. Theoretical D_2^+ asymmetry for v ~8 and 9 for 790 nm intensities of (c) 10^{12} W/cm^2 and (d) 10^{13} W/cm^2 with 395 nm 10% of these, for the same θ range as experiment ($0.4<|\cos\theta|<0.9$).

KER$\lesssim$0.5 eV. By varying the relative phase of the 790 nm and 395 nm pulses we control the interference and thus population transfer between the states, thereby controlling the observed asymmetry. In a classical picture, as the electron oscillates between the nuclear centers of the dissociating D_2^+ it is impeded and localized on one nucleus or the other by the rise of an interatomic potential barrier as R increases. The phase of the two-color field determines the phase of the electron oscillation and hence which nucleus it ends up on when the oscillation ceases.

The *up-down* asymmetry parameter is defined as in Refs. [80, 89] as the difference in D^+ counts in the *up* and *down* directions normalized to their sum, $\mathcal{A}=(P_u-P_d)/(P_u+P_d)$, where P_u and P_d denote the number of events with D^+ emission "up" ($\cos\theta>0$) and "down" ($\cos\theta<0$), respectively. To enhance the spatial asymmetry, $\mathcal{A}$, the results are integrated over $0.4<|\cos\theta|<0.9$ so that the contribution from 790 nm light within this range is reduced (see Fig. 3.28(a); the 790 nm results in a dissociation tail along the laser polarization and at low KER). Figure 3.29(a) and (b) present the normalized asymmetry parameter for D_2^+ dissociation. The spectra in Fig. 3.28(c) are integrated over KER and cosθ for the ν~8 (0.14<KER<0.27 eV) and ν~9 (0.27<KER<0.42 eV) peaks, generating the asymmetries shown in Fig. 3.29(a) and (b).

To help understand the D_2^+ results, the time-dependent Schrödinger equation is solved by Esry and coworkers including nuclear vibration and rotation but neglecting ionization [252, 253]. This treatment provides complete KER-$\cos\theta$ distributions. Our goal was to compare the experimental results and the calculations qualitatively. To achieve a quantitative comparison between the theory and the experiment, one would need to match all the experimental conditions as well as performing intensity averaging. Therefore, without intensity averaging, these distributions cannot be directly compared with experiment. Nevertheless, they provide important qualitative confirmation of our interpretation. For instance, the periodicity of the asymmetry oscillation is exactly reproduced by theory. Moreover, the calculations predict ϕ from Eq. (3.17) to be essentially the same for $v\sim8$ and 9 as indicated by the theoretical asymmetry plotted in Figs. 3.29(d)—in agreement with the experiment.

The $\sim\pi$ phase shift between Figs. 3.29(c) and (d) also shows that ϕ is intensity-dependent, suggesting that the intensity averaging inherent in the experiment is the reason that the observed asymmetry in Figs. 3.29(a) and (b) is not larger. Theory also shows that the asymmetry amplitude is larger for $v\sim9$ than for $v\sim8$ as observed marginally in the experiment and as is consistent with $|A_\alpha|^2$ being closer to $|A_\gamma|^2$ for $v\sim9$ than for $v\sim8$.

3.6.3.2 HD^+

Since controlling the spatial asymmetry of D_2^+ break-up is now understood in depth, fragmentation of HD^+ is explored using a two-color laser field. The requirement that two pathways interfere to produce an asymmetry is further explored by the plots of the asymmetry parameter for fragmentation of HD^+. Being heteronuclear, HD^+ can dissociate to H^++D and H+D^+ which are distinguishable due to electron localization, making it non-trivially different from D_2^+. Importantly, we observe asymmetry for each channel of HD^+ at KER<0.5 eV much like that for D_2^+ as shown in Figs. 3.30(a) and (b) for the same conditions and cuts as used in Fig. 3.29(a) and (b), where "up" and "down" now refer to the direction of the single proton, whether it is in H^+ or H. The spatial distribution thus varies with delay for both electron localizations (H^++D and H+D^+), demonstrating that spatial asymmetry is not equivalent to electron localization.

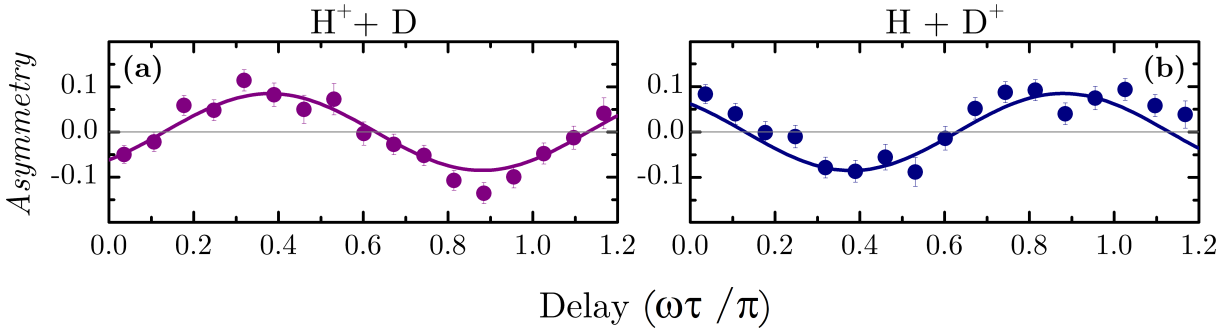

Figure 3.30: Two-color measurements using 790 nm, 6×10^{14} W/cm^2 mixed with 395 nm, 4×10^{12} W/cm^2 pulses: HD^+ asymmetry for fragmentation into (a) H^++D and (b) H+D^+ channel, with KER<0.5 eV. The curves in (a) and (b) are sinusoidal fits with π periodicity. Error bars denote statistical uncertainty.

The physical origin of the *up-down* asymmetry is also the same as D_2^+, resulting from a coherent superposition of population on $2p\sigma$ and $1s\sigma$ states via pathways α and γ, respectively. The case of HD^+, however, is special as the $2p\sigma$ and $1s\sigma$ states have a small energy splitting of ~3.7 meV at $R\to\infty$ [278–281], as shown in Fig. 3.31.

Population on $1s\sigma$ at $R\to\infty$ therefore leads to the H^++D($1s$) channel (as shown by pathway γ in Fig. 3.31), while population on $2p\sigma$ leads to the H($1s$)+D^+ channel, the pathway labeled as α in Fig. 3.31. In addition, HD^+ exhibits a strong non-adiabatic coupling at R~12 a.u. [280], which

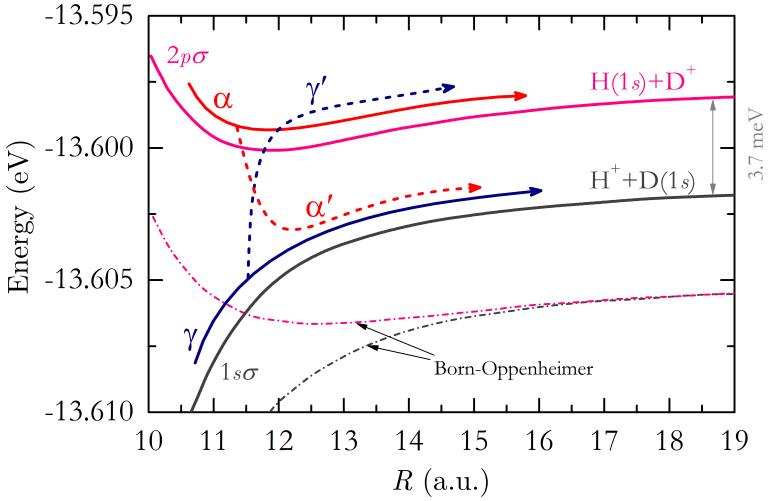

Figure 3.31: Blowup of the -1ω threshold of the diabatic Floquet Born-Oppenheimer potentials of HD^+ [280], showing the correction to these potentials for HD^+ [280]. Pathways are described in the text.

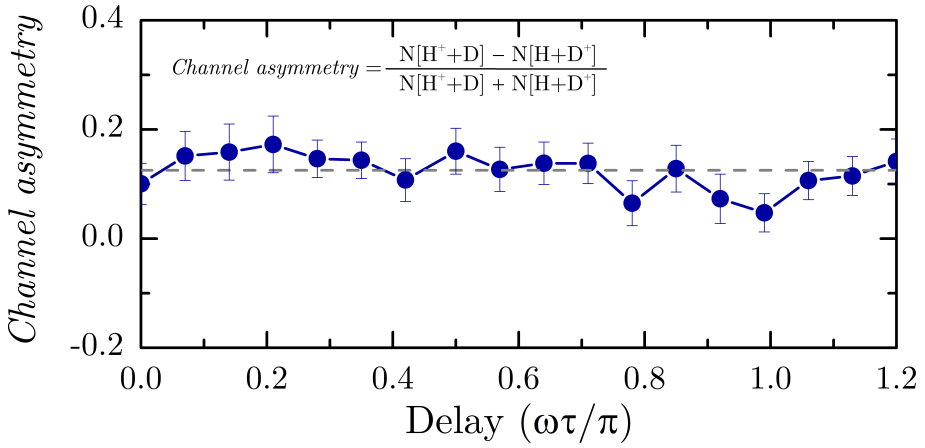

Figure 3.32: The channel asymmetry as a function of delay between the 790 nm and 395 nm laser pulses for the same laser parameters as in Fig. 3.30. The dashed line represents the mean value of the measured channel asymmetry. The error bars denote the statistical uncertainty in the data.

results in mixing the $1s\sigma$ and $2p\sigma$ states via pathway α' and γ' independent of the laser field (see Section 3.5 for more details), as shown schematically in Fig. 3.31. The phase of a two-color field can affect the mixing ratio due to the interference of the pathways marked in Fig. 3.27 leading to the possibility of controlling the dissociation channel of the molecule. However, the results displayed in Fig. 3.32 show no noticeable channel asymmetry as a function of delay within the error bars, as predicted by theory [75].

In the case of HD^+, the probabilities of dissociation to either channel (H^++D($1s$) or H($1s$)+D^+) are written as $|A^o_{\alpha'}+A^e_{\gamma}|^2$ and $|A^o_{\alpha}+A^e_{\gamma'}|^2$, respectively. The superscripts e and o corresponds to even and odd nuclear parity. These amplitudes depend on the energy and angle θ (the angle between laser polarization direction and fragmentation velocity). To evaluate the channel asymmetry, the total probabilities have to be integrated over all angles,

$$\begin{aligned}
\int d\Omega |A^o_{\alpha'} + A^e_{\gamma}|^2 &= \int d\Omega \left[|A^o_{\alpha'}|^2 + |A^e_{\gamma}|^2 + 2|A^o_{\alpha'}||A^e_{\gamma}| \cos(\phi_{\alpha'\gamma} + 2\omega\tau) \right] \\
&= |a^o_{\alpha'}|^2 + |a^e_{\gamma}|^2, \\
\int d\Omega |A^o_{\alpha} + A^e_{\gamma'}|^2 &= \int d\Omega \left[|A^o_{\alpha}|^2 + |A^e_{\gamma'}|^2 + 2|A^o_{\alpha}||A^e_{\gamma'}| \cos(\phi_{\alpha\gamma'} + 2\omega\tau) \right] \\
&= |a^o_{\alpha}|^2 + |a^e_{\gamma'}|^2.
\end{aligned} \tag{3.18}$$

The interference term is overall odd, and therefore the channel probabilities show no $\omega\tau$ dependence [312].

3.6.4 Summary

We have successfully controlled the dissociation of a molecular-ion beam via a classic Brumer-Shapiro [38, 52, 53] two-color scheme. The application of a unique combination of experimental techniques to the benchmark systems D_2^+ and HD^+ have allowed us to unambiguously identify the pathways that interfere to produce the control. We have overcome the challenges faced by two-pulse experiments on ion beams, and our work represents a first step in this unexplored territory. We expect that with continued development of ion beam systems it will soon be feasible to carry out time-resolved imaging and control experiments. Such experiments using ion beams complement studies on neutral molecules and pave the way for exploration of the dynamics of other benchmark systems like HeH^+ and H_3^+ in strong ultrafast fields.

3.7 Pump-probe Studies of a Molecular Ion Beams

Synopsis. In a follow-up study to the two-color experiment (Section 3.6), a pump-probe technique is implemented for studies of the dynamics of molecular ion-beam targets. In a typical pump-probe experiment, the pump pulse ionizes a neutral target and creates a wavepacket. Then, the probe pulse images the wavepacket evolution at different delay times with respect to the pump pulse. In the case of an ion-beam target, the ionization step via a pump pulse is unnecessary so a weak pump pulse can be used to excite or initiate dissociation, and a stronger probe pulse is used to further dissociate or ionize the molecular ion. To demonstrate that such experiments are feasible in spite of the low target density of an ion-beam target, the pump-probe technique is utilized to study fragmentation dynamics in D_2^+ and HD^+ molecular-ion beams.

3.7.1 Introduction

Experimentally, the pump-probe technique has been used to explore molecular dynamics [23, 313, 314]. Depending on the system under study, a pump pulse initiates the dynamics on a specific molecular state, which is then probed by a second laser pulse. The probe pulse is applied after a certain time delay to map the time evolution of the system under investigation. The characteristics of the probe pulse can be modified based upon the objective. For instance, the intensity of the probe pulse can be adjusted to study dissociation or ionization processes. For example, studies focused on Coulomb-explosion imaging use high intensity probe laser pulses [315–317]. The pulse duration of the pump and probe pulses can be designed to examine time-dependent processes with the proper time resolution. One of the applications of such time-resolved pump-probe studies is to control the reaction dynamics of a chemical or biological system [314, 318].

More than two decades ago, Zewail and coworkers employed femtosecond laser pulses to excite and probe the time evolution of a nuclear wavepacket in sodium iodide molecules [23, 313]. Stapelfeldt and coworkers used the pump-probe method in conjunction with the Coulomb explosion (CE) technique to image the motion of nuclear wavepackets [319]. In the past decades, multitudes of such experimental and theoretical works have been performed as evidenced in

Refs. [227, 240, 255, 301, 315, 316, 320–338]. However, all of the experimental studies carried out started from a neutral molecular target. In this section, we present two preliminary pump-probe measurements of molecular ion-beam targets. In the first example, the dissociation of D_2^+ is investigated by 5 fs pump and probe laser pulses. In the second example, the ionization of HD^+ is explored using 25 fs laser pulses. These examples demonstrate the feasibility of performing pump-probe studies of molecular ion-beam targets and point out the difficulties in such measurements. The main challenge of these experiments is linked to the low target density of our ion-beam target. For instance, the ionization rate of an HD^+ ion-beam target into H^++D^+ fragments is about 1–2 Hz using a 10 kHz laser system. As a result, performing a pump-probe scan of up to 200 fs with 5 fs delay per step can take up to 40 hours to acquire a few thousand counts in the whole KER range. Bunching the molecular-ion beam into few-ns bunches is under development, where an improvement of the target density by at least an order of magnitude is expected. This can further enhance the data collection rate and make the pump-probe studies manageable.

3.7.2 Experimental Method

To perform the experiments described above, synchronized pump and probe laser pulses are obtained using a Mach-Zehnder interferometer, as illustrated schematically in Fig. 3.33(a). The incoming laser beam is split into two. The choice of beam splitter results in different ratios between the power in the two beams. Most of our measurements have been performed with a few percent (4–10%) of the total power in the pump and 60–80% in the probe. The two beams recombine on the second beam splitter; however, a portion of the power is lost through this recombination process. For instance, in one configuration, the pump carries 4% of the total power, while the probe has 64% of the total power. To perform a pump-probe experiment, the stability of the interferometer is vital. For this purpose, the interferometer was built as one piece on a small breadboard. This helps with the stability of the interferometer as well as making it portable.

The time delay between the two pulses is controlled by a linear translation stage from Physik Instrumente [339] with sub-femtosecond resolution (position resolution of 0.2 μm — 1 fs corresponds to $\sim$0.3 μm). The stage can travel up to 25 mm, i.e. $\sim$80 ps; however, the pump-probe scanning

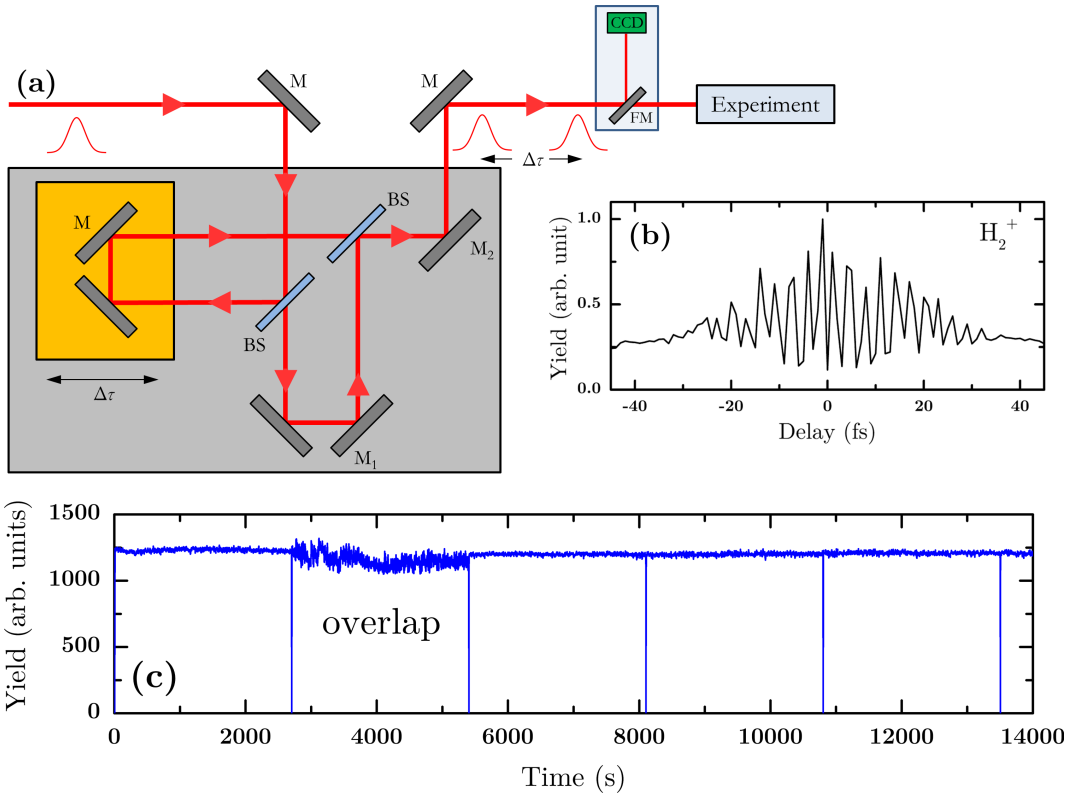

Figure 3.33: (a) Schematic of Mach-Zehnder interferometer. The reflecting mirrors are labeled by M, flipping mirror labeled as FM and the beam splitters are labeled as BS. (b) Interferometric fringes for H_2^+ production from H_2 residual-gas target. The fringe pattern is caused by the constructive and destructive interference of the pump and probe laser pulses as a function of time delay. (c) The power measured after the interaction region as a function of time. The overlap between the pump and probe pulses appears as a fluctuation of power in the spectrum, as indicated on the graph.

range in the present measurement is limited by the low density of the target, i.e. the low counting rate.

The initial spatial overlap is found by examining the focal spot of the combined beams with a lens at near-field. To align the Mach-Zehnder interferometer, one can adjust the mirrors in one of the arms while maintaining the other arm fixed. In this case, the spatial overlap can be checked at near- and far-field by walking the beam using two mirrors in one of the arms (M1 and M2 for example in Fig. 3.33(a)). The final spatial overlap is found by imaging the focal spot of the pump and probe, separately and together, on the CCD camera [340]. The initial temporal overlap is determined by observing the interference pattern of the two pulses on the CCD camera.

Furthermore, the temporal overlap between the pump and the probe pulses is examined in the interaction region using an interferometric method with H_2 residual gas in which the ionization yield is measured as a function of delay between the pump and probe laser pulses [341, 342], as shown in Fig. 3.33(b). In addition, the power of the pump and probe are monitored and recorded after the interaction region. The measured power is shown in Fig. 3.33(c) as a function of time through out the whole experiment. It is evident that the overlap between the pump and probe appears as a fringe pattern on the power measurement, as indicated in Fig. 3.33(c). Lastly, the pulse durations of the pump and probe pulses after the Mach-Zehnder interferometer are characterized using an autocorrelator (see Section 2.5).

The 7 keV D_2^+ or 9 keV HD^+ beam (current 2 nA; cross-section $\sim 0.6 \times 0.6\,\mathrm{mm}^2$) is crossed with the focused laser beam. The resulting fragments, ions and neutrals, are imaged using a time- and position-sensitive detector that provides kinematically complete information on the dissociation. The dissociation or ionization is measured using coincidence 3D momentum imaging (see Section 3.2) [91] as a function of time delay between the pump and the probe laser pulses.

3.7.3 Results

Two measurements are conducted in this section, the first focusing on the dissociation of D_2^+. In the other measurement, the above threshold Coulomb explosion process is explored in the ionization of HD^+.

3.7.3.1 D_2^+

Typical kinetic energy release and angular distribution spectra for D_2^+ breakup are displayed in Fig. 3.34(a) using 5 fs laser pulses with a peak intensity of $\sim 8 \times 10^{13}$ W/cm^2. Figure 3.34(b) shows the KER distribution integrated over all angles. One can observe clearly the ZPD (0.0–0.2 eV) in Fig. 3.34(b) for such short laser pulses, confirming our earlier discussion on bandwidth dependence of the ZPD process (see Section 3.4.4).

Figure 3.35(a) is the density plot of the measured dissociation of D_2^+ as a function of KER and delay time between the pump and probe laser pulses. In the present experiment, 5 fs pump

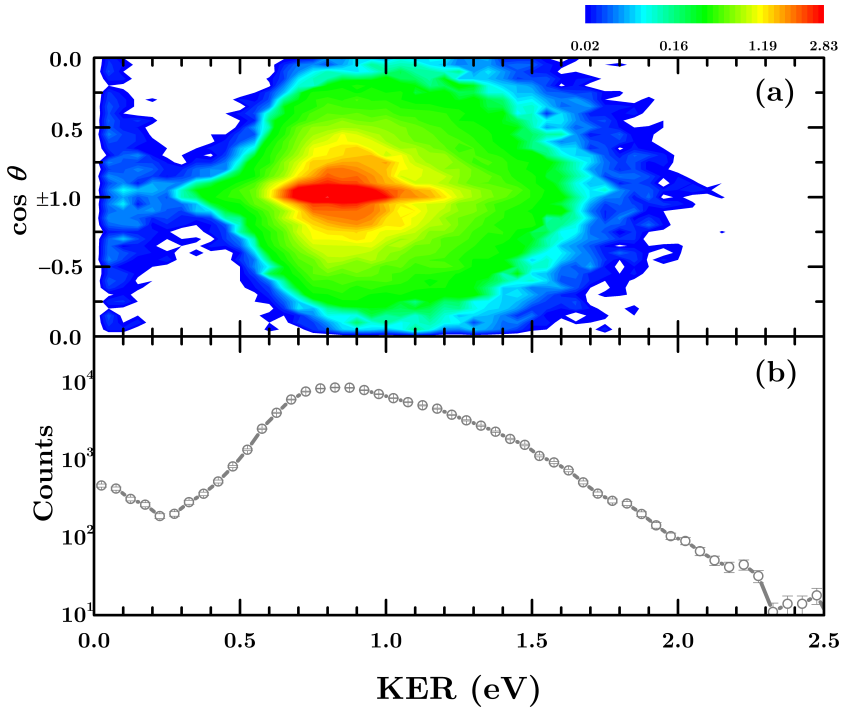

Figure 3.34: (a) Density plot of counts vs. KER and cosθ for D_2^+ dissociation at 740 nm, 5 fs, and a peak intensity of $\sim 8\times10^{13}$ W/cm^2 (log scale). (b) A histogram of counts vs. KER for the same laser parameter integrated over all angles. Error bars in (b) denote statistical uncertainty. Color bar numbers are written in powers of ten.

and probe pulses with intensities of $\sim 7\times10^{12}$ W/cm^2 and $\sim 8\times10^{13}$ W/cm^2, respectively, are used. The zero time delay, determined using the method described in the previous section, was further verified in Fig. 3.35(c) showing that dissociation is enhanced in the KER region (0.2≤KER (eV)≤0.3) corresponding to above-threshold dissociation (ATD) when the pulses are overlapped, since ATD depends strongly on the field strength. The yield in low energy region (KER≤0.2 eV), referred to as the ZPD region, is shown in Fig. 3.35(d). This energy region shows a weak oscillation as a function of delay time. The yield shows an oscillation at positive time delay, followed by reduction in the yield at longer time delays.

In the bond-softening region (0.8–0.9 eV), oscillations are more pronounced for both negative and positive time delays [see Fig. 3.35(b)]. These oscillations may be associated with the evolution of a vibrational wavepacket similar to that observed in the previous studies of neutral molecules (see Refs. [315, 316, 323, 327, 334]). A possible interpretation of these oscillations can be summarized as

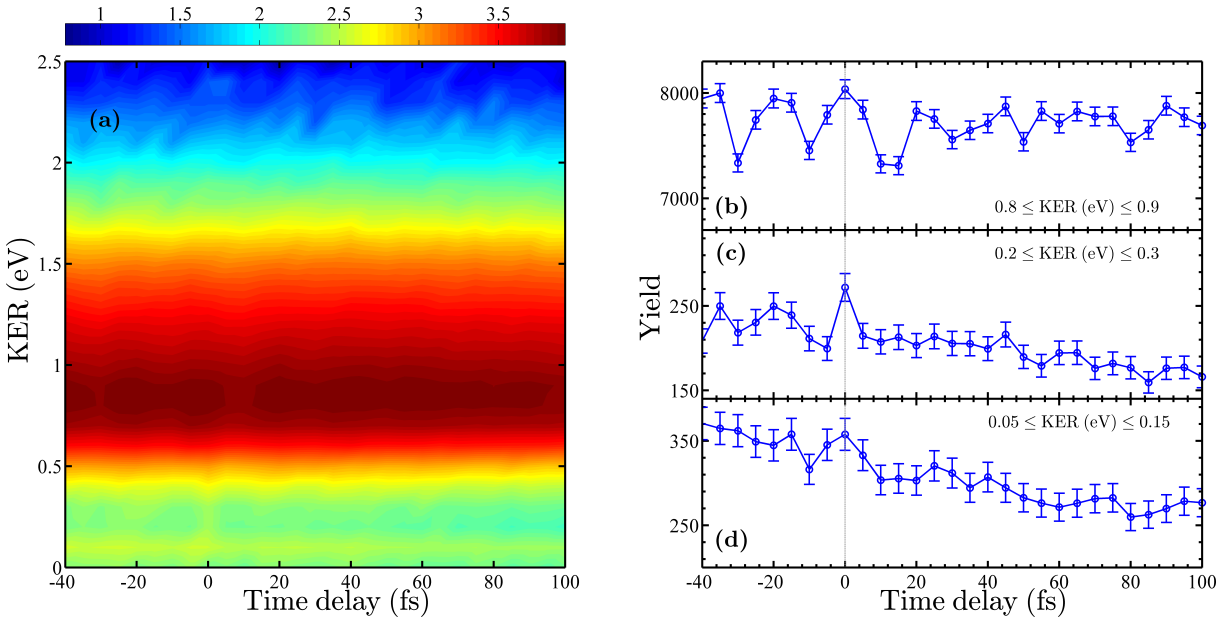

Figure 3.35: (a) Density plot of D_2^+ dissociation counts vs. KER and the delay time between the pump and probe laser pulses (log scale). The peak intensities of the pump and the probe pulses are $\sim 7\times10^{12}$ W/cm^2 and $\sim 8\times10^{13}$ W/cm^2, respectively. (b) – (d) The yield as a function of delay time over the specified range in the KER. Error bars denote statistical uncertainty. Color bar numbers are written in powers of ten.

an interference between different vibrational wavepackets generated by the pump or the probe laser pulse. For instance, a weak pump pulse dissociates a portion of the population, resulting in a bound wavepacket which will be dissociated later by the probe laser pulse. These vibrational wavepackets interfere constructively and destructively. However, our results suggest that the oscillation is stronger for negative time delays, when the strong field initiates the process. This suggests that future experiments should extend to longer delay times in both directions and employ different pump and probe intensities.

To recover the frequencies (or periods) of oscillation in the dissociation observed in Fig. 3.35(a), a Fourier transform analysis is performed on the 2D map as shown in Fig. 3.36(a). Figure 3.36(b)–(e) show the power spectrum as a function of frequency for various KER slices labeled on the individual panels. Due to the small time-delay range of the measured data, the Fourier analysis has poor resolution. For convenience, the results in Fig. 3.36 are converted to period, as shown in Fig. 3.37. The results reveal a dominant oscillation with a period of 20 fs in the bond-softening

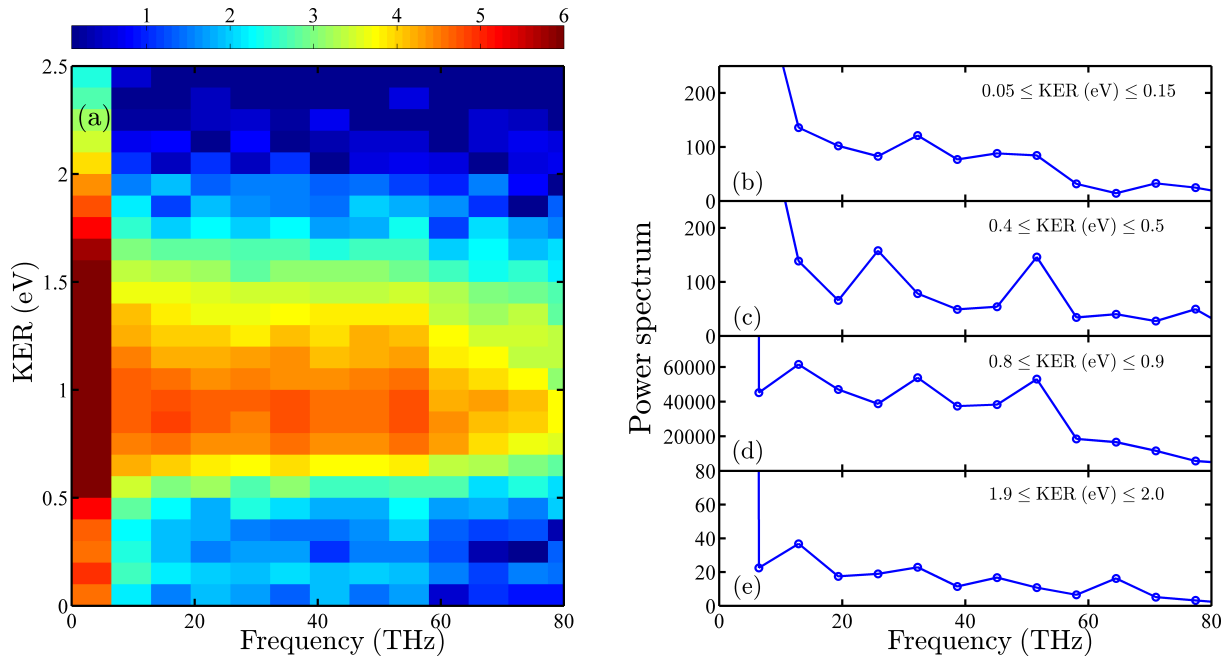

Figure 3.36: (a) Power spectrum of the Fourier transform as a function of frequency and KER for dissociation of D_2^+ with laser parameters listed in Fig. 3.35. (b)–(e) Power spectra as a function of frequency for the specified KER ranges. Color bar numbers are written in powers of ten.

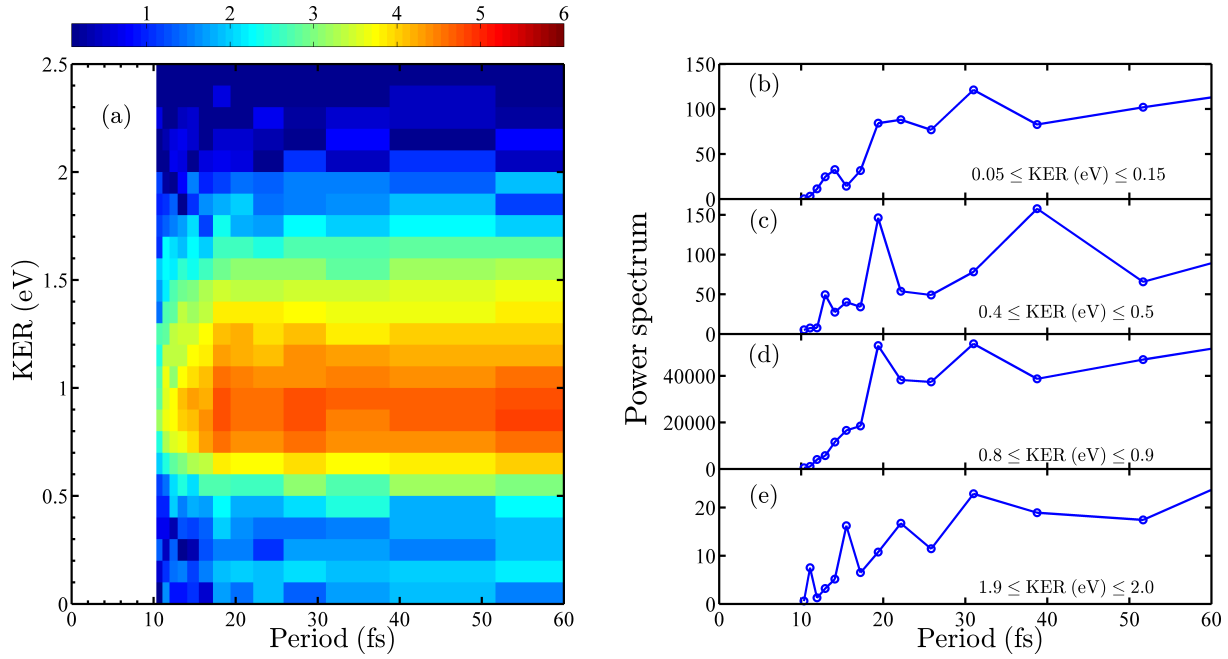

Figure 3.37: (a) Power spectrum of the Fourier transform as a function of period and KER for dissociation of D_2^+ with laser parameters listed in Fig. 3.35. (b)–(e) Power spectra as a function of period for the specified KER ranges. Color bar numbers are written in powers of ten.

region. The measured low- and high-KER regions [Fig. 3.37(b) and (e)] reveal other frequencies involved.

We used the frequencies obtained through the Fourier analysis to fit our measured data. As an example, the bond-softening region is fit with three sinusoidal functions with fixed frequencies retrieved from the Fourier analysis, as shown in Fig. 3.38. Comprehensive calculations may help us understand the source of oscillations in this fundamental quantum system.

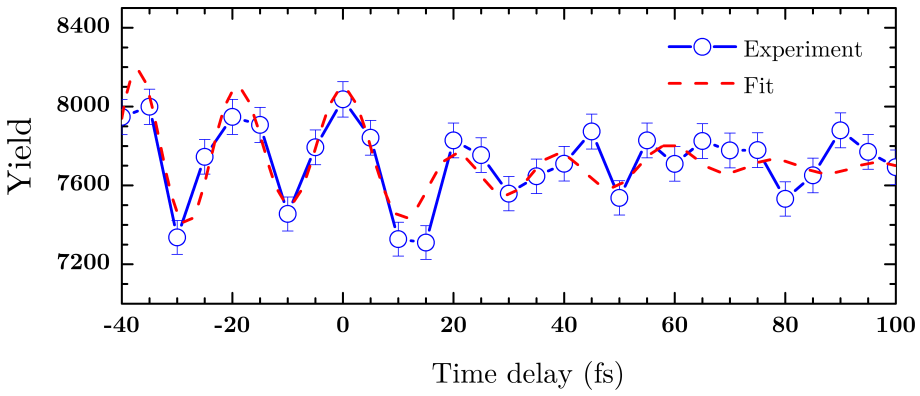

Figure 3.38: Integrated yield in the KER region of 0.8–0.9 eV is fit with three exponentially damped sinusoidal function (dashed line) with damping amplitude and three fixed frequencies of 12.9, 32.2, and 51.1 THz retrieved from the Fourier analysis.

3.7.3.2 HD^+

In the second example, we study the time evolution in the ionization of an HD^+ molecular ion-beam target. Structure in KER spectra measured near the ionization appearance intensity of the simplest diatomic molecules has been explored experimentally and theoretically [226, 228, 239, 343]. A simple model based on Floquet potentials was proposed by Esry and coworkers [226] to assign this structure to resonance multiphoton ionization along different dissociation pathways. This mechanism is referred to as above threshold Coulomb explosion (ATCE) and is illustrated in Fig. 3.39, which shows the Born-Oppenheimer curves of H_2^+ in the diabatic Floquet representation. In the Floquet representation, the emission and absorption of n photons ($\pm n\omega$) translates into the up or down shift of the potential energy curves. For instance, the bond softening (BS) process occurs via absorption of 1 photon through the pathway $|1s\sigma_g\rangle \rightarrow |2p\sigma_u - 1\omega\rangle$. Above threshold

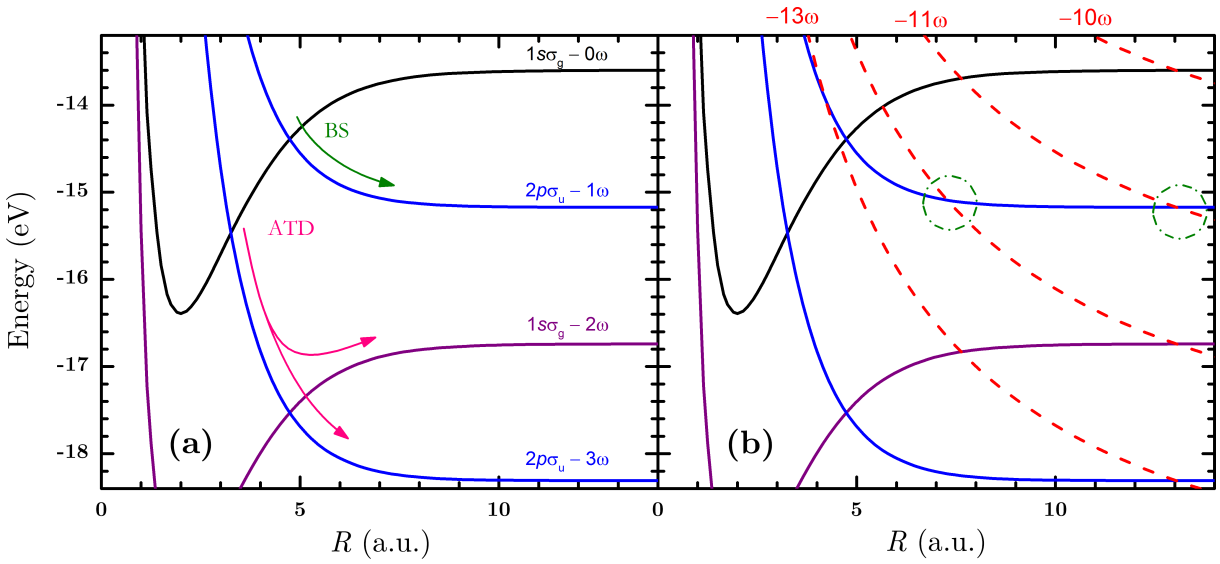

Figure 3.39: (a) The diabatic Floquet potential energy curves for H_2^+ dressed by net absorbed number of photons $n\omega$ for 790 nm light. Bond softening (BS) and above threshold dissociation (ATD) paths are marked with arrows. (b) The same as (a), but including the dressed $1/R$ ionization potential curves. (Adapted from Ref. [226])

dissociation (ATD) [32, 36] occurs through the absorption of 3 photons via the $|1s\sigma_g\rangle \rightarrow |2p\sigma_u - 3\omega\rangle$ pathway or the absorption of 3 photons followed by the stimulated emission of a photon via the $|1s\sigma_g\rangle \rightarrow |2p\sigma_u - 3\omega\rangle \rightarrow |2s\sigma_g - 2\omega\rangle$ pathway.

In addition to the diabatic Floquet potentials of the lowest $1s\sigma_g$ and $2p\sigma_u$ states of H_2^+, one can dress the ionization curves, i.e. $|1/R - n\omega\rangle$, as shown in Fig. 3.39(b). In this picture, a wave packet dissociating through BS can ionize at different internuclear distances via $|1/R - 13\omega\rangle$ to $|1/R - 10\omega\rangle$ resulting in structure in the KER spectrum. To study the time evolution of the nuclear wave packet, a weak pump pulse is used to initiate the dissociation via bond softening. A more intense probe pulse ionizes the dissociating wave packet at various delay times with respect to the pump pulse. In this method, we are able to map the crossing resonances of dressed $1/R - n\omega$ potentials with the dissociation pathways, resulting in ionization with different numbers of photons. One would expect to observe an enhancement in the KER structure corresponding to different numbers of photons when the pump-probe delay matches the travel time of the nuclear wave packet on the $2p\sigma_u$ curve to the corresponding crossing. For instance, in the case of H_2^+ potentials, dissociation from ν=9 reaches the $1/R - 12\omega$ crossing in 8.5 fs. The travel time for the $1/R - 11\omega$ and $1/R - 10\omega$ crossing is

estimated to be 23.5 fs and 130 fs, respectively [226]. To resolve these structures corresponding to the first two crossings in a pump-probe style experiment, ultrashort laser pulses would be crucial.

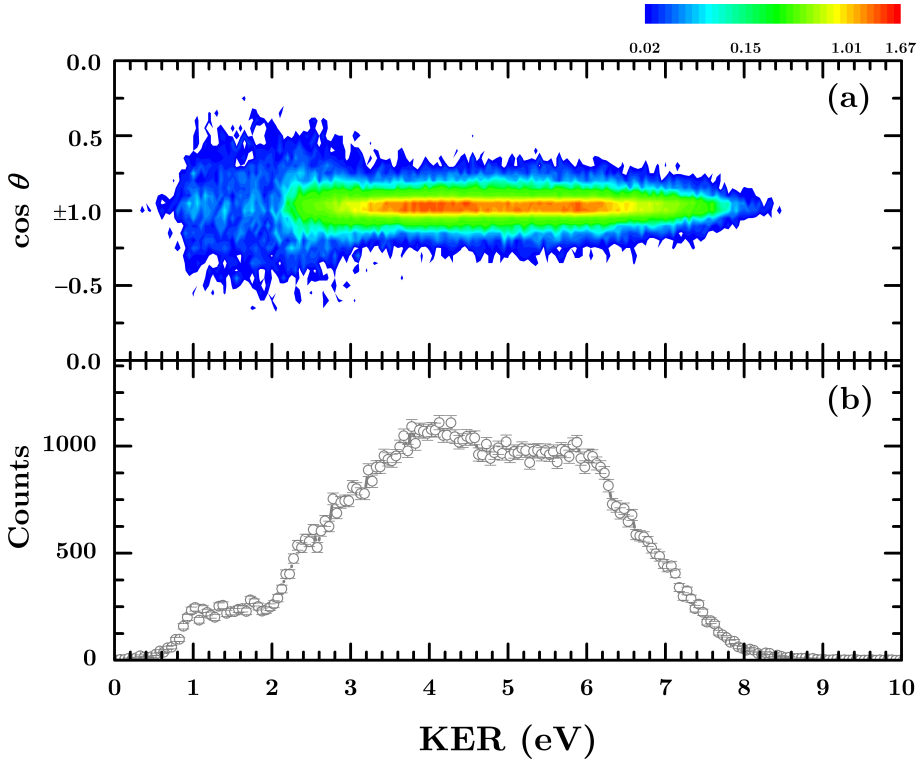

Figure 3.40: (a) Density plot of counts vs. KER and cosθ for HD^+ ionization at 790 nm, 25 fs, and a peak intensity of $\sim 1.3\times10^{14}$ W/cm^2 (log scale). (b) A histogram of counts vs. KER for the same laser parameters integrated over all angles. Error bars denote statistical uncertainty. Color bar numbers are written in powers of ten.

Typical KER and angular distribution spectra for HD^+ ionization are shown in Fig. 3.40(a) using 25 fs laser pulses with a peak intensity of $\sim 1.3\times10^{14}$ W/cm^2. Figure 3.40(b) shows the KER distribution integrated over all angles. This result resembles the structures observed in Ref. [226], however, the intensity and pulse durations are different. In the present experiment, 25 fs pump and probe pulses with intensities of 1.4×10^{12} W/cm^2 and 1.3×10^{14} W/cm^2, respectively, are employed. Figure 3.41(a) is the density plot of measured KER for ionization of HD^+ as a function of time delay between a weak pump and a strong probe laser pulse. The pump-probe scan reveals a weak dependence on time delay. To better explore the ATCE model, the effect of the probe laser pulses is subtracted from the map as displayed in Fig. 3.41(b).

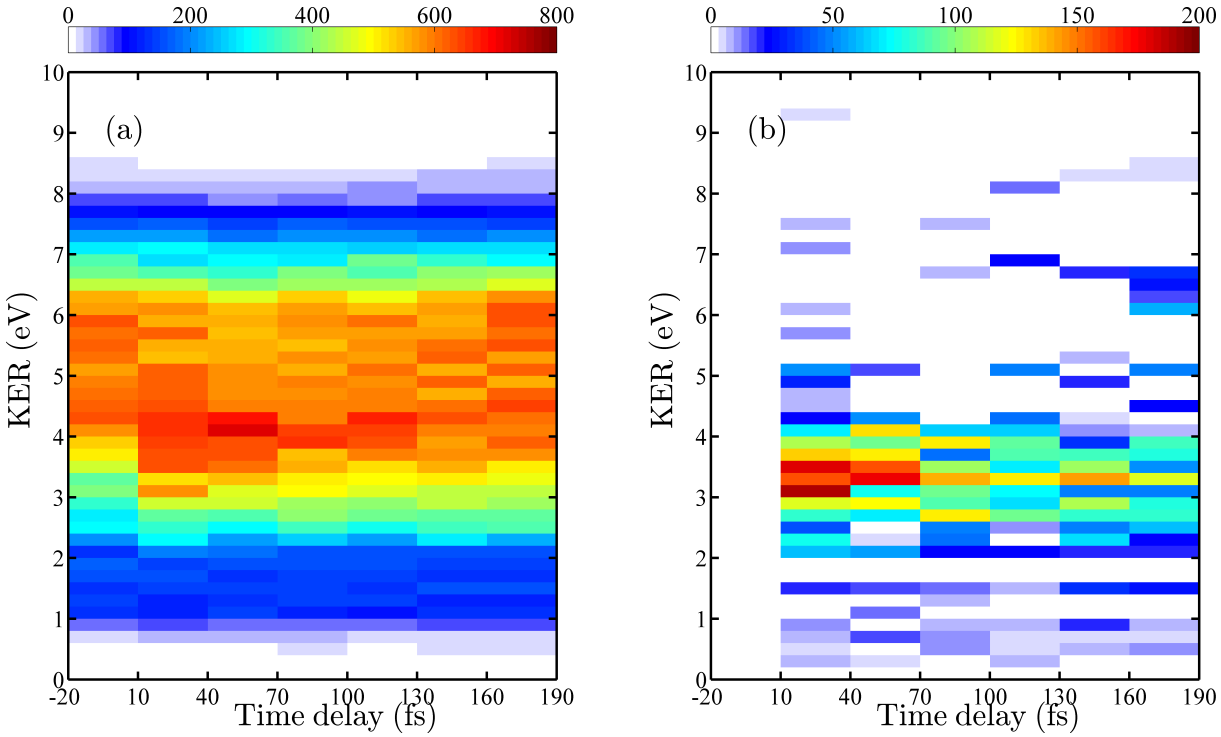

Figure 3.41: (a) Density plot of counts vs. KER and the delay time between the pump and probe laser pulses for HD^+ ionization. The peak intensities of the pump and the probe pulses are $\sim 1.4\times10^{12}$ W/cm^2 and $\sim 1.3\times10^{14}$ W/cm^2, respectively. (b) Density plot of counts vs. KER and the delay time between the pump and probe laser pulses for HD^+ ionization after subtracting the probe laser pulses.

The first two crossings between dissociation through 1ω bond softening and $1/R$ curves occur at ~ 10 and ~ 27 fs in the HD^+ molecule. Experimentally, we are not able to resolve these two crossings, since we were using 25 fs pulses and for other technical reasons were unable to run with shorter pulses. Crossing at a larger internuclear distance, $R\sim 50$ *a.u.*, estimated to occur at 160 fs, results in an enhancement in the ionization yield at the KER below 3.0 eV. However, our measurements do not show such an enhancement at larger time delay. Given the poor statistics of the current measurement, we were not able to accomplish our goal of exploring the ATCE model in HD^+. However, we have taken a major stride forward by demonstrating the feasibility of performing a pump-probe study on a thin molecular ion-beam target. This measurement remains challenging due to the low rate in this ionization channel (1–2 Hz using a 10 kHz laser system) and the low target density of the ion-beam.

3.7.4 Summary

In this section we have implemented a pump-probe scheme to explore the nuclear dynamics in both dissociation and ionization of a molecular ion-beam target. Both examples demonstrate the feasibility of such an experiment and identify the difficulties caused mainly by the low target density. By increasing the scan range of time delays in the dissociation experiment and treating the problem theoretically, we should be able to extract information about the nuclear dynamics of the system. In contrast, studying the ATCE in the ionization of HD^+ is still limited by the counting rate.

Our group is currently working on improving the target density using two different approaches. In the first approach, the target density is improved by bunching the molecular beam. In this case, a portion of the continuous ion-beam is compressed in space by using a pulsed electric field synchronized with laser pulses. The goal is to achieve a factor of 10 gain in the beam current density. In the second approach, our group is assembling a new ion source (duoplasmatron), which is expected to provide higher current densities, thus improving our future measurements significantly.

Chapter 4

Carrier-Envelope Phase Dependences of D_2 Dissociation into Rydberg Deuterium Fragments

Contents

4.1 Introduction

The first measurement demonstrating carrier-envelope Phase (CEP) control on the dissociation of a diatomic molecule was reported by Kling *et al.* [80]. Specifically, the emission direction of D^+ ions was controlled using a few femtosecond CEP-stabilized laser pulse. This experiment illustrates the ability to control electronic motion in molecules by employing CEP-stabilized laser pulses. The observation shows an asymmetry in the emission direction of energetic D^+ ions emerging from

D_2 molecules, which depends on CEP. The results were explained using the electron-recollision process [77, 80]. However, the experiment done by Kling *et al.* left several questions unanswered, which were later investigated by others. For instance, does the first ionization step play an important role in the asymmetry? Why is there no asymmetry for the low energy D^+ ions, despite the prediction by earlier theoretical calculations [76, 230]? Can one use the carrier envelope phase of laser pulses as a control knob in more complex molecules? Some of these questions were answered by the follow-up experiment carried out by Kremer *et al.* [83]. They observed asymmetric proton emission at low KER, which was predicted by Roudnev and Esry [76, 230]. Furthermore, CEP has been used to control electronic and nuclear dynamics in more complex diatomic molecules, such as carbon monoxide [84, 344, 345] and DCl [346], and small polyatomic molecules [285, 347].

Recently, the CEP dependence of dissociating molecules was studied both experimentally and theoretically in great detail for an ion-beam target [89, 90]. In these experiments, the H_2^+ target is prepared through electron-impact ionization in an ion source. The ion-beam target has a well defined initial vibrational population following a Franck-Condon distribution [211]. Experiments performed on the neutral target also assume a Franck-Condon initial distribution of the intermediate H_2^+. However, the measured vibrational population of H_2^+ produced by a laser favors the lower vibrational states rather than the Franck-Condon distribution [223], for some experimental conditions. Moreover, the necessity of modeling the laser-induced ionization step is crucial as it cannot be solved exactly for strong laser fields. State-of-the-art H_2^+ calculations including nuclear rotation and intensity averaging [253, 324] can be used to describe experimental findings from H_2^+ molecular-ion beams. The asymmetry observed in the low energy fragments from dissociation of H_2^+ is in agreement with theoretical calculations performed for the experimental conditions. More details can be found in Refs. [89, 90].

4.1.1 Theory

In order to understand the experimental results presented in this chapter, a brief description of the general theory developed by Esry and coworkers [111, 112] would be beneficial. The material presented in this section is adapted from the Hua and Esry [112] two-channel model, which has a

simple derivation. Although this model is not directly applicable to our experiment, it gives insight into the origin of the observed CEP dependences. In this model, the time-dependent Schrödinger equation (TDSE) is solved numerically in the Born-Oppenheimer representation by including the two lowest electronic states, $1s\sigma_g$ and $2p\sigma_u$, of H_2^+. The molecular axis is fixed parallel to the laser polarization to simplify the calculations. The details of such a calculation are given in Ref. [111, 112]. The total Hamiltonian of a system can be written as $H(\varphi;t) = h_0 + V(\varphi;t)$, where h_0 is the field-free Hamiltonian and the laser-matter interaction is $V(\varphi;t) = -\boldsymbol{d}\cdot\boldsymbol{E}(t)\cos(\omega t+\varphi)$, where $\boldsymbol{E}(t)$ is the laser pulse envelope, ω is the carrier frequency, and φ is the CEP. The electric field is periodic in φ which results in a periodic Hamiltonian. As a result the wavefunction of the system is periodic in φ. Therefore, the nuclear wavefunction can be expanded in a Fourier series in terms of the CEP, φ.

$$\boldsymbol{F}(R,t) = \sum_{n=-\infty}^{\infty} e^{in\varphi}\boldsymbol{F}_n(R,t). \tag{4.1}$$

Here n is the net number of photons. The amplitudes $\boldsymbol{F}_n(R,t)$ can be rewritten as

$$\boldsymbol{F}_n(R,t) = e^{-in\omega t}\boldsymbol{G}_n(R,t). \tag{4.2}$$

By substituting these expressions into the Schrödinger equation, one can find an equation independent of CEP, which means that it is sufficient to solve the TDSE once to get the whole CEP dependence. There is no approximation used in obtaining this equation, and it can be generalized to any system. The amplitudes $\boldsymbol{G}_n$ can be read as n-photon amplitudes; more details are given in Refs. [111, 112]. In the case of H_2^+, the difference between dissociating on the gerade $1s\sigma_g$ and ungerade $2p\sigma_u$ states will define the asymmetry. To calculate the observables such as asymmetry and total dissociation yield we can calculate the dissociation probability on atomic channels A and B. For a given momentum, k, the dissociation into these different atomic channels can be labeled as $|A\,k\rangle$ and $|B\,k\rangle$, which represent the p+H and H+p channels, respectively. These states can be written asymptotically as a superposition of outgoing plane waves, $|g\,E\rangle$ on the gerade $1s\sigma_g$ state

and $|u\,E\rangle$ on the ungerade $2p\sigma_u$ state,

$$|(A,B),k\rangle = \frac{1}{\sqrt{2}}(e^{-i\,\delta_g}|g\,E\rangle \pm e^{-i\,\delta_u}|u\,E\rangle), \tag{4.3}$$

where $\delta_{g,u}$ are the energy-dependent scattering phase shifts and $|g\,E\rangle$ and $|u\,E\rangle$ are the energy-normalized gerade and ungerade eigenstates, respectively. The dissociation probability for being on either channel can be found by projecting the wavefunctions onto the localized states

$$\frac{dP_{A,B}}{dE} = |\langle(A,B),k|F\rangle|^2 = \frac{1}{2}\left|\sum_{n\,\text{even}} e^{in\varphi}e^{i\delta_g}\langle gE|F_n\rangle \pm \sum_{n\,\text{odd}} e^{in\varphi}e^{i\delta_u}\langle uE|F_n\rangle\right|^2. \tag{4.4}$$

We can follow the derivation of Esry and coworkers in the supplementary material of Ref.[89] and Ref. [253] to write the full-dimensional (including nuclear rotation) differential probability density per unit energy per unit angle for dissociating on an asymptotic curve,

$$\frac{\partial^2 P}{\partial\, E \partial\, \theta_k} = 2\pi\left|\sum_{\substack{J\ \text{even}\\ n\ \text{even}}} C_{nJg}Y_{J0}(\theta_k)e^{in\varphi} + \sum_{\substack{J\ \text{odd}\\ n\ \text{odd}}} C_{nJu}\,Y_{J0}(\theta_k)\,e^{in\varphi}\right|^2, \tag{4.5}$$

where $C_{nJp} = C_{nJp}(E) = (-i)^J e^{-i\delta_{Jp}}\langle EJ_p|F_{nJp}\rangle$ with $(p = g, u)$ and θ_k is the angle between k and the laser polarization direction. The partial wave expansion is used for a plane wave to write the differential probability in terms of spherical harmonics with initial state $M = 0$ [89, 253]. The $|F_{nJp}\rangle$ represent $1s\sigma_g$ and $2p\sigma_u$ wavefunctions with total orbital angular momentum J while $|EJp\rangle$ is the energy-normalized scattering state. It's important to note that the first term has even parity while the second term has odd parity.

4.1.1.1 Asymmetry and Yield

An experimental observable for D_2 dissociation is the momentum distribution of D^* fragments. Other observables like kinetic energy release (KER) distributions can be extracted from the momentum distribution, which will be discussed later. From the momentum or KER we can calculate the new observables such as asymmetry and yield. These observables will be the main focus of our discussion later on. In the experiment, the asymmetry is defined as the difference between the number of D^* fragments emitted to the left and the right direction, determined by whether $\cos\theta_k$

is positive or negative, respectively. In the theory we can write the dissociation probability for going to the left or right as

$$\left.\frac{\partial^2 P}{\partial E \partial \theta_k}\right|_{L,R} = 2\pi \left| \sum_{\substack{J \text{ even} \\ n \text{ even}}} C_{nJg} Y_{J0}(\theta_k) e^{in\varphi} \pm \sum_{\substack{J \text{ odd} \\ n \text{ odd}}} C_{nJu}\, Y_{J0}(\theta_k)\, e^{in\varphi} \right|^2 , \tag{4.6}$$

and the asymmetry is

$$\begin{aligned} \mathcal{A}(KER,\varphi) &= \int_0^{\pi/2} \left.\frac{\partial^2 P}{\partial E \partial \theta_k}\right|_L d\theta_k - \int_{\pi/2}^{\pi} \left.\frac{\partial^2 P}{\partial E \partial \theta_k}\right|_R d\theta_k \\ &= 4\pi \mathrm{Re} \sum_{\substack{J \text{ even} \\ n \text{ even}}} \sum_{\substack{J' \text{ odd} \\ n' \text{ odd}}} C^*_{n'J'u} C_{nJg} e^{i(n-n')\varphi} \left[\int_0^{\pi/2} Y_{J'0} Y_{J0} d\theta_k - \int_{\pi/2}^{\pi} Y_{J'0} Y_{J0} d\theta_k \right]. \end{aligned} \tag{4.7}$$

The yield is defined as the total dissociation probability represented by $\mathcal{P}(KER,\varphi)$,

$$\begin{aligned} \mathcal{P}(KER,\varphi) &= \int_0^{\pi/2} \left.\frac{\partial^2 P}{\partial E \partial \theta_k}\right|_L d\theta_k + \int_{\pi/2}^{\pi} \left.\frac{\partial^2 P}{\partial E \partial \theta_k}\right|_R d\theta_k \\ &= 2\pi \sum_{\substack{J \text{ even} \\ n \text{ even}}} |C_{nJg}|^2 \left[\int_0^{\pi/2} |Y_{J0}|^2 d\theta_k + \int_{\pi/2}^{\pi} |Y_{J0}|^2 d\theta_k \right] \\ &+ 2\pi \sum_{\substack{J \text{ odd} \\ n \text{ odd}}} |C_{nJu}|^2 \left[\int_0^{\pi/2} |Y_{J0}|^2 d\theta_k + \int_{\pi/2}^{\pi} |Y_{J0}|^2 d\theta_k \right] \\ &+ 4\pi \mathrm{Re} \sum_{\substack{J \text{ even} \\ n \text{ even}}} \sum_{\substack{J' \text{ even} \\ n' \text{ even}}} C^*_{n'J'g} C_{nJg} e^{i(n-n')\varphi} \left[\int_0^{\pi/2} Y_{J'0} Y_{J0} d\theta_k + \int_{\pi/2}^{\pi} Y_{J'0} Y_{J0} d\theta_k \right] \\ &+ 4\pi \mathrm{Re} \sum_{\substack{J \text{ odd} \\ n \text{ odd}}} \sum_{\substack{J' \text{ odd} \\ n' \text{ odd}}} C^*_{n'J'u} C_{nJu} e^{i(n-n')\varphi} \left[\int_0^{\pi/2} Y_{J'0} Y_{J0} d\theta_k + \int_{\pi/2}^{\pi} Y_{J'0} Y_{J0} d\theta_k \right]. \end{aligned} \tag{4.8}$$

Expressions (4.7) and (4.8) show some interesting features. The CEP dependence in the asymmetry originates from the interference between n-photon pathways ending up with the same final energy in the same θ_k integration range with $\Delta n = n - n'$ being odd. In contrast, the CEP dependence of the total dissociation yield emerges from the interference of distinct n-photon pathways with $\Delta n = n - n'$ being even. The lowest order asymmetry will happen between pathways differing by only one photon while higher order behavior can not be ignored. The normalized asymmetry can

be written as a series of $\cos(\Delta n\varphi)$ function as follows,

$$\begin{aligned}\frac{\mathcal{A}(KER,\varphi)}{\langle\mathcal{P}(KER,\varphi)\rangle_\varphi} &\equiv \frac{1}{\langle\mathcal{P}(KER,\varphi)\rangle_\varphi}\sum_{\Delta n=1,3,5,\ldots}^{\infty} a_{\Delta n}\cos(\Delta n\varphi+\varphi_{\Delta n}) \\ &= \frac{1}{\langle\mathcal{P}(KER,\varphi)\rangle_\varphi}(a_1\cos(\varphi+\varphi_1)+a_3\cos(3\varphi+\varphi_3)+\ldots),\end{aligned} \tag{4.9}$$

where $\Delta n = n - n'$ is the difference between the net number of photons of the two pathways involved in the interference, $\langle\mathcal{P}(KER,\varphi)\rangle_\varphi$ is defined as $\int_0^{2\pi}\mathcal{P}(KER,\varphi)d\varphi$, $a_{\Delta n}$ is the asymmetry amplitude for a given Δn channel, and $\varphi_{\Delta n}$ is an offset phase.

The total dissociation yield, $\mathcal{P}(KER,\varphi)$, can be simplified in a similar manner as a linear combination of $\cos(\Delta n\varphi)$ terms divided by a φ-independent term.

$$\begin{aligned}\frac{\mathcal{P}(KER,\varphi)}{\langle\mathcal{P}(KER,\varphi)\rangle_\varphi} &\equiv 1+\frac{2}{\langle\mathcal{P}(KER,\varphi)\rangle_\varphi}\sum_{\Delta n=0,2,4,\ldots}^{\infty} a_{\Delta n}\cos(\Delta n\varphi+\varphi_{\Delta n}) \\ &= 1+\frac{2}{\langle\mathcal{P}(KER,\varphi)\rangle_\varphi}(a_2\cos(2\varphi+\varphi_2)+a_4\cos(4\varphi+\varphi_4)+\ldots).\end{aligned} \tag{4.10}$$

In the case of H_2^+ interacting with a laser, part of the population can be transferred from $1s\sigma_g$ to $2p\sigma_u$ by absorption of three photons (n=3) following the dipole-selection rules. This population can dissociate through $2p\sigma_u$ and is referred to as above-threshold dissociation(ATD) [31, 32, 36, 200, 237]. During this process a part of the population can be moved to $1s\sigma_g - 2\omega$ by stimulated emission of a photon. This will result in dissociation on $1s\sigma_g$ with n'=2. One would expect to observe a CEP dependent asymmetry as a result of interference between these two channels with $\cos(\varphi)$ oscillation. Recently, these interferences have been observed experimentally and compared with theoretical predictions quantitatively for a H_2^+ ion-beam target [89, 90].

For H_2^+, the $\cos(2\varphi)$ oscillation in the dissociation yield, $\mathcal{P}(KER,\varphi)$, is originated from interference between net zero-photon dissociation on $1s\sigma_g$ and the net two-photon dissociation on $1s\sigma_g$. To acquire such an interference effect, we need to ensure that the bandwidth of the laser can support an overlap between the KER from n=0 and n'=2. However, this simplistic picture might not hold in a multiphoton regime in which the system can absorb and emit many photons. In this regime, the KER peaks are strongly distorted and the overlap between the KER peaks from the net 0 and net 2 photon pathways can result in yield oscillation due to the shift and broadening in

KER distributions.

From the discussion above, we can conclude a few important points. The formalism presented here is general, and it can be extended to more complex systems. By measuring the asymmetry and yield dependences on CEP for a given system, one can find the net number of photons involved in the interference process. This can be done through a Fourier transform analysis as Δn and φ are conjugate variables.

As mentioned earlier, a large spectral bandwidth is necessary to observe such a pathway interference. A small number of cycles or a short laser pulse duration are not essential for observing interference effects. We will show that a 21 fs laser pulse chirped from a 5 fs FTL pulse can be used to observe asymmetry in the dissociation of D^* fragments. Lastly, the higher-order effects are expected to appear at high intensity with a large bandwidth, which will be discussed in more detail later in this chapter.

4.1.2 Singly- and Doubly-Excited States of H_2

Dissociation and ionization of the simplest diatomic molecule, H_2^+, has been studied extensively in recent decades [26, 31, 32, 200, 237]. Studying wave-packet dynamics in the dissociation of H_2^+, by employing methods such as pump-probe spectroscopy, has made it possible to observe the vibrational motion of the molecules [315, 327]. However, the neutral parent molecule, H_2, is far more challenging to study both theoretically and experimentally. This molecule is a good candidate for studying electron-electron correlation and its coupling to nuclear motion. The manifestation of electron-electron correlation is evident in the production of the doubly-excited molecule, H_2^{**}, in which both electrons are excited with the same laser pulse.

The potential energy curves (PEC) of some doubly-excited states of H_2 are shown in Fig. 4.1. These doubly-excited states, labeled as the Q_1 and Q_2 series, lie above the first and second ionization threshold of H_2, where the Q_1 states are built on the first excited state of H_2^+, $^2\Sigma_u^+\,(2p\sigma_u)$, and the Q_2 states are built on the second excited state of H_2^+, $^2\Pi_u\,(2p\pi_u)$ [348].

A large number of calculations were performed for the energy levels of doubly-excited states of H_2 and their resonance widths [349–353]. One of the early attempts at calculating potential

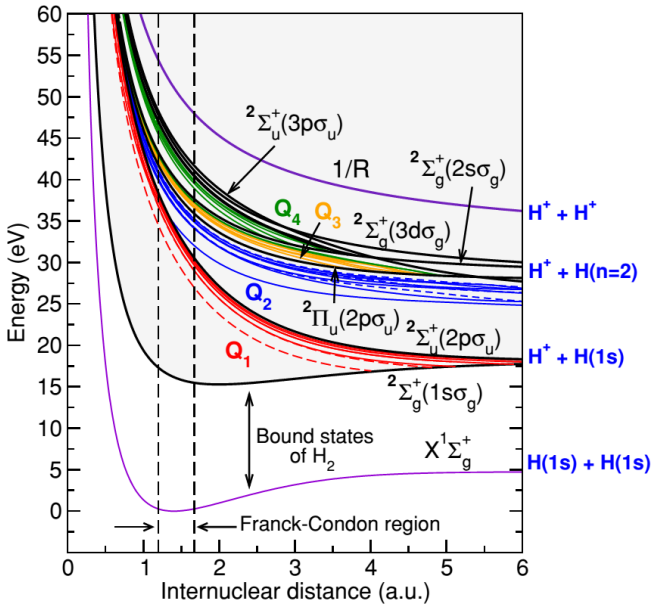

Figure 4.1: Potential energy curves of H_2 and H_2^+ showing some of the doubly-excited Q states. Thin dashed curves: Q states of $^1\Sigma_u^+$ symmetry; thin continuous curves: Q states of $^1\Pi_u$ symmetry. Thick curves: H_2^+ states. The PECs were adapted from Bozek *et al.* [354].

energy curves, resonance widths, and dipole transition moments from the ground state of H_2 to the Q_1 states was performed by Bottcher and Docken [349]. Guberman performed calculations on several Q_1 and Q_2 singlet and triplet doubly-excited potential energy curves using a configuration interaction (CI) method [350]. More recently, Fernández and Martín computed energies and resonance widths of these states based on the Feshbach method, which involves L^{2}B-spline functions as a basis set for molecular continuum states [351–353].

In a diabatic picture, the Q_1 and Q_2 doubly-excited states have $2p\sigma_u(nl\lambda)$ and $2p\pi_u(nl\lambda)$ configurations and are embedded in the ionization continuum, as shown in Fig. 4.1. The Q_1 states are sometimes referred to as autoionizing states. These states have a finite lifetime, i.e. the molecule ejects an electron into the $1s\sigma_g$ continuum due to the resonances [355]. These autoionizing states can lose their autoionizing character at large internuclear distances, $R \gtrsim 4$ a.u. [353]. Q_1 states cross the $1s\sigma_g(nl\lambda)$ Rydberg series and dissociate into two neutral fragments, H($1s$)+ H($n'l'$) with $n' \geq 2$ (see Fig. 4.2), while Q_2 states can dissociate into H($2l'$)+ H($n'l'$) at large internuclear distances. The autoionization time of these doubly-excited states of H_2^{**} are calculated as a function

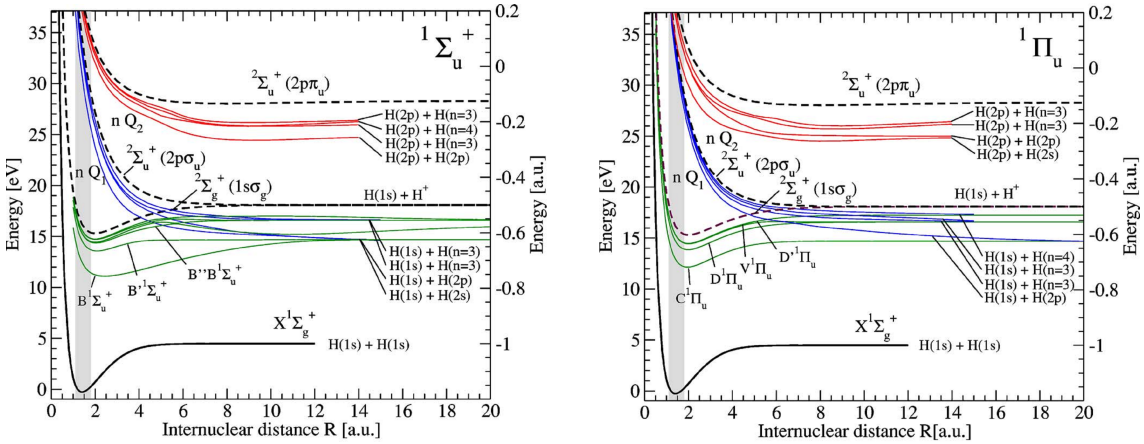

Figure 4.2: (color lines) Potential energy curves of Q_1 and Q_2 $^1\Sigma_u^+$ and $^1\Pi_u$ states of H_2. The ground state of H_2 is depicted as a solid black line. The ground state and 1st excited state of H_2^+ are shown as dashed lines. The Franck-Condon region is shaded with a vertical band. The dissociation limits for the first four Q_1 and Q_2 states in each symmetry are labeled. The $1s\sigma_g(nl\lambda)$ Rydberg series are depicted as green solid line and dissociate into two neutral fragments. The electronic PECs were obtained from José Luis Sanz-Vicario *et al.* [368].

of internuclear distance by Sánchez and Martín [352, 356]. The lifetimes of higher Q_1 states drop significantly at larger internuclear distances ($R \gtrsim 4$ a.u.). Q_3 and Q_4 are the higher doubly-excited states and will not be discussed here. To distinguish the doubly-excited states with the same symmetry, a convention has been used such that the lowest state in the Q_1 series is labeled as $Q_1\,^1\Pi_u(1)$ while the second lowest state can be written as $Q_1\,^1\Pi_u(2)$ and so on [350].

The coupling between the doubly-excited states and the $1s\sigma_g(nl\lambda)$ Rydberg series plays a crucial role in the dissociation of H_2 into two neutral hydrogen atoms [357, 358]. Dissociation into neutral fragments on Q_1 states can compete with the autoionization process. The autoionization lifetimes of some of these Q_1 states are larger than the dissociation times, and therefore they can dissociate diabatically producing two neutral fragments. The lowest Q_1 state makes the main contribution in the autoionization process, while the higher doubly-excited states in the Q_1 series dissociate to neutral fragments [359]. High kinetic energy H($2s$), H($n = 3, 4$ and higher) fragments [358, 360–365] have been observed in electron-impact dissociation of H_2 as well as in photodissociation studies [366, 367].

Recently, doubly-excited levels of hydrogenic molecules have been investigated both experimen-

tally and theoretically [87, 354]. In these studies, photons with a well defined energy are employed to excite the molecules directly into a doubly-excited state. In the case of the hydrogen molecule, an incident photon energy of about ∼26 eV is needed to access the lowest lying doubly-excited Q_1 states [354]. Photodissociation of hydrogen molecules was first studied at the synchrotron facilities, at which a well defined photon energy was attainable [369]. However, nowadays other light sources are available for experiments on singly- and doubly-excited states such as free electron lasers (FELs) and high-harmonic generation (HHG) sources [87, 369]. In addition, *ab initio* calculations of the dissociation process via autoionization of Q_1 and Q_2 states in a XUV-IR pump-probe manner have been studied and compared to the experimental results with qualitative agreement [87]. Most of the recent studies are focused on detecting a charged fragment resulting from the autoionization of doubly-excited states in an H_2 molecule populated by a well defined single photon provided by a synchrotron or HHG source.

4.1.2.1 Pathway Leading to H^*

Fragmentation of H_2 and its isotopologues in an intense laser field through multiphoton processes is still under investigation. The multiphoton processes involved in dissociation as well as a large number of potential energy curves (PEC) result in complicated theoretical treatments. The theoretical approach needs to consider the correlated motion of strongly interacting particles. In this chapter, we will explore the production of excited neutral fragments from H_2 interacting with CEP-tagged few-femtosecond laser pulses. Here is the list of possible processes through which excited neutral fragments can be produced:

$$H_2 + n\hbar\omega \rightarrow H_2^* \rightarrow H(1) + H(n), \tag{4.11}$$

$$\rightarrow H_2^{+*} + e^- \rightarrow H(n) + H^+ + e^-, \tag{4.12}$$

$$\rightarrow H_2^{**} \rightarrow H_2^{+*} + e^- \rightarrow H(n) + H^+ + e^-, \tag{4.13}$$

$$\rightarrow H(n) + H^+ + e^-, \tag{4.14}$$

$$\rightarrow H(n) + H(n'). \tag{4.15}$$

The first process corresponds to the production of a singly-excited molecule, which can dissociate into two neutral fragments, one excited and the other in its ground state. The 2$^{\text{nd}}$ process, (4.12), is a multiphoton ionization leading to an excited state of H_2^+, which consequently breaks into an excited neutral fragment and a proton. The last process, (4.13–4.15), will produce a doubly-excited H_2 molecule [354], which can either autoionize and dissociate or directly dissociate into several possible fragments as listed above. Some of these processes and their related dissociation outcomes are labeled on the PECs shown in Fig. 4.1. The vertical dashed lines represent the "Franck-Condon" region in which the molecular target can go through a vertical transition [370]. As shown in Fig. 4.1, these doubly-excited PECs are strongly repulsive in the Franck-Condon region producing "fast" fragments, although dissociation through the Rydberg series below the H_2^+ ground state curve can also result in "slow" fragments.

The doubly-excited states embedded in the ionization continuum of the hydrogen molecule are also called Rydberg states [366]. We labeled the Rydberg states below $^2\Sigma_u^+(2p\sigma_u)$ as Q_1 states earlier. Some of these Rydberg states exist below the H_2^+ ground state, $^2\Sigma_g^+(1s\sigma_g)$ and are referred to as singly-excited states. Some of these Rydberg states are approximately a replica of the $1s\sigma_g$ PECs, as shown in blue for two different symmetries in Fig. 4.2. The lowest Q_1 state correlates with the $n = 2$ limit, H(1s)+H(2s, p), also illustrated in Fig. 4.2.

Previous theoretical studies on H_2 using photon energies of 25 to 36 eV predict populating the $Q_1\,^1\Sigma_u^+$ states, which subsequently autoionize to $1s\sigma_g$ and produce an ionic fragment with an energy range between 0 and 10 eV [354, 355]. In the experiment of Sansone *et al.*, H^+ fragments with energies ranging between 2–7 eV were measured [87]. In addition, Q_1 states can directly dissociate into the highly excited Rydberg levels with an energy of 7–10 eV per fragment. At photon energies of 31 eV and above, direct ionization to the $Q_2\,^1\Pi_u$ becomes possible resulting in higher fragment energies of 5–15 eV [87].

These "spaghetti-like" PECs are good candidates for studying interference through different dissociation pathways. We chose this simple diatomic molecule with a complicated structure to examine the general theory of CEP dependences developed by Esry and coworkers [111, 112, 253].

The general theory of CEP effects predicts the oscillation of an experimental observable such as asymmetry or yield through interference of different dissociating pathways. One would expect to extract photon pathway information without a prior knowledge of the exact pathway involved in the process. A laser-induced dissociation of D_2 provides an excellent test bed for the general theory that was introduced in an earlier section.

4.1.3 Goals

In the measurements presented in this chapter, control via the CEP is investigated by observing asymmetry in the excited fragment direction from dissociated D_2 molecules. Oscillation in the total dissociation yield is also reported. A general theory of CEP dependences, developed by Esry and coworkers, attributes these oscillations to interference of dissociation pathways involving a different net number of photons [111, 112]. The complexity that arises from the density of Rydberg states of the D_2 molecule can be a good test bed to study CEP control in laser-induced dissociation of D_2 into excited D^* fragments. We defined the goals of this study to be:

- Examine the theoretical prediction in a complex system such as the D_2 Rydberg series
  - Measure the asymmetry and yield CEP dependences
  - Study higher-order effects, *i.e.* larger Δn
- Study the importance of bandwidth vs. pulse duration on the CEP dependent asymmetry and yield
- Study state-selective CEP dependences

We find out that our experimental results are in good agreement with theoretical predictions for the periodicity observed in the asymmetry and yield as a result of interference between different photon pathways. We will discuss the Fourier analysis approach to extract information about higher-order photon pathways.

The theory developed by Esry and coworkers [111, 112] also predicts that the CEP effects depend on the laser bandwidth rather than the laser pulse duration or electric-field asymmetry [371].

To prove this point, we repeated our measurement of long-lived D^* fragments by chirping the FTL 5 fs laser pulses both positively and negatively. In the course of the present work, the asymmetry and yield oscillations are observed for chirped laser pulses of up to 8 cycles indicating the importance of spectral bandwidth.

In addition, by implementing a field ionization method, we were able to detect highly excited D^* fragments for a limited range of excited states. This allows for CEP control studies of small subsets of D^* states, i.e. Rydberg $D(nl)$ with principle quantum number n on the order of 19–44. The key findings will be discussed in section 4.3 after a brief description of the experimental method.

4.2 Experimental Method

Our goal is to measure the CEP dependence of D^* formation from D_2 molecules in intense 5 fs laser pulses. The laser pulses are characterized using an autocorrelator (see Section 2.5). For this purpose, short pulses are produced and the CEP for every laser shot is measured as discussed earlier in section 2.2.3. In addition to the D^* dissociation yield we are interested in the asymmetry, which is determined by measuring D^* fragments ejected in both directions along the laser polarization of the linearly polarized pulses.

4.2.1 Laser

The PULSAR Ti:Sapphire laser was used to produce pulses (centered at 785 nm with a bandwidth of 62 nm) with sub 25 fs duration and 2 mJ energy at 10 kHz, which in turn were used to generate the ultrashort laser pulses for this study. The details of this laser system are described in more detail in section 2.2 and thus only a brief summary is given here. The laser pulses are coupled into a hollow-core fiber (250 μm core diameter, 1 m long) using a 1.5 m focusing lens. The hollow-core fiber (HCF) is filled with 99.99% Argon to a pressure of 0.7 bar. The laser pulses are spectrally broadened through self-phase modulation (SPM) [372] with a bandwidth ranging from about 450 to 1000 nm. The measured spectrum is shown in Fig. 4.3 with a central wavelength of 730 nm. A set of negative chirped mirrors (7 pairs) are used to compensate for the positive dispersion caused

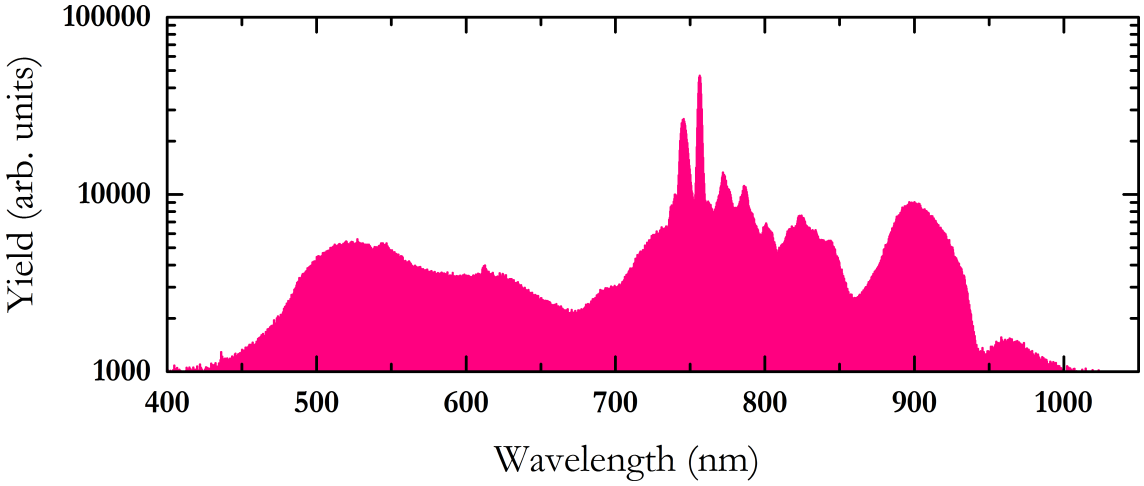

Figure 4.3: The broadened spectrum with central wavelength of 730 nm and pulse energy of 200 μJ generated using an Ar-filled hollow-core fiber. The spectrum is weighted by the spectrometer efficiency to estimate the central wavelength.

by propagation along the fiber and the other optics elements.

The laser pulses are focused on the effusive gas target of D_2 by a f=75 mm spherical mirror mounted inside the vacuum chamber on an XYZ manipulator. A laser beam will obtain a phase shift of π by propagating through a focus, which is denoted as the Gouy phase shift (sometimes called "the phase anomaly near focus") [373]. The Gouy phase shift for a laser beam propagating along the z direction is described by the expression:

$$\varphi(z) = -\arctan(\frac{z}{z_R(\lambda)}), \tag{4.16}$$

where z_R is the Rayleigh range, which depends on the wavelength λ [374]. The Rayleigh range is defined as the distance from the focus to the place where the beam area is doubled. The Gouy phase effect introduces a π shift in the CEP [374]. In order to minimize the Gouy phase shift for the CEP-tagged laser interacting with the D_2 gas target, the interaction region was set at 1 mm in front of the laser focus (twice our Rayleigh range). In addition, the larger interaction volume provides a higher count rate.

The laser pulses are chirped negatively after bouncing off of the chirped mirrors in order to compensate for the dispersion effect due to transmission of the entrance window of the experimental

apparatus. Thus, chirp compensation is essential in generating ultrashort laser pulses at the interaction region. This dispersion is fine tuned by introducing a pair of thin fused silica wedges before the experimental apparatus. By adjusting the thickness of the fused-silica wedges precisely, we can ensure that Fourier-transform limited (FTL) laser pulses are generated at the interaction. To do so, we maximized the relative yield of Ar^{2+} versus Ar^{+} generated from an Argon gas target in the TOF apparatus by using our Wiley-McLaren spectrometer [375].

To monitor the CEP of every laser pulse, we employed a single-shot stereographic above-threshold ionization (ATI) phase meter[1] [123, 192, 193]. The CEP of every laser shot is measured in conjunction with the fragmentation of molecules in the TOF apparatus. A broad bandwidth beamsplitter is used to separate the laser beam. A small portion (20% of the power) of the laser beam is then focused by a f=250 mm spherical mirror into a Xe-filled gas cell of the phase meter. Based on a classical model, there are two major mechanisms that generate an ATI spectrum [188, 376]. The electrons generated through the ionization process can be labeled as either direct or recollision electrons. The direct electrons exhibit a weak CEP dependence and can gain up to two times the pondermotive energy within the laser field. Pondermotive energy, U_p, is the cycle averaged kinetic energy of a free electron in the laser field which can be written as a function of laser intensity and the wavelength,

$$U_p[eV] = 0.09337\, I[\frac{W}{cm^2}]\, \lambda^2[m^2]. \tag{4.17}$$

A small fraction of the ionized electrons return and rescatter from the ionic core. These electrons can gain large kinetic energies, up to $10U_p$, and form a plateau in the high energy part of the ATI spectrum. These electrons are more sensitive to CEP while the direct electrons show smaller CEP sensitivity. The high energy ATI part of the spectrum is a good candidate for measuring CEP effects [122]. To determine the CEP, we record the TOF of electrons ionized from Xe gas and emitted in both directions along the laser polarization. The field-free TOF spectrometers are shielded by μ-metal around the entire path to reduce any stray magnetic field. The direct electrons carry smaller kinetic energy and can be blocked by introducing a negative voltage on the meshes

[1] We used the phase meter implemented by Nora G. Kling in our lab [178]

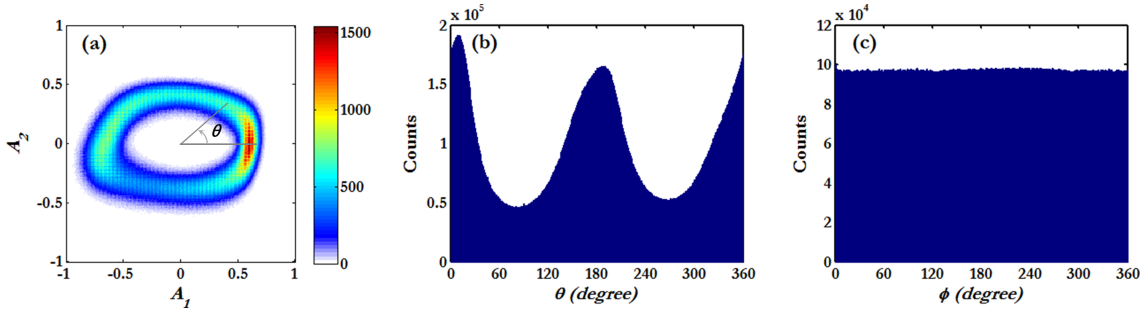

Figure 4.4: (a) The PAP measured for many laser shots (over 3 hours of free running laser) with 5 fs pulse duration, where θ here is related to φ through a linear transformation, (b) histogram of θ and (c) histogram of φ.

in front of each TOF detector (-28.0 Volts).

We quantify the CEP for every laser pulse by introducing an asymmetry parameter for a given electron energy region, $A = \frac{N_{left} - N_{right}}{N_{left} + N_{right}}$ in which N_{left} and N_{right} are the number of electrons emitted toward the left and right detector, respectively. The asymmetry is calculated for two energy regions. We then plot the asymmetry for one energy interval against the asymmetry for another, slightly higher, energy interval. This will result in a phase ellipse, which is commonly known as a "phase potato" or "parametric asymmetry plot" parametric asymmetry plot (PAP) [122, 123, 192, 193]. A typical PAP, from our measurements, is shown in Fig. 4.4(a). Each laser shot represents a point on this graph with a corresponding angle θ. The angle θ defined in Fig. 4.4(a), is directly related to the CEP φ, while the radius (distance from A_1, A_2 origin) is correlated with the amplitude of the asymmetry and the pulse duration [196].

To extract the CEP we need to transform the spectrum in Fig. 4.4(b) to a new angle, φ, for which a flat distribution is expected. This is based on the assumption that the CEP for a free running laser is randomly distributed over the course of the measurement. The details of this transformation are described elsewhere [178, 195]. Fig. 4.4(b,c) show the histogram for θ and φ, respectively. After the transformation, the CEP value for each laser shot is equal to the angle φ.

As explained earlier in section 2.5, there are several optical methods to characterize the pulse duration of ultrashort laser pulses. One of the practical methods is called interferometric autocorrelation. This method is based on a Mach-Zehnder interferometer in which the original laser pulse

interferes with a delayed copy of itself in a nonlinear medium, such as a BBO (Beta Barium Borate) crystal. We used our interferometric autocorrelator (FEMTOMETER^{TM} from FEMTOLASERS) to estimate the upper limit of the pulse duration to be 6 fs [162]. By taking the Fourier transform of the measured spectrum, we estimated the lower limit of the pulse duration to be 3 fs. One can use the radius of the PAP to estimate the pulse duration for every laser shot. However, this method requires calibration by means of another optical measurement such as SPIDER, which is described in Refs. [195, 196].

4.2.2 Fragmentation Imaging

This section describes the time-of-flight (TOF) apparatus used to measure the excited neutral fragments. In addition we will explain the method in which these fragments can be detected directly.

4.2.2.1 Apparatus

The experimental setup, shown schematically in Fig. 4.5, consists of two detectors facing each other with an effusive gas jet target in between them. The laser beam is focused onto the gas jet by a spherical mirror inside the vacuum chamber. The polarization of the laser is set parallel to the time-of-flight (TOF) axis of the apparatus. D^* fragments traveling to both sides are detected by the "left" and "right" detector as described below. This design is similar to the experimental arrangement used in Doppler-Free spectroscopy of several diatomic molecules, namely N_2^{++}, O_2^{++}, NO^{++} and CO^{++} [377–380]. In addition, this setup is similar to the Stereo-ATI phase meter described in section 2.6.

An effusive gas jet of atoms or molecules, D_2 in our case, is introduced into the setup via a hypodermic needle. The base pressure of the chamber is about 1×10^{-9} Torr without gas load, and it increases to 3×10^{-8} Torr by introducing a gas load of D_2 molecules. The target density is adjusted by using a leak valve, to ensure detection of 0.1-0.2 hits in every laser shot. This low detection probability reduces the chance of random coincidences. The system also includes a removable TOF spectrometer in a Wiley-McLaren configuration [375] as shown schematically

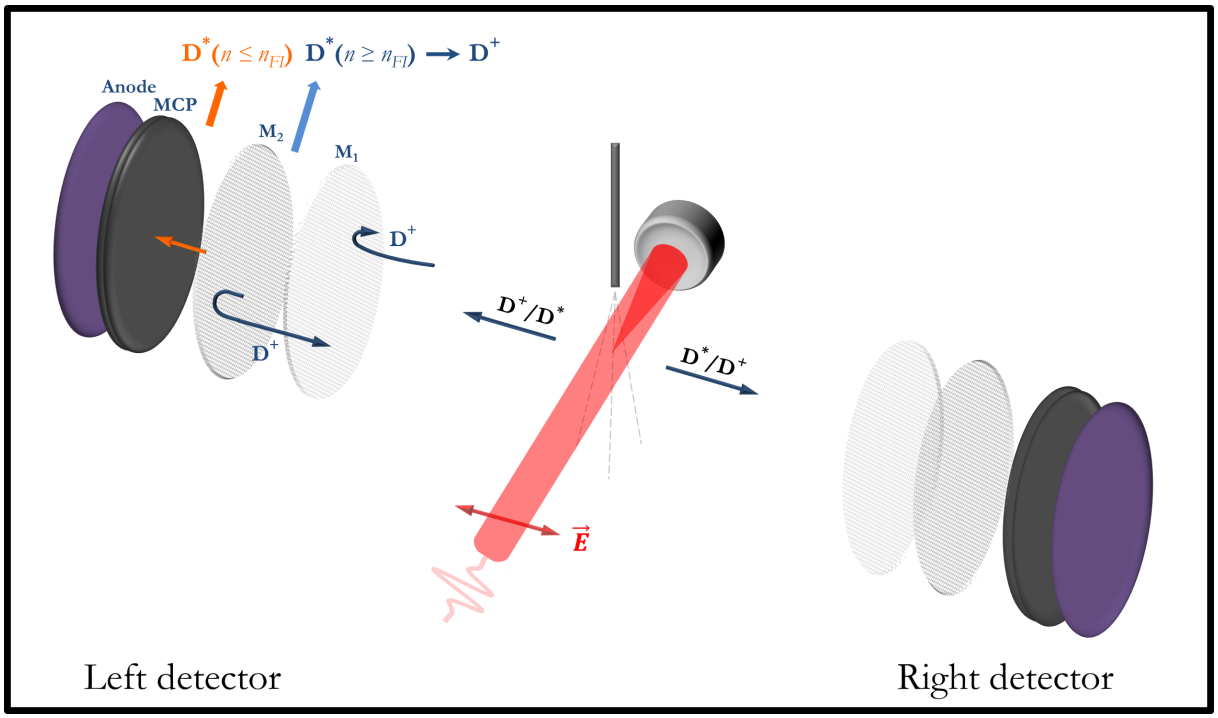

Figure 4.5: Schematic diagram of the time-of-flight apparatus. Located on the left is an MCP detector in a chevron configuration with a backgammon anode. The MCPs and anode are schematically shown as dark plates and labeled accordingly. There are two high transmission meshes in front of the detector, which are labeled as M_1 and M_2, respectively. The right detector is an equivalent detector with the same configuration. The laser beam is focused in the chamber by a spherical mirror. The target is injected through a hypodermic needle effusive gas-jet from the top as shown schematically in grey.

in Fig. 4.6. This allows us to measure ions for calibration purposes in this project, as described earlier. The spectrometer is made up of four parallel rings covered with high transmission meshes (90%). These parallel meshes define an interaction region from which the charged particles are extracted toward the detector. Subsequent acceleration and drift regions are used to focus all the charged particles from the interaction region in time. This spectrometer enables detection of charged particles on both detectors (namely left and right) by flipping the voltages.

4.2.2.2 Direct Detection of Excited Fragments - Field Ionization Method

It is more difficult to study laser-induced dissociation which results in neutral fragments, since the final products cannot be directed toward the detectors as is typically done with ions. As described earlier, the laser interacting with the hydrogen molecules produces a few excited neutral fragments.

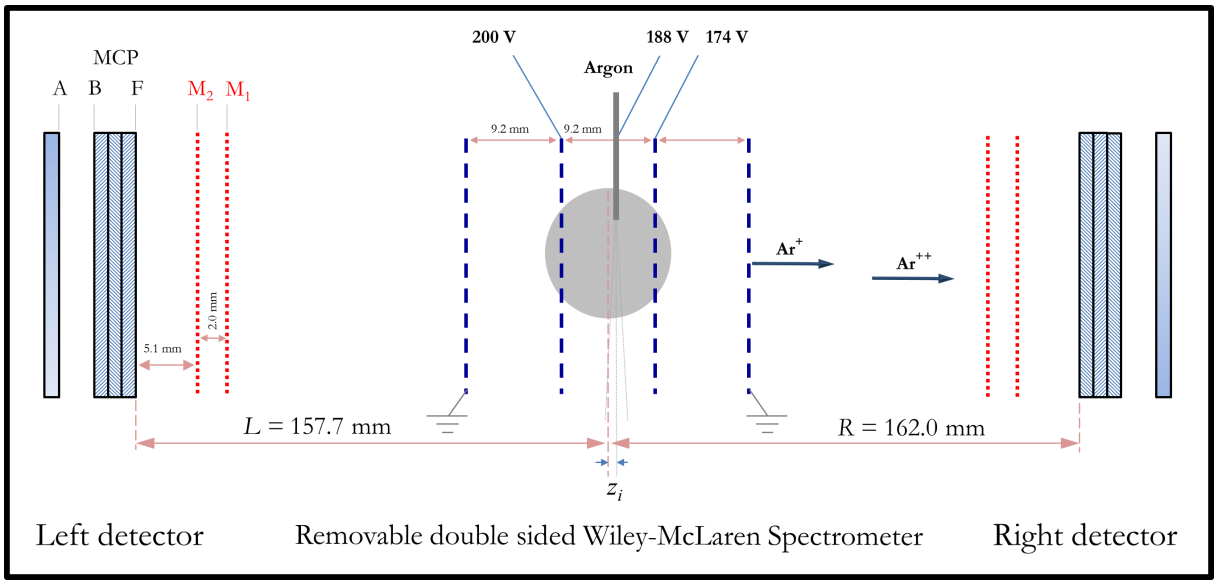

Figure 4.6: Side view of the apparatus with a double sided Wiley-McLaren time-of-flight spectrometer inserted for calibration measurements. The distances between different elements are shown on the figure.

These atomic fragments can be produced in low- or highly-excited Rydberg states with short and long lifetimes, respectively. In our setup it is possible to detect $H^*(n)$ species with a long lifetime as they carry enough potential energy to be detected by a conventional microchannel plate (MCP) detector. On the other hand, some of the $H^*(n)$ with small principal quantum number n are difficult to detect as they are mostly short-lived, and therefore these species will decay to $H(1s)$ before reaching the detector (except $H(2s)$, which can not decay to $H(1s)$ by emitting a single photon – although, $H(2s)$ can decay to $H(1s)$ by the emission of two photons, and the lifetime is about 1/7 of a second). Several methods exist for detecting such a short-lived Rydberg state, in which the fluorescence photon emitted from the excited fragments can be measured. More detail can be found in [358, 381–385] and references within.

There are two common ways, destructive and nondestructive, to measure the long-lived Rydberg states of atoms and molecules. In the nondestructive method, introduced by Mohapatra *et al.* [386], the highly excited Rydberg states (up to $n = 124$) are detected optically using electromagnetically induced transparency electromagnetically induced transparency (EIT). Another method to detect Rydberg states is to apply a static electric field on the system of interest, commonly known as

the field ionization method [387]. In a highly excited Rydberg state, the electron is loosely bound, so by applying a weak electric field the target atom can be ionized. The ions or the electrons produced through field ionization can be detected using conventional methods, such as standard MCP detectors.

By employing the field ionization method one can select different subsets of the principle quantum numbers, n, by adjusting the electric field strength. For instance, the electric field that can ionize fragments in the Rydberg state n_{FI} will ionize all fragments with $n \geq n_{FI}$ with a probability close to unity. The ionization probability for a hydrogen atom in a static electric field, calculated classically by Rakovic and Chu [388], is plotted in Fig. 4.7(a). The figure shows the results for treating the hydrogen atom as a two-dimensional or three-dimensional system (see Ref. [388] for more details). The calculations are in qualitative agreement with previous experimental studies [389, 390]. We used the 3D result to estimate the electric field strength needed to field ionize a subset of n states and perform a state-selective CEP dependence measurement.

In Fig. 4.7(b), the electric field strength is plotted as a function of principle quantum number n for which the probability of ionization for a hydrogen atom in a static electric field is 0.5 (solid line) or between 0.1 to 0.9 (shaded area). We used that as an estimate for $n \geq n_{FI}$, as for most n above n_{FI} the field ionization probability is close to unity. As seen in Fig. 4.7(b), a few hundred volts per cm is sufficient to field ionize a hydrogen atom with $n \simeq 44$ and above. For this purpose, a pair of uniform high transparency meshes (90%) are placed in front of each detector labeled M_1 and M_2 as shown in Fig. 4.5. By applying a strong uniform static electric field between the two meshes the excited D^* fragments with principle quantum number $n \geq n_{FI}$ are field ionized with probability close to unity as described earlier. The resulting ions, D^+, are now rejected by applying a higher positive potential on the 2^{nd} mesh, M_2, and the remaining $D^*(n \leq n_{FI})$ are detected by the MCP detectors. It is also possible to set the potentials to measures both ions and the remaining D^*.

As discussed above, we can control the excited fragment states of the $D^*(n \leq n_{FI})$ arriving at the detector by the choice of the M_1 and M_2 potentials. These excited D^* fragments are measured by the detector through field ionization within the MCP channels. Alternatively, these fragments

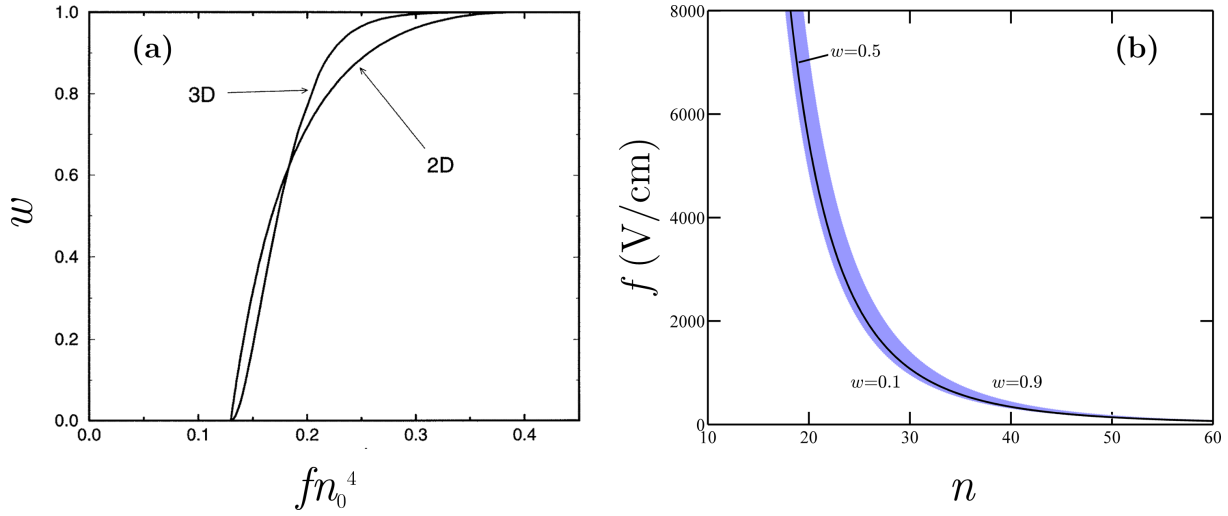

Figure 4.7: (a) Probability of ionization, w, for a hydrogen atom in a static field with intensity f is plotted as a function of the parameter fn_0^4, where n_0 is an initial principal quantum number. This calculation is performed for a classical hydrogen atom in 2D and 3D [388]. All quantities are given in atomic units. (b) Electric field strength, f, for probability of ionization to be 0.5 (solid line) or between 0.1 to 0.9 (blue shade), is plotted as a function of principle quantum number, n, for the hydrogen atom.

are detected directly if their internal excitation energies are higher than the work function of the MCP (∼4.5 eV) [391]. For example, excited D* fragments with principle quantum number $n = 2$ carry 10.2 eV internal excitation energy, which can activate the standard MCP detectors[2] through two essential ionization mechanisms, which are similar to those described in [392] for metal surfaces. The first mechanism is an electron detachment near the surface due to an inelastic collision and the other mechanism is referred to as charge exchange, in which the surface captures the Rydberg electron. Both of these processes result in a free electron, which undergoes amplification within the MCP channels. The MCP stack will generate an avalanche of electrons that can be translated into a detector signal.

Hence, one can achieve a state-selective measurement by using a proper electric field to field ionize and reject a portion of the Rydberg population and to detect the leftover subset of D*($n \leq n_{FI}$) with our MCP detector by the processes described earlier. Moreover, we can subtract different subsets of n to acquire CEP dependence information on narrow subsets of n between n_{FI} and n'_{FI}.

[2]The excited D* fragments with principle quantum number of 2 to 44, D*($2 \leq n \leq 44$), are measured.

4.2.3 Data Analysis

This section describes the techniques used to evaluate the kinetic energy release (KER) distribution of the D^* fragment from the experimental TOF spectra. Later on in this section we will define asymmetry and yield and related topics used to evaluate these observables.

4.2.3.1 Time-of-Flight

The TOF for each fragment is measured with respect to a photodiode signal produced by the laser pulse. Thus, the absolute TOF, i.e. the time it takes the particle to reach the detector starting from the instant of the laser-molecule interaction, is measured, not just the relative TOF, as is commonly the case [375, 393–395]. The measured TOF signals are collected in event mode for a window of up to 50 μs (limited by the time-to-digital converter (TDC) used – CAEN V1290) on the left and right detectors. The TOF signals go through a fast-timing preamplifier and a constant fraction discriminator constant-fraction discriminator (CFD), and are recorded via a time-to-digital converter (TDC). In conjunction with the TOF signal on each detector, the CEP values for every laser shot are measured. A summary of the electronics used in this experiment is given in Appendix G.

In Fig. 4.8 we present a typical TOF spectrum of $D^*(n \leq 44)$ reaching the left detector obtained from 5 fs linearly polarized laser pulses. The electric field between the field ionization meshes is chosen to detect excited fragments with principle quantum numbers of 44 and below. The right detector gives similar results that are not shown here. Figure 4.8 shows the absolute TOF of the fragments, in which the TOF is measured from the moment they are created by the interaction with a laser pulse until they impact the detector, as defined earlier. The absolute TOF of a neutral fragment can be written as

$$t_{neutral} = t_{TDC} - (t_{photon} - \frac{D}{c}), \tag{4.18}$$

where t_{TDC} is the TOF for a fragment recorded relative to the timing signal from a photo-diode which is monitoring the laser pulses in the experiment, t_{photon} is the TOF measured for photons

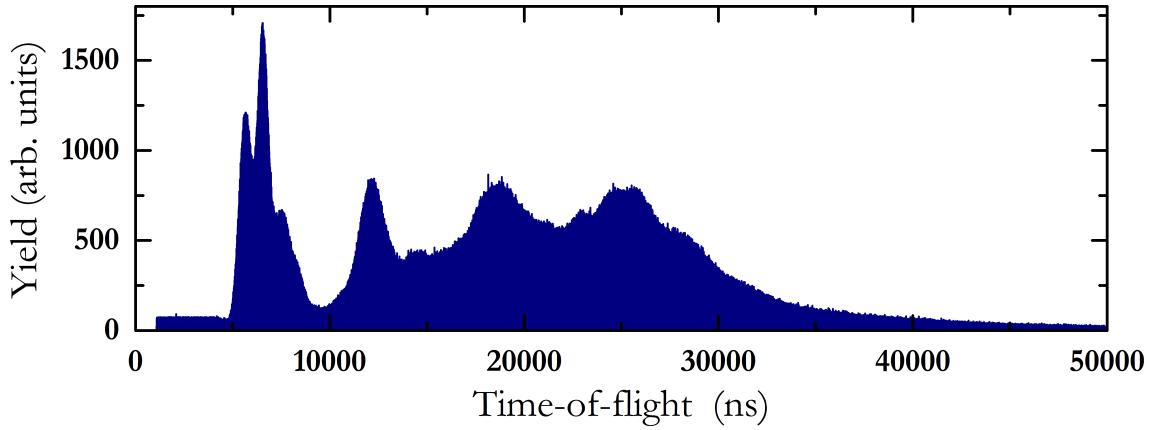

Figure 4.8: Typical $D^*(n \leq 38)$ time-of-flight spectrum from D_2 dissociation integrated over all CEP values using linearly polarized 5 fs laser pulses with a peak intensity of I_0=8×10^{13} W/cm^2.

generated by scattering the laser beam from our effusive jet needle relative to the timing signal from a photo-diode, D is the distance between the effusive jet needle and the detector, and c is the speed of light. This simple imaging equation is similar to what we have used in our ion beam molecular dissociation imaging [91, 197].

4.2.3.2 KER Calculation

Hereafter, we use true times, denoted by t_L and t_R for the left and right detectors, respectively. The measured TOFs on the left and right detectors, at the distance L and R from the interaction point located at z_i relative to the effusive jet needle (see Fig. 4.6), are given by

$$t_L = \frac{L + z_i}{v_L - v_{cm}}, \tag{4.19}$$

and

$$t_R = \frac{R - z_i}{v_R + v_{cm}}, \tag{4.20}$$

respectively, where v_L and v_R are the center of mass velocity components of fragments along the TOF axis, and v_{cm} is the z-velocity component of the target molecule due to its thermal motion. We introduce a free parameter, z_i, as the position of the laser focus along z is not well determined. This parameter can be set to a small value to assure the TOFs from the left and right detectors (integrated over all CEP values) match each other.

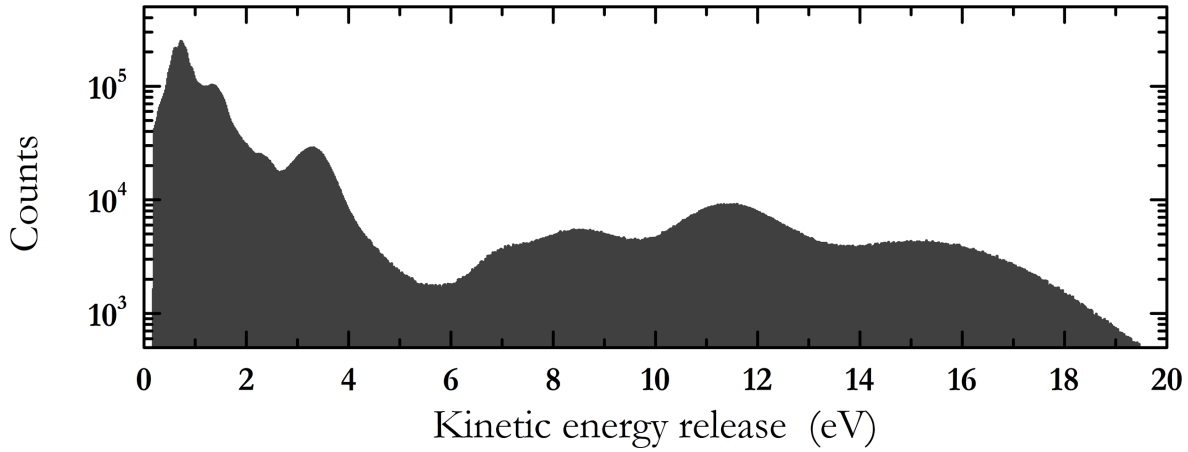

Figure 4.9: A histogram of counts vs. KER for D_2 dissociating into $D^*(n \leq 38)$ fragments integrated over all CEP values using linearly polarized 5 fs laser pulses with a peak intensity of I_0=8×10^{13} W/cm^2.

In this chapter we study a single hit per event on each detector. For instance, at a given CEP value (tagged by our phase meter), one of our detectors, either left or right, registers a hit. To evaluate the dissociation energy for uncorrelated fragments we assume that the center of mass velocity is very small in comparison with the dissociation velocity. For example, for a KER of 1 eV in D_2 dissociation $v_{cm}/v_{R,L} \leq 0.16$ assuming the target gas is at room temperature. The directional flow of the gas is perpendicular to the TOF axis, which effectively leads to lower temperature gas. Therefore, by neglecting the v_{cm} in Eqs. (4.19) and (4.20), we can solve these equations approximately for the dissociation velocity v_L and v_R.

$$v_L \simeq \frac{L + z_i}{t_L}, \tag{4.21}$$

and

$$v_R \simeq \frac{R - z_i}{t_R}. \tag{4.22}$$

By using these velocities and conservation of linear momentum, we calculate both the momentum and therefore the KER of an excited fragment on each detector. The TOF shown in 4.8 is converted into KER as displayed in Fig. 4.9. Kinetic energy release values below 0.2 eV were not measured, as can be seen in Fig. 4.9, due to the limitation on the TOF window size of 50

μs. A brief description of error in the measured KER and the other sources of errors is given in Appendix D. There are several features in the KER spectrum which can be inferred by dividing the spectrum into a few different energy regions. For instance, we observe several broad peaks above 6 eV in the KER spectrum. These peaks can be correlated to the doubly-excited manifold of D_2^{**}, namely the Q_1 and Q_2 Rydberg series, while the KER peaks below 6 eV can be associated with the autoionizing series Q_1 as well as the singly-excited states of D_2^*.

4.2.3.3 Efficiency Correction

The measured number of events on the left and right detectors can be written as

$$M_{L,R}\left(\mathrm{KER},\varphi\right) = \varepsilon_{L,R}\left(\mathrm{KER}\right)\ N_{L,R}\left(\mathrm{KER},\varphi\right),$$

where $\varepsilon_{L,R}\left(\mathrm{KER}\right)$ is the total detection efficiency and $N_{L,R}\left(\mathrm{KER},\varphi\right)$ is the number of events reaching the left- and right-side detectors, respectively. The difference in the detection efficiency for the left and right detectors results in an offset in the asymmetry and yield. However, theory predicts no difference between left and right detectors once the events are integrated over all the CEP values. A symmetric angular distribution is expected about the laser polarization for left and right. In other words, we expect

$$N_R\left(\mathrm{KER}\right) = N_L\left(\mathrm{KER}\right),$$

which leads to a scaling factor as a function of KER

$$\eta\left(\mathrm{KER}\right) = \frac{\varepsilon_R\left(\mathrm{KER}\right)}{\varepsilon_L\left(\mathrm{KER}\right)} = \frac{M_R\left(\mathrm{KER}\right)}{M_L\left(\mathrm{KER}\right)}. \tag{4.23}$$

By using this scaling factor, the offset due to the detection efficiency is corrected. The details are described in Appendix E.

4.2.3.4 Yield Evaluation - Normalization and Offset

In the present work, the yield is defined as the number of D^* fragments emitted toward the left and right detectors within a cone having a 15° angle with respect to the laser polarization direction,

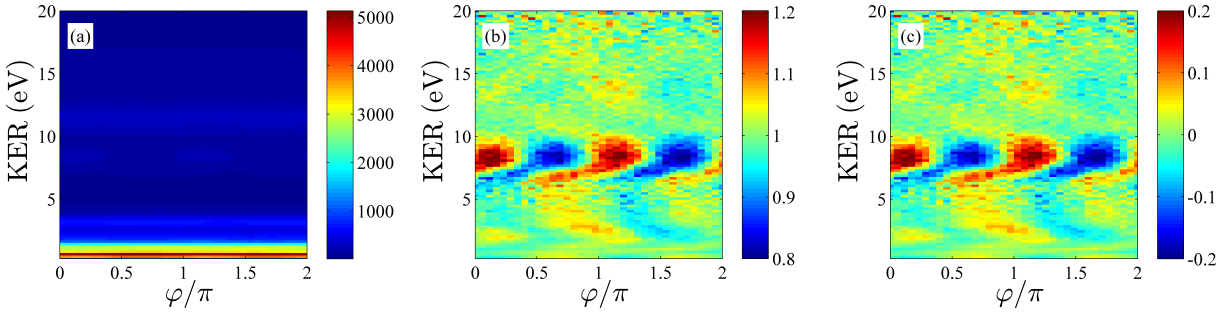

Figure 4.10: (a) Raw yield of D* fragments emitted along the laser polarization as a function of KER and CEP. (b) Normalized yield. (c) Normalized yield after offset subtraction.

$N_L(\mathrm{KER},\varphi) + N_R(\mathrm{KER},\varphi)$, where $N_{L,R}(\mathrm{KER},\varphi)$ is the number of events reaching the left and right detectors for a given KER and phase value. The raw yield map for D* fragments as a function of KER and phase is shown as a density plot in Fig. 4.10(a). In this yield map, the dominant low KER peak ($\leq$2 eV) is obscuring the oscillation in the high KER peaks ($\geq$5 eV). One way to reveal these structures is to evaluate the normalized yield by dividing the yield by its cycle average, $\langle N_L(\mathrm{KER},\varphi) + N_R(\mathrm{KER},\varphi)\rangle_\varphi = \frac{1}{2\pi}\int_0^{2\pi} \left(N_L(\mathrm{KER},\varphi) + N_R(\mathrm{KER},\varphi)\right) \mathrm{d}\varphi$, as follows:

$$\mathcal{P}(\mathrm{KER},\varphi) = \frac{N_L(\mathrm{KER},\varphi) + N_R(\mathrm{KER},\varphi)}{\langle N_L(\mathrm{KER},\varphi) + N_R(\mathrm{KER},\varphi)\rangle_\varphi}. \tag{4.24}$$

Figure 4.10(b) reveals interesting structure that will be discussed in more detail in the next section. The normalized yield map oscillates about 1 as shown by the colorbar in Fig. 4.10(b). We can ensure that the final yield map oscillates around zero by removing this offset of 1 as follows:

$$\mathcal{P}(\mathrm{KER},\varphi) = \frac{N_L(\mathrm{KER},\varphi) + N_R(\mathrm{KER},\varphi)}{\langle N_L(\mathrm{KER},\varphi) + N_R(\mathrm{KER},\varphi)\rangle_\varphi} - \frac{\langle N_L(\mathrm{KER},\varphi) + N_R(\mathrm{KER},\varphi)\rangle_\varphi}{\langle N_L(\mathrm{KER},\varphi) + N_R(\mathrm{KER},\varphi)\rangle_\varphi}. \tag{4.25}$$

Figure 4.10(c) shows the normalized yield map after offset subtraction. More details can be found in Appendix F.

4.2.3.5 Asymmetry Evaluation - Normalization and Offset

The asymmetry is defined as the difference between D* fragments emitted toward the left and right detectors within a cone having a 15° angle with respect to the laser polarization direction,

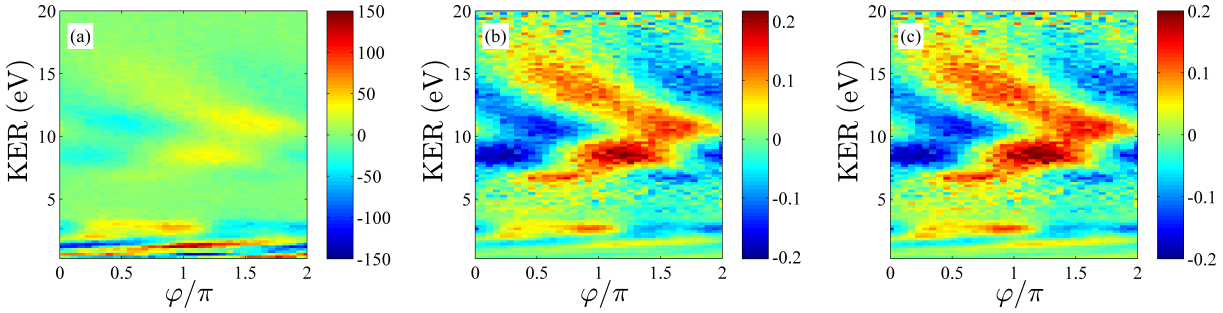

Figure 4.11: (a) Raw asymmetry map of D^* fragments emitted along the laser polarization as a function of KER and CEP. (b) Normalized asymmetry. (c) Normalized asymmetry after offset subtraction.

$N_L(\mathrm{KER},\varphi) - N_R(\mathrm{KER},\varphi)$. Figure 4.11(a) presents such an asymmetry map as a function of KER and φ. We can normalize the asymmetry in a similar manner as described for the yield:

$$\mathcal{A}(\mathrm{KER},\varphi) = \frac{N_L(\mathrm{KER},\varphi) - N_R(\mathrm{KER},\varphi)}{\langle N_L(\mathrm{KER},\varphi) + N_R(\mathrm{KER},\varphi)\rangle_\varphi}. \tag{4.26}$$

The results are shown in Fig. 4.11(b). The asymmetry map oscillates close to 0, but to ensure the oscillation is about zero exactly we introduce an offset correction to our asymmetry map, as

$$\mathcal{A}(\mathrm{KER},\varphi) = \frac{N_L(\mathrm{KER},\varphi) - N_R(\mathrm{KER},\varphi)}{\langle N_L(\mathrm{KER},\varphi) + N_R(\mathrm{KER},\varphi)\rangle_\varphi} - \frac{\langle N_L(\mathrm{KER},\varphi) - N_R(\mathrm{KER},\varphi)\rangle_\varphi}{\langle N_L(\mathrm{KER},\varphi) + N_R(\mathrm{KER},\varphi)\rangle_\varphi}, \tag{4.27}$$

where the asymmetry cycle average, $\langle N_L(\mathrm{KER},\varphi) - N_R(\mathrm{KER},\varphi)\rangle_\varphi$, is defined as

$$\frac{1}{2\pi}\int_0^{2\pi} (N_L(\mathrm{KER},\varphi) - N_R(\mathrm{KER},\varphi))\,\mathrm{d}\varphi.$$

The derivation of the offset correction is described in Appendix F. It is worth mentioning that the asymmetry offset is KER dependent while the yield offset was KER independent. The final asymmetry map after offset subtraction is shown in Fig. 4.11(c).

4.2.3.6 CEP Cycle Duplication

The CEP-tagged data, which goes from 0 to 2π, is commonly duplicated and plotted from 0 to 4π for visualization. In our case, the high statistics data allows us to divide the data into 2 individual data sets. The CEP is distributed randomly within these two data sets. The two sets are analyzed separately, then one of these sets is shifted by 2π and the results are combined together and plotted

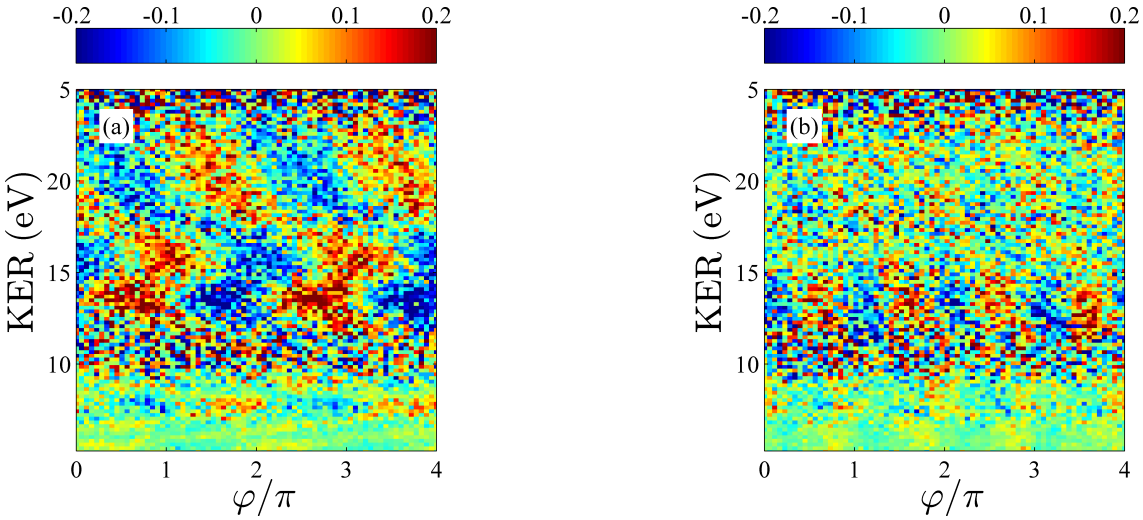

Figure 4.12: Normalized (a) asymmetry and (b) yield after offset subtraction of D^* fragments emitted along the laser polarization as a function of KER and CEP for peak intensity of I_0=4×10^{13} W/cm^2 and pulse duration of 5 fs.

as one distribution from 0 to 4π, as shown in Fig. 4.12(a) and (b). All the results in this chapter are presented in a similar manner.

4.3 Exploring Pathway Interference – Theory vs. Experiment

4.3.1 Yield CEP Dependences

The theoretical treatment by Hua and Esry [112] predicts a weak CEP effect in the total dissociation yield of non-rotating H_2^+ using 5.9 fs, 10^{14} W/cm^2 laser pulses as discussed earlier in section 4.1.1. The recent experiment performed on an H_2 target by Xu *et al.* observed an oscillation with a modulation depth of up to 5% in the yield of $H^+ + H$ [284]. Furthermore, Rathje *et al.* used 4.5 fs laser pulses with a H_2^+ ion-beam target to show a yield oscillation with CEP for 2 different KER regions, 0.1–0.5 eV and 1.75–2.0 eV [90]. To our knowledge, Refs. [90, 284] are the only experiments in which yield oscillation has been reported. A maximum yield oscillation amplitude of a few percent (∼5%) is reported in both measurements [90, 284].

For the data presented in this section, the electric field between the two field-ionizing meshes is chosen to ensure detection of excited fragments with principle quantum numbers of 38 and below, $D^*(n \leq 38)$, as described earlier. As discussed in the theory section 4.1.1, one would expect

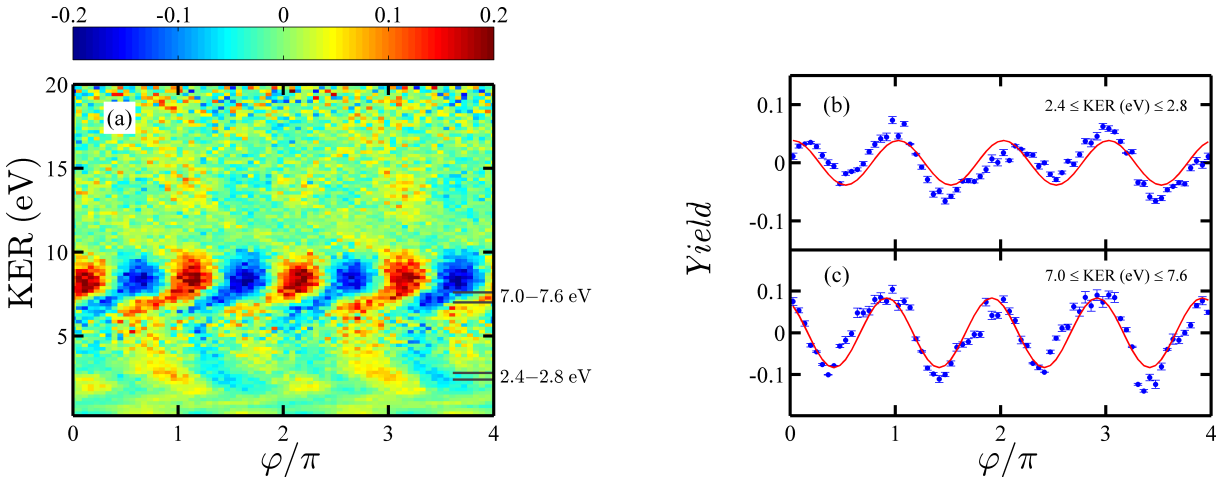

Figure 4.13: (a) The corresponding yield map of $D^*(n \leq 38)$ fragments emitted along the laser polarization as a function of KER and CEP with 5 fs, 8×10^{13} W/cm^2 laser pulses. (b) and (c) The yield parameter integrated over the indicated energy regions and fit to sinusoidal curves (see text).

the yield to oscillate as a $\cos(\Delta n\varphi)$ where Δn=0,2,4,.... The Δn=0 contribution has no CEP dependence, and is removed from the yield map by the offset subtraction. At a glance, the main oscillation in the yield has Δn=2 periodicity in agreement with the theoretical prediction presented in section 4.1.1. These oscillations result from an interference of different photon pathways differing by net two-photons on the same final molecular channel [112].

Figure 4.13(a) shows the yield CEP dependences for $D^*(n \leq 38)$ fragments using 5 fs CEP-tagged linearly polarized laser pulses with intensity 8×10^{13} W/cm^2. A clear CEP-dependent yield is observed in the low KER region (0–4 eV). In addition, a stronger yield modulation is detected in the higher KER region 7–10 eV. The yields within two narrow KER regions are shown in Fig. 4.13(b) and (c) as a function of CEP. More accurately, Fig. 4.13(b) presents the yield for the KER region 2.4–2.8 eV as a function of CEP while Fig. 4.13(c) shows the results for a slice at a higher KER region of 7.0–7.6 eV. The yield was fit to a sinusoidal function, $\mathcal{P}(\varphi) = \alpha\cos(2\varphi+\varphi_0)$ — where α is the yield amplitude and φ_0 is an offset. The fits are plotted as solid lines in Fig. 4.13(b) and (c). The dominant oscillation, Δn=2, is reflected within these fits in Fig. 4.13(b) and (c), although the low KER region does not fit a $\cos(2\varphi)$ very well. Moreover, the tilt in the yield map results from the relative phase between the different interfering pathways and strongly depends on

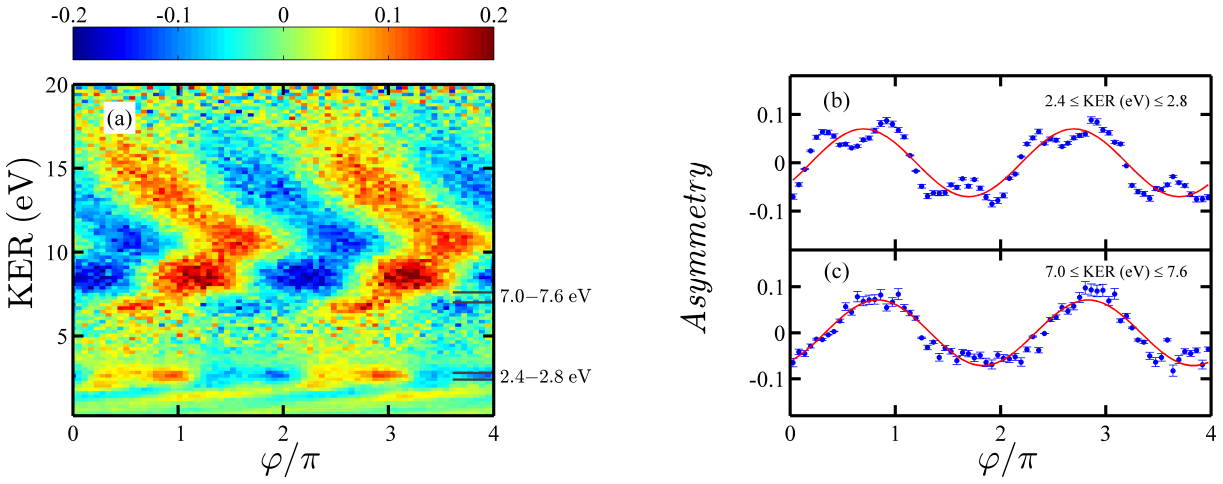

Figure 4.14: (a) The corresponding asymmetry map of $D^*(n \leq 38)$ fragments emitted along the laser polarization vs. KER and CEP with 5 fs, 8×10^{13} W/cm^2 laser pulses. (b) and (c) the asymmetry parameter integrated over the indicated energy regions and fit to sinusoidal curves (see text).

KER. This tilt in the yield map can lead to broadening and shifting effects in a narrow region of KER.

4.3.2 Asymmetry CEP Dependences

The density plot of the asymmetry map is shown as a function of KER and CEP in Fig. 4.14(a) for $D^*(n \leq 38)$ fragments. A broad oscillation pattern is observed across all KER ranges. Figure 4.14(b) and (c) show the asymmetry parameter for two KER regions as labeled on the figure. The results are fit with a sinusoidal function, $\mathcal{A}(\varphi) = \alpha\cos(\varphi + \varphi_0)$, and the fits are plotted as solid lines in Fig. 4.14(b) and (c). The prominent oscillation in the asymmetry map has a Δn=1 periodicity as predicted by theory, while the low KER region has a hint of a higher oscillation frequency. A close look at the asymmetry map reveals higher order oscillations related to a higher net number of photons involved in the interference pathways. We will discuss this in the upcoming section.

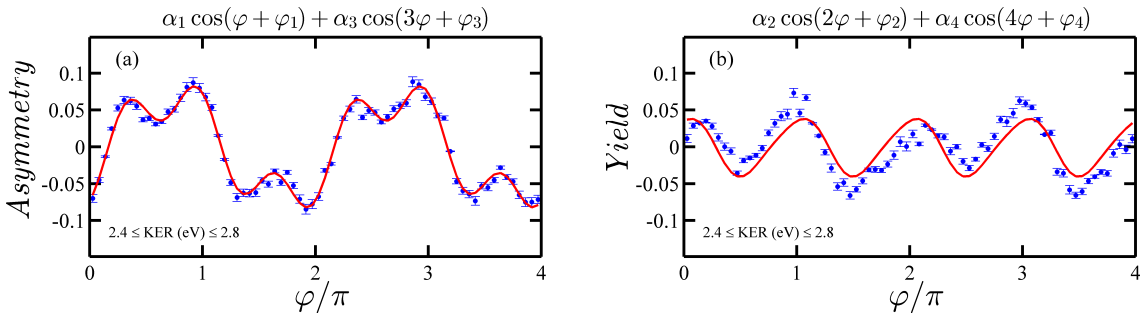

Figure 4.15: The corresponding (a) asymmetry and (b) yield as shown in Fig. 4.13 and Fig. 4.14, integrated over the indicated energy regions, are fit to linear combinations of sinusoidal functions plotted as solid red lines (see text).

4.3.3 Higher-Order CEP Effects

Figure 4.15(a) and (b) are the asymmetry and yield, respectively, plotted as a function of CEP and integrated over a KER region of 2.4–2.8 eV. One way to evaluate the net number of photons involved in generating an interference pattern for this KER region would be to fit a linear combination of $\alpha_{\Delta n}\cos(\Delta n\varphi + \varphi_{\Delta n})$ terms with Δn being odd for the asymmetry and even for the yield.

We fit the asymmetry parameter with a sinusoidal function with lower- and higher-order Δn terms, $\mathcal{A}(\varphi) = \alpha_1\cos(\varphi + \varphi_1) + \alpha_3\cos(3\varphi + \varphi_3)$. The result of this fit is shown in Fig. 4.15(a) with the amplitude ratio of $\alpha_3/\alpha_1 = 0.47$ and $R^2 = 0.98$ for KER region 2.4–2.8. The fitting parameters depend weakly on the choice of KER region. We fit the yield map in a similar way with the sinusoidal function, $\mathcal{P}(\varphi) = \alpha_2\cos(2\varphi + \varphi_2) + \alpha_4\cos(4\varphi + \varphi_4)$. The fit results in an amplitude ratio of $\alpha_4/\alpha_2 = 0.1$ with R^2= 0.63 which is a relatively poor fit as observed in Fig. 4.15(b).

The uncertainty caused by the choice of width in the KER region can account for such poor fit results. The tilt in the yield map, due to the relative phase of the interfering pathways, can appear as a shift in the yield parameter and increase the width of the peaks. However, the asymmetry parameter shows no tilt in the KER region of 2.4–2.8 eV and fitting with a higher-order sinusoidal function clearly shows a strong higher-order CEP effect resulting from interference of pathways differing by Δn=3 on different molecular channels. The other approach to assess the number of photons involved in the interference process would be to perform a Fourier analysis. As we described earlier in the theoretical section, the CEP and net-number of photons are conjugates of

each other and therefore mathematically connected by a Fourier transform.

4.3.3.1 Fourier Analysis

Fourier analysis has been used widely in many areas of physics. The Fourier transform is an important theoretical tool which has been developed to preform a transformation on analytical functions. In practice, our experimental data are composed of discrete samples of signal, and as a result the Fourier transform can be used to compute a discrete set of frequencies. In the frequency domain, the frequency interval from one point to the next is $\Delta f = 1/(N\Delta\tau)$, where N is the number of samples and $\Delta\tau$ is the sampling interval. We can rewrite this equation in term of the angular frequency as, $\Delta\omega = 2\pi/(N\Delta\tau)$, in which $\Delta\tau$ and $\Delta\omega$ are conjugate variables. In our case, the measured CEP is measured between 0 to 2π, so unlike a time series measurement in which the data is collected for a long interval, we need to increase our measured CEP range to acquire better resolution in the Δn domain. Having a limited CEP range will result in $\delta(\Delta n) = 2\pi/(N\delta\varphi) = 1$. In other words, we can resolve between net-number of photons differing by one in our Fourier analysis. In principle we would like to satisfy the condition in which our resolution is higher than the frequency of the signal under study.

In order to distinguish between two different net-number of photons in our spectrum we must satisfy $\delta(\Delta n) \ll \mid \Delta n_1 - \Delta n_2 \mid$. We can improve the resolution in the Δn domain by increasing the CEP interval length. The two dimensional asymmetry or yield map is duplicated to acquire a higher resolution Δn through a discrete Fourier transformation. However, in this method the random noise for an individual data set is getting duplicated, which introduces an amplified noise signal.The result is randomly generated spikes at every integer value of Δn. To avoid these unwanted spikes in the Fourier transform spectrum, we can change our approach in duplicating our data. The high statics of our data set allows us to split the raw data into several equally sized subsets. We analyze each subset individually to generate a yield and asymmetry map. Further, all of these subsets are added together in a random order to ensure no spurious time dependent oscillation from the measurement can affect our findings. The procedure described above is shown schematically in Fig. 4.16.

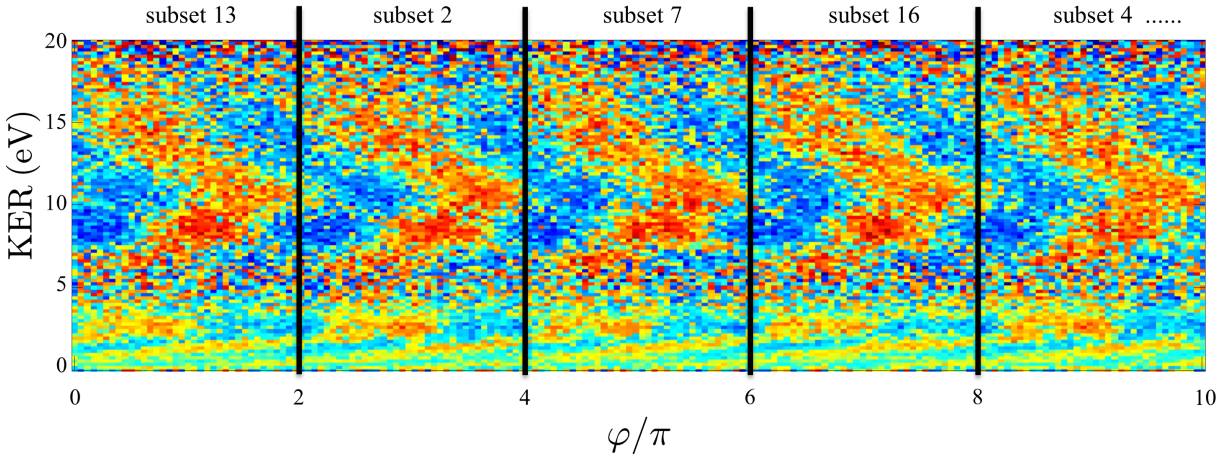

Figure 4.16: The extension of the asymmetry map data to acquire a higher resolution in the Fourier transform (see text).

The Fourier transform power spectrum of the asymmetry map as a function of KER and the Fourier frequency (Δn in our case) is shown as a 2D density plot in Fig. 4.17(a). The dominant feature appears at Δn=1 for a broad range of KER, although a narrow region of KER (2.4–2.8 eV) shows higher-order oscillation effects at Δn=3. Figure 4.17(b) and (c) show the power spectra for given KER regions as labeled on the figure. Figure 4.17(b) shows clear peaks at net one and three photons. In contrast, no higher-order contribution can be seen for the higher KER slice (7.0–7.6 eV) as shown in Fig. 4.17(c). However, there is a weak spurious peak at net two photon which will be discussed below.

Figure 4.18(a) presents the Fourier analysis for the yield map presented earlier and Figure 4.18(b) and (c) are the power spectra for KER slices discussed earlier. As expected from the theoretical prediction, the Δn=2 is the main contribution in the CEP oscillation of the yield, which can be observed in the Fourier analysis. However, there are some other frequencies present in the Fourier spectrum of the yield map, such as Δn=1 at both KER region, and a weak spike at Δn=3 for the low KER region (2.4–2.8 eV). There is a hint of a faint higher-order frequency oscillation, Δn=4, at the (7.0–7.6 eV) KER slice.

A few explanations can be provided for the inconsistency between our findings and the theoretical predictions. Referring to our earlier discussion of the theory in section 4.1.1, the asymmetry

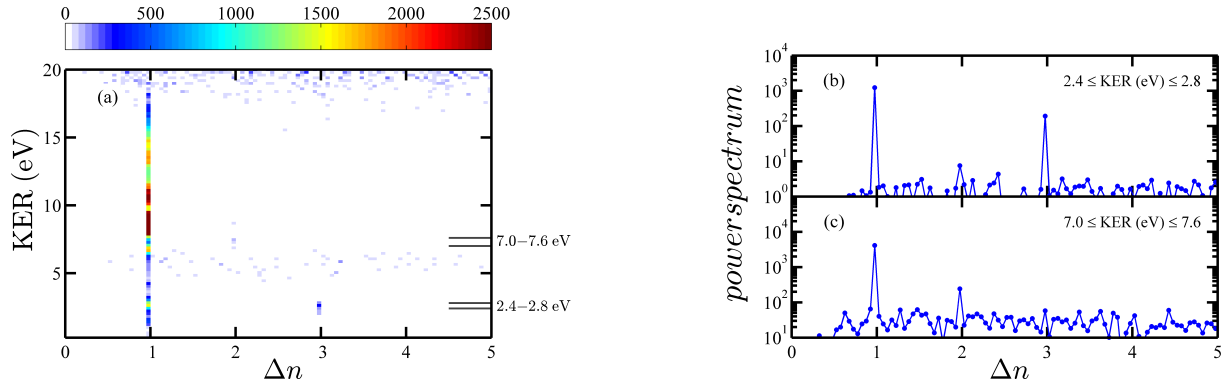

Figure 4.17: (a) Density plot of the Fourier transform of the asymmetry map shown in Fig. 4.14 is plotted as a function of KER and Δn. (b) and (c) The power spectra for two different KER regions as labeled on the figure (see text).

and yield are defined as $\mathcal{A}(\mathrm{KER},\varphi) = \int_0^{\pi/2} \rho(\mathrm{KER},\theta)_L d\theta_k - \int_{\pi/2}^{\pi} \rho(\mathrm{KER},\theta)_R d\theta$ and $\mathcal{P}(\mathrm{KER},\varphi) = \int_0^{\pi/2} \rho(\mathrm{KER},\theta)_L d\theta_k + \int_{\pi/2}^{\pi} \rho(\mathrm{KER},\theta)_R d\theta$, respectively, where $\rho(E,\theta)$ is the differential probability density per unit energy per unit angle for dissociation [253]. It is important to note that the integration is performed over the whole upper and lower halves of the distribution, and more importantly the integration has been done symmetrically. In other words, in our experiment the acceptance cone along the laser polarization for detecting D^* fragments on the left and right detector should be exactly equal.

In the experiment the data is collected within a small cone with an angle of 15° with respect to the laser polarization direction, which enhances the asymmetry or yield amplitude [253]. In

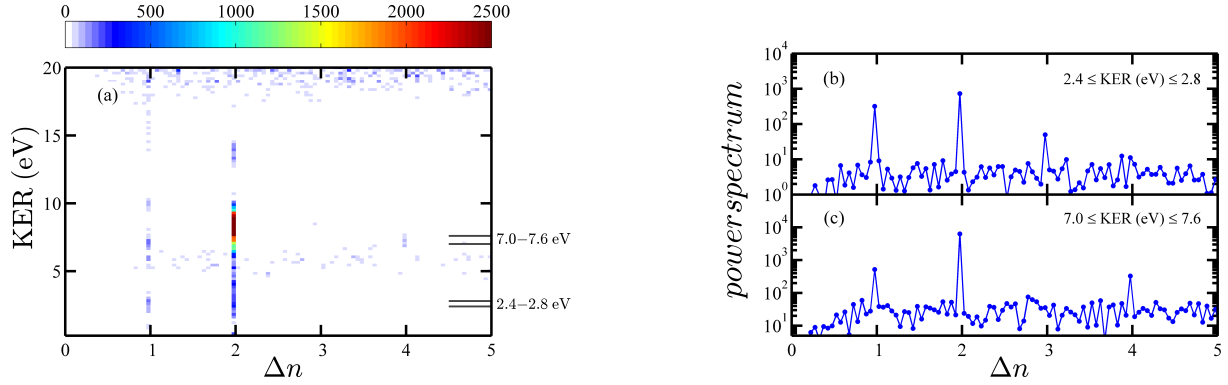

Figure 4.18: (a) Density plot of the Fourier transform of the yield map shown in Fig. 4.13 is plotted as a function of KER and Δn. (b) and (c) The power spectra for two different KER regions as labeled on the figure (see text).

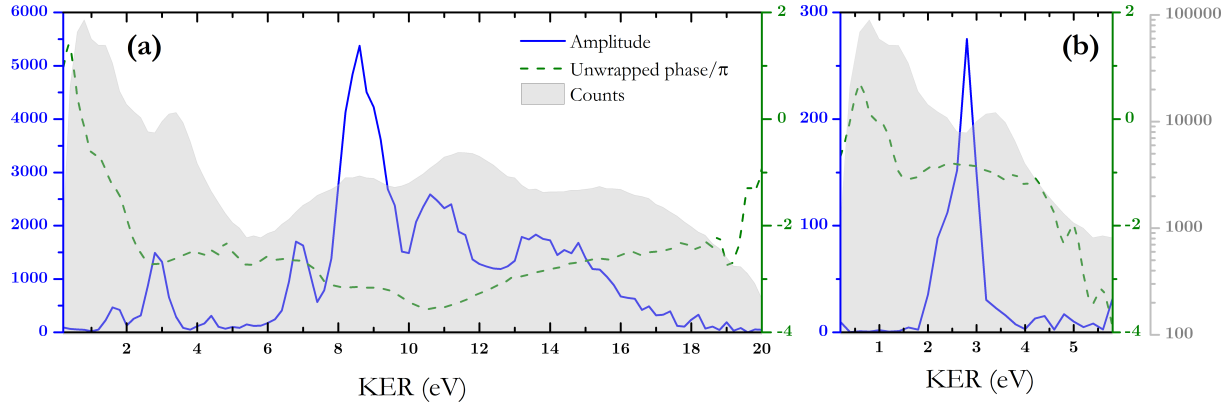

Figure 4.19: Amplitude and phase extracted from the Fourier analysis for (a) Δn=1 and (b) Δn=3. The grey pattern in the background shows the KER averaged over all CEP for D_2 dissociating into $D^*(2 \geq n \leq 38)$ fragments.

addition, the data is not collected exactly symmetrically as the laser polarization can be a few degrees away from the TOF axis, and the interaction can occur slightly away from the center of the apparatus. As a result the integration within the cones on the left and right are not exactly symmetric. Any deviation from the symmetrical integration may introduce spurious frequencies in our Fourier analysis.

Lastly, amplitude and phase of the pathways differing by 1 and 3 are extracted from the Fourier analysis and plotted as a function KER. Figure 4.19(a) shows the extracted amplitude (solid line) and phase (dashed line) of the asymmetry map [Fig. 4.14(a)] as a function of KER for Δn=1. The grey pattern in the background shows the KER averaged over all CEP for D_2 dissociating into $D^*(2 \geq n \leq 38)$ fragments to indicate where dissociation probability is significant. The amplitude of the Δn=1 is small in the KER region of 2–4 eV, although the amplitude is dominant at 8.5 eV as shown in Fig. 4.19(a). Figure 4.19(b) displays the extracted amplitude and phase for Δn=3. A Δn=3 peak is clearly visible in the 2–3 eV range. The extracted amplitude and phase for different Δn can be used to help understanding the origin of these interfering pathways.

In summary, the CEP dependence in the fragmentation of D_2 molecules into D^* has been studied using ultrashort linearly polarized laser pulses. The asymmetry exhibits a dominant oscillation with periodicity of Δn=1, resulting from interference between pathways differing by net-one photon. On the other hand, the D^* yield shows an oscillation with periodicity of Δn=2, which is in agreement

with the theoretical prediction of Esry and coworkers [76, 111, 112]. Finally, we introduce a Fourier analysis method to extract information linked to interference pathways with higher numbers of photons involved.

4.4 CEP Effects with Multicycle Laser Pulses

In this section, we demonstrate the CEP dependence of the dissociation of D_2 into D^* by multicycle chirped laser pulses. Intuitively, changes in the CEP would appear to have less of an effect on multicycle laser pulses in comparison to few-cycle laser pulses. One would expect to observe weaker CEP effects when using multicycle laser pulses based on the idea that the directionality of the electric field is responsible for the asymmetry effect. This simplistic idea does not hold for multicycle pulses. Recent theoretical calculations on H_2^+ show a strong CEP dependence in the electron localization asymmetry [371, 396]. The CEP dependence of the asymmetry in the emission direction of ATI electrons in xenon gas has been measured using 30 fs CEP stabilized laser pulses [397].

The CEP effects in the strong- and weak-field regime have been studied in great detail [76, 111, 112, 192, 230, 324, 398–403]. The origin of CEP effects in these regimes is demonstrated to be a quantum mechanical interference between different multiphoton pathways [111, 192, 371, 404, 405]. The broad spectral bandwidth of the laser plays a crucial rule in these CEP studies. Given the discussion above, the question is, *how does a multicycle chirped laser pulse influence the CEP dependences in the dissociation of* D_2 *into* D^* *fragments?* To answer this question, we repeated our previous measurements while chirping the laser pulses negatively and positively (sometimes referred to as up- and down-chirp) but maintaining the spectral bandwidth fixed to the same level as our 5 fs FTL laser pulses.

We control the amount of chirp by introducing a variable glass thickness into the beam path. The positive and negative chirp is acquired by precisely adjusting a pair of fused-silica wedges. The pulse duration can be estimated by assuming a Gaussian chirped pulse [406], $\tau = \tau_o\sqrt{1+16\ln(2)^2\frac{\beta_2^2}{\tau_o^4}}$, where τ_o is the initial FTL pulse width (FWHM) in fs, τ is the final

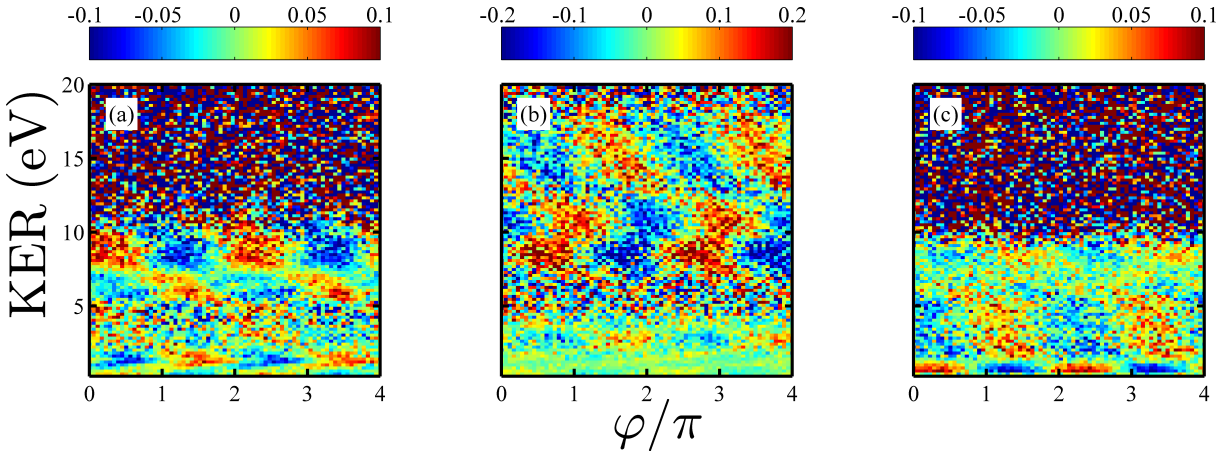

Figure 4.20: Chirp dependence of the asymmetry. The asymmetry map of $D^*(n \leq 38)$ fragments using ∼10 fs, (a) negatively and (c) positively chirped laser pulses with a peak intensity of 4×10^{13} W/cm^2. (b) The asymmetry map of $D^*(n \leq 38)$ fragments using FTL ∼5 fs laser pulses with a peak intensity of 4×10^{13} W/cm^2. By adding or removing 0.5 mm of fused silica glass in the optical path, we generate positively and negatively chirped laser pulses from FTL 5 fs laser pulses, respectively.

pulse width (FWHM) in fs and β_2 is the second-order dispersion, or chirp, in fs^2. For instance, a 5 fs FTL laser pulse can propagate through 0.5 mm of fused silica with a β_2 of 36.9 fs^2 at 800 nm to generate ∼10 fs positively chirped laser pulses.

Figure 4.20(b) shows the asymmetry map for $D^*(n \leq 38)$ fragments using FTL 5 fs laser pulses with a peak intensity of 4×10^{13} W/cm^2. Figure 4.20(a) and (c) show the asymmetry map for ∼10 fs negatively and positively chirped laser pulses, respectively, with an intensity of 4×10^{13} W/cm^2. Due to the broad spectral bandwidth of our laser pulses, the CEP dependence in the asymmetry map persists for a wide range of KER for negatively and positively chirped laser pulses. However, the KER is smaller in comparison to FTL pulses for both chirps. This is clear in the asymmetry maps shown in Fig. 4.20(a) and (c) as the asymmetry vanished above ∼12 eV. To compare negatively and positively chirped laser pulses, we can point out that the asymmetry in the low KER region (≤1 eV) with both chirps shows a dominant oscillation with Δn=1 periodicity, while this asymmetry is slightly stronger for negatively chirped pulses in the higher KER region (7–10 eV).

To quantify our results, we plot the asymmetry amplitudes for the low and high KER regions as shown in Fig. 4.21(a) and (b). In the low KER region the asymmetry amplitude is dominant for

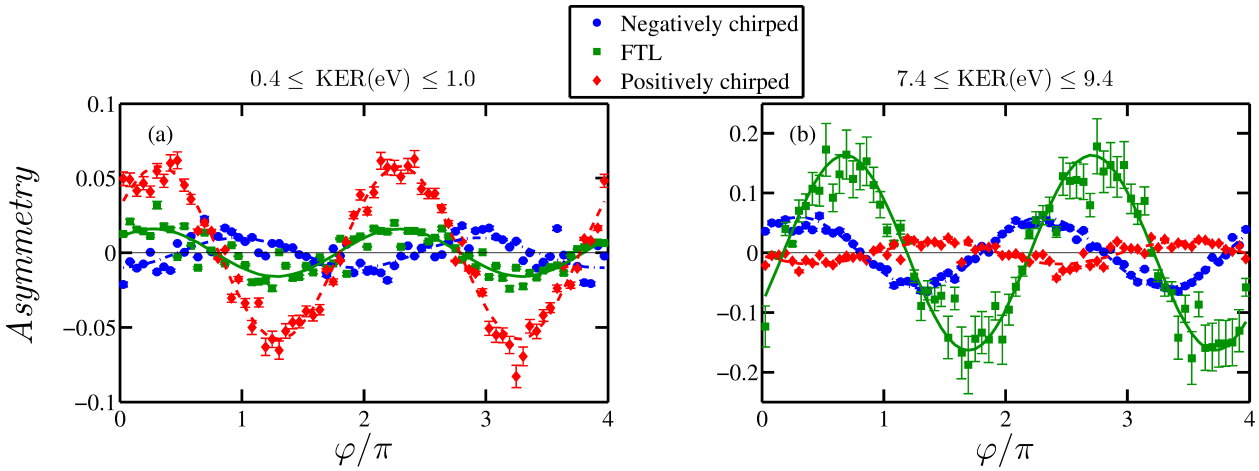

Figure 4.21: The corresponding asymmetries as shown in Fig. 4.20, integrated over the indicated energy regions (a)–(b), are fit to a sinusoidal function with periodicity of Δn=1. The symbols indicate different pulse parameters (see text).

positively chirped laser pulses as plotted in Fig. 4.21(a). The asymmetry amplitude is ∼6 times larger for positively chirped pulses in comparison to negatively chirped and FTL laser pulses. Figure 4.21(b) shows the asymmetry amplitude for KER 7.4–9.4 eV, and the FTL laser pulses reveal a dominant oscillation with periodicity of Δn=1. The asymmetry amplitude in this KER region for negatively chirped pulse is slightly larger than the positively chirped laser pulses by a factor of ∼2.

We also repeated our measurements for longer chirped laser pulses (∼21 fs), again maintaining the spectral bandwidth of the 5 fs FTL laser pulses. The ∼21 fs positively and negatively chirped pulses are generated by propagation through a different thickness of fused silica. 1 mm of fused silica imparts 36.9 fs^2 of linear chirp. The asymmetry maps for D* fragments from the dissociation of D_2 interacting with ∼21 fs negatively chirped, positively chirped and FTL laser pulses are depicted in Fig. 4.22(a)–(c), respectively. The asymmetry map for positively chirped laser pulses shows a clear oscillation at ∼2.0 eV with periodicity of Δn=1. In contrast, the asymmetry is marginally visible at a higher KER region (7–9 eV) for negatively chirped pulses.

The yield maps for ∼10 fs and ∼21 fs negatively and positively chirped laser pulses are shown in Fig. 4.23. Figure 4.23(b) and (e) show the yield maps for 5 fs FTL pulses with peak intensities of 4×10^{13} W/cm^2 and 1.8×10^{13} W/cm^2, respectively. The FTL results display a Δn=2 oscillation

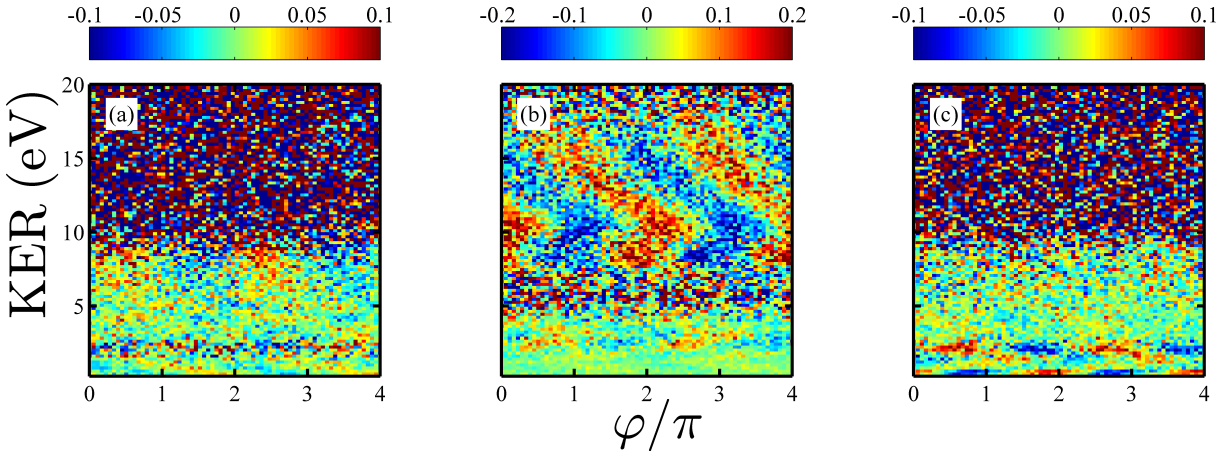

Figure 4.22: Chirp dependence of the asymmetry. (a) and (c) The asymmetry map of $D^*(n \leq 38)$ fragments using ∼21 fs, negatively and positively chirped laser pulses, respectively, with a peak intensity of 1.8×10^{13} W/cm^2. (b) The asymmetry map of $D^*(n \leq 38)$ fragments using FTL ∼5 fs laser pulses with a peak intensity of 1.8×10^{13} W/cm^2. By adding or removing 1.0 mm of fused silica glass in the optical path, we generate positively and negatively chirped laser pulses respectively from FTL 5 fs laser pulses.

in a wide range of KER. The yield map for ∼10 fs negatively chirped laser pulses (Fig. 4.23(a)), exhibits a clear oscillation with Δn=2 periodicity around 6.5 eV. The negatively chirped laser pulses with pulse duration of ∼21 fs reveal a weaker oscillation at around 5 eV with Δn=2 periodicity. However, the yield maps for positively chirped laser pulses show no clear oscillation as shown in Fig. 4.23(c) and (f).

To summarize this section, we would like to point out that due to the wide spectral bandwidth of our 5 fs laser pulses, the interference of different photon pathways persists even with chirped multicycle laser pulses, which agrees with the theoretical prediction of Wang *et al.* for H_2^+ dissociation [371]. This indicates that the bandwidth plays a crucial role in comparison with the number of cycles available in the pulse.

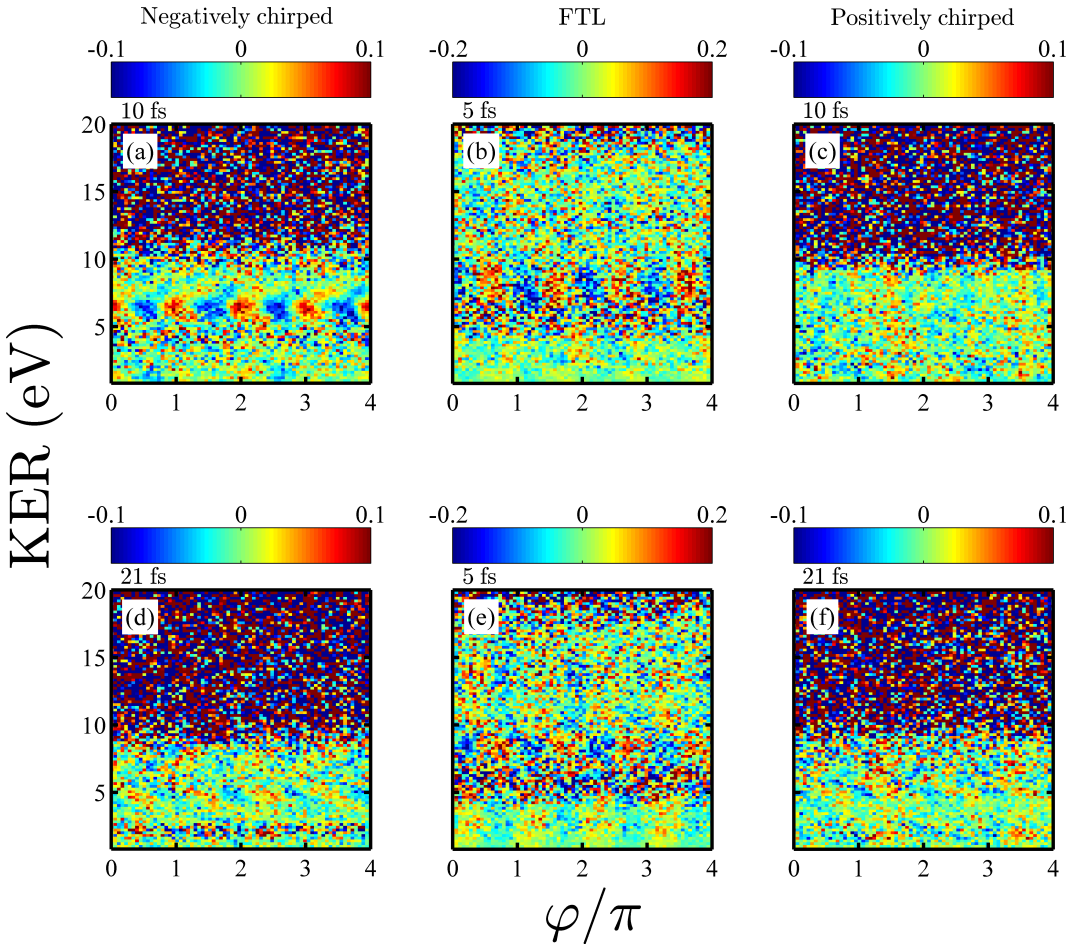

Figure 4.23: The yield maps of $D^*(n \leq 38)$ fragments using ∼10 fs (a) negatively and (c) positively chirped laser pulses with a peak intensity of 4×10^{13} W/cm^2. The yield maps of $D^*(n \leq 38)$ fragments using ∼21 fs (d) negatively and (f) positively chirped laser pulses with a peak intensity of 1.8×10^{13} W/cm^2. The corresponding yield maps for the 5 fs FTL laser pulses with peak intensities of 4×10^{13} W/cm^2 and 1.8×10^{13} W/cm^2 are shown in (b) and (e), respectively.

4.5 State-Selective CEP Dependences

As described earlier, all of the measurements in the previous sections were presented for a subset of excited fragments with $D^*(n \leq 38)$. In this section we will study the asymmetry and yield CEP dependences for distinct subsets of quantum number n. The important question that we would like to address is, *How does the CEP dependence of asymmetry or yield change for different n subsets?* By choosing an appropriate electric field strength between the two meshes (M_1 and M_2), we were able to ionize and reject the higher part of the population. As a result, a well-defined subset of quantum number n can be measured. The list of voltages and associated quantum numbers used in these measurements is given in appendix H.

Figure 4.24(a)–(f) shows the asymmetry maps for the different subsets labeled on each graph using FTL 5 fs pulses with an intensity of $8{\times}10^{13}\,\mathrm{W/cm^2}$. The asymmetry gets stronger as n_{max} increases. Furthermore, the structure in the low KER region changes significantly. We plot the asymmetry amplitude, $\alpha_{asymmetry}$, for different subsets of n, as shown in Fig. 4.26(a). The asymmetry amplitude for the high KER region (7.4$\leq$ KER(eV) $\leq$9.4) increases sharply with n, for the lower n subsets. The asymmetry amplitude does not appear to vary for n above 27. For the KER region of 2.2$\leq$ KER(eV) $\leq$3.2, the asymmetry amplitude varies smoothly and saturates at n=38. Figure 4.25(a)–(f) present the yield maps for the same subsets of n. The yield maps show a similar behavior, namely that the amplitude of the yield increases for a higher subset of n. To quantify this, we plot the yield amplitude, α_{yield}, as a function of n for two KER regions, as shown in Fig. 4.26(b). For the higher KER region (7.4–9.4 eV), the increase in the yield amplitude is almost exponential, while the low KER region (2.2–3.2 eV) shows no substantial change by varying n.

As another example of the information that can be extracted from the data, we show the phase offset between different KER slices from the highly structured 2D asymmetry and yield maps of $D^*(n \leq 38)$ fragments (Fig. 4.24(e) and 4.25(e)). This relative phase shift, φ_0, is plotted as a function of KER in Fig. 4.27(a) and (b) by fitting a sinusoidal function, $\cos(\Delta n\varphi + \varphi_0)$, with Δn=1 periodicity across the asymmetry and yield. Note that this relative phase shift is accurate

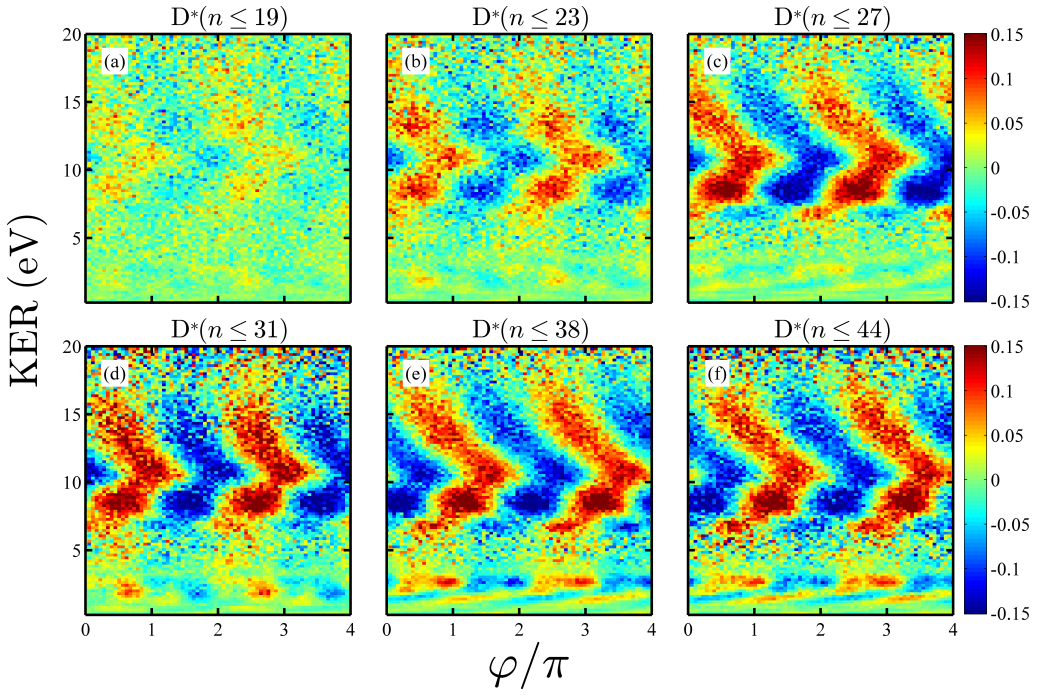

Figure 4.24: (a)–(f) The asymmetry maps of various subsets of excited fragments, $D^*(n_{max})$, after interacting with 5 fs linearly polarized laser pulses with a peak intensity of 8×10^{13} W/cm^2.

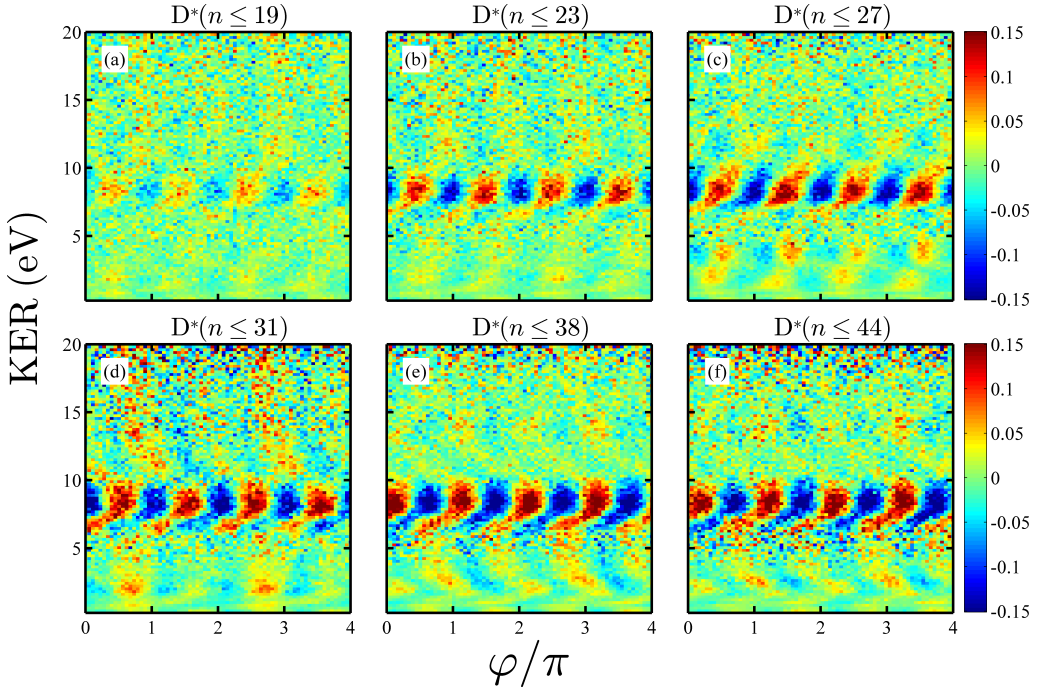

Figure 4.25: (a)–(f) The yield maps of various subsets of excited fragments, $D^*(n_{max})$, after interacting with 5 fs linearly polarized laser pulses with a peak intensity of 8×10^{13} W/cm^2.

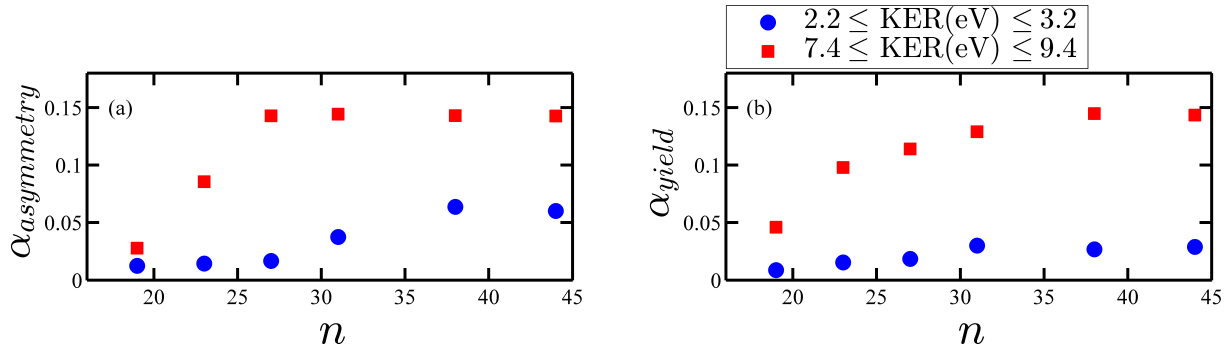

Figure 4.26: (a) The asymmetry parameter amplitude as a function of subset n for two KER regions. (b) The yield parameter amplitude as a function of subset n for two KER regions (see text). The error bars are smaller that the symbols.

along the KER distribution, even though the CEP measured is not absolute. Each interfering pathway accumulates a specific phase along the path, and knowing the phase difference between two KER regions can be used to distinguish between the interfering pathways involved in the process. Therefore, a proper theoretical calculation for this relatively complicated system can be used to identify the specific interfering pathways that underlie each relative phase shift extracted from the data.

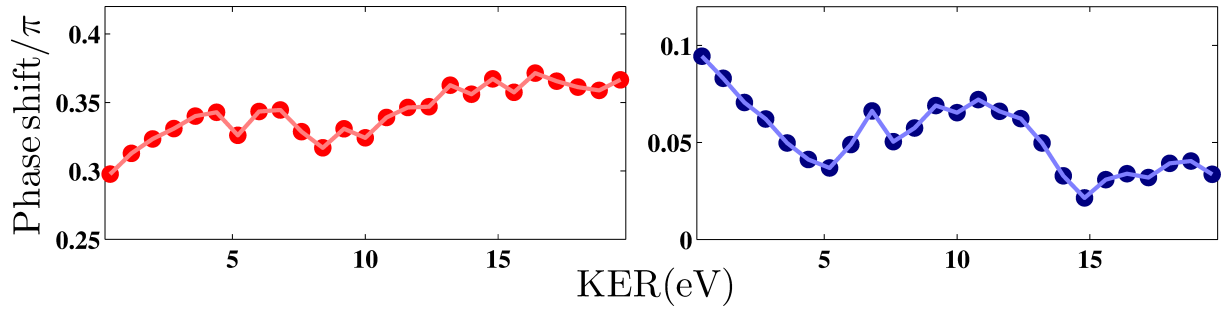

Figure 4.27: The (a) asymmetry and (b) yield parameter phase shifts for D$^*(n \leq 38)$ fragments as a function of KER. The error bars are smaller that the symbols.

4.5.0.2 Quantum State Slices - D$^*(n - n')$

We would like to study a narrow distribution of n states to learn more about how the asymmetry and yield of specific n states depend on CEP. For this purpose, we need to subtract the asymmetry or yield map of two different measurements, which allows us to address a specific range of n values. However, each measurement has a slightly different CEP offset, due to regular fluctuations in

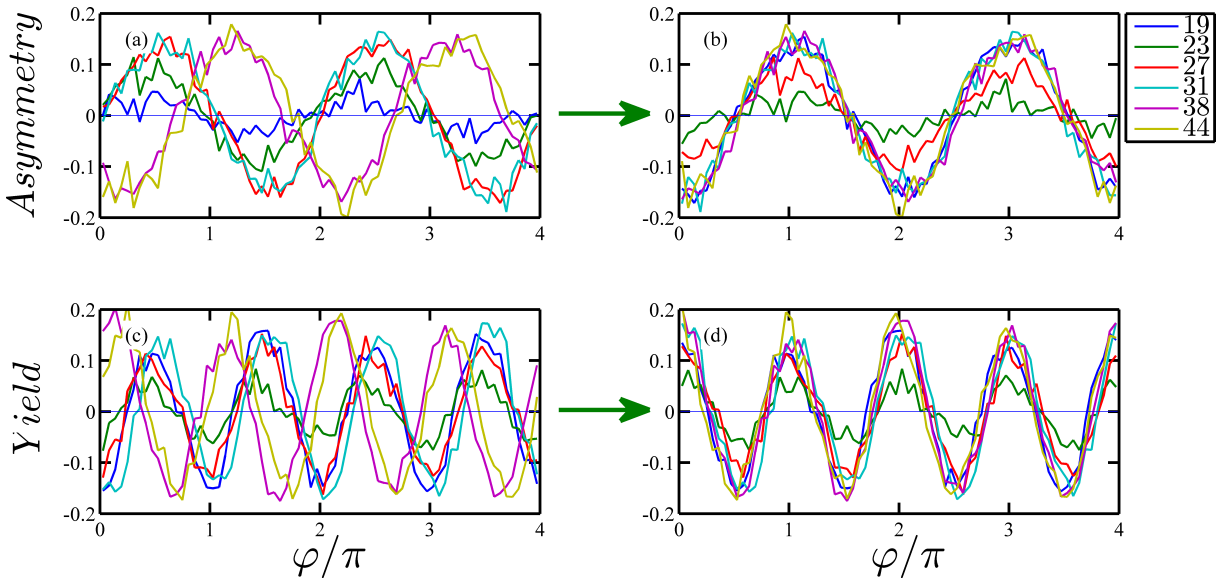

Figure 4.28: The (a) asymmetry and (c) yield parameters within the KER region of 8–8.2 eV for various subsets of n as indicated in the legend. The (b) asymmetry and (d) yield parameters presented in (a) and (c) after offset correction (see text).

the short pulse. The PAP conditions change during different measurements, which results in an offset between different data sets. In the current measurement, we cannot distinguish between an offset due to changes in the CEP tagging condition or a real offset change due to the response of a different narrow slice of n states. The proper way to perform a state-selective measurement is to record all data sets for different n subsets with the same phase potato. This is one of the goals for our near future experiments, and some technical developments to accomplish this goal are underway.

We decided to analyze our current data sets based on a specific assumption. The assumption is that the relative offset phase between different subsets of n is negligible at high KER, since the high KER peak most likely originates from a re-collision process or frustrated tunneling ionization (FTI) [98, 110]. Based on this assumption, we can correct the offset by matching the CEP structure at a KER of ∼8 eV. Figure 4.28(a) shows the asymmetry parameter around a KER region of 8-8.2 eV for different subsets of n (labeled in the legend). Figure 4.28(b) shows the same asymmetry parameter after offset correction of the different subsets. The same correction matches the offset phase in the yield at this KER region, as shown in Fig. 4.28(c) and (d).

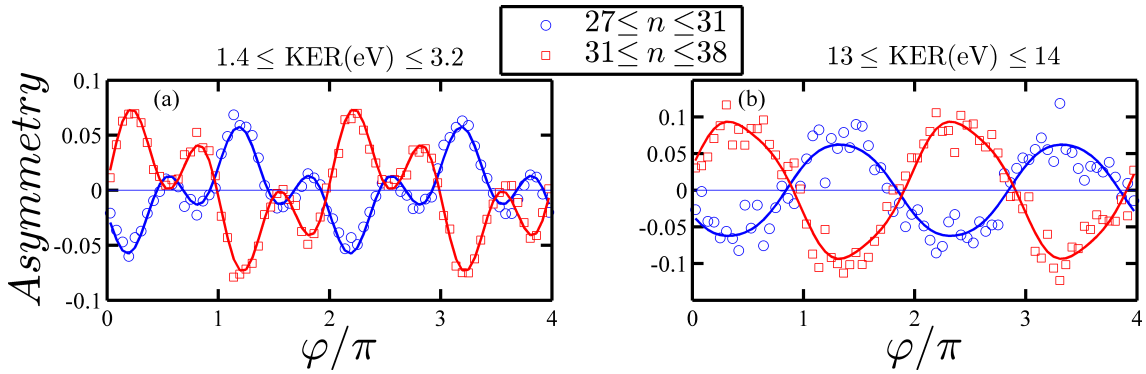

Figure 4.29: The asymmetry parameter within the KER regions of (a) 1.4–3.2 eV and (b) 13–14 eV is plotted for two slices in n to n' states (Fig.4.30 (d) and (e)).

We generate the asymmetry map of different slices n to n', as shown in Fig. 4.30(a)–(f). Narrow slices in the quantum number n reveal interesting structure. For instance, there is an outstanding asymmetry that appears at large KER (≥8 eV), which is shown in Fig. 4.30(a)–(c). In addition, this high KER region exhibits a clear CEP offset between $27 \leq n \leq 31$ and $31 \leq n \leq 38$. In Fig. 4.30(d) and (e), the low KER region (≤4 eV) uncovers a strong asymmetry with a hint of higher oscillation frequencies.

We plot the asymmetry parameter for two KER regions of subsets $27 \leq n \leq 31$ and $31 \leq n \leq 38$, as shown and labeled in Fig. 4.29(a) and (b). We fit the asymmetry parameter with a sinusoidal function, $\alpha_1 \cos(\varphi + \varphi_1) + \alpha_3 \cos(3\varphi + \varphi_3)$, as described earlier, and the results are plotted as solid lines. The asymmetry parameter at a KER region of 1.4–3.2 eV clearly exhibits a dominant oscillation with Δn=1 and a high order oscillation of Δn=3. The amplitude ratio is α_3/α_1=0.87 (0.85) with R^2=0.96 (0.98) for subsets of $27 \leq n \leq 31$ ($31 \leq n \leq 38$). The ratio of amplitudes shows minimal changes, while the phase between different net numbers of photons varies. For instance, the offset phase for Δn=3, φ_3, does not change between subsets of $27 \leq n \leq 31$ and $31 \leq n \leq 38$, while the relative offset phase for Δn=1 between the two subsets changes by $\sim \pi/5$. The asymmetry parameter at a larger KER (13–14 eV) is plotted in Fig. 4.29(b) and shows similar phase shifts as described for Fig. 4.29(a). The slice around $38 \leq n \leq 44$ does not show any dominant feature in the asymmetry map.

The yield map for different slices reveals similar features as described for asymmetry and is

depicted in Fig. 4.31(a)–(f). These preliminary results show promising features within different slices in n based on the assumption we made earlier. In the near future, we would like to repeat our measurements, by switching between different field ionization conditions resulting in distinct subsets of n, without changing the conditions of our phase tagging apparatus.

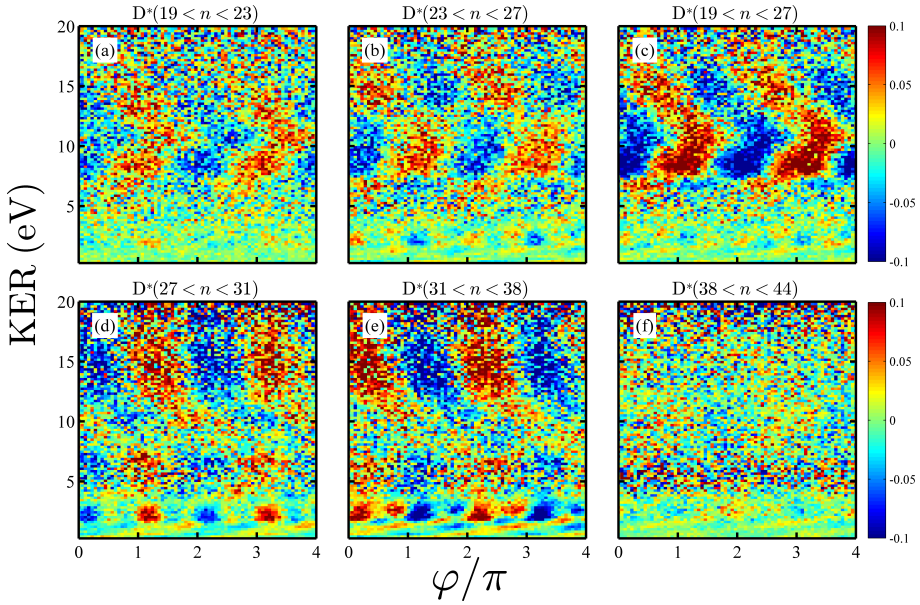

Figure 4.30: The asymmetry maps as a function of KER and φ for different slices in subsets of n labeled accordingly. The laser parameters are the same as Fig. 4.24.

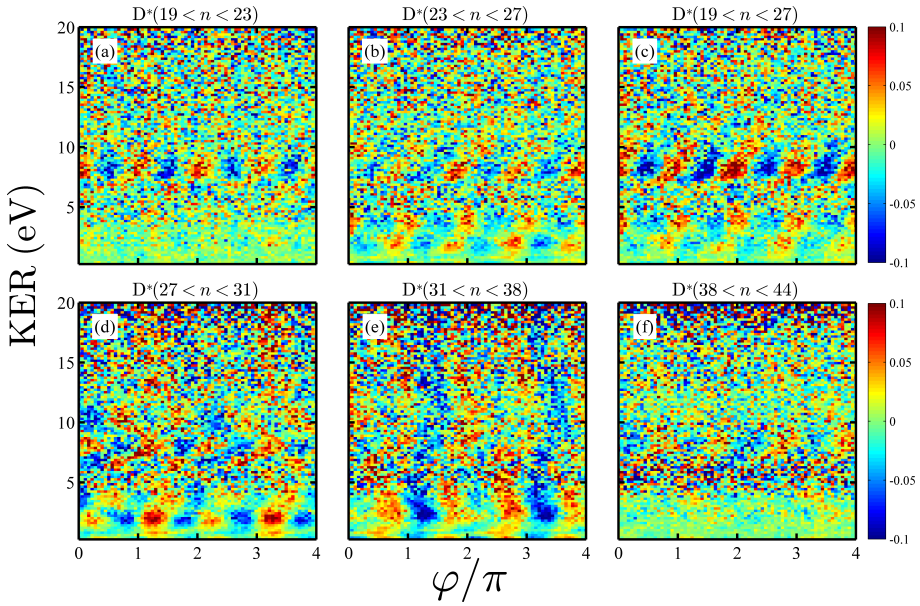

Figure 4.31: The yield maps as a function of KER and φ for different slices in subsets of n labeled accordingly. The laser parameters are the same as Fig. 4.24.

4.6 Summary and Outlook

In summary, we have conducted an in-depth study on the CEP dependence of Rydberg series of hydrogenic molecules by using an intense ultrashort laser pulse. In part one, we performed the detailed measurements of laser-induced dissociation of D_2 molecules into excited neutral fragments, $D^*(n)$.

In the second part, our measurements of long-lived D^* fragments exhibit strong oscillations of the asymmetry and yield with CEP in both low- and high-energy dissociation. As predicted by theory [76, 111, 112], the periodicity of the oscillations shows a 1-photon difference between the interfering pathways in the asymmetry and a 2-photon difference in the yield. Moreover, at some dissociation energies we identify smaller contributions from interfering dissociation paths with a larger net photon-number difference. Furthermore, we Fourier transform the CEP-dependent observables to gain insight into the interfering photon pathways involved in the D^* formation.

We have investigated the CEP dependences of asymmetry and yield maps of these excited $D^*(n)$ fragments by using multicycle chirped laser pulses of ∼10 and ∼21 fs. This resulted in distinct changes in the KER distribution. The asymmetry and yield oscillation is fairly robust, elucidating the importance of quantum mechanical interference due to broad spectral bandwidth [371, 396].

Finally, for the first time, we have examined the CEP dependences in a narrow subset of quantum states, n to n'. These narrow slices of n show interesting features as a function of CEP. By careful analysis of these slices, we can extract information about the relative phase shifts between different subsets of n as well as the asymmetry and yield amplitudes. To understand the exact significance of these measurements, further theoretical work is required to quantify our findings.

For further studies of CEP dependences in the dissociation of excited fragments of D_2, a two-electron theoretical model would be beneficial. We can use the Fourier analysis of asymmetry and yield as feedback to optimize the experimental conditions. For instance, we can ensure our results are exactly integrated symmetrically about the laser polarization direction by examining the Fourier map of asymmetry and yield. Improving our experimental apparatus will enable us

to measure the position information of each hit on the detector, which can give us insight into interference in the momentum distribution of fragments and the importance of these interferences for different angular distributions. In addition, a coincidence measurement between an ionic fragment and an excited neutral ($D^+ + D^*(n)$) can shed light on the interfering pathways involved in the process.

Chapter 5

Summary and Outlook

In this dissertation, we have described fragmentation dynamics and control of a variety of molecular targets driven by strong laser fields. All of the projects discussed in this dissertation have been summarized in the respective sections detailing the work. For brevity, the detailed conclusions will not be repeated here. One of the main objectives of this work was to provide a basic understanding of control mechanisms by exploring benchmark systems such as H_2^+. This understanding was carried over to more complex systems such as O_2^+ and neutral hydrogen molecules.

For instance, our previous understanding was examined by exploring dissociation pathways in O_2^+ induced by fundamental, second- and third-harmonic wavelengths. We previously observed a suppressed dissociation of H_2^+ vibrational states in intense laser pulses, which is a manifestation of the well-known Cooper minima effect [95]. This was further investigated in O_2^+ dissociation by careful inspection of the Cooper minima position. Different wavelengths result in a shift of the Cooper minima, which may be used to identify the dissociation pathways. This idea has been suggested by Brett Esry, and work to extend it to other molecules is underway.

In another example, a general CEP theory [111] was examined by measuring the yield of highly-excited deuterium fragments from D_2 molecules. The general CEP theory predicts that the asymmetry in D^* emission along the laser polarization is due to the interference of n-photon pathways that differ by an odd number of photons, while the CEP dependence of the total dissociation yield emerges from the interference of n-photon pathways differing by an even number of photons. Our experimental results confirm this theoretical prediction. In addition, the asym-

metry also exhibits higher frequency oscillations, which involve interference of pathways differing by the net absorption of three photons or more. Similarly, the total yield shows high-order effects resulting from interference of pathways differing by net four photons. Moreover, we have used Fourier analysis to extract information related to these high-order photon pathways involved in D^* formation. These high-order effects are predicted to be stronger at longer wavelengths, suggesting a natural extension of these studies into the mid-IR in the near future.

To achieve the goal of control several different experimental methods were employed. For instance, to study the CEP dependence of D_2 fragmentation into highly-excited D^*, two detectors facing each other with an effusive gas jet target in between were employed. This setup was further modified to enable state-selective measurements. Future D^* formation experiments will benefit by incorporating a coincidence-imaging technique in which an ionic fragment and an excited neutral $[D^+ + D^*(n)]$ will be measured in coincidence, while the imaging will provide 3D momentum distribution of these fragments.

In the ion-beam studies, we implemented pump-probe style experiments, such as two-color, on ion-beam targets. We were successful in controlling the dissociation of molecular-ion beams using the relative phase between two-color laser pulses in spite of the low target density. The results were interpreted as an interference between vibrationally-resolved dissociation pathways. Our two-color experiments can be further expanded to other fundamental systems such as H_3^+ and HeH^+, if the ion-beam target current density is increased. In fact, steps toward more complex systems have begun and analysis of O_2^+ dissociation in a two-color field is in progress.

In addition, we implemented a pump-probe technique to study fragmentation dynamics on benchmark molecular ion-beam targets in order to check the feasibility of these challenging experiments. The dissociation yield reveals interesting structure as a function of delay between the pump and probe pulses, and more theoretical work is needed to understand these dynamics. In contrast, the ionization results are currently limited by the low counting rate. A higher target density is essential to the succuss of these experiments. We plan to produce this improvement either by upgrading the ion source or bunching the ion beam.

The ability to perform vibrationally resolved measurements on H_2^+ and O_2^+ can motivate further pump-probe studies. For instance, the effect of a pump pulse on the vibrational population can be studied by probing the beating frequency between neighboring vibrational levels. These pump-probe style experiments on ion-beam targets will be further improved by the enhancements mentioned in the previous paragraph.

Every project described in this work can be further explored by taking advantage of our new laser capability at longer wavelengths (1100–2200 nm). For instance, the current study on D_2 fragmentation into highly excited D^* has shown some interesting results. One possible mechanism for D^* production is through electron recollision. It is known that for longer wavelengths the electron can gain more energy from the laser field through the pondermotive force. We can explore the population of the D^* excited states by using longer laser wavelengths. Moreover, the rate of fragmentation is high for these D^* excited states. Thus, in future studies the laser pulses can be tailored to control the population of these excited states using genetic algorithms.

Bibliography

[1] M. Laue, Die dreizählig-symmetrischen Röntgenstrahlaufnahmen an regulären Kristallen, Ann. Phys. **347**, 397 (1913).

[2] W. Friedrich, P. Knipping, and M. Laue, Interferenzerscheinungen bei Röntgenstrahlen, Ann. Phys. **346**, 971 (1913).

[3] W. L. Bragg, *The Diffraction of Short Electromagnetic Waves by a Crystal*, Proceedings of the Cambridge Philosophical Society, 1913.

[4] L. Pauling, The crystal structure of magnesium stannide, J. Am. Chem. Soc. **45**, 2777 (1923).

[5] L. Pauling, The principles determining the structure of complex ionic crystals, J. Am. Chem. Soc. **51**, 1010 (1929).

[6] L. Pauling, *The Nature of the Chemical Bond*, Cornell University Press, 1960.

[7] M. Eckert, Max von Laue and the discovery of X-ray diffraction in 1912, Ann. Phys. **524**, A83 (2012).

[8] M. Laue, The nobel prize in physics 1914, `http://www.nobelprize.org/nobel_prizes/physics/laureates/1914/`.

[9] J. D. Watson and F. H. C. Crick, A structure for deoxyribose nucleic acid, Nature **171**, 737 (1953).

[10] M. H. F. Wilkins, A. R. Stokes, and H. R. Wilson, Molecular structure of deoxypentose nucleic acids, Nature **171**, 738 (1953).

[11] B. Chance, The accelerated flow method for rapid reactions, J. Franklin Inst. **229**, 613 (1940).

[12] B. Chance, The stopped-flow method and chemical intermediates in enzyme reactions — a personal essay, in *Discoveries in Photosynthesis*, edited by Govindjee, J. Beatty, H. Gest, and J. Allen, volume **20** of *Advances in Photosynthesis and Respiration*, pages 621–632, Springer Netherlands, 2005.

[13] R. G. W. Norrish and G. Porter, Chemical reactions produced by very high light intensities, Nature **164**, 658 (1949).

[14] G. Porter, Flash photolysis and spectroscopy. a new method for the study of free radical reactions, Proc. R. Soc. A **200**, 254 (1950).

[15] G. Porter, *Technique of Organic Chemistry*, volume **8**, Interscience, New York, 1963.

[16] P. M. Rentzepis, Direct measurements of radiationless transitions in liquids, Chem. Phys. Lett. **2**, 117 (1968).

[17] D. von der Linde, A. Laubereau, and W. Kaiser, Molecular vibrations in liquids: Direct measurement of the molecular dephasing time; determination of the shape of picosecond light pulses, Phys. Rev. Lett. **26**, 954 (1971).

[18] A. Laubereau, D. von der Linde, and W. Kaiser, Direct measurement of the vibrational lifetimes of molecules in liquids, Phys. Rev. Lett. **28**, 1162 (1972).

[19] T. L. Netzel, P. M. Rentzepis, and J. Leigh, Picosecond kinetics of reaction centers containing bacteriochlorophyll, Science **182**, 238 (1973).

[20] R. Anderson, P. M. Hochstrasser, H. Lutz, and G. W. Scott, Measurements of intersystem crossing kinetics using 3545 Å picosecond pulses: nitronaphthalenes and benzophenone, Chem. Phys. Lett. **28**, 153 (1974).

[21] K. J. Kaufmann and P. M. Rentzepis, Picosecond spectroscopy in chemistry and biology, Acc. Chem. Res. **8**, 407 (1975).

[22] D. R. Herschbach, Y. T. Lee, and J. C. Polanyi, The nobel prize in chemistry 1986, http://www.nobelprize.org/nobel_prizes/chemistry/laureates/1986/.

[23] A. H. Zewail, Laser femtochemistry, Science **242**, 1645 (1988).

[24] M. J. Rosker, M. Dantus, and A. H. Zewail, Femtosecond real-time probing of reactions. I. The technique, J. Chem. Phys. **89**, 6113 (1988).

[25] A. H. Zewail, The nobel prize in chemistry 1999, http://www.nobelprize.org/nobel_prizes/chemistry/laureates/1999/.

[26] P. H. Bucksbaum, A. Zavriyev, H. G. Muller, and D. W. Schumacher, Softening of the H_2^+ molecular bond in intense laser fields, Phys. Rev. Lett. **64**, 1883 (1990).

[27] G. H. Dunn, Photodissociation of H_2^+ and D_2^+: Theory, Phys. Rev. **172**, 1 (1968).

[28] F. von Busch and G. H. Dunn, Photodissociation of H_2^+ and D_2^+: Experiment, Phys. Rev. A **5**, 1726 (1972).

[29] J. B. Ozenne, D. Pham, and J. Durup, Photodissociation of H_2^+ by monochromatic light with energy analysis of the ejected H^+ ions, Chem. Phys. Lett. **17**, 422 (1972).

[30] P. H. Bucksbaum and A. Zavriyev, Above-threshold photodissociation and bond softening at high intensities, in *Coherence Phenomena in Atoms and Molecules in Laser Fields*, edited by A. Bandrauk and S. Wallace, volume **287** of *NATO ASI Series*, pages 53–63, Springer US, 1992.

[31] A. Giusti-Suzor, X. He, O. Atabek, and F. H. Mies, Above-threshold dissociation of H_2^+ in intense laser fields, Phys. Rev. Lett. **64**, 515 (1990).

[32] G. Jolicard and O. Atabek, Above-threshold-dissociation dynamics of H_2^+ with short intense laser pulses, Phys. Rev. A. **46**, 5845 (1992).

[33] A. Assion, T. Baumert, J. Helbing, V. Seyfried, and G. Gerber, Molecular ATI and ATD with femtosecond laser pulses, in *Ultrafast Phenomena X*, edited by P. Barbara, J. Fujimoto, W. Knox, and W. Zinth, volume **62** of *Springer Series in Chemical Physics*, pages 270–271, Springer Berlin Heidelberg, 1996.

[34] A. Assion, T. Baumert, U. Weichmann, and G. Gerber, Photofragmentation of Na_2^+ in intense femtosecond laser fields: From photodissociation on light-induced potentials to field ionization, Phys. Rev. Lett. **86**, 5695 (2001).

[35] Q. Zhang, J. W. Hepburn, and M. Shapiro, Observation of above-threshold dissociation of $Na_2{}^+$ in intense laser fields, Phys. Rev. A **78**, 021403 (2008).

[36] J. McKenna, A. M. Sayler, F. Anis, B. Gaire, N. G. Johnson, E. Parke, J. J. Hua, H. Mashiko, C. M. Nakamura, E. Moon, Z. Chang, K. D. Carnes, B. D. Esry, and I. Ben-Itzhak, Enhancing high-order above threshold dissociation of H_2^+ beams with few-cycle laser pulses, Phys. Rev. Lett. **100**, 133001 (2008).

[37] J. McKenna, A. M. Sayler, F. Anis, N. G. Johnson, B. Gaire, U. Lev, M. Zohrabi, K. D. Carnes, B. D. Esry, and I. Ben-Itzhak, Vibrationally cold CO^{2+} in intense ultrashort laser pulses, Phys. Rev. A **81**, 061401 (2010).

[38] P. Brumer and M. Shapiro, Control of unimolecular reactions using coherent light, Chem. Phys. Lett. **126**, 541 (1986).

[39] M. Shapiro and P. Brumer, Laser control of product quantum state populations in unimolecular reactions, J. Chem. Phys. **84**, 4103 (1986).

[40] A. Assion, T. Baumert, M. B. T. Brixner, B. Kiefer, V. Seyfried, M. Strehle, and G. Gerber, Control of chemical reactions by feedback-optimized phase-shaped femtosecond laser pulses, Science **282**, 5390 (1998).

[41] T. Frohnmeyer, M. Hofmann, M. Strehle, and T. Baumert, Mapping molecular dynamics (Na_2) in intense laser fields: another dimension to femtochemistry, Chem. Phys. Lett. **312**, 447 (1999).

[42] D. J. Tannor and S. A. Rice, Control of selectivity of chemical reaction via control of wave packet evolution, J. Chem. Phys. **83**, 5013 (1985).

[43] D. J. Tannor, R. Kosloff, and S. R. Rice, Coherent pulse sequence induced control of selectivity of reactions: Exact quantum mechanical calculations, J. Chem. Phys. **85**, 5805 (1986).

[44] S. A. Rice, Molecular dynamics: Optical control of reactions, Nature **403**, 496 (2000).

[45] E. Charron, A. Giusti-Suzor, and F. H. Mies, Coherent control of photodissociation in intense laser fields, J. Chem. Phys. **103**, 7359 (1995).

[46] J. Manz and G. K. Paramanov, Laser control scheme for state-selective ultrafast vibrational excitation of the HOD molecule, J. Phys. Chem. **97**, 12625 (1993).

[47] L. Zhu, V. Kleiman, X. Li, S. P. Lu, K. Trentelman, and R. J. Gordon, Coherent laser control of the product distribution obtained in the photoexcitation of HI, Science **270**, 5233 (1995).

[48] B. Sheehy, B. Walker, and L. F. DiMauro, Phase-control in the 2-color photodissociation of HD^+, Phys. Rev. Lett. **74**, 4799 (1995).

[49] C. Z. Bisgaard, M. D. Poulsen, E. Péronne, S. S. Viftrup, and H. Stapelfeldt, Observation of enhanced field-free molecular alignment by two laser pulses, Phys. Rev. Lett. **92**, 173004 (2004).

[50] K. F. Lee, E. A. Shapiro, D. M. Villeneuve, and P. B. Corkum, Coherent creation and annihilation of rotational wave packets in incoherent ensembles, Phys. Rev. A **73**, 033403 (2006).

[51] O. Ghafur, A. Rouzée, A. Gijsbertsen, W. K. Siu, S. Stolte, and M. J. J. Vrakking, Impulsive orientation and alignment of quantum-state-selected NO molecules, Nature Phys. **5**, 289 (2009).

[52] M. Shapiro and P. Brumer, *Principles of the Quantum Control of Molecular Processes*, Wiley-Interscience, 2003.

[53] M. Shapiro and P. Brumer, Coherent control of molecular dynamics, Rep. Prog. Phys. **66**, 859 (2003).

[54] P. Brumer and M. Shapiro, Laser control of molecular processes, Annu. Rev. Phys. Chem. **43**, 257 (1992).

[55] C. Brif, R. Chakrabarti, and H. Rabitz, Control of quantum phenomena: past, present and future, New J. Phys. **12**, 075008 (2010).

[56] R. S. Judson and H. Rabitz, Teaching lasers to control molecules, Phys. Rev. Lett. **68**, 1500 (1992).

[57] T. Brixner, N. H. Damrauer, P. Niklaus, and G. Gerber, Photoselective adaptive femtosecond quantum control in the liquid phase, Nature **414**, 57 (2001).

[58] T. Brixner, C. Dietl, G. Krampert, P. Niklaus, E. Papastathopoulos, T. Pfeifer, R. Selle, G. Vogt, D. Walter, C. Winterfeldt, and G. Gerber, Adaptive femtosecond quantum control, in *Ultrafast Optics IV*, edited by F. Krausz, G. Korn, P. Corkum, and I. Walmsley, volume **95** of *Springer Series in optical sciences*, pages 119–128, Springer New York, 2004.

[59] J. L. Herek, W. Wohlleben, R. J. Cogdell, D. Zeidler, and M. Motzkus, Quantum control of energy flow in light harvesting, Nature **417**, 533 (2002).

[60] R. Kosloff, S. A. Rice, P. Gaspard, and S. T. D. J. Tannor, Wavepacket dancing: Achieving chemical selectivity by shaping light pulses, Chem. Phys. **139**, 201 (1989).

[61] S. A. Rice and M. Zhao, *Optical Control of Molecular Dynamics*, Wiley-Interscience, 2000.

[62] S. A. Rice, New ideas for guiding the evolution of a quantum system, Science **258**, 412 (1992).

[63] D. J. Tannor, *Molecules in Laser Fields*, Marcel Dekker, New York, 1994.

[64] S. Shi, A. Woody, and H. Rabitz, Optimal control of selective vibrational excitation in harmonic linear chain molecules, J. Chem. Phys. **88**, 6870 (1988).

[65] W. S. Warren, H. Rabitz, and M. Dahleh, Coherent control of quantum dynamics: The dream is alive, Science **259**, 1581 (1993).

[66] W. Jakubetz, J. Manz, and V. Mohan, Model preparation of H_2O hyperspherical modes by visible versus infrared multiphoton excitation, J. Chem. Phys. **90**, 3686 (1989).

[67] J. E. Combariza, C. D. B. Just, E. Kades, E. Kolba, J. Manz, W. Malisch, G. K. Paramonov, and B. Warmuth, *Isotope Effects in Gas Phase Chemistry*, volume **502**, ACS Symposium Series, American Chemical Society, Washington, DC., 1992.

[68] M. Shapiro and P. Brumer, Total N-channel control in the weak field domain, J. Chem. Phys. **97**, 6259 (1992).

[69] M. Shapiro and P. Brumer, Weak field optimal control over product yields. the pump–dump scenario, Chem. Phys. Lett. **208**, 193 (1993).

[70] A. Monmayrant, S. Weber, and B. Chatel, A newcomer's guide to ultrashort pulse shaping and characterization, J. Phys. B: At. Mol. Opt. Phys. **43**, 103001 (2010).

[71] E. Wells, C. E. Rallis, M. Zohrabi, R. Siemering, B. Jochim, P. R. Andrews, U. Ablikim, B. Gaire, S. De, K. D. Carnes, B. Bergues, R. de Vivie-Riedle, M. F. Kling, and I. Ben-Itzhak, Adaptive strong-field control of chemical dynamics guided by three-dimensional momentum imaging, Nature Commun. **4**, 3895 (2013).

[72] A. Assion, T. Baumert, J. Helbing, V. Seyfried, and G. Gerber, Coherent control by a single phase shaped femtosecond laser pulse, Chem. Phys. Lett. **259**, 488 (1996).

[73] V. S. Prabhudesai, U. Lev, A. Natan, B. D. Bruner, A. Diner, O. Heber, D. Strasser, D. Schwalm, I. Ben-Itzhak, J. J. Hua, B. D. Esry, Y. Silberberg, and D. Zajfman, Tracing the photodissociation probability of H_2^+ in intense fields using chirped laser pulses, Phys. Rev. A **81**, 023401 (2010).

[74] A. Natan, U. Lev, V. S. Prabhudesai, B. D. Bruner, D. Strasser, D. Schwalm, I. Ben-Itzhak, O. Heber, D. Zajfman, and Y. Silberberg, Quantum control of photodissociation by manipulation of bond softening, Phys. Rev. A **86**, 043418 (2012).

[75] E. Charron, A. Giusti-Suzor, and F. H. Mies, Coherent control of isotope separation in HD^+ photodissociation by strong fields, Phys. Rev. Lett. **75**, 2815 (1995).

[76] V. Roudnev, B. D. Esry, and I. Ben-Itzhak, Controlling HD^+ and H_2^+ dissociation with the carrier-envelope phase difference of an intense ultrashort laser pulse, Phys. Rev. Lett. **93**, 163601 (2004).

[77] X. M. Tong and C. D. Lin, Dynamics of light-field control of molecular dissociation at the few-cycle limit, Phys. Rev. Lett. **98**, 123002 (2007).

[78] F. He, C. Ruiz, and A. Becker, Control of electron excitation and localization in the dissociation of H_2^+ and its isotopes using two sequential ultrashort laser pulses, Phys. Rev. Lett. **99**, 083002 (2007).

[79] M. R. Thompson, M. K. Thomas, P. F. Taday, J. H. Posthumus, A. J. Langley, L. J. Frasinski, and K. Codling, One and two-colour studies of the dissociative ionization and Coulomb explosion of H_2 with intense Ti:sapphire laser pulses, J. Phys. B: At. Mol. Opt. Phys. **30**, 5755 (1997).

[80] M. F. Kling, C. Siedschlag, A. J. Verhoef, J. I. Khan, M. Schultze, T. Uphues, Y. Ni, M. Uiberacker, M. Drescher, F. Krausz, and M. J. J. Vrakking, Control of electron localization in molecular dissociation, Science **312**, 246 (2006).

[81] D. Ray, F. He, S. De, W. Cao, H. Mashiko, P. Ranitovic, K. P. Singh, I. Znakovskaya, U. Thumm, G. G. Paulus, M. F. Kling, I. V. Litvinyuk, and C. L. Cocke, Ion-energy dependence of asymmetric dissociation of D_2 by a two-color laser field, Phys. Rev. Lett. **103**, 223201 (2009).

[82] B. Fischer, M. Kremer, T. Pfeiffer, B. Feuerstein, V. Sharma, U. Thumm, C. Hofrichter, A. Rudenko, U. Thumm, C. D. Schröter, R. Moshammer, and J. Ullrich, Steering the electron in H_2^+ by nuclear wave packet dynamics, Phys. Rev. Lett. **105**, 223001 (2010).

[83] M. Kremer, B. Fischer, B. Feuerstein, V. L. B. de Jesus, V. Sharma, C. Hofrichter, A. Rudenko, U. Thumm, C. D. Schröter, R. Moshammer, and J. Ullrich, Electron localization in molecular fragmentation of H_2 by carrier-envelope phase stabilized laser pulses, Phys. Rev. Lett. **103**, 213003 (2009).

[84] I. Znakovskaya, P. von den Hoff, S. Zherebtsov, A. Wirth, O. Herrwerth, M. J. J. Vrakking, R. de Vivie-Riedle, and M. F. Kling, Attosecond control of electron dynamics in carbon monoxide, Phys. Rev. Lett. **103**, 103002 (2009).

[85] K. P. Singh, F. He, P. Ranitovic, W. Cao, S. De, D. Ray, S. Chen, U. Thumm, A. Becker, M. M. Murnane, H. C. Kapteyn, I. V. Litvinyuk, and C. L. Cocke, Control of electron localization in deuterium molecular ions using an attosecond pulse train and a many-cycle infrared pulse, Phys. Rev. Lett. **104**, 023001 (2010).

[86] M. F. Kling, C. Siedschlag, I. Znakovskaya, A. J. Verhoef, S. Zherebtsov, F. Krausz, M. Lezius, and M. J. J. Vrakking, Strong-field control of electron localization during molecular dissociation, Mol. Phys. **106**, 455 (2008).

[87] G. Sansone, F. Kelkensberg, J. F. Pérez-Torres, F. Morales, M. F. Kling, W. Siu, O. Ghafur, P. Johnsson, M. Swoboda, E. Benedetti, F. Ferrari, F. L. Lépine, J. L. Sanz-Vicario, S. Zherebtsov, I. Znakovskaya, A. L'Huillier, M. Yu. Ivanov, M. Nisoli, F. Martín, and M. J. J. Vrakking, Electron localization following attosecond molecular photoionization, Nature **465**, 763 (2010).

[88] K. J. Betsch, D. W. Pinkham, and R. R. Jones, Directional emission of multiply charged ions during dissociative ionization in asymmetric two-color laser fields, Phys. Rev. Lett. **105**, 223002 (2010).

[89] Nora G. Kling, K. J. Betsch, M. Zohrabi, S. Zeng, F. Anis, U. Ablikim, Bethany Jochim, Z. Wang, M. Kübel, M. F. Kling, K. D. Carnes, B. D. Esry, and I. Ben-Itzhak, Carrier-envelope phase control over pathway interference in strong-field dissociation of H_2^+, Phys. Rev. Lett. **111**, 163004 (2013).

[90] T. Rathje, A. M. Sayler, S. Zeng, P. Wustelt, H. Figger, B. D. Esry, and G. G. Paulus, Coherent control at its most fundamental: CEP-dependent electron localization in photodissoziation of a H_2^+ molecular ion beam target, Phys. Rev. Lett. **111**, 093002 (2013).

[91] I. Ben-Itzhak, P. Q. Wang, J. F. Xia, A. M. Sayler, M. A. Smith, K. D. Carnes, and B. D. Esry, Dissociation and ionization of H_2^+ by ultrashort intense laser pulses probed by coincidence 3D momentum imaging, Phys. Rev. Lett. **95**, 073002 (2005).

[92] P. Q. Wang, A. M. Sayler, K. D. Carnes, J. F. Xia, M. A. Smith, B. D. Esry, and I. Ben-Itzhak, Dissociation of H_2^+ in intense femtosecond laser fields studied by coincidence 3D momentum imaging, Phys. Rev. A **74**, 043411 (2006).

[93] I. Ben-Itzhak, *"Molecular ion beams interrogated with ultrashort intense laser pulses", in Progress in Ultrafast Intense Laser Science IV*, volume **91** of *Springer Series in Chemical Physics*, Springer, New York, 2009.

[94] J. McKenna, A. M. Sayler, B. Gaire, N. G. Johnson, M. Zohrabi, K. D. Carnes, B. D. Esry, and I. Ben-Itzhak, Permanent dipole transitions remain elusive in HD^+ strong-field dissociation, J. Phys. B: At. Mol. Opt. Phys. **42**, 121003 (2009).

[95] J. McKenna, F. Anis, B. Gaire, N. G. Johnson, M. Zohrabi, K. D. Carnes, B. D. Esry, and I. Ben-Itzhak, Suppressed dissociation of H_2^+ vibrational states by reduced dipole coupling, Phys. Rev. Lett. **103**, 103006 (2009).

[96] I. Ben-Itzhak, Fragmentation of molecular-ion beams in intense ultrashort laser pulses, in *Fragmentation Processes: Topics in Atomic and Molecular Physics*, edited by C. T. Whelan, Cambridge University Press, Cambridge, 2013.

[97] J. McKenna, A. M. Sayler, B. Gaire, N. G. Johnson, K. D. Carnes, B. D. Esry, and I. Ben-Itzhak, Benchmark measurements of H_3^+ nonlinear dynamics in intense ultrashort laser pulses, Phys. Rev. Lett. **103**, 103004 (2009).

[98] J. McKenna, S. Zeng, J. J. Hua, A. M. Sayler, M. Zohrabi, N. G. Johnson, B. Gaire, K. D. Carnes, B. D. Esry, and I. Ben-Itzhak, Frustrated tunneling ionization during laser-induced D_2 fragmentation: Detection of excited metastable D^*atoms, Phys. Rev. A **84**, 043425 (2011).

[99] B. Gaire, J. McKenna, M. Zohrabi, K. D. Carnes, B. D. Esry, and I. Ben-Itzhak, Dynamics of D_3^+ slow dissociation induced by intense ultrashort laser pulses, Phys. Rev. A **85**, 023419 (2012).

[100] A. M. Sayler, J. McKenna, B. Gaire, Nora G. Kling, K. D. Carnes, and I. Ben-Itzhak, Measurements of intense ultrafast laser-driven D_3^+ fragmentation dynamics, Phys. Rev. A **86**, 033425 (2012).

[101] A. M. Sayler, J. McKenna, B. Gaire, Nora G. Kling, K. D. Carnes, B. D. Esry, and I. Ben-Itzhak, Elucidating isotopic effects in intense ultrafast laser-driven D_2H^+ fragmentation, J. Phys. B: At. Mol. Opt. Phys. **47**, 031001 (2014).

[102] A. M. Sayler, P. Q. Wang, K. D. Carnes, B. D. Esry, and I. Ben-Itzhak, Determining laser-induced dissociation pathways of multielectron diatomic molecules: Application to the dissociation of O_2^+ by high-intensity ultrashort pulses, Phys. Rev. A **75**, 063420 (2007).

[103] J. McKenna, A. M. Sayler, B. Gaire, N. G. Johnson, E. Parke, K. D. Carnes, B. D. Esry, and I. Ben-Itzhak, Intensity dependence in the dissociation branching ratio of ND^+ using intense femtosecond laser pulses, Phys. Rev. A **77**, 063422 (2008).

[104] M. Zohrabi, J. McKenna, B. Gaire, N. G. Johnson, K. D. Carnes, S. De, I. A. Bocharova, M. Magrakvelidze, D. Ray, I. V. Litvinyuk, C. L. Cocke, and I. Ben-Itzhak, Vibrationally resolved structure in O_2^+ dissociation induced by intense ultrashort laser pulses, Phys. Rev. A **83**, 053405 (2011).

[105] Bethany Jochim, M. Zohrabi, U. Ablikim, B. Gaire, F. Anis, Tereza Uhlíková, K. D. Carnes, E. Wells, B. D. Esry, and I. Ben-Itzhak, Evidence of the dominant role of multiphoton permanent dipole transitions in strong-field dissociation of NO^{2+}, in preparation .

[106] E. Wells, J. McKenna, A. M. Sayler, B. Jochim, N. Gregerson, R. Averin, M. Zohrabi, K. D. Carnes, and I. Ben-Itzhak, Closed-loop control of vibrational population in CO^{2+}, J. Phys. B: At. Mol. Opt. Phys. **43**, 015101 (2009).

[107] E. Wells, M. Todt, B. Jochim, N. Gregerson, R. Averin, N. G. Wells, N. L. Smolnisky, N. Jastram, J. McKenna, A. M. Sayler, N. G. Johnson, M. Zohrabi, B. Gaire, K. D. Carnes, and I. Ben-Itzhak, Examining the feedback signals used in closed-loop control of intense laser fragmentation of CO^+, Phys. Rev. A **80**, 063402 (2009).

[108] Bethany Jochim, R. Averin, Neal Gregerson, J. McKenna, S. De, D. Ray, M. Zohrabi, B. Bergues, K. D. Carnes, M. F. Kling, I. Ben-Itzhak, and E. Wells, Velocity map imaging as a tool for gaining mechanistic insight from closed-loop control studies of molecular fragmentation, Phys. Rev. A **83**, 043417 (2011).

[109] C. E. Rallis, T. G. Burwitz, P. R. Andrews, M. Zohrabi, R. Averin, S. De, B. Bergues, Bethany Jochim, A. V. Voznyuk, Neal Gregerson, B. Gaire, I. Znakovskaya, J. McKenna, K. D. Carnes, M. F. Kling, I. Ben-Itzhak, and E. Wells, Incorporating real time velocity map image reconstruction into closed-loop coherent control, Rev. Sci. Instrum. (2014), submitted.

[110] B. Manschwetus, T. Nubbemeyer, K. Gorling, G. Steinmeyer, U. Eichmann, H. Rottke, and W. Sandner, Strong laser field fragmentation of H_2: Coulomb explosion without double ionization, Phys. Rev. Lett. **102**, 113002 (2009).

[111] V. Roudnev and B. D. Esry, General theory of carrier-envelope phase effects, Phys. Rev. Lett. **99**, 220406 (2007).

[112] J. J. Hua and B. D. Esry, The role of mass in the carrier-envelope phase effect for H_2^+ dissociation, J. Phys. B: At. Mol. Opt. Phys. **42**, 085601 (2009).

[113] S. Backus, J. Peatross, C. P. Huang, M. M. Murnane, and H. C. Kapteyn, Ti:sapphire amplifier producing millijoule-level, 21-fs pulses at 1 khz, Opt. Lett. **20**, 2000 (1995).

[114] H. Wang, S. Backus, Z. Chang, R. Wagner, K. Kim, X. Wang, D. Umstadter, T. Lei, M. Murnane, and H. Kapteyn, Generation of 10-w average-power, 40-tw peak-power, 24-fs pulses from a Ti:sapphire amplifier system, J. Opt. Soc. Am. B **16**, 1790 (1999).

[115] C. Li, E. Moon, H. Mashiko, C. M. Nakamura, P. Ranitovic, C. M. Maharjan, C. L. Cocke, Z. Chang, and G. G. Paulus, Precision control of carrier-envelope phase in grating based chirped pulse amplifiers, Opt. Exp. **14**, 11468 (2006).

[116] J. Dong and P. Deng, Ti:sapphire crystal used in ultrafast lasers and amplifiers, J. Crys. Growth **261**, 514 (2004).

[117] Q. Fu, F. Seier, S. K. Gayen, and R. R. Alfano, High-average-power kilohertz-repetition-rate sub-100-fs Ti:sapphire amplifier system, Opt. Lett. **22**, 712 (1997).

[118] J. H. Sung, S. K. Lee, T. J. Yu, T. M. Jeong, and J. Lee, 0.1 Hz 1.0 PW Ti:sapphire laser, Opt. Lett. **35**, 3021 (2010).

[119] T. J. Yu, S. K. Lee, J. H. Sung, J. W. Yoon, T. M. Jeong, and J. Lee, Generation of high-contrast, 30 fs, 1.5 PW laser pulses from chirped-pulse amplification Ti:sapphire laser, Opt. Exp. **20**, 10807 (2012).

[120] R. W. Boyd, *Nonlinear Optics*, Second edition. Academic Press, San Diego, 2003.

[121] M. Nisoli, S. D. Silvestri, and O. Svelto, Generation of high energy 10 fs pulses by a new pulse compression technique, Appl. Phys. Lett. **68**, 2793 (1996).

[122] T. Wittmann, B. Horvath, W. Helml, M. G. Schätzel, X. Gu, A. L. Cavalieri, G. G. Paulus, and R. Kienberger, Single-shot carrier-envelope phase measurement of few-cycle laser pulses, Nature Phys. **5**, 357 (2009).

[123] T. Rathje, N. G. Johnson, M. Möller, F. Süßmann, D. Adolph, M. Kübel, R. Kienberger, M. F. Kling, G. G. Paulus, and A. M. Sayler, Review of attosecond resolved measurement and control via carrier-envelope phase tagging with above-threshold ionization, J. Phys. B: At. Mol. Opt. Phys. **45**, 074003 (2012).

[124] J. C. Diels and W. Rudolph, *Ultrashort laser pulse phenomena*, Academic Press, 1996.

[125] D. E. Spence, P. N. Kean, and W. Sibbett, 60-fsec pulse generation from a self-mode-locked Ti:sapphire laser, Opt. Lett. **16**, 42 (1991).

[126] M. Piché, Beam reshaping and self-mode-locking in nonlinear laser resonators, Opt. Commun. **86**, 156 (1991).

[127] H. Telle, G. Steinmeyer, A. Dunlop, J. Stenger, D. Sutter, and U. Keller, Carrier-envelope offset phase control: A novel concept for absolute optical frequency measurement and ultrashort pulse generation, Appl. Phys. B **69**, 327 (1999).

[128] A. Apolonski, A. Poppe, G. Tempea, C. Spielmann, T. Udem, R. Holzwarth, T. W. Hänsch, and F. Krausz, Controlling the phase evolution of few-cycle light pulses, Phys. Rev. Lett. **85**, 740 (2000).

[129] D. J. Jones, S. A. Diddams, J. K. Ranka, A. Stentz, R. S. Windeler, J. L. Hall, and S. T. Cundiff, Carrier-envelope phase control of femtosecond mode-locked lasers and direct optical frequency synthesis, Science **288**, 635 (2000).

[130] S. Koke, C. Grebing, B. Manschwetus, and G. Steinmeyer, Fast f-to-2f interferometer for a direct measurement of the carrier-envelope phase drift of ultrashort amplified laser pulses, Opt. Lett. **33**, 2545 (2008).

[131] M. Kakehata, H. Takada, Y. Kobayashi, K. Torizuka, Y. Fujihira, T. Homma, and H. Takahashi, Single-shot measurement of carrier-envelope phase changes by spectral interferometry, Opt. Lett. **26**, 1436 (2001).

[132] L. Song, C. Zhang, J. Wang, Y. Leng, and R. Li, Accurate measurement of carrier-envelope phase drift for infrared femtosecond laser pulses, Opt. Exp. **16**, 21383 (2008).

[133] D. Strickland and G. Mourou, Compression of amplified chirped optical pulses, Opt. Commun. **55**, 447 (1985).

[134] R. Goldstein, Pockels cell primer, Laser focus **4**, 21 (1968).

[135] E. Moon, C. Li, Z. Duan, J. Tackett, K. L. Corwin, B. R. Washburn, and Z. Chang, Reduction of fast carrier-envelope phase jitter in femtosecond laser amplifiers, Opt. Exp. **14**, 9758 (2006).

[136] Z. Chang, Carrier-envelope phase shift caused by grating-based stretchers and compressors, Appl. Opt. **45**, 8350 (2006).

[137] H. Wang, C. Li, J. Tackett, H. Mashiko, C. Nakamura, E. Moon, and Z. Chang, Power locking of high-repetition-rate chirped pulse amplifiers, Appl. Phys. B: Lasers Opt. **89**, 275 (2007).

[138] C. Li, E. Moon, H. Wang, H. Mashiko, C. Nakamura, J. Tackett, and Z. Chang, Determining the phase-energy coupling coefficient in carrier-envelope phase measurements, Opt. Lett. **32**, 796 (2007).

[139] H. Mashiko, C. M. Nakamura, C. Li, E. Moon, H. Wang, J. Tackett, and Z. Chang, Carrier-envelope phase stabilized 5.6 fs, 1.2 mJ pulses, Appl. Phys. Lett. **90**, 161114 (2007).

[140] M. Nisoli, S. D. Silvestri, O. Svelto, R. Szipöcs, K. Ferencz, C. Spielmann, S. Sartania, and F. Krausz, Compression of high-energy laser pulses below 5 fs, Opt. Lett. **22**, 522 (1997).

[141] B. Schenkel, J. Biegert, U. Keller, C. Vozzi, M. Nisoli, G. Sansone, S. Stagira, S. D. Silvestri, and O. Svelto, Generation of 3.8-fs pulses from adaptive compression of a cascaded hollow fiber supercontinuum, Opt. Lett. **28**, 1987 (2003).

[142] A. Baltuška, M. Uiberacker, E. Goulielmakis, R. Kienberger, V. S. Yakovlev, T. Udem, T. W. Hänsch, and F. Krausz, Phase-controlled amplification of few-cycle laser pulses, IEEE J. Sel. Top. Quant. Electron. **9**, 972 (2003).

[143] T. Pfeifer, C. Spielmann, and G. Gerber, Femtosecond x-ray science, Rep. Prog. Phys. **69**, 443 (2006).

[144] M. Nisoli and G. Sansone, New frontiers in attosecond science, Prog. Quant. Electron. **33**, 17 (2009).

[145] B. E. A. Saleh and M. C. Teich, *Fundamentals of Photonics*, Wiley, 2007.

[146] R. J. Yu and X. J. Chen, *Optical Fibers Research Advances*, Nova Publisher, 2007.

[147] W. T. Mohamed, J. An, and D. E. Kim, *Selected Topics on Optical Fiber Technology*, InTech, 2012.

[148] E. A. J. Marcatili and R. A. Schmeltzer, Hollow metallic and dielectric waveguides for long distance optical transmission and lasers, Bell Syst. Tech. J. **43**, 1783 (1964).

[149] R. L. Abrams, Coupling losses in hollow waveguide laser resonators, IEEE J. Quant. Electron. **8**, 838 (1972).

[150] P. Belland and J. Crenn, Matching of a gaussian beam into hollow oversized circular waveguides, Int. J. Infrared Milli. **10**, 1279 (1989).

[151] T. Pfeifer and M. C. Downer, Direct experimental observation of periodic intensity modulation along a straight hollow-core optical waveguide, J. Opt. Soc. Am. B **24**, 1025 (2007).

[152] A. E. Siegman, *Lasers*, University Science Books, 1986.

[153] T. M. GmbH, TEM Messtechnik GmbH, http://www.tem-messtechnik.de.

[154] M. Trachy, *Photoassociative ionization in cold rubidium*, PhD thesis, Kansas State University, 2008.

[155] P. A. Franken, A. E. Hill, C. W. Peters, and G. Weinreich, Generation of optical harmonics, Phys. Rev. Lett. **7**, 118 (1961).

[156] V. G. Dmitriev, G. G. Gurzadyan, and D. N. Nikogosyan, *Handbook of Nonlinear Optical Crystals*, Springer, 3rd ed., 1999.

[157] J. Lekner, Reflection and refraction by uniaxial crystals, J. Phys.: Condens. Matter **3**, 6121 (1991).

[158] D. Haertle, M. Jazbinšek, G. Montemezzani, and P. Günter, Nonlinear optical coefficients and phase-matching conditions in $Sn_2P_2S_6$, Opt. Exp. **13**, 3765 (2005).

[159] C. M. Griot, CVI Melles Griot, http://www.mellesgriot.com/.

[160] D. N. Nikogosyan, *Nonlinear Optical Crystals: A Complete Survey*, Springer, 2005.

[161] C. Rullière, *Femtosecond Laser Pulses: Principles and Experiments*, Springer, 2005.

[162] Femtolasers, FEMTOMETER Few cycle pulse characterization, http://www.femtolasers.com/FEMTOMETER-TM.120.0.html.

[163] K. Yamane, T. Kito, R. Morita, and M. Yamashita, Experimental and theoretical demonstration of validity and limitations in fringe-resolved autocorrelation measurements for pulses of few optical cycles, Opt. Exp. **12**, 2762 (2004).

[164] J. H. Chung and A. M. Weiner, Ambiguity of ultrashort pulse shapes retrieved from intensity autocorrelation and the power spectrum, IEEE J. Sel. Top. Quant. Electron. **7**, 656 (2001).

[165] A. Watanabe, H. Saito, Y. Ishida, and T. Yajima, Computer-assisted spectrum-resolved SHG autocorrelator for monitoring phase characteristics of femtosecond pulses, Opt. Commun. **63**, 320 (1987).

[166] R. Trebino and D. J. Kane, Using phase retrieval to measure the intensity and phase of ultrashort pulses: frequency-resolved optical gating, J. Opt. Soc. Am. A **10**, 1101 (1993).

[167] D. J. Kane and R. Trebino, Characterization of arbitrary femtosecond pulses using frequency-resolved optical gating, IEEE J. Quant. Electron. **29**, 571 (1993).

[168] R. Trebino, K. W. DeLong, D. N. Fittinghoff, J. N. Sweetser, M. A. Krumbügel, B. A. Richman, and D. J. Kane, Measuring ultrashort laser pulses in the time-frequency domain using frequency-resolved optical gating, Rev. Sci. Instrum. **68**, 3277 (1997).

[169] A. M. Weiner, *Ultrafast Optics*, John Wiley & Sons, 2011.

[170] K. W. DeLong, B. Kohler, K. Wilson, D. N. Fittinghoff, and R. Trebino, Pulse retrieval in frequency-resolved optical gating based on the method of generalized projections, Opt. Lett. **19**, 2152 (1994).

[171] D. J. Kane, Real-time measurement of ultrashort laser pulses using principal component generalized projections, IEEE J. Sel. Top. Quant. Electron. **4**, 278 (1998).

[172] P. O'Shea, M. Kimmel, X. Gu, and R. Trebino, Highly simplified device for ultrashort-pulse measurement, Opt. Lett. **26**, 932 (2001).

[173] G. Stibenz and G. Steinmeyer, Interferometric frequency-resolved optical gating, Opt. Exp. **13**, 2617 (2005).

[174] K. W. DeLong, R. Trebino, and W. E. White, Simultaneous recovery of two ultrashort laser pulses from a single spectrogram, J. Opt. Soc. Am. B **12**, 2463 (1995).

[175] T. S. Clement, D. J. Kane, and A. J. Taylor, Single-shot measurement of the amplitude and phase of ultrashort laser pulses in the violet, Opt. Lett. **20**, 70 (1995).

[176] R. Trebino, *Frequency–Resolved Optical Gating: The Measurement of Ultrashort Laser Pulses*, Kluwer Academic Publishers, 2002.

[177] U. Graf, M. Fieß, M. Schultze, R. Kienberger, F. Krausz, and E. Goulielmakis, Intense few-cycle light pulses in the deep ultraviolet, Opt. Exp. **16**, 18956 (2008).

[178] Nora G. Kling, *Controlling the dynamics of electrcons and nuclei in ultrafast strong laser fields*, PhD thesis, Kansas State University, 2013.

[179] M. Takeda, H. Ina, and S. Kobayashi, Fourier-transform method of fringe-pattern analysis for computer-based topography and interferometry, J. Opt. Soc. Am. **72**, 156 (1982).

[180] K. Yamanouchi and K. Midorikawa, *Multiphoton Processes and Attosecond Physics*, Springer, 2014.

[181] K. Yamanouchi and K. Midorikawa, *Progress in Ultrafast Intense Laser Science: Volume IX*, Springer, 2013.

[182] A. Baltuška, T. Fuji, and T. Kobayashi, Controlling the carrier-envelope phase of ultrashort light pulses with optical parametric amplifiers, Phys. Rev. Lett. **88**, 133901 (2002).

[183] D. Brida, C. Manzoni, D. Polli, and G. Cerullo, Carrier-envelope-phase stable few-optical-cycle pulses from optical parametric amplifiers, in *Advanced optical materials*, page AMD1, Optical Society of America, 2011.

[184] B. E. Schmidt, A. D. Shiner, P. Lassonde, J.-C. Kieffer, P. B. Corkum, D. M. Villeneuve, and F. Légaré, CEP stable 1.6 cycle laser pulses at 1.8 μm, Opt. Exp. **19**, 6858 (2011).

[185] G. Cerullo, A. Baltuška, O. D. Mücke, and C. Vozzi, Few-optical-cycle light pulses with passive carrier-envelope phase stabilization, Laser Photon. Rev. **5**, 323 (2011).

[186] P. B. Corkum, Plasma perspective on strong-field multiphoton ionization, Phys. Rev. Lett. **71**, 1994 (1993).

[187] M. Lewenstein, P. Balcou, M. Ivanov, A. L'Huillier, and P. Corkum, Theory of high-harmonic generation by low-frequency laser fields, Phys. Rev. A **49**, 2117 (1994).

[188] J. L. Krause, K. J. Schafer, and K. C. Kulander, High-order harmonic generation from atoms and ions in the high intensity regime, Phys. Rev. Lett. **68**, 3535 (1992).

[189] C. D. Lin, Anh-Thu Le, Z. Chen, T. Morishita, and R. Lucchese, Strong-field rescattering physics—self-imaging of a molecule by its own electrons, J. Phys. B: At. Mol. Opt. Phys. **43**, 122001 (2010).

[190] D. B. Milošević, G. G. Paulus, D. Bauer, and W. Becker, Above-threshold ionization by few-cycle pulses, J. Phys. B: At. Mol. Opt. Phys. **39**, R203 (2006).

[191] G. G. Paulus, W. Becker, W. Nicklich, and H. Walther, Rescattering effects in above-threshold ionization: a classical model, J. Phys. B: At. Mol. Opt. Phys. **27**, L703 (1994).

[192] G. G. Paulus, F. Lindner, H. Walther, A. Baltuška, E. Goulielmakis, M. Lezius, and F. Krausz, Measurement of the phase of few-cycle laser pulses, Phys. Rev. Lett. **91**, 253004 (2003).

[193] G. G. Paulus, A meter of the "absolute" phase of few-cycle laser pulses, Laser Phys. **15**, 843 (2005).

[194] B. Fischer, *Time resolved studies of* H_2^+ *dissociation with phase-stabilized laser pulses*, PhD thesis, University of Heidelberg, 2010.

[195] A. M. Sayler, T. Rathje, W. Müller, K. Rühle, R. Kienberger, and G. G. Paulus, Precise, real-time, every-single-shot, carrier-envelope phase measurement of ultrashort laser pulses, Opt. Lett. **36**, 1 (2011).

[196] A. M. Sayler, T. Rathje, W. Müller, C. Kürbis, K. Rühle, G. Stibenz, and G. G. Paulus, Real-time pulse length measurement of few-cycle laser pulses using above-threshold ionization, Opt. Exp. **19**, 4464 (2011).

[197] A. M. Sayler, *Measurements of ultrashort intense laser-induced fragmentation of simple molecular ions*, PhD thesis, Kansas State University, 2008.

[198] B. Gaire, *Imaging of slow dissociation of the laser induced fragmentation of molecular ions*, PhD thesis, Kansas State University, 2011.

[199] A. Giusti-Suzor, F. H. Mies, L. F. DiMauro, E. Charron, and B. Yang, Dynamics of H_2^+ in intense laser fields, J. Phys. B: At. Mol. Opt. Phys. **28**, 309 (1995).

[200] J. H. Posthumus, The dynamics of small molecules in intense laser fields, Rep. Prog. Phys. **67**, 623 (2004).

[201] O. Atabek, R. Lefebvre, and T. Nguyen-Dang, Theory of intense laser-induced molecular dissociation: From simulation to control, in *Special Volume, Computational Chemistry*, edited by C. L. Bris, volume **10** of *Handbook of Numerical Analysis*, pages 745 – 802, Elsevier, 2003.

[202] J. F. McCann and J. H. Posthumus, Molecular dynamics in intense laser fields, Phil. Trans. R. Soc. Lond. A **357**, 1309 (1999).

[203] J. D. Alexander, C. R. Calvert, R. B. King, O. Kelly, L. Graham, W. A. Bryan, G. R. A. J. Nemeth, W. R. Newell, C. A. Froud, I. C. E. Turcu, E. Springate, I. D. Williams, and J. B. Greenwood, Photodissociation of D_3^+ in an intense, femtosecond laser field, J. Phys. B: At. Mol. Opt. Phys. **42**, 141004 (2009).

[204] E. Lötstedt and K. Midorikawa, Laser-induced electron localization in a triatomic molecular ion, Phys. Rev. A **88**, 041402 (2013).

[205] E. Lötstedt, T. Kato, and K. Yamanouchi, A classical model of H_3^+ in an intense laser field, J. Phys. B: At. Mol. Opt. Phys. **46**, 235601 (2013).

[206] E. Lötstedt, T. Kato, and K. Yamanouchi, D_3^+ in intense laser fields studied with a quasiclassical model, Phys. Rev. A **85**, 053410 (2012).

[207] E. Lötstedt, T. Kato, and K. Yamanouchi, Classical dynamics of laser-driven D_3^+, Phys. Rev. Lett. **106**, 203001 (2011).

[208] L. J. Frasinski, J. H. Posthumus, J. Plumridge, K. Codling, P. F. Taday, and A. J. Langley, Manipulation of bond hardening in H_2^+ by chirping of intense femtosecond laser pulses, Phys. Rev. Lett. **83**, 3625 (1999).

[209] A. Zavriyev, P. H. Bucksbaum, J. Squier, and F. Saline, Light-induced vibrational structure in H_2^+ and D_2^+ in intense laser fields, Phys. Rev. Lett. **70**, 1077 (1993).

[210] J. T. Lin and T. F. Jiang, Photodissociation of H_2^+ in intense chirped laser fields, Phys. Rev. A **63**, 013408 (2000).

[211] Z. Amitay, A. Baer, M. Dahan, J. Levin, Z. Vager, D. Zajfman, L. Knoll, M. Lange, D. Schwalm, R. Wester, A. Wolf, I. F. Schneider, and A. Suzor-Weiner, Dissociative recombination of vibrationally excited HD^+: State-selective experimental investigation, Phys. Rev. A. **60**, 3769 (1999).

[212] H. Postma, Multiply charged heavy ions produced by energetic plasmas, Phys. Lett. A **31**, 196 (1970).

[213] R. Geller, *Electron cyclotron resonance ion sources and ECR plasmas*, Taylor & Francis Group, 1996.

[214] D. Winklehner, *Ion Beam Extraction From Electron Cyclotron Resonance Ion Sources and The Subsequent Low Energy Beam Transport*, PhD thesis, Michigan State University, 2013.

[215] J. J. Barroso and M. O. Terra, Beam transport in a quadrupole electrostatic system, Brazilian J. Phys. **34** (2004).

[216] M. Marynowski, W. Franzen, and M. El-Batanouny, Analysis of the properties of an electrostatic triplet quadrupole lens used as an electron beam transport device, Rev. Sci. Instrum. **65**, 3718 (1994).

[217] The detector used for molecular beam fragment imaging is comprised of a chevron stack of microchannel plates (MCPs) [391] and a hex delay-line anode [407, 408]. A hit on the MCP generates an electron avalanche, which is further amplified and exits the MCP to impinge on the hex delay-line anode. An electronic signal is extracted through a resistor-capacitor decoupling unit from the MCP, providing a TOF signal. A signal from the delay-line anode, sometimes referred to as a position information signal, is then processed through a differential pre-amplifier. More details are given in Refs. [197, 409]. A schematic of the electronic-signal processing can be found in Appendix C of Ref. [197] and Appendix A of Ref. [178].

[218] I. Ben-Itzhak, *Progress in Ultrafast Intense Laser Science IV*, Springer, 2009.

[219] J. Moseley and J. Durup, Fast ion beam photofragment spectroscopy, Annu. Rev. Phys. Chem. **32**, 53 (1981).

[220] H. Helm, D. P. de Bruijn, and J. Los, Fast neutral-beam photofragment spectroscopy of H_2, Phys. Rev. Lett. **53**, 1642 (1984).

[221] H. Helm and P. C. Cosby, Photodissociation measurement of rovibrational energies and populations of molecules in fast beams, J. Chem. Phys. **86**, 6813 (1987).

[222] J. P. Bouhnik, I. Gertner, B. Rosner, Z. Amitay, O. Heber, D. Zajfman, E. Y. Sidky, and I. Ben-Itzhak, Measurements of the mean lifetime and kinetic-energy release of metastable CO^{2+}, Phys. Rev. A **63**, 032509 (2001).

[223] X. Urbain, B. Fabre, E. M. Staicu-Casagrande, N. de Ruette, V. M. Andrianarijaona, J. Jureta, J. H. Posthumus, A. Saenz, E. Baldit, and C. Cornaggia, Intense-laser-field ionization of molecular hydrogen in the tunneling regime and its effect on the vibrational excitation of H_2^+, Phys. Rev. Lett. **92**, 163004 (2004).

[224] L. P. H. Schmidt, S. Schössler, F. Afaneh, M. Schöffler, K. E. Stiebing, H. Schmidt-Böcking, and R. Dörner, Young-type interference in collisions between hydrogen molecular ions and helium, Phys. Rev. Lett. **101**, 173202 (2008).

[225] SIMION, SIMION Industry standard charged particle optics simulation software, http://simion.com/.

[226] B. D. Esry, A. M. Sayler, P. Q. Wang, K. D. Carnes, and I. Ben-Itzhak, Above threshold Coulomb explosion of molecules in intense laser pulses, Phys. Rev. Lett. **97**, 013003 (2006).

[227] Th. Ergler, A. Rudenko, B. Feuerstein, K. Zrost, C. D. Schröter, R. Moshammer, and J. Ullrich, Spatiotemporal imaging of ultrafast molecular motion: Collapse and revival of the D_2^+ nuclear wave packet, Phys. Rev. Lett. **97**, 193001 (2006).

[228] A. Staudte, D. Pavičić, S. Chelkowski, D. Zeidler, M. Meckel, H. Niikura, M. Schöffler, S. Schossler, B. Ulrich, P. P. Rajeev, T. Weber, T. Jahnke, D. M. Villeneuve, A. D. Bandrauk, C. L. Cocke, P. B. Corkum, and R. Dörner, Attosecond strobing of two-surface population dynamics in dissociating H_2^+, Phys. Rev. Lett. **98**, 073003 (2007).

[229] D. Ray, B. Ulrich, I. A. Bocharova, C. Maharjan, P. Ranitovic, B. Gramkow, M. Magrakvelidze, S. De, I. V. Litvinyuk, A. T. Le, T. Morishita, C. D. Lin, G. G. Paulus, and C. L. Cocke, Large–angle electron diffraction structure in laser-induced rescattering from rare gases, Phys. Rev. Lett. **100**, 143002 (2008).

[230] V. Roudnev and B. D. Esry, HD^+ in a short strong laser pulse: Practical consideration of the observability of carrier-envelope phase effects, Phys. Rev. A **76**, 023403 (2007).

[231] R. Dörner, V. Mergel, O. Jagutzki, L. Spielberger, J. Ullrich, R. Moshammer, and H. Schmidt-Böcking, Cold target recoil ion momentum spectroscopy: a "momentum microscope" to view atomic collision dynamics, Phys. Rep. **330**, 95 (2000).

[232] J. Ullrich, R. Moshammer, A. Dorn, R. Dörner, L. P. H. Schmidt, and H. Schmidt-Böcking, Recoil-ion and electron momentum spectroscopy: reaction-microscopes, Rep. Prog. Phys. **66**, 1463 (2003).

[233] André T. J. B. Eppink and David. H. Parker, Velocity map imaging of ions and electrons using electrostatic lenses: Application in photoelectron and photofragment ion imaging of molecular oxygen, Rev. Sci. Instrum. **68**, 3477 (1997).

[234] L. Dinu, André T. J. B. Eppink, F. Rosca-Pruna, H. L. Offerhaus, W. J. van der Zande, and M. J. J. Vrakking, Application of a time-resolved event counting technique in velocity map imaging, Rev. Sci. Instrum. **73**, 4206 (2002).

[235] T. T. Nguyen-Dang, H. Abou-Rachid, N. A. Nguyen, N. Mireault, J. Lévesque, K. Vijayalakshmi, and S. L. Chin, Perpendicular dissociation of D_2^+ in intense Ti:sapphire laser pulses, Phys. Rev. A **67**, 013405 (2003).

[236] B. A. Khan, S. Saha, and S. S. Bhattacharyya, Kinetic-energy-angle differential distribution of photofragments in multiphoton above-threshold dissociation of D_2^+ by linearly polarized 400-nm intense laser fields: Effects of highly excited electronic states, Phys. Rev. A **73**, 023423 (2006).

[237] A. Zavriyev, P. H. Bucksbaum, H. G. Muller, and D. W. Schumacher, Ionization and dissociation of H_2 in intense laser fields at 1.064 m, 532 nm, and 355 nm, Phys. Rev. A **42**, 5500 (1990).

[238] K. Sändig, H. Figger, and T. W. Hänsch, Dissociation dynamics of H_2^+ in intense laser fields: Investigation of photofragments from single vibrational levels, Phys. Rev. Lett. **85**, 4876 (2000).

[239] D. Pavičić, A. Kiess, T. W. Hänsch, and H. Figger, Intense-laser-field ionization of the hydrogen molecular ions H_2^+ and D_2^+ at critical internuclear distances, Phys. Rev. Lett. **94**, 163002 (2005).

[240] W. A. Bryan, J. McKenna, E. M. L. English, J. Wood, C. R. Calvert, R. Torres, D. S. Murphy, I. C. E. Turcu, J. L. Collier, J. F. McCann, I. D. Williams, and W. R. Newell, Isolated vibrational wavepackets in D_2^+: Defining superposition conditions and wavepacket distinguishability, Phys. Rev. A **76**, 053402 (2007).

[241] A. Kiess, D. Pavičić, T. W. Hänsch, and H. Figger, HD^+ in a beam in intense pulsed laser fields: Dissociation and ionization with high-energy resolution of the fragments, Phys. Rev. A **77**, 053401 (2008).

[242] J. T. Moselev, M. Tadjeddine, J. Durup, J. B. Ozenne, C. Pernot, and A. Tabché-Fouhaillé, High resolution threshold photofragment spectroscopy of O_2^+ ($a^4\Pi_u \rightarrow f^4\Pi_g$), Phys. Rev. Lett. **37**, 891 (1976).

[243] H. Helm, P. C. Cosby, and D. L. Huestis, Laser predissociation spectroscopy of the $f^4\Pi_g$ state of O_2^+, J. Chem. Phys. **73**, 2629 (1980).

[244] C. M. Marian, R. Marian, S. D. Peyerimhoff, B. A. Hessb, R. J. Buenkerb, and G. Seger, *Ab initio* CI calculation of O_2^+ predissociation phenomena induced by a spin-orbit coupling mechanism, Mol. Phys. **46**, 779 (1982).

[245] D. W. Vance, Auger electron emission from clean Mo bombarded by positive ions. III. Effect of electronically excited ions, Phys Rev. A **169**, 263 (1968).

[246] A. Tabché-Fouhaillé, J. Durup, J. T. Moseley, J. B. Ozenne, C. Pernot, and M. Tadjeddine, Laser photofragment spectroscopy of O_2^+ :$a^4\Pi_u \rightarrow ^4\Pi_g$, Chem. Phys. **17**, 81 (1976).

[247] B. R. Turner, J. A. Rutherford, and D. M. J. Compton, Abundance of excited ions in O^+ and O_2^+ ion beams, J. Chem. Phys. **48**, 1602 (1968).

[248] J. Franck and E. G. Dymond, Elementary processes of photochemical reactions, Trans. Faraday Soc. **21**, 536 (1926).

[249] E. U. Condon, Nuclear motions associated with electron transitions in diatomic molecules, Phys. Rev. **32**, 858 (1928).

[250] E. Y. Sidky and I. Ben-Itzhak, Phase-amplitude method for calculating resonance energies and widths for one-dimensional potentials, Phys. Rev. A **60**, 3586 (1999).

[251] A. Hishikawa, S. Liu, A. Iwasaki, and K. Yamanouchi, Light-induced multiple electronic-state coupling of O_2^+ in intense laser fields, J. Chem. Phys. **114**, 9856 (2001).

[252] F. Anis and B. D. Esry, Role of nuclear rotation in dissociation of H_2^+ in a short laser pulse, Phys. Rev. A **77**, 033416 (2008).

[253] F. Anis, *Role of nuclear rotation in* H_2^+ *dissociation by ultrashort laser pulses*, PhD thesis, Kansas State University, 2009.

[254] J. W. Cooper, Photoionization from outer atomic subshells. A model study, Phys. Rev. **128**, 681 (1962).

[255] B. Feuerstein, Th. Ergler, A. Rudenko, K. Zrost, C. Schröter, R. Moshammer, J. Ullrich, T. Niederhausen, and U. Thumm, Complete characterization of molecular dynamics in ultrashort laser fields, Phys. Rev. Lett. **99**, 153002 (2007).

[256] S. De, I. A. Bocharova, M. Magrakvelidze, D. Ray, W. Cao, B. Bergues, U. Thumm, M. F. Kling, I. V. Litvinyuk, and C. L. Cocke, Tracking nuclear wave-packet dynamics in molecular oxygen ions with few-cycle infrared laser pulses, Phys. Rev. A **82**, 013408 (2010).

[257] V. S. Prabhudesai, A. Natan, B. D. Bruner, Y. Silberberg, U. Lev, O. Heber, D. Strasser, D. Schwalm, D. Zajfman, and I. Ben-Itzhak, Effect of linear chirp on strong field photodissociation of H_2^+, J. Korean Phys. Soc. **59**, 2890 (2011).

[258] H. Niikura, V. R. Bhardwaj, F. Legare, I. Litvinyuk, P. Dooley, D. Rayner, M. Y. Ivanov, P. Corkum, and D. Villeneuve, *Strong Field Laser Physics*, volume **134**, Springer, 2008.

[259] V. I. Prokhorenko, A. M. Nagy, S. A. Waschuk, L. S. Brown, R. R. Birge, and R. J. D. Miller, Coherent control of retinal isomerization in bacteriorhodopsin, Science **313**, 5791 (2006).

[260] S. De, I. Znakovskaya, D. Ray, F. Anis, N. G. Johnson, I. A. Bocharova, M. Magrakvelidze, B. D. Esry, C. L. Cocke, I. V. Litvinyuk, and M. F. Kling, Field-free orientation of CO molecules by femtosecond two-color laser fields, Phys. Rev. Lett. **103**, 153002 (2009).

[261] M. Dantus and V. V. Lozovoy, Experimental coherent laser control of physicochemical processes, Chem. Rev. **104**, 1813 (2004).

[262] T. Brixner and G. Gerber, Quantum control of gas-phase and liquid-phase femtochemistry, Chem. Phys. Chem. **4**, 418 (2003).

[263] T. B. P. Nuernberger, G. Vogt and G. Gerber, Femtosecond quantum control of molecular dynamics in the condensed phase, Phys. Chem. Chem. Phys. **9**, 2470 (2007).

[264] B. Kohler, V. V. Yakovlev, J. Che, J. L. Krause, M. Messina, K. R. Wilson, N. Schwentner, R. M. Whitnell, and Y. Yan, Violation of Kohler's rule in the normal-state magnetoresistance of $YBa_2Cu_3O_{7-\delta}$ and $La_2Sr_xCuO_4$, Phys. Rev. Lett. **74**, 3360 (1995).

[265] X. Li, I. Thanopulos, and M. Shapiro, Three-dimensional photodissociation in strong laser fields: Memory-kernel effective-mode expansion, Phys. Rev. A **83**, 033415 (2011).

[266] A. Giusti-Suzor and F. H. Mies, Vibrational trapping and suppression of dissociation in intense laser fields, Phys. Rev. Lett. **68**, 3869 (1992).

[267] J. H. Posthumus, J. Plumridge, L. J. Frasinski, K. Codling, E. J. Divall, A. J. Langley, and P. F. Taday, Slow protons as a signature of zero-photon dissociation of H_2^+ in intense laser fields, J. Phys. B: At. Mol. Opt. Phys. **33**, L563 (2000).

[268] L. J. Frasinski, C. R. Courtney, J. H. Posthumus, K. Codling, P. F. Taday, E. J. Divall, and A. J. Langley, Counterintuitive alignment of H_2^+ in intense femtosecond laser fields, Phys. Rev. Lett. **86**, 2541 (2001).

[269] M. Wollenhaupt, A. Assion, and T. Baumert, *Femtosecond Laser Pulses: Linear Properties, Manipulation, Generation and Measurement*, Springer, 2007.

[270] N. Dudovich, T. Polack, A. Peér, and Y. Silberberg, Simple route to strong-field coherent control, Phys. Rev. Lett. **94**, 083002 (2005).

[271] S. A. Hosseini and D. Goswami, Coherent control of multiphoton transitions with femtosecond pulse shaping, Phys. Rev. A **64**, 033410 (2001).

[272] M. Wollenhaupt, A. Pr´akelt, C. Sarpe-Tudoran, D. Liese, and T. Baumert, Quantum control by selective population of dressed states using intense chirped femtosecond laser pulses, Appl. Phys. B: Lasers Opt. **82**, 183 (2006).

[273] E. W. Lerch, X. C. Dai, E. A. Torres, J. B. Ballard, H. U. Stauffer, and S. R. Leone, Manipulation of ro-vibronic wave packet composition using chirped ultrafast laser pulses, J. Phys. B: At. Mol. Opt. Phys. **41**, 074015 (2008).

[274] B. D. Bruner, H. Suchowski, N. V. Vitanov, and Y. Silberberg, Strong-field spatiotemporal ultrafast coherent control in three-level atoms, Phys Rev. A **81**, 063410 (2010).

[275] S. Ruetzel, C. Stolzenberger, S. Fechner, F. Dimler, T. Brixner, and D. J. Tannor, Molecular quantum control landscapes in von Neumann time-frequency phase space, J. Chem. Phys. **133**, 164510 (2010).

[276] B. Gaire, J. McKenna, F. Anis, M. Zohrabi, J. J. Hua, A. M. Sayler, N. G. Johnson, K. D. Carnes, B. D. Esry, and I. Ben-Itzhak, Molecular fragmentation below the n-photon dissociation threshold in strong laser fields, in preparation .

[277] J. V. Hernández and B. D. Esry, Few-cycle phenomena produced with many-cycle pulses, private communication.

[278] R. E. Moss and I. A. Sadler, Symmetry breaking effects in HD^+, Mol. Phys. **61** (1987).

[279] J. Macek and K. A. Jerjian, Adiabatic hyperspherical treatment of HD^+, Phys. Rev. A **33**, 233 (1986).

[280] B. D. Esry and H. R. Sadeghpour, Adiabatic formulation of heteronuclear hydrogen molecular ion, Phys. Rev. A **60**, 3604 (1999).

[281] I. Ben-Itzhak, E. Wells, K. D. Carnes, V. Krishnamurthi, O. L. Weaver, and B. D. Esry, Symmetry breakdown in ground state dissociation of HD^+, Phys. Rev. Lett. **85**, 58 (2000).

[282] E. Wells, K. D. Carnes, B. D. Esry, and I. Ben-Itzhak, Charge transfer and elastic scattering in very slow H^++D($1s$) half collisions, Phys. Rev. Lett. **86**, 4803 (2001).

[283] E. Wells, B. D. Esry, K. D. Carnes, and I. Ben-Itzhak, Asymmetric branching ratio for the dissociation of $HD^+(1s\sigma)$, Phys. Rev. A **62**, 062707 (2000).

[284] H. Xu, J.-P. Maclean, D. E. Laban, W. C. Wallace, D. Kielpinski, R. T. Sang, and I. V. Litvinyuk, Carrier-envelope-phase-dependent dissociation of hydrogen, New J. Phys. **15**, 023034 (2013).

[285] X. Xie, K. Doblhoff-Dier, S. Roither, M. S. Schöffler, D. Kartashov, H. Xu, T. Rathje, G. G. Paulus, A. Baltuška, S. Gräfe, and M. Kitzler, Attosecond-recollision-controlled selective fragmentation of polyatomic molecules, Phys. Rev. Lett. **109**, 243001 (2012).

[286] S. Miura, T. Ando, K. Ootaka, A. Iwasaki, H. Xu, T. Okino, K. Yamanouchi, D. Hoff, T. Rathje, G. G. Paulus, M. Kitzler, A. Baltuška, G. Sansone, and M. Nisoli, Carrier-envelope-phase dependence of asymmetric C—D bond breaking in C_2D_2 in an intense few-cycle laser field, Chem. Phys. Lett. **595–596**, 61 (2014).

[287] A. D. Bandrauk and S. Chelkowski, Asymmetric electron-nuclear dynamics in two-color laser fields: Laser phase directional control of photofragments in H_2^+, Phys. Rev. Lett. **84**, 3562 (2000).

[288] T. Kanai and H. Sakai, Numerical simulations of molecular orientation using strong, nonresonant, two-color laser fields, J. Chem. Phys. **115**, 5492 (2001).

[289] R. Tehini and D. Sugny, Field-free molecular orientation by non-resonant and quasi-resonant two-color laser pulses, Phys. Rev. A **77**, 023407 (2008).

[290] M. Muramatsu, Field-free molecular orientation by an intense nonresonant two-color laser field with a slow turn on and rapid turn off, Phys. Rev. A **79**, 011403 (2009).

[291] V. Tagliamonti, H. Chen, and G. N. Gibson, Internuclear-separation-resolved asymmetric dissociation of I_2 in a two-color laser field, Phys. Rev. A **84**, 043424 (2011).

[292] P. Nuernberger, D. Wolpert, H. Weiss, and G. Gerber, Femtosecond quantum control of molecular bond formation, Proc. Natl. Acad. Sci. **107**, 10366 (2010).

[293] B. J. Sussman, D. Townsend, M. Yu. Ivanov, and A. Stolow, Dynamic stark control of photochemical processes, Science **314**, 278 (2006).

[294] R. J. Levis, G. M. Menkir, and H. Rabitz, Selective bond dissociation and rearrangement with optimally tailored, strong-field laser pulses, Science **292**, 709 (2001).

[295] P. Anfinrud, R. de Vivie-Riedle, and V. Engel, Ultrafast detection and control of molecular dynamics, Proc. Natl. Acad. Sci. **96**, 8328 (1999).

[296] C. Zhou, S. Matsika, M. Kotur, and T. C. Weinacht, Fragmentation pathways in the uracil radical cation, J. Phys. Chem. A **116**, 9217 (2012).

[297] B. D. Esry, H. R. Sadeghpour, E. Wells, and I. Ben-Itzhak, Charge exchange in slow H^++D($1s$) collisions, J. Phys. B: At. Mol. Opt. Phys. **33**, 5329 (2000).

[298] B. Dutta, R. Bhattacharya, and S. S. Bhattacharyya, Resonance enhancement of two-frequency multiphoton dissociation of HD^+, Phys. Rev. A **80**, 043413 (2009).

[299] R. Bhattacharya and S. S. Bhattacharyya, Dissociation dynamics of HD^+ in intense femtosecond laser pulses by one-dimensional wave-packet propagation, Phys. Rev. A **79**, 043415 (2009).

[300] S. Chatterjee and S. S. Bhattacharyya, Ultrashort-laser-pulse-mediated asymmetry in the branching of dissociated fragments of HD^+: Effects of a weak third pulse and carrier envelope phase of the dissociating pulse, Phys. Rev. A **88**, 023408 (2013).

[301] R. Bhattacharya, S. Chatterjee, and S. S. Bhattacharyya, Preparation and probing of coherent vibrational wave packets in the ground electronic state of HD^+, Phys. Rev. A **85**, 033424 (2012).

[302] B. Dutta, S. Sen, S. Saha, and S. S. Bhattacharyya, Branching and angular distribution of photofragments in two-frequency intense-field multiphoton dissociation of HD^+, Phys. Rev. A **68**, 013401 (2003).

[303] S. Chatterjee, B. Dutta, and S. S. Bhattacharyya, Asymmetric branching of dissociated photofragments of HD^+ in an intense femtosecond laser field, Phys. Rev. A **83**, 063413 (2011).

[304] Q. Su, Y. Han, and S. Cong, Quantum control of multi-photon dissociation of HCl^+ with intense femtosecond laser pulses, J. Chem. Phys. **138**, (2013).

[305] B. Rigsbee and B. D. Esry, in preparation .

[306] J. Posthumus, *Molecules and Clusters in Intense Laser Fields*, Cambridge University Press, 2001.

[307] S. I. Chu and D. Telnov, Beyond the Floquet theorem: generalized Floquet formalisms and quasienergy methods for atomic and molecular multiphoton processes in intense laser fields, Phys. Rep. **390**, 1 (2004).

[308] J. McKenna, M. Zohrabi, B. Gaire, D. Ray, K. D. Carnes, D. Ursrey, J. Hernandez, F. Anis, B. D. Esry, and I. Ben-Itzhak, Coherent control over dissociation of a molecular ion beam, J. Phys.: Conf. Ser. **388**, 032045 (2012).

[309] C. Wunderlich, H. Figger, and T. W. Hänsch, Tunneling through light-induced molecular potentials in Ar_2^+, Phys. Rev. A **62**, 023401 (2000).

[310] I. D. Williams, P. McKenna, B. Srigengan, I. M. G. Johnston, W. A. Bryan, J. H. Sanderson, A. El-Zein, T. R. J. Goodworth, W. R. Newell, P. F. Taday, and A. J. Langley, Fast-beam study of H_2^+ ions in an intense femtosecond laser field, J. Phys. B: At. Mol. Opt. Phys. **33**, 2743 (2000).

[311] J. V. Hernandez and B. D. Esry, Attosecond pulse trains as multi-color coherent control, arXiv:0911.2693.

[312] B. D. Esry, Pathway analysis for understanding the two-color dissociation of HD^+, private communication, 2012.

[313] A. Mokhtari, P. Cong, J. L. Herek, and A. H. Zewail, Direct femtosecond mapping of trajectories in a chemical reaction, Nature **348**, 225 (1990).

[314] F. C. D. Schryver, S. D. Feyter, and G. Schweitzer, editors, *Femtochemistry: With the Nobel Lecture of A. Zewail*, Wiley-VCH Verlag GmbH, 2001.

[315] Th. Ergler, A. Rudenko, B. F. K. Zrost, C. D. Schröter, and R. M. J. Ullrich, Ultrafast mapping of H_2^+ (D_2^+) nuclear wave packets using time-resolved Coulomb explosion imaging, J. Phys. B: At. Mol. Opt. Phys. **39**, S493 (2006).

[316] C. R. Calvert, J. McKenna, W. A. Bryan, J. Wood, E. M. L. English, I. C. E. Turcu, J. M. Smith, K. G. Ertel, O. Cheklov, E. J. Divall, W. R. Newell, and I. D. Williams, Dynamic imaging of a dissociative D_2^+ nuclear wavepacket in intense laser fields, J. Phys.: Conf. Ser. **58**, 379 (2007).

[317] I. A. Bocharova, A. S. Alnaser, U. Thumm, T. Niederhausen, D. Ray, C. L. Cocke, and I. V. Litvinyuk, Time-resolved Coulomb-explosion imaging of nuclear wave-packet dynamics induced in diatomic molecules by intense few-cycle laser pulses, Phys. Rev. A **83**, 013417 (2011).

[318] A. H. Zewail, Femtochemistry:Atomic-scale dynamics of the chemical bond, J. Phys. Chem. A **104**, 5660 (2000).

[319] H. Stapelfeldt, E. Constant, and P. B. Corkum, Wave packet structure and dynamics measured by Coulomb explosion, Phys. Rev. Lett. **74**, 3780 (1995).

[320] S. Chelkowski, P. B. Corkum, and A. D. Bandrauk, Femtosecond Coulomb explosion imaging of vibrational wave functions, Phys. Rev. Lett. **82**, 3416 (1999).

[321] A. D. Bandrauk and S. Chelkowski, On laser Coulomb explosion imaging of proton motion, Chem. Phys. Lett. **336**, 518 (2001).

[322] A. D. Bandrauk and S. S. Chelkowski, Dynamic imaging of nuclear wave functions with ultrashort UV laser pulses, Phys. Rev. Lett. **87**, 273004 (2001).

[323] B. Feuerstein and U. Thumm, Mapping of coherent and decohering nuclear wave-packet dynamics in D_2^+ with ultrashort laser pulses, Phys. Rev. A **67**, 063408 (2003).

[324] F. Anis and B. D. Esry, Enhancing the intense field control of molecular fragmentation, Phys. Rev. Lett. **109**, 133001 (2012).

[325] A. S. Alnaser, B. Ulrich, X. M. Tong, I. V. Litvinyuk, C. M. Maharjan, P. Ranitovic, T. Osipov, R. Ali, S. Ghimire, Z. Chang, C. D. Lin, and C. L. Cocke, Simultaneous real-time tracking of wave packets evolving on two different potential curves in H_2^+ and D_2^+, Phys. Rev. A **72**, 030702 (2005).

[326] F. Légaré, K. F. Lee, I. V. Litvinyuk, P. W. Dooley, A. D. Bandrauk, D. M. Villeneuve, and P. B. Corkum, Imaging the time-dependent structure of a molecule as it undergoes dynamics, Phys. Rev. A **72**, 052717 (2005).

[327] Th. Ergler, A. Rudenko, B. F. K. Zrost, C. D. Schröter, and R. M. J. Ullrich, Time-resolved imaging and manipulation of H_2 fragmentation in intense laser fields, Phys. Rev. Lett. **95**, 093001 (2005).

[328] J. McKenna, C. R. Calvert, W. A. Bryan, E. M. L. English, J. Wood, D. S. Murphy, I. C. E. Turcu, J. M. Smith, K. G. Ertel, O. Chekhlov, E. J. Divall, J. F. McCann, W. R. Newell, and I. D. Williams, Imaging quantum vibrations on an ultrashort timescale: the deuterium molecular ion, J. Phys.: Conf. Ser. **58**, 375 (2007).

[329] C. R. Calvert, W. A. Bryan, W. R. Newell, and I. D. Williams, Time-resolved studies of ultrafast wavepacket dynamics in hydrogen molecules, Phys. Rep. **491**, 1 (2010).

[330] A. González-Castrillo, J. F. Pérez-Torres, A. Palacios, and F. Martín, Probing vibrational wave packets in molecular excited states, Theor. Chem. Acc. **128**, 735 (2011).

[331] J. Mckenna, W. A. Bryan, C. R. Calvert, E. M. L. English, J. Wood, D. S. Murphy, I. C. E. Turcu, J. M. Smith, K. G. Ertel, O. Chekhlov, E. J. Divall, J. F. Mccann, W. R. Newell, and I. D. Williams, Observing time-dependent vibrational quantum dynamics in deuterium hydride molecular ions, J. Mod. Opt. **54**, 1127 (2007).

[332] H. Katsuki, H. Chiba, B. Girard, C. Meier, and K. Ohmori, Visualizing picometric quantum ripples of ultrafast wave-packet interference, Science **311**, 1589 (2006).

[333] E. Goll, G. Wunner, and A. Saenz, Formation of ground-state vibrational wave packets in intense ultrashort laser pulses, Phys. Rev. Lett. **97**, 103003 (2006).

[334] Th. Ergler, B. Feuerstein, A. Rudenko, K. Zrost, C. D. Schröter, R. Moshammer, and J. Ullrich, Quantum-phase resolved mapping of ground-state vibrational D_2 wave packets via selective depletion in intense laser pulses, Phys. Rev. Lett. **97**, 103004 (2006).

[335] I. V. Hertel and W. Radloff, Ultrafast dynamics in isolated molecules and molecular clusters, Rep. Prog. Phys. **69**, 1897 (2006).

[336] C. Altucci, R. Velotta, and J. P. Marangos, Ultra-fast dynamic imaging: an overview of current techniques, their capabilities and future prospects, J. Mod. Opt. **57**, 916 (2010).

[337] S. Baker, J. S. Robinson, C. A. Haworth, H. Teng, R. A. Smith, C. C. Chirilă, M. Lein, J. W. G. Tisch, and J. P. Marangos, Probing proton dynamics in molecules on an attosecond time scale, Science **312**, 424 (2006).

[338] A. Palacios, A. González-Castrillo, and F. Martín, Molecular interferometer to decode attosecond electron-nuclear dynamics, Proc. Natl. Acad. Sci. **111**, 3973 (2014).

[339] P. Instrumente, Physik Instrumente, `http://www.pimicos.com/index.html`.

[340] Point Grey Chameleon USB 2.0 Camera – Edmund optics, `http://http://www.edmundoptics.com/`.

[341] M. Kakehata, H. Takada, K. Torizuka, R. Ueda, and M. Obara, Measurement of high-intensity laser pulse widths by use of tunneling ionization of atoms and ions, J. Opt. Soc. Am. B **17**, 1490 (2000).

[342] W. A. Bryan, I. C. E. Turcu, J. M. Smith, E. J. Divall, C. J. Hooker, S. J. Hawkes, A. J. Langley, J. L. Collier, E. M. L. English, J. Wood, S. L. Stebbings, W. R. Newell, J. McKenna, C. R. Calvert, and I. D. Williams, Tunnel ionization as a high-dynamic range at-focus ultrafast pulse measurement, Central Laser Facility Annual Report (2006).

[343] B. D. Esry and I. Ben-Itzhak, Time-dependent dynamics of an intense laser-induced above-threshold Coulomb explosion, Phys. Rev. A **82**, 043409 (2010).

[344] Y. Liu, X. Liu, Y. Deng, C. Wu, H. Jiang, and Q. Gong, Selective steering of molecular multiple dissociative channels with strong few-cycle laser pulses, Phys. Rev. Lett. **106**, 073004 (2011).

[345] K. J. Betsch, N. G. Johnson, B. Bergues, M. Kübel, O. Herrwerth, A. Senftleben, I. Ben-Itzhak, G. G. Paulus, R. Moshammer, J. Ullrich, M. F. Kling, and R. R. Jones, Controlled directional ion emission from several fragmentation channels of CO driven by a few-cycle laser field, Phys. Rev. A **86**, 063403 (2012).

[346] I. Znakovskaya, P. von den Hoff, N. Schirmel, G. Urbasch, S. Zherebtsov, B. Bergues, R. de Vivie-Riedle, K.-M. Weitzel, and M. F. Kling, Waveform control of orientation-dependent ionization of DCl in few-cycle laser fields, Phys. Chem. Chem. Phys. **13**, 8653 (2011).

[347] D. Mathur, K. Dota, A. K. Dharmadhikari, and J. A. Dharmadhikari, Carrier-envelope-phase effects in ultrafast strong-field ionization dynamics of multielectron systems: Xe and CS_2, Phys. Rev. Lett. **110**, 083602 (2013).

[348] I. Sánchez and F. Martín, Origin of unidentified structures in resonant dissociative photoionization of H_2, Phys. Rev. Lett. **79**, 1654 (1997).

[349] C. Bottcher and K. Docken, Autoionizing states of the hydrogen molecule, J. Phys. B: At. Mol. Opt. Phys. **7**, L5 (1974).

[350] S. L. Guberman, The doubly excited autoionizing states of H_2, J. Chem. Phys. **78**, 1404 (1983).

[351] J. Fernández and F. Martín, Autoionizing $^1\Sigma_u^+$ and $^1\Pi_u$ states of H_2 above the third and fourth ionization thresholds, J. Phys. B: At. Mol. Opt. Phys. **34**, 4141 (2001).

[352] I. Sánchez and F. Martín, Doubly excited autoionizing states of H_2 above the second ionization threshold: the Q_2 resonance series, J. Chem. Phys. **110**, 6702 (1999).

[353] F. Martín, Ionization and dissociation using B-splines: photoionization of the hydrogen molecule, J. Phys. B: At. Mol. Opt. Phys. **32**, R197 (1999).

[354] J. D. Bozek, J. E. Furst, T. J. Gay, H. Gould, A. L. D. Kilcoyne, J. R. Machacek, F. Martín, K. W. McLaughlin, and J. L. Sanz-Vicario, Production of excited atomic hydrogen and deuterium from H_2 and D_2 photodissociation, J. Phys. B: At. Mol. Opt. Phys. **39**, 4871 (2006).

[355] J. L. Sanz-Vicario, J. F. Pérez-Torres, F. Morales, E. Plessiat, and F. Martín, Probing H_2 autoionizing states with femto– and attosecond laser pulses, J. Phys.: Conf. Ser. **194**, 012013 (2009).

[356] I. Sánchez and F. Martín, The doubly excited states of the H_2 molecule, J. Chem. Phys. **106**, 7720 (1997).

[357] M. Glass-Maujean, Photodissociation of doubly excited states of H_2, HD, and D_2, J. Chem. Phys. **85**, 4830 (1986).

[358] M. Glass-Maujean, Photodissociation of doubly excited states of H_2: Emission of balmer lines, J. Chem. Phys. **89**, 2839 (1988).

[359] I. Borges Jr and C. E. Bielschowsky, Doubly excited states of molecular hydrogen: theoretical absorption and photodissociation cross sections, J. Phys. B: At. Mol. Opt. Phys. **33**, 1713 (2000).

[360] M. Leventhal, R. T. Robiscoe, and K. R. Lea, Velocity distribution of metastable H atoms produced by dissociative excitation of H_2, Phys. Rev. **158**, 49 (1967).

[361] R. Clampitt, H($2s$) atoms produced by dissociative excitation of molecules, Phys. Lett. A **28**, 581 (1969).

[362] M. Misakian and J. C. Zorn, Dissociative excitation of molecular hydrogen by electron impact, Phys. Rev. A **6**, 2180 (1972).

[363] J. J. Spezeski, O. F. Kalman, and L. C. McIntyre, Time-of-flight study of H($2s$) and D($2s$) produced by electron impact on H_2 and D_2: Fast peaks, Phys. Rev. A **22**, 1906 (1980).

[364] R. S. Freund, J. A. Schiavone, and D. F. Brader, Dissociative excitation of H_2: Spectral line shapes and electron impact cross sections of the Balmer lines, J. Chem. Phys. **64**, 1122 (1976).

[365] A. K. Edwards and Q. Zheng, Excitation of the $Q_1\,{}^1\Sigma_g^+$ doubly excited state of H_2 by electron impact, J. Phys. B: At. Mol. Opt. Phys. **34**, 1539 (2001).

[366] M. Glass-Maujean, H. Frohlich, and P. Martin, H_2 doubly-excited-state assignment from the determination of the orbital state of the $H^*(n{=}3)$ photodissociation fragments, Phys. Rev. A **52**, 4622 (1995).

[367] M. Glass-Maujean and H. Schmoranzer, Dissociation dynamics of doubly excited states of molecular hydrogen, J. Phys. B: At. Mol. Opt. Phys. **38**, 1093 (2005).

[368] J. L. Sanz-Vicario, H. Bachau, and F. Martín, Time-dependent theoretical description of molecular autoionization produced by femtosecond XUV laser pulses, Phys. Rev. A **73**, 033410 (2006).

[369] F. Martín, J. Fernández, T. Havermeier, L. Foucar, T. Weber, K. Kreidi, M. Schöffler, L. Schmidt, T. Jahnke, O. Jagutzki, A. Czasch, E. Benis, T. Osipov, A. Landers, A. Belkacem, M. Prior, H. Schmidt-Böcking, C. L. Cocke, and R. Dörner, Single photon-induced symmetry breaking of H_2 dissociation, Science **315**, 629 (2007).

[370] B. H. Bransden and C. J. Joachain, *Physics of Atoms and Molecules*, volume 2nd Ed., Prentice-Hall, New York, 2003.

[371] Y. Wang, J. V. Hernández, M. Zohrabi, B. Berry, U. Ablikim, Nora G. Kling, Travis Severt, B. Jochim, K. D. Carnes, I. Ben-Itzhak, and B. D. Esry, Significant carrier-envelope phase effects for intense, many-cycle laser pulses, in preparation .

[372] R. H. Stolen and C. Lin, Self-phase-modulation in silica optical fibers, Phys. Rev. A **17**, 1448 (1978).

[373] L. G. Gouy, *Sur une propriété nouvelle des ondes lumineuses*, volume **110** of *Mélanges scientifiques*, Gauthier-Villars, 1890.

[374] F. Lindner, G. G. Paulus, H. Walther, A. Baltuška, E. Goulielmakis, M. Lezius, and F. Krausz, Gouy phase shift for few-cycle laser pulses, Phys. Rev. Lett. **92**, 113001 (2004).

[375] W. C. Wiley and I. H. McLaren, Time-of-flight mass spectrometer with improved resolution, Rev. Sci. Instrum. **26**, 1150 (1955).

[376] P. B. Corkum, Plasma perspective on strong field multiphoton ionization, Phys. Rev. Lett. **71**, 1994 (1993).

[377] M. Lundqvist, P. Baltzer, D. Edvardsson, L. Karlsson, and B. Wannberg, Novel time of flight instrument for Doppler free kinetic energy release spectroscopy, Phys. Rev. Lett. **75**, 1058 (1995).

[378] M. Lundqvist, D. Edvardsson, P. Baltzer, and B. Wannberg, Doppler-free kinetic energy release spectrum of N_2^{2+}, J. Phys. B: At. Mol. Opt. Phys. **29**, 1489 (1996).

[379] M. Lundqvist, D. Edvardsson, P. Baltzer, M. Larsson, and B. Wannberg, Observation of predissociation and tunnelling processes in O_2^{2+}: a study using Doppler free kinetic energy release spectroscopy and *ab initio* CI calculations, J. Phys. B: At. Mol. Opt. Phys. **29**, 499 (1996).

[380] D. Edvardsson, M. Lundqvist, P. Baltzer, B. Wannberg, and S. Lunell, Doppler-free kinetic energy release spectrum of NO^{2+} and *ab initio* CI calculations, Chem. Phys. Lett. **256**, 341 (1996).

[381] L. Ishikawa, T. Odagiri, K. Yachi, N. Ohno, T. Tsuchida, M. Kitajima, and N. Kouchi, Doubly excited states of H_2 as studied by angle-resolved electron energy loss spectroscopy in coincidence with detecting Lyman-α photons, J. Phys. B: At. Mol. Opt. Phys. **44**, 065203 (2011).

[382] T. Odagiri, Y. Kumagai, M. Nakano, T. Tanabe, I. H. Suzuki, M. Kitajima, and N. Kouchi, Formation of metastable atomic hydrogen in the $2s$ state from symmetry-resolved doubly excited states of molecular hydrogen, Phys. Rev. A **84**, 053401 (2011).

[383] E. M. García, J. A. Ruiz, S. Menmuir, E. Rachlew, P. Erman, A. Kivimäki, M. Glass-Maujean, R. Richter, and M. Coreno, Fluorescence study of doubly excited states of molecular hydrogen, J. Phys. B: At. Mol. Opt. Phys. **39**, 205 (2006).

[384] M. Glass-Maujean, S. Klumpp, L. Werner, A. Ehresmann, and H. Schmoranzer, Photodissociation of doubly excited states of H_2 into $H(2s)$ and $H(2p)$ fragments, J. Phys. B: At. Mol. Opt. Phys. **37**, 2677 (2004).

[385] S. Arai, T. Kamosaki, M. Ukai, K. Shinsaka, Y. Hatano, Y. Ito, H. Koizumi, A. Yagishita, K. Ito, and K. Tanaka, Lyman–α, Lyman–α coincidence detection in the photodissociation of doubly excited molecular hydrogen into two $H(2p)$ atoms, J. Chem. Phys. **88**, 3016 (1988).

[386] A. K. Mohapatra, T. R. Jackson, and C. S. Adams, Coherent optical detection of highly excited Rydberg states using electromagnetically induced transparency, Phys. Rev. Lett. **98**, 113003 (2007).

[387] T. F. Gallagher, *Rydberg Atoms*, Cambridge University Press, 2005.

[388] M. J. Rakovic and S. Chu, Ionization of hydrogen atoms by static and circularly polarized fields: Classical adiabatic theory, J. Phys. B: At. Mol. Opt. Phys. **31**, 1989 (1998).

[389] W. E. Cooke and T. F. Gallagher, Dependence of Rydberg-state field-ionization thresholds on $\mid m_l \mid$, Phys. Rev. A **17**, 1226 (1978).

[390] F. Merkt, R. J. Rednall, S. R. Mackenzie, and T. P. Softley, Electric field ionization of high Rydberg states of Ar with sequences of identical pulses, Phys. Rev. Lett. **76**, 3526 (1996).

[391] J. L. Wiza, Microchannel plate detectors, Nucl. Instrum. and Methods **162**, 587 (1979).

[392] A. K. Chaplik, Ionization of highly excited atoms near a metallic surface, J. Exp. Theor. Phys. **27**, 178 (1968).

[393] W. Stephens, A pulsed mass spectrometer with time dispersion, Phys. Rev. **69**, 691 (1946).

[394] A. Cameron and D. Eggers, An ion "velocitron", Rev. Sci. Instrum. **19**, 605 (1948).

[395] M. Guilhaus, Principles and instrumentation in time–of–flight mass spectrometry, J. Mass Spectrom. **30**, 1519 (1995).

[396] P. Lan, E. J. Takahashi, K. Liu, Y. Fu, and K. Midorikawa, Carrier envelope phase dependence of electron localization in the multicycle regime, New J. Phys. **15**, 063023 (2013).

[397] K. S. Kang, K. Kim, J. Lee, J. Lee, C. M. Kim, and C. H. Nam, Carrier-envelope-phase-dependent above-threshold ionization of xenon observed with multi-cycle laser pulses, Opt. Exp. **22**, 3684 (2014).

[398] V. Roudnev and B. D. Esry, HD^+ photodissociation in the scaled coordinate approach, Phys. Rev. A **71**, 013411 (2005).

[399] D. Yang and S. Cong, Nuclear interference in dissociating of HD^+ in ultrashort laser fields, Phys. Rev. A **84**, 013424 (2011).

[400] G. K. Paramonov and O. Kühn, State-selective vibrational excitation and dissociation of H_2^+ by strong infrared laser pulses: Below-resonant versus resonant laser fields and electron-field following, J. Phys. Chem. A **116**, 11388 (2012).

[401] E. Cormier and P. Lambropoulos, Effect of the initial phase of the field in ionization by ultrashort laser pulses, Eur. Phys. J. D **2**, 15 (1998).

[402] T. Nakajima and E. Cormier, Effects of the carrier-envelope phase of chirped laser pulses in the multiphoton ionization regime, Opt. Lett. **32**, 2879 (2007).

[403] T. Nakajima and S. Watanabe, Effects of the carrier-envelope phase in the multiphoton ionization regime, Phys. Rev. Lett. **96**, 213001 (2006).

[404] M. J. Abel, T. Pfeifer, A. Jullien, P. M. Nagel, M. J. Bell, D. M. Neumark, and S. R. Leone, Carrier-envelope phase-dependent quantum interferences in multiphoton ionization, J. Phys. B: At. Mol. Opt. Phys. **42**, 075601 (2009).

[405] M. Abel, D. M. Neumark, S. R. Leone, and T. Pfeifer, Classical and quantum control of electrons using the carrier-envelope phase of strong laser fields, Laser Photon. Rev. **5**, 352 (2011).

[406] A. Jullien, L. Canova, O. Albert, D. Boschetto, L. Antonucci, Y.-H. Cha, J. Rousseau, P. Chaudet, G. Chriaux, J. Etchepare, S. Kourtev, N. Minkovski, and S. Saltiel, Spectral broadening and pulse duration reduction during cross-polarized wave generation: influence of the quadratic spectral phase, Appl. Phys. B **87**, 595 (2007).

[407] O. Jagutzki, A. Cerezo, A. Czasch, R. Dorner, M. Hattass, M. Huang, V. Mergel, U. Spillmann, K. Ullmann-Pfleger, T. Weber, H. Schmidt-Bocking, and G. Smith, Multiple hit read-out of a microchannel plate detector with a three-layer delay-line anode, in *Nuclear Science Symposium Conference Record, 2001 IEEE*, volume **2**, pages 850–854 vol.2, 2001.

[408] RoentDek, RoentDek Handels GmbH, `http://www.roentdek.com`.

[409] A. Staudte, *Subfemtosecond electron dynamics of* H_2 *in strong fields*, PhD thesis, Johann Wolfgang Goethe Universität, 2005.

Appendix A

Optics Layout

The schematic layout of our optics table (provided by Ben Berry) is shown in Fig. A.1.

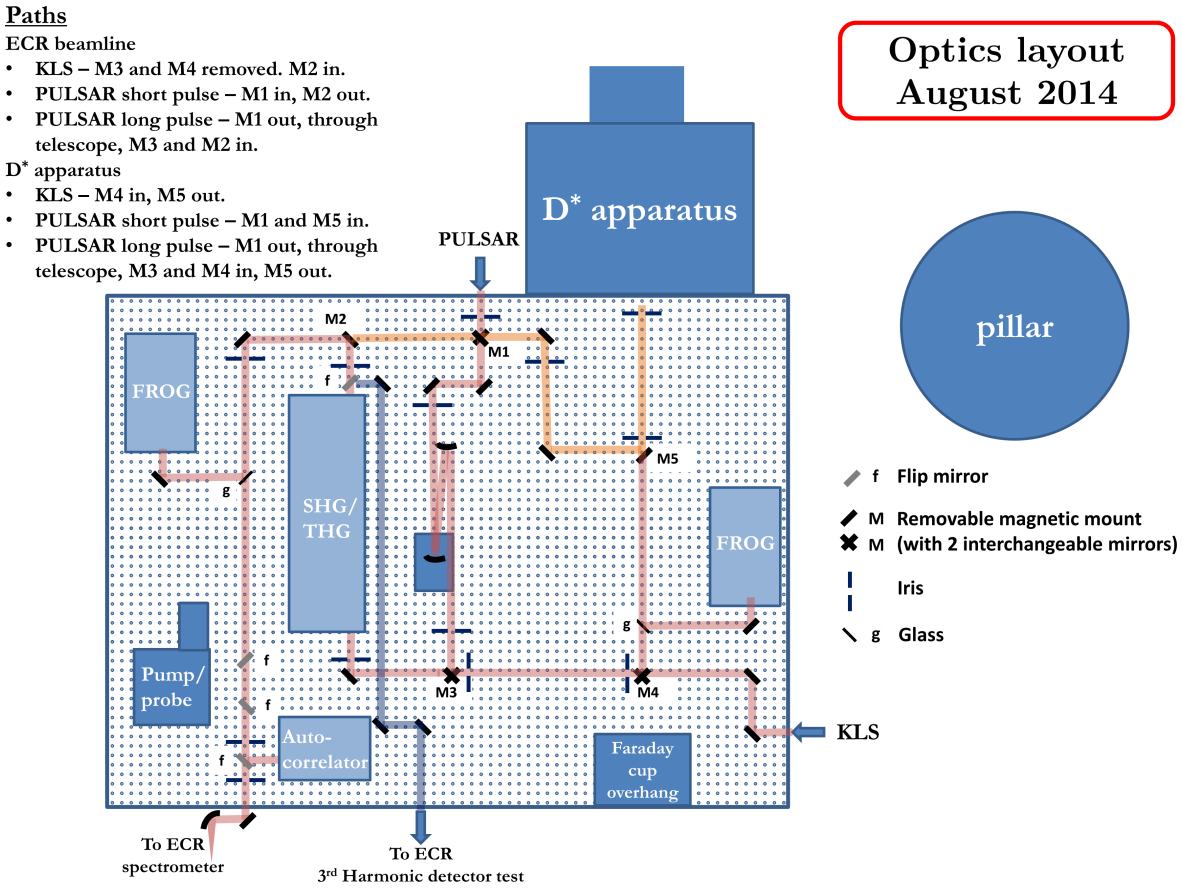

Figure A.1: The schematic layout of our optics table.

Appendix B

Third Harmonic Generation

In section 3.3.4, we studied laser-induced dissociation of O_2^+ using laser pulses with various wavelengths. Careful inspection unveils an apparent suppression in the dissociation of particular vibrational states — observed in the kinetic energy release KER spectra of O_2^+ dissociation. This phenomenon is a manifestation of the well-known Cooper minima effect [93, 95, 104]. The suppression is caused by the small dipole coupling matrix element between the relevant states leading to dissociation. The dynamics of O_2^+ in the strong laser field can be interpreted by first-order perturbation theory. We implemented such a theory to study the vibrational suppression observed in O_2^+ dissociation via the net one photon dissociation pathway, $|a\,^4\Pi_u\rangle \rightarrow |f\,^4\Pi_g - 1\omega\rangle$. In that study, we also employed THG as a source of laser pulses with a central wavelength of 260 nm ($\sim$4.76 eV) to measure the KER distribution from O_2^+ dissociation. In this appendix, we describe the alignment procedure required to generate THG laser pulses.

The schematic of the THG apparatus is shown in Fig. B.1(c) and Fig. 2.6 in section 2.3.3. We used a collinear setup to generate THG from the fundamental IR laser pulses. Three steps are necessary to generate THG laser pulses as shown in Fig. B.1(a)–(c). The setup consists of two BBO crystals, a zero-order half waveplate, a calcite crystal and four harmonic separators. The first step is to set the zero-order waveplate angle and minimize the fundamental laser pulses at the output by using a power meter as shown in Fig. B.1(a). The zero-order waveplate is necessary as described later. To generate the THG signal, the fundamental wave and second harmonic signal need to have similar polarization direction (parallel to the table in our case). In the second step, we generate

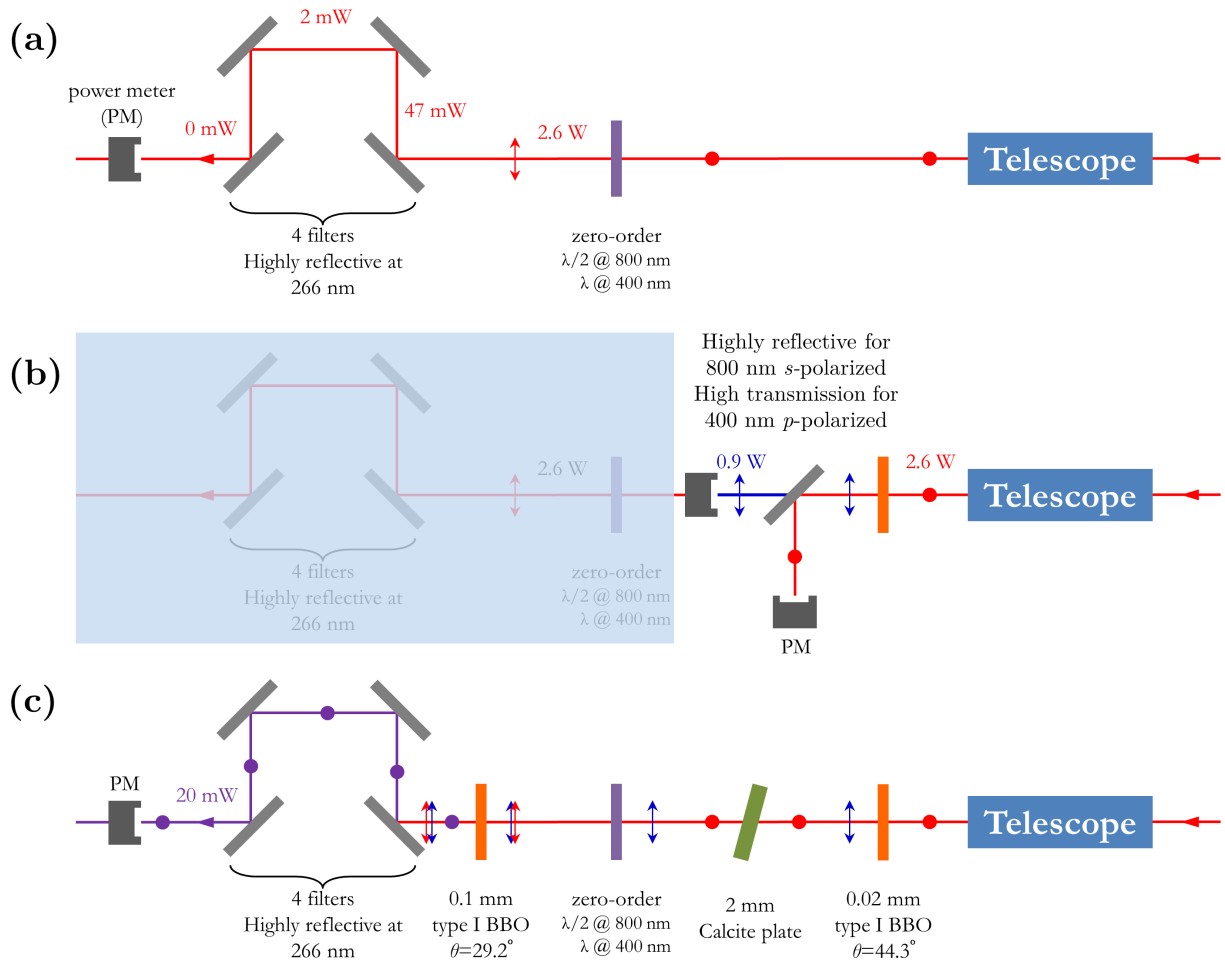

Figure B.1: (a)–(c) The schematic layouts for third harmonic generation from the fundamental laser wavelength. The laser propagates from right to left, as shown by an arrow (see text for more details).

the second harmonic by using a BBO crystal (type-I BBO d=250 μm, θ=29.2°). The angle and tilt of the BBO crystal can be adjusted by separating the fundamental pulses from the associated second harmonic and maximizing the second harmonic output power as shown schematically in Fig. B.1(b). For this purpose the compressor grating position of the driving laser can be adjusted to maximize the second harmonic generation. We were able to achieve 28–34% conversion efficiency repeatedly.

In the last step, we mix the fundamental 800 nm and generated second harmonic pulses inside the a second BBO crystal (type-I BBO d=1 mm, θ=44.3°). In order to generate the third harmonic efficiently, we need to ensure that the polarization of fundamental and second harmonic pulses are

parallel to each other (parallel to the table in our case) as well as minimizing the time delay between the pulses. After the first BBO crystal, the fundamental laser pulse and the second harmonic have perpendicular polarizations. The zero-order half waveplate rotates the polarization of the800 nm pulse by 90° without rotating the polarization of the 400 nm pulse.

The 800 and 400 nm pulses have a time delay, which is caused by propagation through the BBO crystal and the zero-order waveplate. For a type-I BBO crystal (θ=29.2°) with normal incidence, the time delay between the fundamental wavelength and second-harmonic pulses is calculated to be 194 fs/mm [156, 160] (i.e. ∼50 fs in our 250 μm BBO crystal). A calcite crystal (d=2 mm) is used to compensate the time delay between the two pulses. The calcite crystal, like the BBO crystal, is made of negative uniaxial material ($n_o > n_e$), and thus it can be used to introduce a delay to the fundamental beam (o-ray) with respect to the second harmonic (e-ray). By adjusting the tilt angle of the calcite crystal with respect to the laser beam propagation, we can compensate and fine-tune the temporal delay between the two pulses. The overall efficiency of the THG process is 2-3% relative to the input energy of the fundamental laser pulse.

Appendix C

Investigating the Momentum Distribution in the Two-color Experiment

In section 3.6, we describe our experimentally demonstrated control over spatial asymmetry in the dissociation of molecular-ion beam targets. By varying the relative phase between temporally-overlapped 790 nm and 395 nm pulses, we control the spatial asymmetry in the dissociation of D_2^+ and monitor it using coincidence 3D momentum imaging. The measured momentum distribution of D^+ fragments from the dissociation of D_2^+ using 790 nm laser pulses is shown in Fig. C.1.

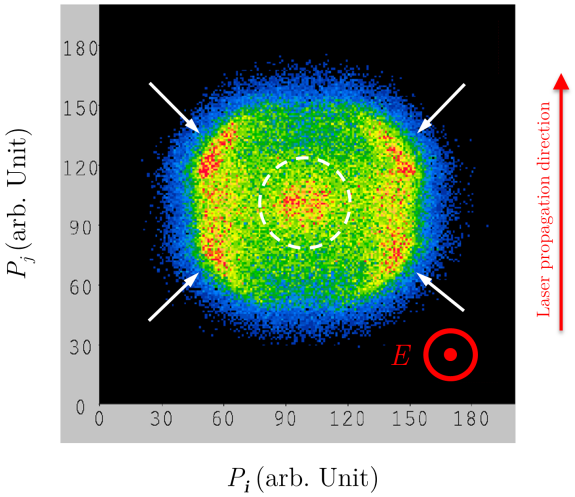

Figure C.1: Measured momentum distribution of D^+ fragments of D_2^+ dissociation into D^++D using 800 nm laser pulses. Laser polarization is along the $\hat{k}$ direction, and the laser propagation direction is along $\hat{j}$ as labeled by an arrow.

In the case of D_2^+ dissociation, breakup is strongly aligned along the laser polarization direction, $\hat{k}$, indicated by a dashed circle in Fig. C.1. In addition to the expected dissociation along the field, which is visible within the dashed circle, the momentum distribution reveals an unexpected four lobe structure perpendicular to the laser polarization direction. This structure is present when the experiment is repeated with only one color, 790 nm. Molecules that dissociate perpendicular to the laser polarization direction should result in a ring structure in the momentum distribution. However, the observed structure (indicated by arrows in Fig C.1) does not resemble a ring. Moreover, the Faraday cup is along the $\hat{i}$ direction, resulting in losses along that axis. This suggests that the outer part of the measured momentum distribution might originate from dissociation along the electric field along the $\hat{i}$ direction, and we address that issue here.

To resolve the issue described above, we repeated the measurements using the two-color collinear setup shown in Fig. C.2(a). For simplicity, the optics needed to generate SHG are physically removed from the collinear setup (the BBO and one of the calcite crystals) as shown schematically in Fig. C.2(b). We used the configuration shown in Fig. C.2(b) to investigate the structure in the momentum distribution of D_2^+ dissociation.

Figure C.3 shows the measured power transmitted for both polarization directions through a calcite crystal as a function of angle of the calcite crystal. Calcite is a uniaxial birefringent crystal consisting of an ordinary and extraordinary axis. The input polarization angle was kept fixed, perpendicular with respect to the optics table, and the rotation angle of the calcite crystal in the plane perpendicular to the propagation direction of the laser, ξ, is varied as shown in Fig. C.3. For ξ=0 the input light has only a vertical polarization component. However, changing the calcite angle by 10° results in a mixture of both polarization directions. In this case, 10% of the laser power has horizontal polarization resulting in a weak dissociation perpendicular to the main dissociation caused by the dominant vertical-polarization field.

We repeated the measurements using 790 nm laser pulses with vertical polarization traversing a calcite with ξ =0 and 15°. Figure. C.4(a) and (b) show the momentum distribution of D^+ fragments for these two angles. It is clear that Fig. C.4(b) resembles the momentum distribution

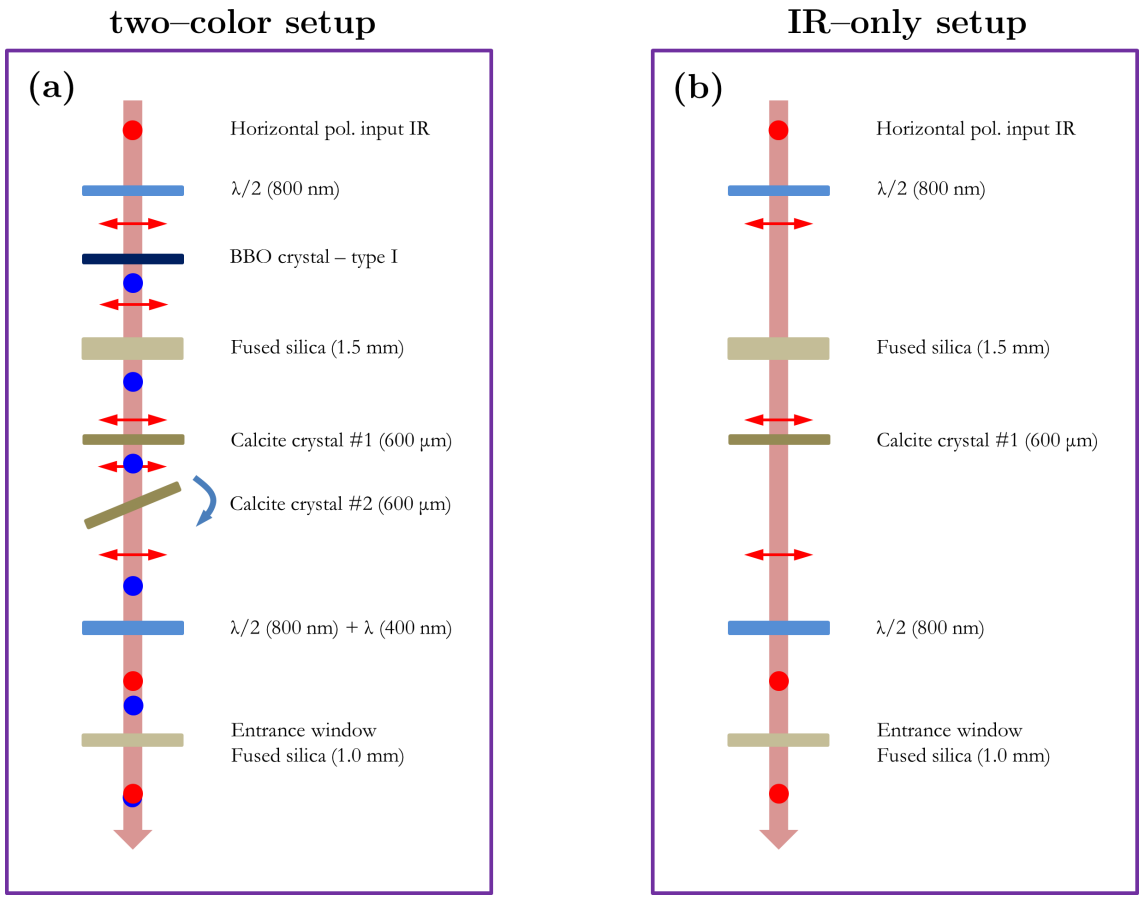

Figure C.2: (a) The schematic two-color collinear setup. (b) The schematic two-color collinear setup without the BBO crystal and one of the calcite crystals. Looking down on the table and dots represent the polarization perpendicular to the optics table (*s*-polarized).

from the two-color measurements as a result of mixing polarization components perpendicular to each other.

Once the origin of this unexpected angular distribution in the momentum spectra of our two-color measurements was understood, we were able to analyse the data by selecting the events parallel to the laser polarization direction (i.e. those within the dashed circle in Fig. C.1). Recalling the results from section 3.6.3.1, mixing the two-color pulses leads to a spatial asymmetry, which originates from interference of dissociation pathways α and γ at KER below 0.5 eV.

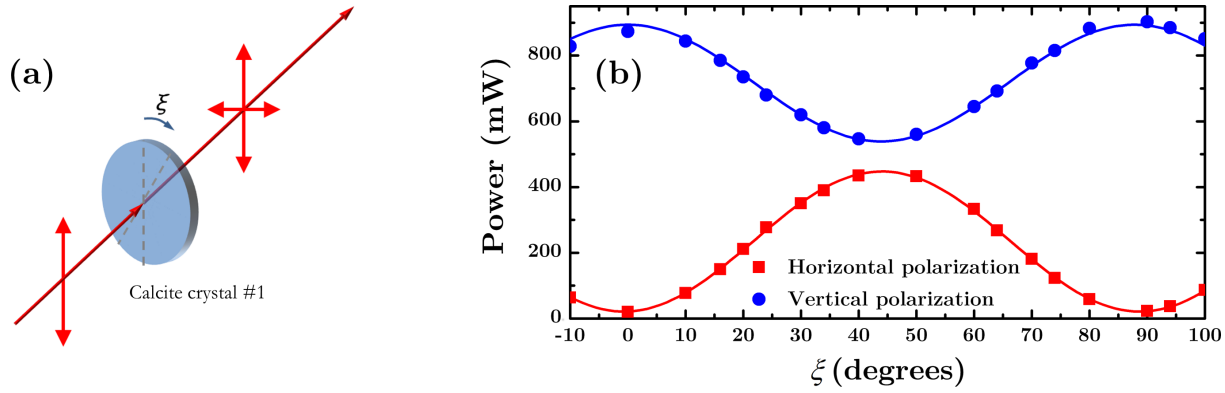

Figure C.3: (a) The schematic of IR light propagated through the calcite crystal with rotation angle ξ (b) Measured power for both IR polarizations through a calcite crystal as a function of rotation angle in the plane perpendicular to the propagation direction of the laser. The solid lines are sinusoidal fits.

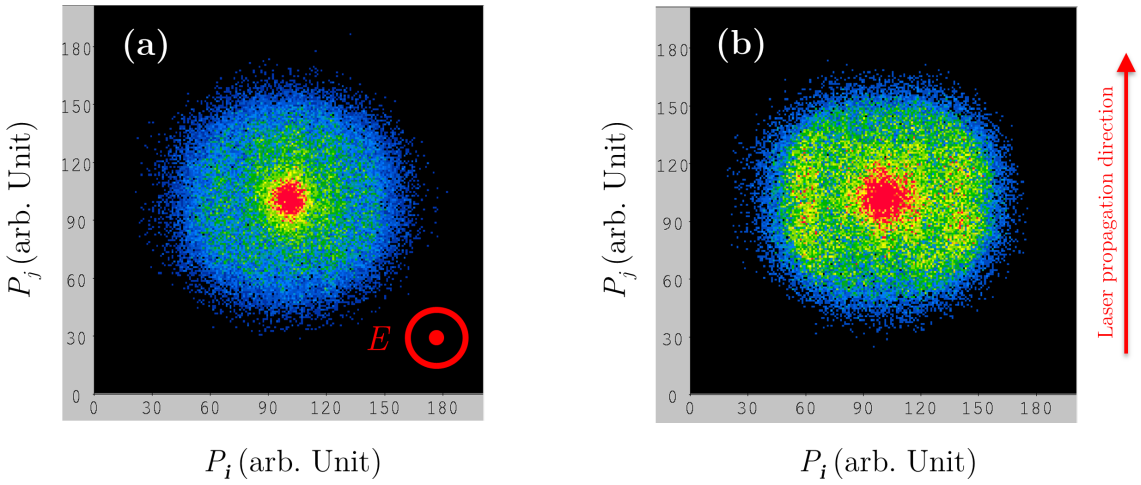

Figure C.4: Measured momentum distribution of D^+ fragments from D_2^+ dissociation into D^++D for calcite angle (a) 0° and (b) 15°, respectively.

Appendix D

Error Sources and Estimates

The sources of uncertainty and error analysis for measurements employing the coincidence 3D momentum imaging method (Chapter 3) were previously described by Gaire in Ref [198] Appendix A. In Chapter 4, we presented measurements of the CEP dependence of D^* formation from D_2 molecules in intense 5 fs laser pulses. We evaluate the kinetic energy release (KER) distributions of the D^* fragments from the measured TOF spectra as described in section 4.2.3. For a given KER and CEP value, we calculated the asymmetry and total dissociation yield (see sections 4.2.3.5 and 4.2.3.4). In this appendix, we estimate the uncertainty in these quantities.

D.1 Kinetic Energy Release

The dissociation velocities, v_L and v_R, are defined in Eqs. 4.21 and 4.22 as

$$v_i \simeq \frac{d_i \pm z}{t_i}, \tag{D.1}$$

where d is the measured distance from the interaction point located at z relative to the center of the effusive jet needle to the detector (see Fig. 4.6) and t is the true TOF. The subscript, i, denote the left and right detectors, L and R.The uncertainty in the dissociation velocity is given by

$$(\Delta v_i)^2 = \left(\frac{\partial v_i}{\partial d_i}\Delta d_i\right)^2 + \left(\frac{\partial v_i}{\partial t_i}\Delta t_i\right)^2, \tag{D.2}$$

or explicitly

$$(\Delta v_i)^2 = \left(\frac{\Delta d_i}{t_i}\right)^2 + \left(\frac{(d_i \pm z)\Delta t_i}{t_i^2}\right)^2, \tag{D.3}$$

where Δd_i and Δt_i are the uncertainties in the measured distances and TOF to the left and right detectors, respectively. The KER upon dissociation for a homonuclear molecule is given by

$$\text{KER} = \frac{1}{2}(m_1 + m_2)v_i^2, \tag{D.4}$$

The uncertainty in the KER can be written as $\Delta\text{KER} = \sqrt{\left(\frac{\partial \text{KER}}{\partial v_i}\Delta v_i\right)^2} = \frac{\partial \text{KER}}{\partial v_i}\Delta v_i$. We can simplified ΔKER as

$$\Delta\text{KER} = (m_1 + m_2)v_i\Delta v_i = \text{KER}\,\frac{2\Delta v_i}{v_i}, \tag{D.5}$$

The relative error can be written as

$$\frac{\Delta\text{KER}}{\text{KER}} = 2\frac{\Delta v_i}{v_i}. \tag{D.6}$$

For d_L ~157.7 mm with uncertainty Δd_L ~0.5 mm, and t_L ~8.1 μs for D* fragments with uncertainty Δt_L ~1 ns, we get v_L=0.0197 mm/ns with uncertainty Δv_L ~0.00006 mm/ns, i.e. $\frac{\Delta v_L}{v_L}$ ~0.3%. This results in KER of 8.1 eV with ΔKER ~9 meV, i.e. $\frac{\Delta\text{KER}}{\text{KER}}$ ~0.11%.

D.2 Angular Acceptance

The geometry of the apparatus can be a source of error in the experiment described in Chapter 4.2.3.5. Figure 4.6 displays a side view of the apparatus. The angular acceptance of D* fragments is limited by the size of the detector and the distance of the detector from the interaction point. In the experiment described in Chapter 4, this angle along the laser polarization was estimated to be 15° for detecting D* fragments and should be exactly equal for both detectors. Any deviation from this angle can result in inconsistency between experimental results and theoretical predictions.

In the experiment, the data is not collected exactly symmetrically, as the laser polarization can have a slight angle with respect to the TOF axis. Also, the interaction point can be slightly shifted from the center of the apparatus. As a result, the integration within the cones on the left and right sides are not exactly equal. This issue could be resolved by improving our detection method. For instance, adding a position-sensitive anode to both detectors could be used to generate a symmetric distribution about the polarization axis, i.e., with a similar angular acceptance range

on each detector. This position information can be further used to align the apparatus.

D.3 Asymmetry and Yield

The asymmetry (yield) is defined (see sections 4.2.3.5, 4.2.3.4 and Appendix E) as the difference (sum) between the number of D^* fragments emitted toward the left and right detectors within a cone having a 15° angle with respect to the laser polarization direction,

$$\mathcal{A}(\mathrm{KER},\varphi) = \frac{\eta(\mathrm{KER})\, M_L(\mathrm{KER},\varphi) - M_R(\mathrm{KER},\varphi)}{\langle \eta(\mathrm{KER})\, M_L(\mathrm{KER},\varphi) + M_R(\mathrm{KER},\varphi)\rangle_\varphi}, \tag{D.7}$$

where $M_{L,R}(\mathrm{KER},\varphi)$ is the number of measured events reaching the left and right detectors, respectively, for a given KER and CEP value. The number of measured events on the left and right detectors integrated over all the CEP values is defined as $M_{L,R}(KER) \equiv \langle M_{L,R}(KER,\varphi)\rangle_\varphi$. The relative detection efficiency of the two detectors can be written as $\eta\,(\mathrm{KER}) = \frac{\varepsilon_R(\mathrm{KER})}{\varepsilon_L(\mathrm{KER})} = \frac{M_R(\mathrm{KER})}{M_L(\mathrm{KER})}$, in which no difference is expected between the left and right detectors once the events are integrated over all the CEP values, $N_R\,(\mathrm{KER}) = N_L\,(\mathrm{KER})$. In our case, the asymmetry and total yield can be simplified to

$$\mathcal{A}(\mathrm{KER},\varphi) = \frac{\eta(\mathrm{KER}) M_L(\mathrm{KER},\varphi) - M_R(\mathrm{KER},\varphi)}{2M_R(\mathrm{KER})} \tag{D.8}$$

and

$$\mathcal{P}(\mathrm{KER},\varphi) = \frac{\eta(\mathrm{KER}) M_L(\mathrm{KER},\varphi) + M_R(\mathrm{KER},\varphi)}{2M_R(\mathrm{KER})}, \tag{D.9}$$

respectively. The uncertainty in the asymmetry is given by

$$\begin{aligned}\Delta\mathcal{A}(\mathrm{KER},\varphi) = \Bigg[&\Big(\frac{\partial\mathcal{A}}{\partial M_L(\mathrm{KER},\varphi)}\Delta M_L(\mathrm{KER},\varphi)\Big)^2 \\ &+\Big(\frac{\partial\mathcal{A}}{\partial M_R(\mathrm{KER},\varphi)}\Delta M_R(\mathrm{KER},\varphi)\Big)^2 \\ &+\Big(\frac{\partial\mathcal{A}}{\partial M_R(\mathrm{KER})}\Delta M_R(\mathrm{KER})\Big)^2 \\ &+\Big(\frac{\partial\mathcal{A}}{\partial \eta(\mathrm{KER})}\Delta \eta(\mathrm{KER})\Big)^2\Bigg]^{\frac{1}{2}},\end{aligned}$$

or explicitly

$$\begin{aligned}\Delta\mathcal{A}(\mathrm{KER},\varphi) = \Bigg[&\left(\frac{\eta(\mathrm{KER})}{2M_R(\mathrm{KER})}\Delta M_L(\mathrm{KER},\varphi)\right)^2 \\ &+\left(\frac{1}{2M_R(\mathrm{KER})}\Delta M_R(\mathrm{KER},\varphi)\right)^2 \\ &+\left(\frac{\eta(\mathrm{KER})\mathrm{M_L}(\mathrm{KER},\varphi)-\mathrm{M_R}(\mathrm{KER},\varphi)}{2M_R^2(\mathrm{KER})}\Delta M_R(\mathrm{KER})\right)^2 \\ &+\left(\frac{M_L(\mathrm{KER},\varphi)}{2M_R(\mathrm{KER})}\Delta\eta(\mathrm{KER})\right)^2\Bigg]^{\frac{1}{2}}.\end{aligned} \tag{D.10}$$

The uncertainty in the yield results in a similar equation,

$$\begin{aligned}\Delta\mathcal{P}(\mathrm{KER},\varphi) = \Bigg[&\left(\frac{\eta(\mathrm{KER})}{2M_R(\mathrm{KER})}\Delta M_L(\mathrm{KER},\varphi)\right)^2 \\ &+\left(\frac{1}{2M_R(\mathrm{KER})}\Delta M_R(\mathrm{KER},\varphi)\right)^2 \\ &+\left(\frac{\eta(\mathrm{KER})\mathrm{M_L}(\mathrm{KER},\varphi)+\mathrm{M_R}(\mathrm{KER},\varphi)}{2M_R^2(\mathrm{KER})}\Delta M_R(\mathrm{KER})\right)^2 \\ &+\left(\frac{M_L(\mathrm{KER},\varphi)}{2M_R(\mathrm{KER})}\Delta\eta(\mathrm{KER})\right)^2\Bigg]^{\frac{1}{2}},\end{aligned} \tag{D.11}$$

where $\Delta\eta/\eta$ can be written as $\sqrt{\left[\frac{\Delta M_L(\mathrm{KER})}{M_L(\mathrm{KER})}\right]^2+\left[\frac{\Delta M_R(\mathrm{KER})}{M_R(\mathrm{KER})}\right]^2}$. $\Delta M_{L,R}$ are given by the statistical uncertainty in the measured data, i.e. $\Delta M_L(\mathrm{KER}) = \sqrt{M_L(\mathrm{KER})}$. Using Eq. D.10, we can evaluate the error for a given KER and CEP. For instance, from Fig. 4.14 presented in Chapter 4, we can evaluate the error in the asymmetry for KER=8.6 eV and CEP=1.2π. Here, the asymmetry

is $\sim$0.2, and the corresponding error is estimated to be $\Delta\mathcal{A}$=0.03. The relative error in the asymmetry is then about $\frac{\Delta\mathcal{A}}{\mathcal{A}} = 15\%$. For clarity of presentation, we did not show the error bars in the asymmetry and yield maps in Chapter 4. We can evaluate the uncertainty in the yield in a similar manner. For the same KER and CEP noted above, the yield is 0.2, and the relative error in the yield is about $\frac{\Delta\mathcal{P}}{\mathcal{P}} = 33\%$.

Appendix E

Correcting the Offset in the Asymmetry and Yield

In section 4.2.3.5 and 4.2.3.4, we discussed the asymmetry and total dissociation yield of D^* formation from D_2 molecules. The difference in the detection efficiency for the left and right detectors results in an offset in the asymmetry and yield. However, theory predicts no difference between left and right detectors once the events are integrated over all the CEP values.

The offset in the total yield can be corrected as explained below. Recall that the measured number of events on the left and right detectors in the D^* case is given by

$$M_{L,R}(\mathrm{KER}, \varphi) = \varepsilon_{L,R}(\mathrm{KER})\ N_{L,R}(\mathrm{KER}, \varphi), \tag{E.1}$$

where $\varepsilon_{L,R}(\mathrm{KER})$ is the total detection efficiency on the left or right side for a given KER value, respectively, and $N_{L,R}(\mathrm{KER}, \varphi)$ is the true number of events. We can define the total yield as a function of the true number of events

$$\mathcal{P}(\mathrm{KER}, \varphi) = \frac{N_L(\mathrm{KER}, \varphi) + N_R(\mathrm{KER}, \varphi)}{\langle N_L(\mathrm{KER}, \varphi) + N_R(\mathrm{KER}, \varphi)\rangle_\varphi} \tag{E.2}$$

where the cycle average yield, $\langle N_L(\mathrm{KER}, \varphi) + N_R(\mathrm{KER}, \varphi)\rangle_\varphi$, is defined as

$$\frac{1}{2\pi}\int_0^{2\pi} (N_L(\mathrm{KER}, \varphi) + N_R(\mathrm{KER}, \varphi))\, \mathrm{d}\varphi.$$

Substituting Eq. E.1 into Eq. E.2 yields

$$\mathcal{P}(\mathrm{KER},\varphi)=\frac{\frac{1}{\varepsilon_L(\mathrm{KER})}M_L(\mathrm{KER},\varphi)+\frac{1}{\varepsilon_R(\mathrm{KER}}M_R(\mathrm{KER},\varphi)}{\langle\frac{1}{\varepsilon_L(\mathrm{KER})}M_L(\mathrm{KER},\varphi)+\frac{1}{\varepsilon_R(\mathrm{KER}}M_R(\mathrm{KER},\varphi)\rangle_\varphi} \tag{E.3}$$

which can be written as

$$\mathcal{P}(\mathrm{KER},\varphi)=\frac{\eta(\mathrm{KER})\,M_L(\mathrm{KER},\varphi)+M_R(\mathrm{KER},\varphi)}{\langle\eta(\mathrm{KER})\,M_L(\mathrm{KER},\varphi)+M_R(\mathrm{KER},\varphi)\rangle_\varphi}, \tag{E.4}$$

where $\eta\left(\mathrm{KER}\right)\equiv\varepsilon_R\left(\mathrm{KER}\right)/\varepsilon_L\left(\mathrm{KER}\right)$ is the relative detection efficiency of the two detectors, on the left and right sides.

To determine $\eta\left(\mathrm{KER}\right)$ we divide $M_L\left(\mathrm{KER}\right)$ by $M_R\left(\mathrm{KER}\right)$ (i.e. the KER spectrum of the right side by that of the left-side averaged over all the CEP) and get

$$\frac{M_R\left(\mathrm{KER}\right)}{M_L\left(\mathrm{KER}\right)}=\frac{\varepsilon_R\left(\mathrm{KER}\right)}{\varepsilon_L\left(\mathrm{KER}\right)}\frac{N_R\left(\mathrm{KER}\right)}{N_L\left(\mathrm{KER}\right)}.$$

However, theory predicts no left-right difference once the events are integrated over all CEP values. Therefore

$$\frac{N_R\left(\mathrm{KER}\right)}{N_L\left(\mathrm{KER}\right)}=1$$

leading to

$$\eta\left(\mathrm{KER}\right)\equiv\frac{\varepsilon_R\left(\mathrm{KER}\right)}{\varepsilon_L\left(\mathrm{KER}\right)}=\frac{M_R\left(\mathrm{KER}\right)}{M_L\left(\mathrm{KER}\right)}. \tag{E.5}$$

Finally, using the expression for $\eta(\mathrm{KER})$ above the total yield can be corrected to eliminate the offset using Eq. E.4.

The offset in the spatial asymmetry can be corrected following a similar procedure. Explicitly we write

$$\mathcal{A}(\mathrm{KER},\varphi)=\frac{N_L(\mathrm{KER},\varphi)-N_R(\mathrm{KER},\varphi)}{\langle N_L(\mathrm{KER},\varphi)+N_R(\mathrm{KER},\varphi)\rangle_\varphi}, \tag{E.6}$$

which after a few lines of algebra yields

$$\mathcal{A}(\mathrm{KER},\varphi)=\frac{\eta(\mathrm{KER})\,M_L(\mathrm{KER},\varphi)-M_R(\mathrm{KER},\varphi)}{\langle\eta(\mathrm{KER})\,M_L(\mathrm{KER},\varphi)+M_R(\mathrm{KER},\varphi)\rangle_\varphi}. \tag{E.7}$$

Appendix F

Centering CEP-Dependent Asymmetry and Yield Oscillations About Zero

In section 4.2.3.5 and 4.2.3.4, we discussed the asymmetry and total dissociation yield of D^* formation from D_2 molecules. The asymmetry is typically defined [80, 81, 88] as

$$\mathcal{A}'(\mathrm{KER},\varphi) = \frac{N_L(\mathrm{KER},\varphi) - N_R(\mathrm{KER},\varphi)}{N_L(\mathrm{KER},\varphi) + N_R(\mathrm{KER},\varphi)},$$

then $A'\,(KER,\varphi)$ might include a CEP effect due to the denominator (i.e. yield) and not just the asymmetry. Therefore, we use the cycle average value for the denominator, which yields

$$\mathcal{A}(\mathrm{KER},\varphi) = \frac{N_L(\mathrm{KER},\varphi) - N_R(\mathrm{KER},\varphi)}{\int_0^{2\pi}[N_L(\mathrm{KER},\varphi) + N_R(\mathrm{KER},\varphi)]\,d\varphi},$$

With this definition, $\mathcal{A}(\mathrm{KER},\varphi)$ – which we call a normalized left-right difference – is not guaranteed to oscillate around zero, but may oscillate around an arbitrary number given by

$$\int_0^{2\pi} \mathcal{A}(\mathrm{KER},\varphi)\,d\varphi = \int_0^{2\pi} \frac{N_L(\mathrm{KER},\varphi) - N_R(\mathrm{KER},\varphi)}{\int_0^{2\pi}[N_L(\mathrm{KER},\varphi) + N_R(\mathrm{KER},\varphi)]\,d\varphi} d\varphi,$$

which can be rewritten as

$$\int_0^{2\pi} \mathcal{A}(\mathrm{KER},\varphi)\,d\varphi = \frac{1}{\int_0^{2\pi}[N_L(\mathrm{KER},\varphi) + N_R(\mathrm{KER},\varphi)]\,d\varphi} \int_0^{2\pi} [N_L(\mathrm{KER},\varphi) - N_R(\mathrm{KER},\varphi)]\,d\varphi.$$

Note that the first term depends only on KER.

It is clear from the expression above that the asymmetry parameter, $\mathcal{A}(\mathrm{KER},\varphi)$, is very likely to oscillate around an arbitrary number that depends on any artificial left-right asymmetry in the detection system (caused by, for example, detector efficiencies, difference in the solid angles or alignment and, etc.), which we know is far from being perfect. Therefore, an additional correction is needed to assure that the oscillations will be around zero. The correct definition of the asymmetry parameter, which oscillates about zero, requires subtraction of the cycle averaged normalized left-right difference, and is given by

$$\mathcal{A}(\mathrm{KER},\varphi)=\frac{[N_L(\mathrm{KER},\varphi)-N_R(\mathrm{KER},\varphi)]}{\int_0^{2\pi}[N_L(\mathrm{KER},\varphi)+N_R(\mathrm{KER},\varphi)]\,d\varphi}-\frac{\frac{1}{2\pi}\int_0^{2\pi}[N_L(\mathrm{KER},\varphi)-N_R(\mathrm{KER},\varphi)]\,d\varphi}{\int_0^{2\pi}[N_L(\mathrm{KER},\varphi)+N_R(\mathrm{KER},\varphi)]\,d\varphi}.$$

It can be rewritten in a simpler (see Eq. 4.27 in section 4.2.3.5) form as

$$\mathcal{A}(\mathrm{KER},\varphi)=\frac{[N_L(\mathrm{KER},\varphi)-N_R(\mathrm{KER},\varphi)]-\frac{1}{2\pi}\int_0^{2\pi}[N_L(\mathrm{KER},\varphi)-N_R(\mathrm{KER},\varphi)]d\varphi}{\int_0^{2\pi}[N_L(\mathrm{KER},\varphi)+N_R(\mathrm{KER},\varphi)]d\varphi}.$$

To verify that the expression above oscillates around zero, we integrate it over one cycle

$$\int_0^{2\pi}\mathcal{A}(\mathrm{KER},\varphi)d\varphi=$$
$$\int_0^{2\pi}\frac{[N_L(\mathrm{KER},\varphi)-N_R(\mathrm{KER},\varphi)]-\frac{1}{2\pi}\int_0^{2\pi}[N_L(\mathrm{KER},\varphi)-N_R(\mathrm{KER},\varphi)]\,d\varphi}{\int_0^{2\pi}[N_L(\mathrm{KER},\varphi)+N_R(\mathrm{KER},\varphi)]d\varphi}d\varphi=0$$

Finally, one should note that this definition of the asymmetry has some similarities to the expression we have for the yield parameter,

$$\mathcal{P}(\mathrm{KER},\varphi)=\frac{[N_L(\mathrm{KER},\varphi)+N_R(\mathrm{KER},\varphi)]-\frac{1}{2\pi}\int_0^{2\pi}[N_L(\mathrm{KER},\varphi)+N_R(\mathrm{KER},\varphi)]d\varphi}{\int_0^{2\pi}[N_L(\mathrm{KER},\varphi)+N_R(\mathrm{KER},\varphi)]d\varphi}.$$

To verify that this final expression will oscillate around zero we integrate it over one cycle

$$\int_0^{2\pi}\mathcal{P}(\mathrm{KER},\varphi)d\varphi=$$
$$\int_0^{2\pi}\frac{[N_L(\mathrm{KER},\varphi)+N_R(\mathrm{KER},\varphi)]-\frac{1}{2\pi}\int_0^{2\pi}[N_L(\mathrm{KER},\varphi)+N_R(\mathrm{KER},\varphi)]\,d\varphi}{\int_0^{2\pi}[N_L(\mathrm{KER},\varphi)+N_R(\mathrm{KER},\varphi)]d\varphi}d\varphi=0$$

Appendix G

Electronics

The electronics for the measurements employing the laser-induced molecular dissociation imaging LIMDI method is described previously in Nora Kling's Ph.D. thesis [178] Appendix A. Figure G.1 illustrate the electronics used in the D* measurements from D_2 molecules presented in Chapter 4.

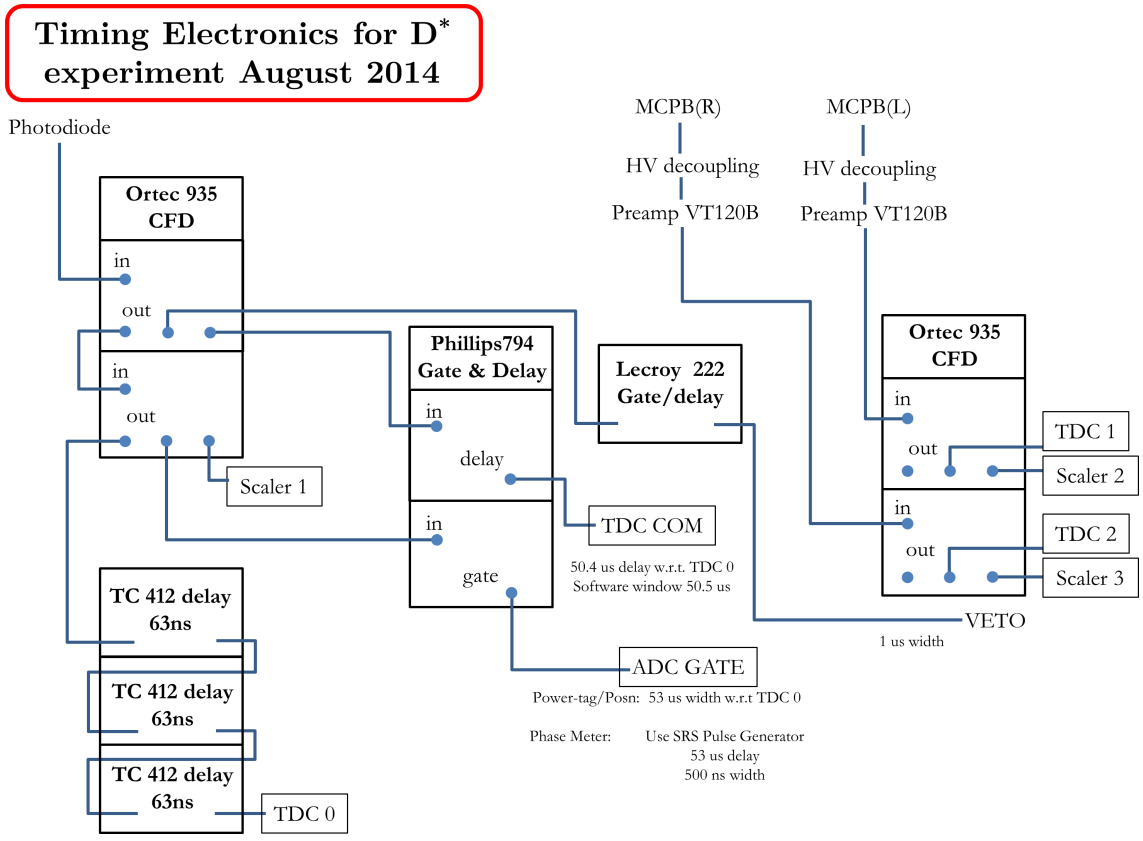

Figure G.1: Electronics and connections for experiments presented in Chapter 4.

Appendix H

Voltages Applied for State-Selective Measurements of D$^*(nl)$

In section 4.5.0.2, we employed the field ionization method to select different subsets of the principle quantum numbers, n, by adjusting the electric-field strength between a pair of meshes placed in front of the detectors (see Fig. 4.5). For instance, the electric field that can ionize fragments in the Rydberg state n_{FI} will ionize all fragments with $n \geq n_{FI}$ with a probability close to unity. The ionization probability for a hydrogen atom in a static electric field, calculated classically by Rakovic and Chu [388], is plotted in Fig. 4.7(a). By choosing an appropriate electric field strength between the two meshes (M_1 and M_2), we were able to ionize and reject the higher part of the population. As a result, a well-defined subset of quantum number n can be measured. Table H.1 shows the mesh and detector voltages with associated measured quantum numbers,

	M_1 (V)	M_2 (V)	MCP_{front} (V)	MCP_{back} (V)	Anode (V)
$2 \leq n \leq 19$	100	1500	-200	1830	1930
$2 \leq n \leq 23$	150	800	-200	1830	1930
$2 \leq n \leq 27$	150	500	-200	1830	1930
$2 \leq n \leq 31$	150	350	-100	1930	2030
$2 \leq n \leq 38$	0	85	-100	1930	2030

Table H.1: Table of voltages used on the detectors and meshes with the associated measured quantum numbers. The voltage difference on the MCP stack is kept constant at 2030 V to keep the amplification of the detector fixed.